Local spectroscopy of atomically thin MoS$_2$: electronic states at 1D defects, charge transfer and screening

Inaugural-Dissertation
zur
Erlangung des Doktorgrades
der Mathematisch-Naturwissenschaftlichen Fakultät
der Universität zu Köln

vorgelegt von
Clifford David Hughes Murray
aus Miami

Köln 2020

Erster Berichterstatter: Prof. Dr. Thomas Michely
Zweiter Berichterstatter: Prof. Dr. Paul van Loosdrecht

Vorsitzender der Prüfungskommission: Prof. Dr. Achim Rosch
Tag der mündlichen Prüfung: 24.09.2020

Die vorliegende Dissertation wurde von der Mathematisch-Naturwissenschaftlichen Fakultät der Universität zu Köln angenommen.

Abstract

The last decade has seen immense research effort dedicated to atomically thin transition metal dichalcogenide layers. This owes itself to their wide range of exotic properties and to the possibility of combining them with other two-dimensional materials, such as graphene, in a heterostructure. There is particular interest in MoS_2 and its analogues $MoSe_2$, WS_2 and WSe_2 because they are intrinsically semiconducting, opening up new possibilities for electronic and optoelectronic devices at the nanoscale. Transition metal dichalcogenide layers are typically prepared by exfoliation from the bulk, chemical vapour deposition or molecular beam epitaxy. The last offers samples of superlative quality and of scalable size, but for many years the community struggled to grow transition metal disulfides – including the paradigmatic MoS_2 – by this method.

Thanks to recent advances by our group, we can synthesise high-quality MoS_2 layers on graphene on Ir(111) by a molecular beam epitaxy variant known as *van der Waals epitaxy*. Performed under ultra-high vacuum conditions, the MoS_2 surface is kept free of adsorbates and local spectroscopic investigation is facilitated. Furthermore, the growth method leads to excellent epitaxial alignment of the MoS_2 layer with its weakly interacting substrate. This results in the only common defects being well-defined and one-dimensional: atomically straight island edges, and mirror twin boundaries which form due to the reduced symmetry of MoS_2 (three-fold) compared to graphene (six-fold). As the fabrication of transition metal dichalcogenides improves, such defects will become increasingly relevant for devices.

This thesis studies the electronic properties of two-dimensional MoS_2 and its one-dimensional defects, and how these properties are dependent on their environment. This is principally performed with scanning tunnelling microscopy and spectroscopy at 5 K, on the substrate graphene/Ir(111) which only weakly influences the MoS_2 layer. The main focus is on 4|4E mirror twin boundaries, which represent metallic, one-dimensional wires. Their one-dimensionality, their electronic isolation from the semiconducting layer, and the lack of screening in two dimensions leads to extraordinary electron-interaction behaviour, both in and around the boundary. The thesis is composed of four manuscripts, each presented in their entirety. They are bookended by an introduction of relevant theoretical and experimental background information, and by a discussion of the outcomes, possible future experiments, and a brief look at the state of play within the community.

First, the electronic band structures of mono-, bi- and trilayer MoS_2 on graphene/Ir(111) are characterised by 'comprehensive' tunnelling spectroscopy, whereby three different spectroscopic modes are used and compared. This shows monolayer MoS_2 to be quasi-freestanding on this substrate, with a 2.53 eV band gap size which is larger than that reported for other metallic substrates. Through this com-

prehensive spectroscopy, we can also identify critical point energies within the MoS_2 band structure and compare them with theoretical predictions. It additionally allows us to follow the dynamics of interlayer coupling as the MoS_2 thickness is increased from mono- up to trilayer. Through the MoS_2 case study and thorough technical discussion, this work also demonstrates that traditional tunnelling spectroscopy (only using constant height mode) is inadequate for accurate estimation of the electronic band gap.

Second, electronic states which exist along the axis of MoS_2 4|4E mirror twin boundaries are examined. These boundaries can be viewed as one-dimensional wires of finite length. In high-resolution tunnelling spectroscopy they exhibit a wire-length-dependent energy gap around the Fermi level, quantised energy levels beyond this, and periodic modulation of the electron density along their axis. Together with density functional theory and model Hamiltonian calculations, we explain our observations to be unambiguous evidence for the existence of a confined Tomonaga-Luttinger liquid. Due to the lack of electrostatic screening, the electrons experience a strong Coulomb interaction and act as coherent, bosonic excitations. Moreover, the electronic excitations in the wire are split into collective modes of spin and charge density, consistent with our spectroscopic data. This represents the first real-space observation of spin-charge separation, and provides a rare opportunity to probe Tomonaga-Luttinger liquid physics locally.

In the third manuscript, we investigate how the surrounding MoS_2 layer is influenced by its line defects, such as island edges and the 4|4E and 4|4P mirror twin boundary types. Focussing on the 4|4E boundary again, we find that it causes a large upwards bending of the MoS_2 valence and conduction bands over a 5 nm range. Remarkably, this occurs stepwise in the valence band, producing characteristic quantised states. Using tunnelling spectroscopy, density functional theory and electrostatic continuum modelling, we elucidate the origin of the bending and quantisation. Inherent interface polarisation charge is counteracted by charge from the surrounding layer and charge donated by the substrate, often leaving the line defects with an excess electron density. The resultant electrostatic potential bends the MoS_2 bands, and creates a hole-confining quantum well. Additionally, the boundary is found to suppress the transport of holes across it, leaving independent quantum wells on either side.

Finally, the three previous manuscripts are built upon when we modify the graphene/Ir(111) substrate through Eu- or O- intercalation. This changes the electronic environment of the MoS_2 layer, but keeps it chemically pristine with graphene acting as a buffer layer. Via tunnelling spectroscopy, the electrostatic response of MoS_2 can be observed in its band structure, the states confined along mirror twin boundaries and the quantised band bending around them. The effects are strongest in MoS_2 on graphene/Eu/Ir(111), where the Eu strongly n-dopes the graphene. This leads to n-gating of MoS_2 and large band gap renormalisation due to the increased screening efficiency in graphene. Meanwhile, more electrons are donated to the 4|4E boundary – this is evidenced by a changed periodicity of its confined states. In the band bending, the boundary charge is better screened by the heavily doped graphene, leading to a much narrower potential well. The O-intercalation layer has the opposite effect; the boundary charge experiences weaker screening due to decoupling from Ir, leading to a wider potential well. This in turn affects the quantised valence band states. In both cases, the band bending and resultant quantised states can be reproduced by electrostatic modelling.

In the Scientific Appendix we show that the graphene/Ir(111) moiré causes a superperiodic potential which locally modulates the $\mathrm{MoS_2}$ band structure by $30\,\mathrm{meV}$, motivating further studies with more strongly corrugated substrates. Additionally, we characterise the electronic properties of two point defect types in $\mathrm{MoS_2}$, revealing their distinctly different in-gap states and their electrostatic influence on their surroundings.

Deutsche Kurzzusammenfassung
(German Abstract)

Im letzten Jahrzehnt wurden immense Forschungsanstrengungen für atomar dünne Übergangsmetalldichalkogenide unternommen. Dies verdanken sie ihrer breiten Vielfalt an exotischen Eigenschaften und der Möglichkeit, sie mit anderen zweidimensionalen Materialien, wie z.B. Graphen, in einer Heterostruktur zu kombinieren. Besonderes Interesse besteht an MoS_2 und seinen Analoga $MoSe_2$, WS_2 und WSe_2, da sie von Natur aus halbleitend sind und neue Möglichkeiten für elektronische und optoelektronische Bauelemente im Nanobereich eröffnen. Übergangsmetalldichalkogenid-Schichten werden üblicherweise durch Exfoliation, chemische Gasphasenabscheidung oder Molekularstrahlepitaxie hergestellt. Letztere ergibt Proben von hervorragender Qualität und skalierbarer Größe, aber viele Jahre lang hatte die Community Mühe, Übergangsmetalldisulfide – wie das paradigmatische MoS_2 – mit dieser Methode zu wachsen.

Dank der jüngsten Fortschritte unserer Gruppe können wir mittels einer Molekularstrahlepitaxie-Variante, die als *van-der-Waals-Epitaxie* bekannt ist, hochwertige MoS_2-Schichten auf Graphen auf Ir(111) herstellen. Die unter Ultrahochvakuumbedingungen durchgeführte Epitaxie hält die MoS_2-Oberfläche frei von Adsorbaten und erleichtert lokale spektroskopische Untersuchungen. Darüber hinaus führt die Wachstumsmethode zu einer ausgezeichneten epitaktischen Ausrichtung der MoS_2-Schicht mit ihrem schwach wechselwirkenden Substrat. Dies führt dazu, dass die einzigen häufigen Defekte gut definiert und eindimensional sind: Atomar gerade Inselkanten und Zwillingsgrenzen, die sich aufgrund der reduzierten Symmetrie von MoS_2 (dreifach) im Vergleich zu Graphen (sechsfach) bilden. In dem Maße, wie sich die Herstellung von Übergangsmetall-Dichalkogeniden verbessert, werden solche Defekte für Bauelemente zunehmend relevant werden.

Diese Arbeit untersucht die elektronischen Eigenschaften von zweidimensionalen MoS_2 und seinen eindimensionalen Defekten und wie diese Eigenschaften von ihrer Umgebung abhängen. Dies wird hauptsächlich mit Rastertunnelmikroskopie und -spektroskopie bei 5K und auf dem nur schwach wechselwirkenden Substrat Graphen/Ir(111) durchgeführt. Das Hauptaugenmerk liegt hierbei auf den 4|4E-Zwillingsgrenzen, die metallische, eindimensionale Drähte darstellen. Ihre elektronische Isolierung von der halbleitenden Schicht und die fehlende Abschirmung in zwei Dimensionen führt zu einem außergewöhnlichen Verhalten der elektronischen Wechselwirkung, sowohl in als auch um die Korngrenze herum. Die Arbeit besteht aus vier Manuskripten, die in ihrer Gesamtheit präsentiert werden. Sie werden durch eine Einführung mit relevanten theoretischen und experimentellen Hintergrundinformationen so-

wie durch eine Diskussion der Ergebnisse, möglicher zukünftiger Experimente und einen kurzen Blick auf den Stand der Dinge in der Community ergänzt.

Zunächst werden die elektronischen Bandstrukturen von Mono-, Bi- und Trilagen MoS_2 auf Graphen/Ir(111) durch „comprehensive“ Tunnelspektroskopie charakterisiert, wobei drei verschiedene spektroskopische Moden verwendet und verglichen werden. Dies ergibt zum einen, dass Monolage MoS_2 auf Graphen/Ir(111) nahezu freistehende Eigenschaften zeigt, und zum anderen, dass die elektronische Bandlücke mit 2,53 eV größer ist, als die für MoS_2 auf jedem anderen bisher untersuchten metallischen Substrat. Durch diese comprehensive Spektroskopie können wir zusätzlich kritische Punktenergien innerhalb der MoS_2-Bandstruktur identifizieren und mit theoretischen Vorhersagen vergleichen. Ferner sind wir in der Lage, die Dynamik der Orbitalkopplung zwischen den Lagen zu studieren, wenn beispielsweise statt einer Monolage eine Trilage MoS_2 untersucht wird. Überdies zeigen die Ergebnisse dieser Fallstudie am Beispiel von MoS_2, dass traditionelle Tunnelspektroskopie (nur unter Verwendung des sogenannten „constant height“-Modus) nur eine unzureichende Beschreibung der elektronischen Bandstruktur und Bandlücke ermöglicht.

Im zweiten Teil werden elektronische Zustände untersucht, die entlang der Achse von MoS_2 4|4E-Zwillingsgrenzen existieren. Diese Korngrenzen können prinzipiell wie eindimensionale Drähte endlicher Länge betrachtet werden. In der hochauflösenden Tunnelspektroskopie zeigen sie um das Fermi-Niveau eine Energielücke, deren Größe entscheidend von der realen Länge des Drahtes abhängt. Darüber hinaus werden in der elektronischen Zustandsdichte quantisierte Energieniveaus beobachtet, die entlang des Drahtes moduliert sind. Dichtefunktionaltheorie- und Modell-Hamilton-Berechnungen erlauben uns, unsere Beobachtungen als einen eindeutigen Beweis für die Existenz einer eingeschlossenen Tomonaga-Luttinger-Flüssigkeit zu erklären. Aufgrund der fehlenden Abschirmung erfahren die Elektronen eine starke Coulomb-Wechselwirkung und wirken als kohärente, bosonische Anregungen. Darüber hinaus werden die elektronischen Anregungen im Draht in kollektive Modi von Spin- und Ladungsdichte aufgespalten, was mit unseren spektroskopischen Daten übereinstimmt. Dies stellt die erste Beobachtung der Spin-Ladungs-Trennung im realen Raum dar und bietet eine seltene Gelegenheit, die Physik der Tomonaga-Luttinger-Flüssigkeit lokal zu untersuchen.

Im dritten Manuskript untersuchen wir, wie die MoS_2-Schicht durch ihre Liniendefekte, wie beispelsweise Inselkanten, 4|4E- oder 4|4P-Zwillingsgrenzen, beeinflusst wird. Am Beispiel der 4|4E-Korngrenze stellen wir fest, dass diese eine starke Aufwärtsbiegung der MoS_2-Valenz- und Leitungsbänder über einen Bereich von 5 nm verursacht. Bemerkenswerterweise geschieht dies im Valenzband schrittweise, wodurch charakteristische quantisierte Zustände entstehen. Mittels Tunnelspektroskopie, Dichtefunktionaltheorie und elektrostatischer Kontinuumsmodellierung klären wir den Ursprung der Biegung und Quantisierung auf. Der inhärenten Grenzlinienpolarisationsladung wird durch Umgebungsladung und Ladung, die vom Substrat abgegeben wird, entgegengewirkt, wodurch die Liniendefekte oft mit einer überschüssigen Elektronendichte zurückbleiben. Das resultierende elektrostatische Potential biegt die MoS_2-Bänder und erzeugt dadurch einen Quantentopf für die Löcher in der Bandstruktur. Zusätzlich wird festgestellt, dass die Korngrenze den Transport von Löchern über sie hinweg unterdrückt, sodass auf beiden Seiten unabhängige Quantentöpfe zurückbleiben.

Schließlich bauen wir auf den drei vorhergehenden Manuskripten auf, wenn wir das Graphen/Ir(111)-Substrat durch Eu- oder O-Interkalation modifizieren. Dies verändert die elektronische Umgebung der MoS_2-Schicht, hält sie aber chemisch rein, wobei das Graphen als Pufferschicht fungiert. Mit Hilfe von Tunnelspektroskopie kann der elektrostatische Effekt der Interkalation auf die Bandstruktur der MoS_2-Schicht, den entlang der Zwillingsgrenzen eingeschlossenen Zuständen, und der quantisierten Bandverbiegung in deren Nähe beobachtet werden. Die Effekte sind am stärksten in MoS_2 auf Graphen/Eu/Ir(111), hervorgerufen durch die starke n-Dotierung des Graphens durch das Eu. Dies führt zu einem n-Gating von MoS_2 und einer daraus resultierenden Renormierung der Bandlücke aufgrund der erhöhten Abschirmungseffizienz in Graphen. Außerdem werden zusätzliche Elektronen in die 4|4E-Korngrenze übertragen, was sich durch eine veränderte Periodizität ihrer eingeschlossenen Zustände äußert. In direkter Umgebung der 4|4E-Korngrenzen hat die Interkalation zur Folge, dass die Ladung auf der Korngrenze durch das stark dotierte Graphen besser abgeschirmt wird, was zu einer wesentlich schmaleren Potentialsenke führt. Interkalation mit O hat den gegenteiligen Effekt: Die Grenzladung erfährt durch die Entkopplung von Ir eine schwächere Abschirmung, was zu einer breiteren Potentialsenke führt. Dies wirkt sich wiederum auf die quantisierten Valenzbandzustände aus. In beiden Fällen können die Potentialsenken und die daraus resultierende Quantisierung mit elekrostatischer Modellierung reproduziert werden.

Überdies zeigen wir im letzen Kapitel, dem *Scientific Appendix*, dass das Graphen/Ir(111)-Moiré ein superperiodisches Potential verursacht, das die MoS_2-Bandstruktur lokal mit 30 meV moduliert und damit weitere Studien mit stärker gewellten Substraten motiviert. Zusätzlich charakterisieren wir die elektronischen Eigenschaften von zwei Punktdefekttypen in MoS_2, wobei wir ihre deutlich unterschiedlichen In-Gap-Zustände und den elektrostatischen Einfluss auf ihre Umgebung aufdecken.

Frequently used Acronyms and Abbreviations

1D	-	one-dimensional
2D	-	two-dimensional
3D	-	three-dimensional
ARPES	-	angle-resolved photoemission spectroscopy
BL	-	bilayer
BZ	-	Brillouin zone
CB	-	conduction band
CDW	-	charge density wave
CVD	-	chemical vapor deposition
DFT	-	density functional theory
(L)DOS	-	(local) density of states
FT	-	Fourier transformation
GB	-	grain boundary
Gr	-	graphene
h-BN	-	hexagonal boron nitride
HOPG	-	highly oriented pyrolytic graphite
LEED	-	low-energy electron diffraction
MBE	-	molecular beam epitaxy
ML	-	monolayer
MTB	-	mirror twin boundary
STM	-	scanning tunnelling microscopy
STS	-	scanning tunnelling spectroscopy
TLL	-	Tomonaga-Luttinger liquid
TMDC	-	transition metal dichalcogenide
UHV	-	ultra-high vacuum
VB	-	valence band
vdW	-	van der Waals
vdWE	-	van der Waals epitaxy
zz	-	zigzag

Contents

PART I

Introduction and Background

CHAPTER 1

Overview

One of the amusing quirks in the advent of two-dimensional (2D) materials is that some of these layers have been in our lives since time immemorial, ubiquitous yet inaccessible. In the first week of my doctorate we installed a pyrite (FeS_2) evaporator onto the vacuum chamber. Beforehand, a sketch of the geometry was made with a graphite pencil and a few flakes of once-elusive graphene were isolated unwittingly on paper. One of our final steps was to lubricate the manipulator screw thread using a thick, grey paste: molybdenum disulfide (MoS_2). Bulk, 3D MoS_2 has been used as a dry lubricant for centuries because of its stability at high temperatures [4], such as those involved in the bake-out of an ultra-high vacuum (UHV) system. Another key feature of dry lubricants such as bulk MoS_2 or graphite is their low friction coefficient [5]. This is principally due to their structure as layered materials: they exhibit strong in-plane covalent bonding but only weak van der Waals (vdW) bonding between the planes, meaning that the layers can be made to slide relative to each other. It is the same quality which enables the solid graphite core of a pencil to shed a few of its layers on paper.

Despite their ubiquity as bulk constituents, and half a century of theoretical prophecy [6], the age of 2D materials could only begin once they were isolated under controlled conditions in 2004 [7,8]. These early successes took advantage of the weak vdW forces to exfoliate – simply peel off – individual layers in a 'top-down' approach. Since then, new avenues have opened based on 'bottom-up' synthesis, whereby the necessary constituent atoms or molecules are supplied and the growth takes place on a substrate. Though typically not yet offering the large-wafer quality of exfoliated samples, these bottom-up techniques have the scalability needed for an industry-level implementation of 2D materials in useable devices [9–11], and single crystals of excellent quality can be grown in UHV [12].

2D materials are attractive for electronics and optoelectronics. This is due to their two-dimensionality in itself, of obvious benefit where constantly expanding computing capabilities should be squeezed into ever-smaller gadgets. Moreover, it is due to the remarkable physical properties which emerge *as a consequence of* two-dimensionality. In 2D, electrons cannot avoid each other: they are quantum confined in the plane and their interactions with each other are greatly enhanced. Because 2D materials are made up entirely of surface, they are also extremely sensitive to their environment.

Despite the popularity of graphene and the many exciting results that have been achieved with it, one inconvenience of this material persists. Modern electronic devices are based on semiconductors, the small but finite band gap of which allows electrical currents to be switched on and off. In its intrinsic form, graphene has no band gap; it is a semi-metal. Hexagonal boron nitride (h-BN) – probably the second-most popular 2D material – does not tick the box either. It has many interesting properties and uses, but is a wide-gap insulator. Thus the call for 2D semiconductors is answered by single layer MoS_2 and a few of its transition metal dichalcogenide (TMDC) cousins, such as $MoSe_2$ and WS_2. This partly explains the immense research effort that has been dedicated to them in the last decade.

However, for these materials and their qualities to be successfully incorporated into devices, their properties must be characterised and understood. Of particular real-world importance for electronics is to examine how a 2D layer interacts with adjacent layers and/or its substrate. Of equal importance are defects, which inevitably exist within the layer or at its juncture with the environment. Both substrate and defect can be utilised, tuning the 2D material towards an intended purpose or giving it new properties altogether. On the other hand they can be detrimental, even fatal, for device performance.

The properties of a 2D material, as well as the influence of its substrate and defects, can be investigated macroscopically. However, to fully understand the origin of these properties the material must also be examined on the atomic scale. Through this we can understand local behaviours which underpin the macroscopic behaviour of a material; this is the essence of solid state physics research. Moreover, studying 2D materials reveals localised electronic phenomena, which can find usage in the expanding field of nano-electronics and beyond. On a more fundamental and personal level, observing 2D materials at the atomic scale, and seeing the new and unusual ways in which electrons behave in this otherworldly environment, serves to satisfy scientific curiosity and really is a joy in itself.

This doctoral thesis studies single layers of MoS_2, which is both the archetypal TMDC and the archetypal 2D semiconductor. Due to recent advances made by our group, we are able to grow MoS_2 in very high quality. In our investigations the MoS_2 layer typically rests on top of a graphene layer, which itself sits atop an iridium(111) single crystal. It will be shown that the MoS_2 is close to *freestanding* in this configuration – in other words, it is not strongly affected by the presence of its substrate – allowing us to learn about inherent properties of the material. At the same time, this configuration allows us to purposefully manipulate the environment and observe how MoS_2 responds, without compromising its two-dimensionality.

In our MoS_2 samples a common defect is an atomically straight chain of 'out-of-place' atoms, called a *mirror twin boundary*. These atomic chains represent truly one-dimensional (1D) metallic wires. They are structurally isolated by the two-dimensionality of their host layer. Furthermore, they are electronically isolated from the host layer itself, because the metallic states of the wire are situated within the MoS_2 band gap. To call them 'defects' is almost a disservice, as they are rather a thing of beauty, a natural wonder of the nano-world. A large part of this thesis is dedicated to discovering the strange, exciting physics occurring in and around these 1D wires.

We principally use the scanning tunnelling microscopy (STM) technique, whereby an atomically sharp, metal tip raster-scans over the surface of the 2D layers, allowing individual atoms to be imaged. The atom at the tip apex is roughly half a nanometre (*i.e.* 0.0000000005 m) from the atoms at the surface, a distance $100{,}000$ times smaller than a hair's breadth. When the atoms are this close, electrons can quantum tunnel from the tip to the surface or *vice versa*, and we record a tiny current. As the tip scans over the surface, the recorded current will go up and down with the hills and valleys of the atomic landscape (the *topography*); this occurs line-by-line until an atomically resolved image of the material surface is built up. Perhaps the more powerful tool in our arsenal, however, is scanning tunnelling spectroscopy (STS). In this technique, the tip stays at a fixed location above the sample while the voltage across them is ramped. At certain voltages the sample will allow more electrons to tunnel than others – these voltages directly correspond to energies, and tells us at which energies the sample has states and at which it does not. Thereby we can peer into the electronic structure of the sample with STS, at the specific locations chosen by STM: local spectroscopy. Both STM and STS are carried out close to liquid helium temperature, $-268°$C; one can imagine the atoms and electronic states being frozen stiff. This stability allows probing of the sample with high spatial and energetic resolution.

This thesis is structured as follows: the remainder of Part I introduces background information and concepts particularly relevant to this work. Specifically, in Chapter 2 the crystalline and electronic properties of single- to few-layer MoS_2 and practical aspects of its synthesis are discussed. In Chapter 3 some the line defects common to semiconducting TMDCs are discussed, with a focus on mirror twin boundaries (MTBs) and their properties as reported in literature. Chapter 4 introduces some of the electronic interactions which are particularly relevant to this thesis. Thus Part I also serves as a ’motivation’ for this thesis, as it should illustrate the exciting physics underpinning the discussed topics and also highlight where there is still progress to be made. Note that our measurement techniques are described in Part II and are thus omitted from the Introduction.

Part II consists of three published papers (Chapters 5, 6 & 7) and a manuscript which remains in its preparatory stages (Chapter 8). In Chapter 5, the electronic band structure of atomically thin MoS_2 on graphene/Ir(111) is characterised and shows the TMDC layers to be quasi-freestanding on this substrate. In Chapter 6, electronic states confined along MTBs in MoS_2 on graphene/Ir(111) are investigated, and found to exhibit Tomonaga-Luttinger Liquid behaviour. In Chapter 7, the electronic environment orthogonal to these MTBs and other 1D defects is investigated. Therein it is discovered that the charged defect causes strong band bending in the surrounding MoS_2 layer, and that this leads to a 1D quantisation of valence band states. Lastly, in Chapter 8, the electronic environment of the MoS_2 is modified via the intercalation of dopant atoms between graphene and Ir(111). The response of the MoS_2 band structure and its 1D states at MTBs is investigated under these changed conditions.

In Part III, we give a brief retrospective discussion of the results. This includes a consideration of advances that have been made in the respective fields since our results were published, and a view to the future.

CHAPTER 2

MoS_2: A 2D Transition Metal Dichalcogenide Semiconductor

This Chapter should serve as a brief introduction to 2D MoS_2. We begin with its structural and electronic properties, followed by a discussion of its synthesis. The former should partly motivate our interest in the material; the latter should partly motivate our experimental approaches. This, of course, is a very limited introduction to MoS_2. The interesting properties of this material (and the amount of work published on it) are seemingly endless; the reader is referred to some of the early reviews regarding general properties [13–15] and more recent reviews regarding progress in growth and applications [11, 16, 17]. The electronic properties of 2D MoS_2 are well-described in early theoretical works [18–25] and are reviewed in Ref. [26, 27]. In this Chapter and thesis one may assume that we refer to the 2H-phase, monolayer (ML) material unless specified otherwise. This Chapter (and indeed, this thesis) concerns itself with the free-particle or 'electronic' *band gap of MoS_2; for a discussion of the* 'optical' *band gap and excitons, the reader is referred to Section 4.1.3.*

The transition metal dichalcogenides (TMDCs) have long been known in their bulk form [28, 29], and in a few special cases thin and even single layers were studied in the last century [30, 31]. Interest in 2D TMDC layers was reignited after the so-called 'rise of graphene' [32], and has truly exploded in the last decade. They exhibit a wealth of extraordinary properties – distinct from those seen in the bulk and from those seen in graphene (Gr) – due to which they are touted for application in everything from catalysis [17] to medicine [33].

Most talked about, however, is their potential usage in electronic and optoelectronic devices. In the case of the metallic 2D TMDCs, this is due to charge density wave (CDW) order, superconductivity, magnetism and other correlation phenomena [34]. In the case of MoS_2 and its semiconducting analogues, this is due to their finite band gap (in contrast to Gr) and other special features of their band structures. Moreover, most of these properties are tunable with layer number, while combining different 2D layers into vertical or lateral heterostructures gives birth to whole new properties [35]. It is easy to see why 2D TMDCs – together with Gr, h-BN, black phosphorus, MXenes and others [36, 37] – have become a proverbial playground for experimental and theoretical physicists alike.

2.1 Crystal and electronic structure

TMDCs have the general formula $\mathrm{MX_2}$, where M is a Group IV-VII transition metal (most commonly V, Nb, Ta, Mo or W) and X is one of the chalcogenides S, Se or Te. Each layer is made up of three covalently bonded planes stacked X-M-X; in each plane the respective species forms a hexagonal lattice, see Fig. 2.1(a,b). Each layer is only weakly bound to adjacent layers by vdW forces.

The 2D TMDCs typically take one of two structural phases: the 2H trigonal prismatic phase of D_{3h} symmetry, shown in Fig. 2.1(c), or the 1T octahedral phase of D_{3d} symmetry. $\mathrm{MoS_2}$ and its Group VI analogues (VI-$\mathrm{MX_2}$) are mostly found in the 2H phase, and so we limit our discussion thereto. For more information on the 1T phase, other phases and structure in general, the reader is referred to some of the many review articles [15, 38] or the doctoral thesis of J. Hall [39]. In bilayer TMDCs and up to the bulk, the different possible stacking of layers gives rise to further polytypes, see Ref. [39].

We narrow our focus to 2D $\mathrm{MoS_2}$, but note that a description of $\mathrm{MoSe_2}$, $\mathrm{WS_2}$ and $\mathrm{WSe_2}$ would be qualitatively the same[1], and much of the physics applies to the whole TMDC family due to their common structural characteristics. The hexagonal Brillouin zone (BZ) of ML-$\mathrm{MoS_2}$ is shown in Fig. 2.1(d) and its band structure close to the Fermi level in (e), leftmost panel. It has a direct band gap of $\approx 2.8\,\mathrm{eV}$ [20, 21, 23] at the inequivalent K and K$'$ high-symmetry points, located at the corners of the BZ. In the conduction band (CB), at slightly higher energy than the band edge at K, there lies a local minimum at the Q-point.[2]

The valence band (VB) maximum at the K-point of ML-$\mathrm{MoS_2}$ is spin-split by around $150\,\mathrm{meV}$; the CB is also spin-split at K, but only by a few meV [19, 21]. This large splitting appears only when thinning to a ML, because only then is inversion symmetry (and thus Kramer's degeneracy) broken [19]. The spin-orbit interaction is a relativistic effect and is thus stronger for heavier elements, making the spin splitting progressively larger in $\mathrm{MoS_2}$, $\mathrm{MoSe_2}$, $\mathrm{WS_2}$ up to $460\,\mathrm{meV}$ in $\mathrm{WSe_2}$. The VB also has a local maximum at the centre of the BZ, the Γ-point, at a similar energy to the split K bands in $\mathrm{MoS_2}$. Note that the general shape of the band structure shown in (e) applies also to the Group V TMDC monolayers, but with the Fermi level intersecting the lower band [VB in (e)] thus making them metallic. The Group V transition metals have one less valence electron than those in Group VI, leaving the band unfilled.

In Fig. 2.1(f) the main orbitals of the $\mathrm{MoS_2}$ bands at relevant high-symmetry points are illustrated. In reality, the orbital-projected band structure shows a mixture of Mo d and S p orbitals everywhere and is much more complex than (f) illustrates [24, 25]. However, for the purpose of visualising how a $\mathrm{MoS_2}$ layer interacts with subsequent layers or a STM tip, it is sufficient to consider where the significant orbitals are located and into which planes they extend.

The band extrema at the K-points are mostly composed of Mo d orbitals. In the CB they are of d_{z^2} nature and in the VB of d_{xy}, $d_{x^2-y^2}$ nature, *i.e.* out-of-plane and in-plane respectively. The CB at the

---

[1] From this point on we refer to $\mathrm{MoS_2}$, $\mathrm{MoSe_2}$, $\mathrm{WS_2}$ and $\mathrm{WSe_2}$ by 'VI-$\mathrm{MX_2}$'; the tellurides should also belong to this notation but $\mathrm{MoTe_2}$ is less frequently studied, while $\mathrm{WTe_2}$ is a semimetal [40].

[2] The intrinsic location of the CB minimum of $\mathrm{WSe_2}$ is debated [19, 26, 41, 42]

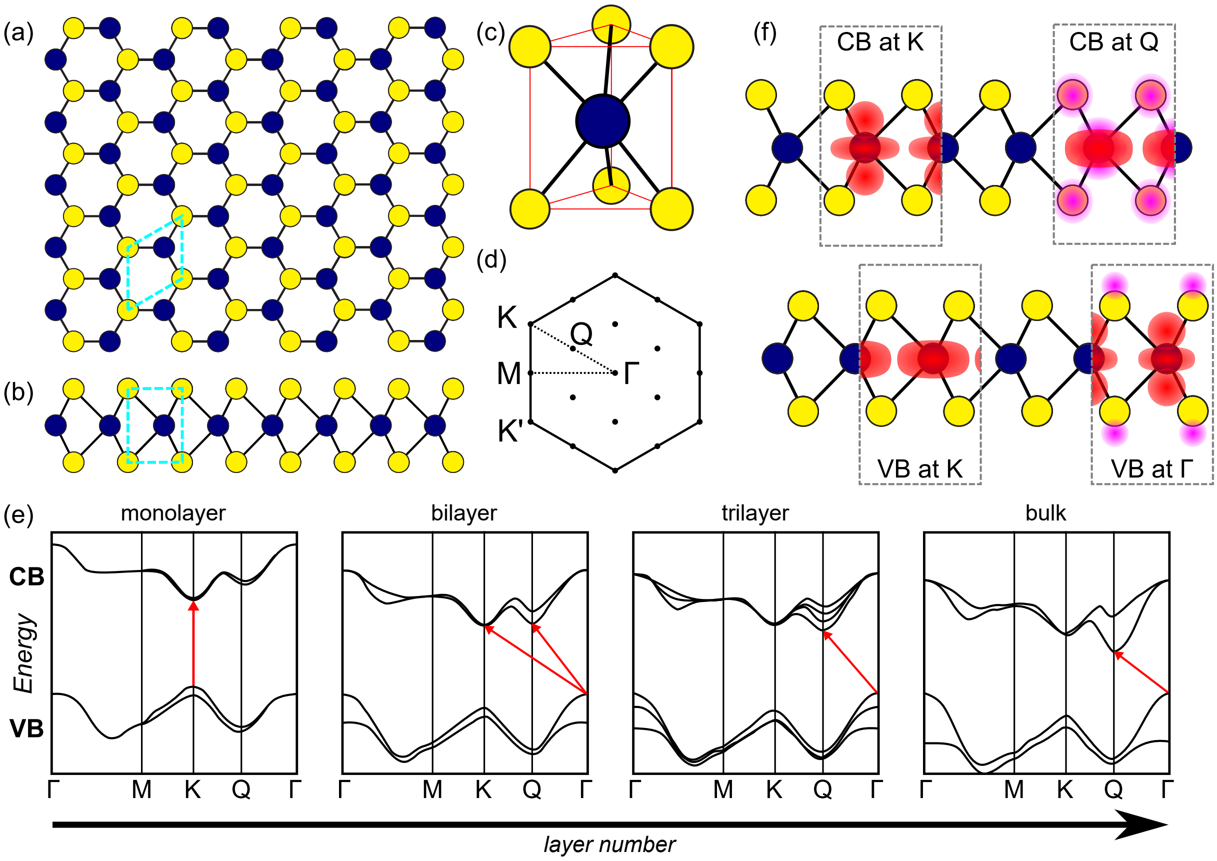

Figure 2.1: Basic crystalline and electronic structure of 2D MoS_2. (a) and (b) show the atomic structure of a single 2H-phase MoS_2 layer, in top and side view respectively. Metal (Mo) atoms are navy, chalcogen (S) atoms yellow. The primitive unit cell is marked in cyan. The ML-MoS_2 lattice constant is $a = 3.15\,\text{Å}$, the separation between upper and lower S planes $3.1\,\text{Å}$ and the Mo-S bond length is $2.4\,\text{Å}$. [43, 44]. (c) Perspective view, illustrating the trigonal prismatic molecular geometry. (d) Hexagonal first BZ of MoS_2 (and the other TMDCs). The high-symmetry points are indicated. (e) Band structures of mono-, bi-, trilayer and bulk MoS_2, showing the bands closest to the Fermi level. The band gap is indicated by a red arrow in each case. Based on Refs. [25,45]. (f) Significant orbital character at high-symmetry points of the monolayer band structure, compare Table 2.1. Majority (minority) orbital character is displayed as red (pink) clouds, not to scale. Based on from Refs. [26,46].

Table 2.1: Significant orbital character at high-symmetry points of the MoS_2 BZ [19, 24–27, 47]. Both K-points and the CB Q point have some minority p_x and p_y orbital character, omitted for clarity. Where d_{xy} is given, $d_{x^2-y^2}$ orbitals are also present but omitted for brevity.

band location	CB K	CB Q	VB K	VB Γ
majority orbitals	d_{z^2}	d_{xy}	d_{xy}	d_{z^2}
minority orbitals	–	d_{z^2}, p_z	–	p_z
main plane	out	in	in	out

Q-point is dominated by a mixture of in-plane Mo d orbitals; the VB at the Γ-point is dominated by out-of-plane d orbitals. Signifcantly, at both the Q- and Γ-point there is also minority S p_z orbital character.

This is summarised in Table 2.1. For a deeper discussion of the electronic properties of MoS_2 (and the other VI-MX_2) the reader is referred to the review by Liu *et al.* [27]. The strongly bound excitons which sit inside the MoS_2 electronic band gap, giving it a significantly smaller 'optical' gap, will be discussed in Section 4.1.3.

2.2 Layer-dependence of the electronic structure

To better understand the MoS_2 electronic structure and what makes this material so special in the 2D limit, we consider how the band structure evolves with increasing layer number. Much of this applies to the rest of the VI-MX_2 semiconductors, while in general all the TMDCs show a wealth of thickness-dependent properties underpinned by similar principles, including layer-dependent superconductivity [48], CDW order [49, 50] and metal-insulator transitions [51–53].

In the BL band structure, Fig. 2.1(e), the bands are no longer spin-split around the K-point due to the restoration of inversion symmetry – this can be understood by geometrical consideration of the 2H-stacked BL shown in (f). Furthermore, in the BL the VB maximum is no longer located at K but at Γ; the band has moved up at Γ (that is, closer to the vacuum level). Similarly, in the CB the Q-point moves down until it eventually becomes the CB minimum as layer number is increased. This phenomenon is explained by interlayer hopping – essentially the layer-layer interaction [46, 54, 55]. Interlayer hopping is stronger at Q and Γ because of the short distance between S p_z orbitals in neighbouring layers. Each new layer adds a band, and these bands interact particularly strongly at Q and Γ causing them to split in energy [24, 56].

Thus the band gap size reduces with increased layer number. Furthermore, the direct band gap at K in the ML becomes an indirect band gap in the BL and beyond [45, 57–59]. The band gap first transitions to Γ-K and then to Γ-Q where it remains until the bulk, as indicated in Fig. 2.1(e).

The layer number at which the Q-point becomes the CB minimum is debated, with many conflicting reports regarding BL-MoS_2 [60]. Theoretical prediction is difficult due to a strong dependence on in- and out-of-plane lattice parameters [61]. It is also experimentally difficult to verify because the CB extrema at the K- and Q-point shift relative to each other when the lattice is strained – the Q-point is much more sensitive to strain due to its in-plane majority orbital character. This phenomenon is the crux of strain engineering, whereby TMDCs and other 2D materials are elastically deformed to tune their (opto)electronic properties [62, 63]. This illustrates the importance of understanding the complex interplay of the MoS_2 lattice and its band structure, and investigating these at the atomic scale.

2.3 Preparation of TMDCs

2D TMDC layers are prepared via three main methods. We briefly introduce these and consider their advantages and drawbacks. More detailed comparisons are available in recent review papers [9, 17, 64, 65], and a more thorough discussion of TMDC growth from the perspective of our work group is available in Ref. [39].

Exfoliation

Mechanical exfoliation is the cleaving or ‘peeling off’ of layers from a bulk layered crystal, and is the method by which the early breakthroughs in preparing Gr other 2D materials were achieved [7, 8]. Other variants such as liquid exfoliation have also come into the fore in recent years [64]. It is possible to produce high-quality 2D layers by exfoliation and, as such, the method has proven invaluable to the research community. However, it suffers from low yield, limitations of flake size and residue contamination. Thus, it is not considered to be a practically feasible method for industrial-scale fabrication of TMDC layers [9–11, 14, 66].

Chemical vapour deposition

Chemical vapour deposition (CVD) typically involves precursor powders and a target substrate, which are heated inside a tube furnace with a background pressure of a carrier gas, such that the desired material forms on the substrate. Adlayer and substrate are then transferred together to wherever they will be investigated, or the adlayer is separated from the substrate by the exfoliation methods discussed above. CVD is relatively cheap and easy, making it a plausible candidate for industrial-scale implementation in some cases. However, it has its drawbacks: due to the low-to-ambient pressures typically involved during growth and *ex situ* transfer, the 2D layer is susceptible to contamination and defect formation. This is often compounded by residue contamination if the adlayer is transferred to an insulating substrate [67].

Due to the nature of a 2D material, any adsorbates or in-plane imperfections can have a huge effect on its electronic properties [68–71]. Depending on the intended application, these imperfections may be tolerable. In fundamental research however, they can obstruct an unambiguous understanding of the material in question.

Molecular beam epitaxy

Molecular beam epitaxy (MBE) works by directed evaporation of atoms or molecules onto a heated substrate in UHV [72]. *Epitaxy* refers to growth on a well-defined substrate which controls the orientation of the new layer, preventing multi-crystallinity. *In situ* growth at pressures of order 10^{-10} mbar allows a clean sample preparation, free of adsorbates or substitutional defects. Additionally, it is typically performed at lower substrate temperatures than those required by CVD, which may make it more suitable for fabrication of devices containing thermally sensitive components [66, 73].

The particular variant of MBE used in this thesis is van der Waals epitaxy (vdWE) [65,74]. A substrate with a completely terminated or passivated surface is used. The lack of dangling bonds means that the adlayer is bound to the substrate only by the weak vdW interaction, rather than covalent or ionic bonds.

Thus the adlayer should better retain its intrinsic electronic properties and is not strained by any mismatch with the substrate.

vdWE has been used to grow TMDC layers since the 1980s [75], and interest therein was renewed with the dawn of the 2D material era. However, a problem persisted. This is illustrated by looking at Table 2 of a 2016 review paper by McDonnell and Wallace [66], summarising TMDC thin films successfully grown by vdWE: there is a range of transition metal diselenides ($ZrSe_2$, $HfSe_2$, $NbSe_2$, $MoSe_2$, WSe_2) [76–80] and even a ditelluride ($MoTe_2$) [81], yet conspicuous by their absence are the revered disulfides MoS_2 and WS_2. This was principally due to the 'sulfur problem' [39]. The high vapour pressure of sulfur makes it unsuitable for UHV [82], while workarounds involving precursors such as H_2S gas proved sub-optimal [83]. The solution to this problem was available but in some senses forgotten: also included in the aforementioned table was a humble HfS_2 sample [84], grown using pyrite (FeS_2) as a solid-state sulfur source. We have revisited this approach and found it to be very effective in growing transition metal disulfides by vdWE [85].

2.4 The role of the substrate

The choice of substrate upon which to grow and/or investigate a TMDC layer is hugely important. While this is of course true for any material, it becomes especially important at the 2D limit, as every single atom of the layer is exposed at the interface. Substrate requirements vary widely depending on the community – for example optical spectroscopy or charge transport – and which TMDC properties one actually wishes to probe or alter. In this section we restrict ourselves to some of the considerations relevant to UHV-grown samples to be studied by STM/STS.

The use of STM typically requires a conducting substrate, so that a bias voltage can be applied.[3] This immediately poses some difficulties for growth. Metallic substrates are liable to strong chemical interaction – this can limit diffusion of the adatoms, leading to multi-crystallinity and strain [65]. This is precisely what one is seeking to avoid through the use of vdWE, as discussed above.

It is nonetheless possible to grow good-quality TMDC layers on metallic substrates, the prime example of this being the many samples grown on Au(111) by the Aarhus group [83, 86–88]. Despite the high crystalline quality of the TMDC layers, however, their electronic properties are heavily influenced by the substrate. Au(111) bands strongly hybridise with those of the TMDC. The effect is non-uniform in k-space, as it depends on the main plane of the orbitals and the energetic location of each TMDC band. This leads to a distortion of the band structure in MoS_2 [89], and even a semiconductor-to-metal transition in WS_2 on Ag(111) [90]. Metallic TMDCs are also strongly affected [91], to the extent that CDW order is suppressed [92]. In the case of TaS_2 on Au(111), the hybridisation was originally mistaken for substrate doping [93], with the true mechanism uncovered later and termed 'pseudo-doping' [94]. These substrate-induced modifications can have advantages, and can aid our understanding of the material in question.

---

[3] Insulating substrates can be used if a contact electrode is added post-growth.

But a strong substrate-adlayer interaction typically comes with a complex interplay of hybridisation, charge exchange and lattice distortion which can be difficult to disentangle.

It would be tempting to imagine that vdW substrates would alleviate these issues, leaving the TMDC intrinsic, but this is only partly true. For example, $MoSe_2$ showed a 'giant' $240\,\mathrm{meV}$ band gap renormalisation on graphite (HOPG) as compared to bilayer-Gr/SiC in STS measurements [79]. This was attributed to greater screening by the HOPG substrate. As an other example, the electronic band gap of ML-MoS_2 ranges from $2.01\,\mathrm{eV}$ on Gr/SiC [95] to 2.20 on Gr/Au [96] to $2.35\,\mathrm{eV}$ on h-BN [97] to $2.40\,\mathrm{eV}$ on HOPG [98], as measured by constant height STS. The discrepancies in that list are partly due to the measurement technique – addressed in Chapter 5. Nonetheless, they illustrate how much the electronic properties of 2D TMDCs can be influenced by their substrate, even when the topmost part of the substrate is also a vdW layer in principle.

Gr on Ir(111) as a substrate for MoS_2

Using other 2D materials as a substrate is attractive, because it should be possible to 'stack' the desired layer on top and have it bound only by weak vdW forces [99]. Gr is an obvious choice, as the best-established 2D material. Moreover, it is quite chemically inert [100] and, as a truly 2D semi-metal, will not screen strongly in its intrinsic state. Calculations of MoS_2-Gr vertical heterostructures predict negligible interaction between MoS_2 bands and Gr bands, leaving each layer near-independent [47]. However, a single layer of Gr is not a practically feasible substrate; it must be supported by a bulk crystal for most purposes. And if the Gr-bulk interaction is too strong, the Gr will no longer act like a non-intrusive vdW substrate. This is evidenced by the strongly reduced MoS_2 band gaps on Gr/SiC [95] and Gr/Au [96], for example.

With this in mind, Gr on Ir(111) presents itself as a candidate upon which to grow and study TMDCs. Gr interacts strongly enough with Ir(111) such that a single crystalline Gr layer with extremely low defect density can be grown epitaxially [12, 101, 102]. At the same time, the interaction is weak enough such that the Gr is only physisorbed [103], with a $60\,\mathrm{pm}$ corrugation due to the Gr/Ir(111) moiré. The Gr bandstructure is close to pristine [104]. It is slightly p-doped, with the Dirac point shifted $0.1\,\mathrm{eV}$ above the Fermi level [104]. Due to the unique band structure of Gr [105], this corresponds to only a small expansion of its Fermi surface *i.e.* only a small increase in charge carrier density [106]. Thus it should remain a kind of weak-screening 'buffer layer' above the Ir(111).

A hole in the market

Indeed, Gr/Ir(111) proved to be an excellent substrate for 2D TMDCs. Coupled with the aforementioned solution to the 'sulfur problem', a modest breakthrough was made within our group in the MBE-growth of MoS_2, WS_2 and TaS_2 monolayers [85]. Not only were the TMDCs of high crystalline quality, there were several indications that they were only weakly interacting with their substrate. This included the fact that the TMDC layers could be moved around by the STM tip, and preliminary constant height STS measurements showed a relatively large band gap. The next logical step was to analyse the electronic properties of these quasi-freestanding TMDC layers with low-temperature, high-resolution STS. As a starting point we chose the veritable poster child of the TMDC world: molybdenum disulfide.

CHAPTER 3

1D Defects and Interfaces in VI-MX_2

This Chapter should serve as a brief introduction to line defects in MoS_2 and its VI-MX_2 analogues, including the tellurides. This motivates the research conducted in Chapters 6-8. The reader is referred to literature reviews on defects in 2D TMDCs for further information [107–110]; of particular relevance is a 2018 review of mirror twin boundaries in molybdenum dichalcogenides [111]. The Chapter concludes with an introduction to polar discontinuities at 1D defects.

"*...in this world nothing can be said to be certain, except death and taxes*" opined Benjamin Franklin in 1789, overseeing the fact that crystallographic defects are also inescapable. Every bulk crystal has surfaces, and every 2D material has edges. Moreover, every crystal will contain a finite, temperature-dependent number of vacancy defects [112], and additional defects are inevitably introduced during growth. Defects can induce strain, store charge, dope, scatter excitations, and break symmetries – in general they alter the electronic landscape of the host material. They tend to be detrimental to the intended function of a material, but they can also be utilised, giving the material new properties. Either way, they must be characterised and understood. Atomic-scale probe techniques such as STM and STS play a key role in this.

Considerable research effort has been dedicated to TMDC defects [107–110], but they remain an obstacle on the road towards TMDC-based devices [9–11]. Vacancy point defects are the most commonly studied defect type in TMDCs [108, 113]. Substitutional defects, where the vacancy is filled by a foreign species, are also of great interest [37, 110]. This is due to their ability to dope the layer, and for the pragmatic reason that they can be common in samples grown outside of UHV. Point defects in MoS_2 are investigated in Appendix A.2, but it is line defects that are the focus of this thesis.

Line defects – for example, flake edges and grain boundaries – typically mark the limit of a 2D crystal domain. The behaviour of charge carriers at these defects determines the transport properties of the material, and thus can determine the quality of many TMDC-based devices. The study of line defects in TMDCs has thus far been dominated by irregular, non-symmetric tilt grain boundaries [98, 114–121]. This is because they are the most common defects in samples prepared by CVD and similar methods. As MBE-growth of TMDCs has become more established, so has the study of regular, symmetric, 180°-tilt grain boundaries known as mirror-twin boundaries (MTBs) [111]. Due to their low formation energy

[122], these MTBs may be the most persistent grain boundary type even as TMDC growth techniques are optimised.

As well as their implications for charge carrier mobility [123], MTBs in semiconducting TMDCs have been of interest due to the states hosted within them. Early studies predicted them to be metallic [124, 125], while the electronic phenomena they exhibited in experiment were even more exotic than that [126, 127]. Similarly exciting physics has been predicted for the straight 1D edges of MoS$_2$ [128]. In general, it will be important to understand the physics at well-defined 1D interfaces (such as MTBs and edges) as the TMDC community moves towards ever-smaller and more precise device configurations, including those of lateral heterostructures.

3.1 Grain boundaries

Grain boundaries (GBs) are formed at the juncture of misoriented domains. Common to 2D materials are *tilt*-type GBs, labelled with a tilt angle defining the difference between the crystallographic direction of each domain. In VI-MX$_2$ (including the tellurides) GBs are typically made up of 4-6, 6-8 and 5-7 defects stitched together [69, 114–116]. However, practically every GB is different because its precise composition depends on the tilt angle, any local strain fields, and the stoichiometry during growth. For this reason their effects on the properties of the TMDC can vary considerably [117, 129], although in general they are bad for electrical conductivity. They can exhibit in-gap states and strain the layer; both of these effects will locally change the MoS$_2$ band structure [130, 131]. As will be discussed in Chapter 7, it is difficult to disentangle the charge and strain effects of GBs, and this is only complicated by the diversity of their structural make-up.

GBs are most often formed when misoriented domains meet during growth. Thus they are more common when the adlayer-substrate interaction is strong, such that there is a high nucleation density and low diffusion. Low growth temperature can lead to increased GB formation for the same reason. Additionally, if the growth process is fast then there will be more domains and they will meet more quickly, increasing GB formation [132].

3.2 Mirror twin boundaries

MBE-growth takes place comparatively slowly due to the low pressures and fluxes involved. Furthermore, in vdWE the crystal domains should be free to align themselves with the substrate along energetically favoured directions, especially at raised substrate temperatures. In principle this could allow for the growth of a single crystal TMDC, but in practice there will be multiple nucleation sites and there may be multiple possible alignments. For example, a MoS$_2$ monolayer has C_{3v} symmetry whereas Gr has C_{6v} symmetry, allowing two equivalent but opposite orientations of MoS$_2$ with respect to the Gr substrate. When two such domains meet, a mirror twin boundary (MTB) is formed[1] – this is a special class of GB

---

[1] They can also be created by slightly imperfect stoichiometry during growth [133], post-growth metal deposition [134], or post-growth electron-beam irradiation [69, 133, 135].

with a tilt angle of 180° (or rather 60°, by convention). This is most easily visualised by the MTB shown in Fig. 3.1(a). The crystallographic directions of the two domains are opposite, highlighted by triangles. Where the two domains meet, they each have the same kind of edge, in this case a S-terminated zigzag (S-zz) edge. They form a boundary in which they share S atoms. This boundary is a mirror plane – on either side of the boundary the transition metal and chalcogen lattice sites are inverted. MTBs are thus also known as *inversion domain boundaries*.

The study of MTBs in VI-MX_2 layers is a small but growing field, and was reviewed fairly recently by Batzill [111]. In 2013 a few MTB types were predicted [124], and some experimental observations in CVD-grown MoS_2 [69, 115] and then MBE-grown $MoSe_2$ soon followed [133, 136, 137]. Two of these MTB types are shown in Fig. 3.1. These are known as 4|4P and 4|4E MTBs and, owing to the fact that they are the most energetically favourable types in MoS_2 and $MoSe_2$ [122], they are the MTBs most frequently seen in the literature. A third MTB type is seen in WSe_2 [138], but will not be discussed here. The 4|4P boundary is made up of 4-membered rings which share a point, while the 4|4E is made up of 4-membered rings which share an edge [as indicated in (a) and (b) respectively], this gives them their names [69]. In the 4|4P, the S atoms are bonded to 4 Mo atoms instead of 3; in the 4|4E, the Mo atoms are bonded to 5 S atoms instead of 6. Both MTBs are therefore chalcogen deficient. What differentiates the two, is that in the 4|4E the right-hand domain is shifted by half a lattice constant in the y-direction.

Both the 4|4P and 4|4E MTBs were predicted to host metallic states by various groups [69, 122, 124, 125, 139]. An exciting prospect, as this would represent a 1D metallic wire, isolated electronically from the semiconducting layer around it. Indeed it proved true: in 2014 Liu *et al.* reported on a "dense triangular network" of metallic 4|4P MTBs in MBE-grown ML-$MoSe_2$ [136]. Furthermore, the metallic wires showed intensity undulations in STM, a periodic beating along the length of the wire. This was ascribed to a combination of quantum confinement due to the finite MTB length and a superlattice potential imposed by the moiré created between $MoSe_2$ and its HOPG substrate. Barja *et al.* instead ascribed the undulations, which had a periodicity of $3a$ close to E_F, to a 3×1 CDW in the 4|4P MTB at 5 K [126]. A Peierls distortion (trimerisation in this case) of the lattice was too small to detect in STM/STS and did not come naturally from DFT. A third group, that of Batzill *et al.*, also observed dense 4|4P networks in MBE-grown $MoTe_2$ [140] and $MoSe_2$ [141]. Their conclusions on 4|4P MTBs in $MoSe_2$ compli-

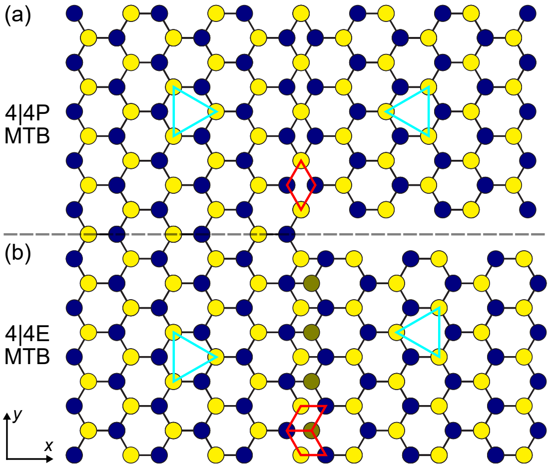

Figure 3.1: Mirror twin boundary (MTB) types common to VI-MX_2. Metal atoms are navy, top layer chalcogen atoms yellow, bottom layer chalcogen atoms dark yellow. The cyan triangles indicate the lattice registry of each domain. Indicated in red are the 4-membered rings which make up each MTB and give them their names. Note that in (a) there are two 4-membered rings which are degenerate from this perspective. MTB side views are shown in Fig. 1 of Chapter 7.

cated the picture further: as well as observing CDW behaviour up to 235 K, they found evidence for a Tomonaga-Luttinger liquid at room temperature [127]. This was inferred from angle resolved photoemission spectroscopy (ARPES), in other words the result is in an average of the ensemble of 4|4P MTBs.

The above describes the state of the field as we began investigating the 1D metallic states in 4|4P and 4|4E MTBs in MoS_2. It is worth noting that until that point the 4|4E MTB had received much less attention in the literature; the 4|4P is far more energetically favourable in $MoSe_2$, and there was a lack of MBE-grown disulfides (see Section 2.3). Our findings are the main topic of Chapter 6, and also play an important role in Chapters 7 & 8. The 1D states in MTBs remain a topic of active research; recent developments will be addressed in the Discussion, Part III.

Though the electronic properties along the axis of 4|4P MTBs were examined by multiple groups, the electronic properties normal to the VI-MX_2 MTBs – that is, in the plane of the MX_2 layer – received less attention. Theoretical studies predicted band bending at MTBs [142], and charge carrier filtering across them [123, 133]. An STS investigation of the area around 4|4P MTBs in $MoSe_2$ was influenced by the dense network of boundaries interfering with each other [141]. Transport measurements were carried out but on a different, less symmetric MTB type in CVD-grown MoS_2, consisting of 4|4P segments interspersed with 8-membered rings. They found it to have negligible [115] or even enhancing [143] influence on inter-grain mobility (though in the latter case the MTB identification is unclear). In this context we investigated the electronic influence of 4|4P and 4|4E MTBs on the MoS_2 layer around them – this is the main topic of Chapter 7 and is addressed again in Chapter 8.

3.3 Island edges

MoS_2 edges are typically zigzag, with armchair edges rarely found [110, 144]. This partially explains why the 4|4E and 4|4P MTBs form and not some of the other theoretically possible MTB structures. Zigzag edges can terminate in both the metal and chalcogen direction, for example in Fig. 3.1 there are Mo-zz edges on the left and right of the islands (with the S-zz edges joined at the MTB). In reality, the edge termination is non-trivial and can involve various reconstructions [145–147] and they may be passivated with adsorbates such as hydrogen [146]. Transmission electron microscopy [115, 147] or non-contact atomic force microscopy [148] are usually required to determine edge-termination.

Atomically straight MoS_2 edges have also exhibited 1D metallic states along their length [149], with multiple theoretical works predicting this and additional interesting properties [150–155]. In Chapter 7 we investigate the electronic landscape at straight edges in ML- and BL-MoS_2.

3.3.1 Lateral heterostructures

A discussion of line defects in TMDCs would not be complete without mentioning lateral heterostructures. In what is a rapidly growing field, two different 2D TMDC layers are arranged in the same plane to create new functionalities [35, 37, 156, 157]. Of particular interest is the combination of dissimilar 2D semiconductors (in which case the term lateral hetero*junction* may be used). For example, MoS_2 and WSe_2 have been grown adjacently to create 2D p-n diodes [158, 159]. A type-II band alignment can separate electrons and holes at the lateral heterostructure interface, and this has already been utilised in a WS_2-WSe_2 photodiode [160], a MoS_2-$MoSe_2$ photodetector [161] and a MoS_2-WSe_2 solar cell [162]. Alternatively, an STM tip can create a heterostructure of the 1H- and 1T′-phases in a single layer of WSe_2, with topologically protected edge states residing at the phase boundary [163, 164].

3.4 Polarisation charge at 1D defects

In this Section we discuss the concept of the polar discontinuity, which can occur normal to 1D defects and can bestow a 'bound' or 'polarisation charge' upon them. Despite the popularity of 2D materials and their 1D defects, their connection to this concept has received comparably little attention [165]. It will play an important role in Chapter 7. To understand this concept we must first introduce the modern theory of polarisation. The following explanation is heavily based on a "beginner's guide" by Spaldin [166].

The modern theory of polarisation

Consider the 1D chain of equally spaced anions and cations depicted in Fig. 3.2(a). Two possible choices of unit cell are indicated. The properties of a crystal are typically defined by averaging over its unit cell. As trivial examples one can think of atomic number density (in this case $2/a$) or charge (in this case zero), and these are obviously independent of chosen unit cell. Next we consider polarisation $\vec{P}$, which is the bulk equivalent of the electric dipole moment. This is easily definable for a CO molecule, for example, but in a crystal it is seemingly dependent on the choice of unit cell, as shown in (a). This caused considerable bafflement, until it was resolved in the *'modern theory of polarisation'* by Vanderbilt, King-Smith and Resta in 1993 [166–169].

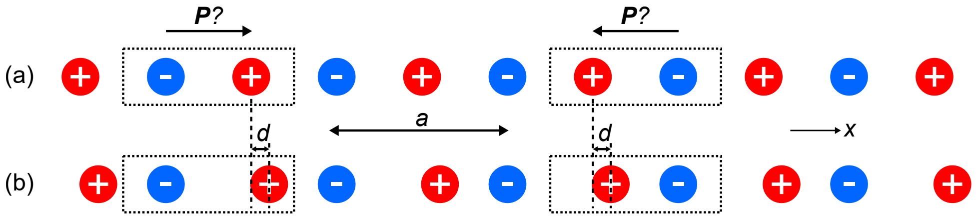

Figure 3.2: 1D chains of cations and anions with charge $q = e$ and $-e$ respectively. In (a) they are equally spaced, in (b) the cations are shifted by distance d. Based on Ref. [166].

We return to Fig. 3.2(a) more formally. The electron dipole moment of a collection of point charges q_i

at positions $\vec{r_i}$ is defined $\vec{d} = \sum_i q_i\vec{r_i}$. The polarisation of a crystal is defined as the dipole moment per unit volume, or unit length in the case of (a). Thus for the left-hand unit cell we have:

$$\vec{P} = \frac{1}{a}\sum_i q_i\hat{x}_i = \frac{1}{a}(-e \times \frac{a}{4} + e \times \frac{3a}{4})\hat{x} = \frac{1}{2}e\hat{x}. \tag{3.1}$$

Performing the same calculation for the right-hand cell of (a), one finds $\vec{P} = -\frac{1}{2}e\hat{x}$. This seems problematic, as the polarisation value is dependent on choice of unit cell. Worse still, the crystal shown in (a) is not actually a polar material – it is inversion symmetric and thus non-polar by definition – and yet we obtain finite polarisation values. These apparent paradoxes are resolved within the modern theory of polarisation, which states that the *formal polarisation* of a material is defined as a lattice rather than a single vector. In the case of the chain (a), the lattice points are at $\pm\frac{e}{2}\hat{x}, \pm\frac{3e}{2}\hat{x}, \pm\frac{5e}{2}\hat{x}$, and so on, separated by the polarisation quantum $\vec{P_q} = 1e\hat{x}$. The formal polarisation of (a) is thus described $\vec{P} = (\frac{1}{2} \pm n)\vec{P_q}$. It can be shown that such lattices – and also those described $\vec{P} = 0 \pm n\vec{P_q}$ correspond to non-polar materials [166, 167]. A polarisation lattice which is symmetric around zero is the sign of a material which is itself inversion symmetric, *i.e.* non-polar [170].

The other main tenet of the modern theory of polarisation is that it is the *changes* in formal polarisation which are instructive, rather than absolute values [166]. To illustrate this we consider the chain in (b), which is no longer inversion symmetric and is now polar. The left-hand unit cell of (b) has polarisation $\vec{P} = (\frac{1}{2} + \frac{d}{a})e\hat{x}$ and the right-hand unit cell polarisation $\vec{P} = (-\frac{1}{2} + \frac{d}{a})e\hat{x}$. It appears as though we have the same 'problems' as before. However, if we consider the change in polarisation between the left-hand cells of (a) and (b) we find $\delta\vec{P} = \frac{d}{a}e\hat{x}$. Comparing the right-hand cells gives precisely the same result. Thus, although the absolute polarisation of each crystal can take multiple values, if we consider the *change* in polarisation we arrive at a single, well-defined value. This finite value illustrates that from (a) to (b) the material has become polar [166].

Interface theorem: Polar discontinuities

An important issue is the polarisation discontinuity which occurs where polar materials terminate. There was controversy surrounding the surface termination of bulk crystals – such as the observation of charge at the surface of insulators – until this was partially resolved by the *interface theorem* within the modern theory of polarisation [168]. Namely, at any interface there will be a *bound charge*

$$\sigma = (\vec{P_1} - \vec{P_2}) \cdot \hat{n}_{1,2}, \tag{3.2}$$

where $\vec{P}_{1,2}$ are the respective formal polarisations of the two domains making up the interface, and

$\hat{n}_{1,2}$ a unit vector orthogonal to said interface, pointing from domain 1 to domain 2 [171]. In essence, we simply consider the *change* in polarisation as we go from one material to another, just as before.[2]

We explain this further in 2D, taking MoS_2 as a case study. First we are required to express the formal polarisation $\vec{P}$ of MoS_2. It is not sufficient to consider the atoms as point charges as we did above; one must take the molecular orbitals into account. This can be done by mapping the ground state of the system onto a set of localised Wannier functions [173], and then considering point charges to be at the centres of these Wannier functions [174]; these points are shown for MoS_2 in Fig. 3.3. The problem is further simplified by the C_3 rotational symmetry of the MoS_2 lattice. It has been shown that the polarisation values of C_3 lattices fall into three classes, taking values (modulo a quantum of $\vec{P}$):

$$\vec{P} = 0, \ \frac{e(\vec{a_1} + \vec{a_2})}{3\Omega} \ \text{or} \ \frac{2e(\vec{a_1} + \vec{a_2})}{3\Omega}, \tag{3.3}$$

with $\vec{a}_i$ the lattice unit vectors and Ω the area of a unit cell [165, 175]. For example, h-BN takes the first value – it has zero formal polarisation [175]. MoS_2, meanwhile, belongs to the third class; using its Wannier functions one finds its formal polarisation to be given by $\vec{P} = -\frac{2e}{3a}\hat{x} + \frac{2e}{\Omega}\vec{R}$. Here $\hat{x}$ is a unit vector always pointing along an armchair direction as in Fig. 3.3 – this is important, as we shall see shortly. $\vec{R}$ is a generic Bravais lattice vector [172] – by arbitrarily adding the MoS_2 lattice vectors to the quantised value $\vec{P} = -\frac{2e}{3a}\hat{x}$, we can create the polarisation lattice of MoS_2. Importantly, this lattice is not symmetric about the origin and MoS_2 has a finite formal polarisation.

Returning to Equation 3.2 for the bound charge at bulk interfaces, we may reduce this to its 2D equivalent $\lambda = (\vec{P_1} - \vec{P_2}) \cdot \hat{n}_{1,2}$, where λ is the bound charge of the 1D interface (in units of charge per length) [174]. We first apply this to the Mo-zz edge on the left side of Fig. 3.3. The vacuum has no polarisation, while the formal polarisation of MoS_2 points towards the Mo-zz edge, leaving us with a bound charge $\lambda = \frac{2e}{3a}$. Conversely, a S-zz edge would have bound charge $\lambda = -\frac{2e}{3a}$ [172]. The armchair edges at the top and bottom of Fig. 3.3 are non-polar, with $\hat{n}_{1,2} \perp \vec{P}$.

We next turn our attention to the 4|4P MTB shown in Fig. 3.3. Owing to the mirror symmetry of the interface, the formal polarisation vectors on either side are anti-parallel. One may equivalently say that their polarisation lattices are 60° rotated with respect to each other. Applying the equation for λ to this interface would yield a bound charge $-\frac{4e}{3a}$ at first glance. However, as pointed out in Ref. [172], one must account for the changed atomic lattice at the interface. In the case of the 4|4P MTB this results in a corrected value $\lambda = -\frac{4e}{3a} + \frac{2e}{a} = \frac{2e}{3a}$, and similar analysis can be applied to hydrogenated zigzag edges, for example [172].

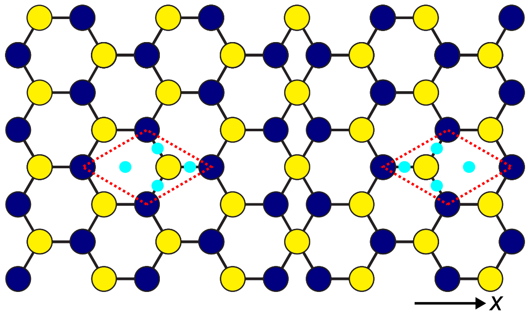

Figure 3.3: Polar discontinuities at MoS_2 interfaces. Mo atoms are navy; S atoms yellow. Within a chosen unit cell (red) the Wannier function centres are shown (cyan) [174]. Note that there are 6 Wannier centres around each S atom (but only 3 visible from this perspective). For each domain there are multiple possible choices of primitive unit cell – taking the polarisation value of each one yields the formal polarisation lattice for that domain. However, the unit cells (and thus the formal polarisation values) on either side of the MTB are inequivalent.

---

[2] A related term *polarisation charge* is also used in the literature [172].

Looking at the ribbon in Fig. 3.3, we note that it would be possible to exchange the 4|4P with a 4|4E type MTB (see Fig. 3.1) and thus, by symmetry and charge neutrality arguments, the 4|4E MTB should have the same bound charge as the 4|4P.

Charge compensation

The bound charge at the 1D interfaces in the above section would create an electrostatic potential in the surrounding layer, and this would diverge with increasing domain width [176]. This is obviously unphysical, and indeed nature will seek to neutralise the bound charge and avoid a 'polar catastrophe'. In the above example of the MTB-containing MoS_2 ribbon, Gibertini and Marzari [172] showed that free charge from the surrounding layer will flow to the line defects; if the ribbon is large enough the bound charge will be fully compensated. Compensation may also be ionic, via a lattice reconstruction or the acceptance of foreign atoms.

The most famous example of charge compensation supposedly occurs at the interface between the layered oxides $LaAlO_3$ and $SrTiO_3$ [177, 178]. Although both oxides are insulators, a 2D electron gas exists at their interface if (amongst other things) the interface is sufficiently clean and the polar material $LaAlO_3$ is sufficiently thick [179, 180]. The leading explanation for this phenomenon is that the polar discontinuity at the interface leads to a bound charge σ. This must be compensated to avoid a potential which diverges with increasing oxide thickness – a polar catastrophe – and so electrons move from the bulk oxides towards the interface until it eventually becomes conducting [170, 181, 182]. This is where the term 'polar catastrophe' originates from and is where most research into polar discontinuities has traditionally been focussed. However, the same concepts in 2D materials have attracted some attention in recent years [172, 174–176, 183].

CHAPTER 4

Electronic Interactions

This chapter introduces a few electronic interaction phenomena which are particularly relevant to this thesis. Of course, there are myriad electronic interactions taking place in the systems studied here, and not all of them can be described. Instead we focus on a few concepts which (i) are perhaps not common knowledge to a Masters-level solid state physicist, and (ii) have not been covered in previous theses of our work group.

We introduce the ideas of electrostatic screening, and specifically its relevance for 2D semiconductors: band gap renormalisation and excitons. The reader is referred to an introduction to screening by Chazalviel [184] and a recent review of screening in 2D TMDCs [185], although the latter is written from rather a theoretical, optics point of view. The review of excitons in 2D TMDCs by Wang et al. *[186] is highly recommended, especially for its overview of the different contributions to the Coulomb interaction and their respective relevance.*

Secondly, we introduce the Tomonaga Luttinger liquid in as simple a way as possible. The reader is referred to works by Giamarchi [187, 188] and an experiment-oriented review in Ref. [189].

4.1 Screening

The Coulomb potential felt by one electron due to another at distance r decays with $1/r$ in the vacuum. In many real situations the decay occurs faster than $1/r$, and this is termed *screening* [184]. There are various causes of screening. For the purposes of our discussion – that of a semiconducting layer on top of a metal substrate – there are two that are relevant.

The first of these is screening by the dielectric polarisability of the medium in which an electron finds itself. Consider a positively charged point defect in an insulator. The nearby core electrons of the lattice will shift towards it slightly due to the field it has caused. Now consider the viewpoint from a core electron a few lattice sites away: there is a positive point charge, but immediately around it there is a region of *increased* electron density. The Coulomb potential it experiences due to this point charge is reduced, compared to how it would be in vacuum. Specifically, this describes the electronic polarisability; materials can also exhibit vibrational and orientational polarisability, but all are based on the formation of electric dipoles. Together, the polarisability of a material is described by its dielectric tensor κ, essentially a measure of its ability to screen charge. [184]

A more efficient type of screening is that due to conduction electrons. Imagine a sea of electrons in a uniform background of positive charge, *i.e.* a jellium. Due to the Coulomb interaction, each electron creates a region around it in which the electron density is depleted. This region is effectively a cloud of positive charge. All the other electrons in the system now see the net result – this electron plus its positive 'screening cloud' – and the potential they experience due to that electron is reduced. This positive screening cloud is not strictly real; there is no cloud of protons flying around the electron. But it is a convenient way of incorporating (both mentally and mathematically) the complicated many-body effects of the system into a simplified, single-particle picture. The electron in this context is thus a quasi-particle composed of a real electron and its screening cloud. The attractive interaction between the electron and its screening cloud is described by the *self-energy* of the quasi-particle. In other words this is the energy of the electron due to the changes it has caused to its environment. [190]

For the next part of our thought experiment, we magically turn up the screening in our jellium. We can consider each electron to have a more effective screening cloud, or equivalently say that its self-energy is increased. The electrons are less Coulomb-repulsed by each other, and we are closer to the situation of a Fermi gas of non-interacting electrons.

Our discussion has been classical, only considering the *long-range*, *direct* Coulomb interaction. We have neglected the *short-range* aspects concerning the overlap of wave-functions. Moreover, we have neglected the Coulomb-*exchange* interaction, which stems from the Pauli exclusion principle requiring anti-symmetric wave-functions. A full, quantum-mechanical description of screening in many-electron systems goes far beyond the scope of this work. The reader is referred to Ref. [186] which gives a simple overview of these different contributions and their relative magnitudes, or Refs. [184, 191, 192] for a deeper discussion. Nonetheless, the basic idea of a reduced Coulomb interaction due to the rearrangement of electrons – valid for both screening by a dielectric and by conduction electrons – should suffice for the purposes of this thesis.

4.1.1 Band gap renormalisation

Screening is known to effect the band gap size in semiconductors in what is termed *band gap renormalisation*. Imagine an intrinsic semiconductor at absolute zero. To excite an electron from the valence to the conduction band, one must overcome the electron-hole recombination energy.[1] One can imagine having to bring the electron and hole sufficiently far away from each other, such that their attractive potentials do not overlap. Better screening corresponds to a more effective cloud for each quasi-particle, and thus a shorter-range potential. Therefore, less energy is required to separate electron and hole, and the band gap is smaller. In the quasi-particle picture, increased screening means an increased self-energy and a

---

[1] We refer here to the creation of independent electron and hole and thus the free-particle or 'electronic' band gap. A discussion of a bound electron-hole pair (exciton) and the 'optical' band gap will come later.

more stable quasi-particle [193]. Simply speaking, the addition of an electron (or hole) to a band will cause less perturbation to a well-screened system, and thus a lower energy penalty is associated [194].

It should be made clear that these quasi-particles are single, independent electron and hole excitations. The electronic band gap may also be defined as "*the sum of energies needed to separately tunnel an electron and hole into the system*", Liu *et al.* [27]. This situation is distinct from that of the exciton quasi-particle, a bound electron-hole pair simultaneously excited. That requires less energy (by an amount equal to the exciton binding energy). Excitons, the optical band gap, and their relationship to the electronic band gap will be discussed shortly.

4.1.2 Screening in two dimensions

Screening is greatly reduced in 2D: rather than a sphere of charge carriers surrounding each point, the screening cloud is confined to the plane of the layer. This, combined with the confinement of the 2D layer, results in charge carriers experiencing a much stronger Coulomb interaction. It partly explains why the band gap in ML-MoS$_2$ (2.8 eV) is much larger than that of the bulk material (1.3 eV). It also explains why most substrates, even those only interacting via vdW forces, will cause a considerable band gap renormalisation compared to the free-standing band structure [193, 195]. The 3D electric field lines between charge carriers extend out of the 2D plane, and so it is critical whether this space is occupied by vacuum or matter [196].

Band gap sizes are additionally increased in 2D materials because of quantum confinement in the out-of plane direction, which increases the kinetic energy of the charge carriers. TMDCs are layered materials and so this out-of-plane confinement effect is already significant in the bulk [194], but it is lifted by interlayer coupling to some extent (see Section 2.2).

4.1.3 Excitons

Another consequence of the confinement and reduced screening in 2D VI-MX$_2$ semiconductors is a large excitonic binding energy E_b [20, 21, 57]. Excitons are bound electron-hole pairs which have a reduced energy compared to a free electron and hole due to their Coulomb attraction. They result in a reduced, ‘optical’ band gap $E_\mathrm{opt} = E_\mathrm{g} - E_\mathrm{b}$ as depicted in Fig. 4.1. Their motion is correlated, and they can move through the lattice as a quasi-particle of neutral charge. Due to the increased Coulomb interaction in 2D, they are very strongly bound: the exciton binding energy is around 500 meV in ML-MoS$_2$. By comparison, in 3D semiconductors and even in quasi-2D systems such as GaAs quantum wells, the exciton binding energy is of order $10 - 100$ meV [197–199].

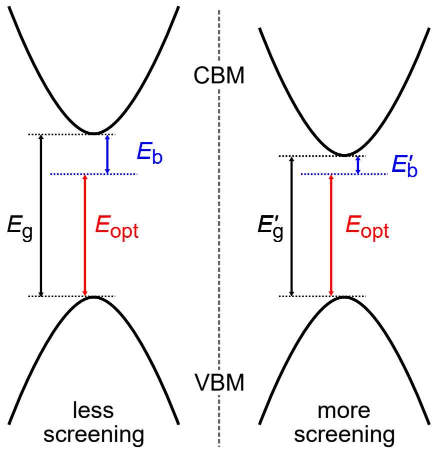

Figure 4.1: The electronic E_g and optical E_opt band gaps of VI-MX$_2$ and their response to screening. Increased screening causes a reduction in exciton binding energy ($E'_\mathrm{b} < E_\mathrm{b}$) and electronic gap ($E'_\mathrm{g} < E_\mathrm{g}$). These effects largely cancel out however, leaving the optical gap unchanged ($E'_\mathrm{opt} \approx E_\mathrm{opt}$).

Increased screening means a weaker Coulomb interaction and a lower binding energy for the exciton. This is closely related to the renormalisation of the electronic band gap outlined in Section 4.1.1, in which the self-energy of the free particles *increased*. The result is that the free-particle band edge moves closer to the Fermi level, while the exciton resonances move closer to the band edge. This change under increased screening is depicted in Fig. 4.1. In fact, because the renormalisations of free-particle band gap and exciton binding energy are mostly underpinned by the same mechanism – the Coulomb interaction – this occurs with approximately equal but opposite magnitude. Therefore, the optical band gap remains largely unchanged by screening and the relationship $E_\mathrm{g} = E_\mathrm{opt} + E_\mathrm{b}$ holds for different substrates [79, 194, 200]. For this reason, it is common to measure or calculate two of these quantities and from this infer the third quantity [79,196,201,202].

As above, we have neglected the Coulomb-exchange interaction and short-range interactions, which (together with consideration of the spin-valley physics at the $\mathrm{MoS_2}$ K-point) are necessary to explain exciton fine structure, the splitting of bright and dark excitons and other subtleties. The reader is again referred to the helpful overview given by Wang *et al.* [186].

4.2 Tomonaga-Luttinger Liquid

Breakdown of the Fermi liquid theory

In the same way that screening is reduced in 2D, the reduction is even more drastic in 1D materials. In a 1D chain of atoms, each electron will only have a screening cloud to its left and right. They are confined to the axis, and the addition or movement of one electron will require all other electrons to shift like a domino effect. Thus the electrons are forced to behave collectively in 1D. This is in contrast to *Fermi liquid* theory, the framework within which Section 4.1 took place.

In a many-body system of interacting electrons, one can describe the low-energy excitations (that is, close to E_F) with weakly-interacting, fermionic quasi-particles – the Fermi liquid. The perturbations that an electron causes in the material are included in the dressed quasi-particle, as above, via its *effective mass*. The strength of the interactions are manifested in the effective mass and thereby the energy-momentum (dispersion) relationship of the quasi-particles in the material. Fermi liquid theory is successful for many metals and semiconductors, in which long-range Coulomb interactions are dampened by screening and it is the short-range interactions which determine many properties [203,204].

The Fermi liquid theory breaks down in 1D, however. The confinement and inefficient screening means that any excitation in the chain must be a collective one – the electrons are strongly correlated and long-range Coulomb interactions survive. In 1D, their behaviour is better described by the *Tomonaga-Luttinger liquid* (TLL) theory. A 1950 work by Tomonaga [205] was later developed into a model by Luttinger [206]; in 1981 Haldane generalised this model [207].

A proper description of the TLL theory requires mathematical treatment – one arrives at a 1D interacting Hamiltonian with the fermionic operators replaced by bosonic operators, so-called *bosonisation*. This goes beyond the scope of this thesis, and is addressed in an introductory manner in the literature [188, 208]. Instead, here we attempt to describe the theory and its experimental observables in a very simplified manner.

Fermions become bosons

The key point of the TLL theory is that, in a 1D system under certain conditions, the low-energy excitations of electron-hole quasi-particles actually behave rather like bosons. In real space, the addition of an extra electron will induce a quantised displacement of all the other electrons in the liquid. These quantised displacements are like a superposition of harmonic waves, like sound quanta, and are bosonic. The electron that we insert is 'bosonised' in the sense that the excitation it causes is very non-local and collective, as it displaces a large portion of the liquid [189]. In momentum-space, a 1D metal will have a single band crossing the Fermi energy – one of key assumptions of TLL theory is that this band is linear around E_F (like an acoustic phonon).[2] Thus its Fermi surface will consist only of two points, at $\pm k_\mathrm{F}$, corresponding to left and right movers in the chain. Low-energy particle-hole excitations can only occur with momentum $q \approx 0$ or $q \approx 2k_\mathrm{F}$, in contrast to 2D or 3D in which a range of q-values are possible [188].

Spin-charge separation

When one performs the aforementioned bosonisation of the 1D Hamiltonian, its splits into a spin and a charge sector; so-called *spin-charge separation* is predicted, the hallmark of TLL theory. The spin and charge of the electron behave as independent quasi-particles called *spinons* (with spin but no charge) and *holons*[3] (with charge but no spin) respectively. Single, fermionic, particle-hole excitations appear to split up into collective, bosonic excitations, one carrying spin like a spin-wave and the other charge like a charge-wave. Moreover, these collective excitations propagate with their own, distinct velocities v_s and v_c respectively.

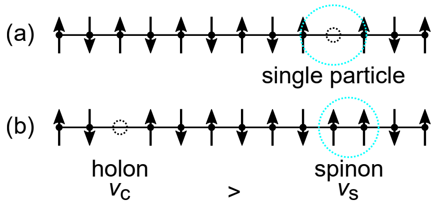

Figure 4.2: A highly simplified schematic illustrating the concept of spin-charge separation. In (a) a single particle is removed from the 1D chain. This creates excitations in both spin and charge, which can move independently with distinct velocities, as in (b). Adapted from Giamarchi [188].

A real-space sketch of the concept is shown in Fig. 4.2. In (a) we remove a fermion – a single-particle excitation – and in the process perturb both the spin density $\sigma(x)$ and the charge density $\rho(x)$ in the chain. These two excitations may travel along the chain with their own velocities, leading to the situation show in (b). The spinon and holon can separate, and thus the initial fermionic excitation has dissociated into these separate quasi-particles.[4] As exotic as it sounds, spin-charge separation is not just a fanciful prediction; it has been observed experimentally in various 1D and quasi-1D systems [209–211]. If one

---

[2] Thankfully, this is a reasonable assumption for the low-energy excitations with which we concern ourselves.

[3] Also sometimes called *chargons*.

[4] Actually our schematic still depicts things in a fermionic way: the spinon and holon are depicted as localised excitations rather than collective, bosonic excitations [188].

witnesses spin and charge move through the wire with different velocities, it is clear that electrons acting individually cannot be responsible – it would require some electrons to have different properties from others. The phenomenon can only be explained by collective, strongly correlated electron behaviour [188, 189].

The extent to which v_s and v_c differ from each other (and from v_F) is determined by the interaction strength of the electrons. This is incorporated in the Luttinger liquid parameters K_s and K_c. Values $K_\mathrm{s} = K_\mathrm{c} = 1$ represent the non-interacting Fermi-gas; values closer to 0 represent stronger interaction and a larger deviation from the v_F dispersion. In many cases the interactions in the wire are spin-independent, in which case $K_\mathrm{s} = 1$, but in the presence of spin-orbit coupling or dipole-dipole coupling this can change [212]. The relationships between $v_\mathrm{s,c}$ and $K_\mathrm{s,c}$ are addressed and visualised in Chapter 6.

Zero bias anomaly and power law

It should be clear from the above discussion that adding an additional electron to a 1D wire will require some amount of energy, as it will significantly perturb the system. As a result the tunnelling probability into the 1D wire is reduced around E_F – this is known as a zero bias anomaly (ZBA) and can be observed experimentally via STS [213] or capacitance measurements [214], for example. By contrast, a 3D metal of well-screened, weakly interacting electrons should in theory show a flat density of states around E_F. Moreover, the ZBA of a TLL is predicted to follow a power-law behaviour with bias, namely $dI/dV \approx V^\alpha$, and similarly with temperature. The exponent α depends on the electron-correlation strength and the one-dimensionality of the wire. The larger α is, the stronger the interactions, while $\alpha = 0$ corresponds to the non-interacting Fermi-gas. The TLL parameters α and K_c are related by a simple expression, the details of which depend on the particular system [127, 215]. As has been noted in the literature [189, 216], a ZBA is not necessarily 'smoking gun' evidence for TLL behaviour, since ZBAs are seen in a multitude of systems of various dimensionalities [217–219] and may just be a general property of low-dimensional metals with disorder [216, 220].

In experiment

Due to the immense difficulties in fabricating and actually measuring 1D systems, the experimental history of the TLL is relatively short, and not without controversy [189, 216, 221–223]. With progress in the synthesis and isolation of 2D materials over the last 15 years, however, new opportunities have and continue to present themselves. One of these has been the MTBs hosted in semiconducting TMDC monolayers [127], introduced in Section 3.2. Within this context, the work of Chapter 6 took place. More recent developments in this field will be looked at in Part III.

PART II

Experimental Results

CHAPTER 5

Manuscript [1]: Comprehensive tunneling spectroscopy of quasifreestanding MoS_2 on graphene on Ir(111)

This chapter wholly consists of the above-named publication, published in Physical Review B *on 26th March 2019, available online.*

The experiments were proposed by W. Jolie, C. Murray, C. Busse and T. Michely. All sample growth and measurement was performed at $_{\mathrm{T}}$STM. *The samples were grown by C. Murray and W. Jolie with advice given by J. Hall. The STM and STS measurements were carried out by C. Murray and W. Jolie; J. A. Fischer assisted on the multi-layer sample. The data analysis was performed principally by C. Murray; C. van Efferen made a significant contribution to the understanding and analysis of* $(\mathrm{d}I/\mathrm{d}Z)_I$ *or 'κ-mode' STS. Discussions were held with N. Ehlen and A. Grüneis to compare our STS data with their ARPES data on the same system (published in Ref. [224]), improving our understanding of the respective results. N. Ehlen performed additional analysis of the Ref. [224] data, providing us with information on the energy-location and dispersion of certain bands as seen in ARPES.*

C. Murray wrote the manuscript and finalised it in close collaboration with T. Michely.

Some of the results shown in this Chapter can be found in the doctoral thesis of W. Jolie [225] and, to a minor extent, the Master's thesis of C. van Efferen.

PHYSICAL REVIEW B **99**, 115434 (2019)

Comprehensive tunneling spectroscopy of quasifreestanding MoS_2 on graphene on Ir(111)

Clifford Murray,[1,*] Wouter Jolie,[1,2] Jeison A. Fischer,[1] Joshua Hall,[1] Camiel van Efferen,[1]
Niels Ehlen,[1] Alexander Grüneis,[1] Carsten Busse,[1,2,3] and Thomas Michely[1]
[1]*II. Physikalisches Institut, Universität zu Köln, Zülpicher Straße 77, 50937 Köln, Germany*
[2]*Institut für Materialphysik, Westfälische Wilhelms-Universität Münster, Wilhelm-Klemm-Straße 10, 48149 Münster, Germany*
[3]*Department Physik, Universität Siegen, 57068 Siegen, Germany*

(Received 25 January 2019; revised manuscript received 8 March 2019; published 26 March 2019)

We apply scanning tunneling spectroscopy to determine the band gaps of mono-, bi-, and trilayer MoS_2 grown on a graphene single crystal on Ir(111). Besides the typical scanning tunneling spectroscopy at constant height, we employ two additional spectroscopic methods giving extra sensitivity and qualitative insight into the k vector of the tunneling electrons. Employing this comprehensive set of spectroscopic methods in tandem, we deduce a band gap of 2.53 ± 0.08 eV for the monolayer. This is close to the predicted values for freestanding MoS_2 and larger than is measured for MoS_2 on other substrates. Through precise analysis of the "comprehensive" tunneling spectroscopy we also identify critical point energies in the mono- and bilayer MoS_2 band structures. These compare well with their calculated freestanding equivalents, evidencing the graphene/Ir(111) substrate as an excellent environment upon which to study the many celebrated electronic phenomena of monolayer MoS_2 and similar materials. Additionally, this investigation serves to expand the fledgling field of the comprehensive tunneling spectroscopy technique itself.

DOI: 10.1103/PhysRevB.99.115434

I. INTRODUCTION

The various exciting properties of monolayer molybdenum disulfide (ML-MoS_2), the paradigmatic semiconducting transition metal dichalcogenide (TMDC), are well documented [1,2]. Among these, its large, direct band gap is promising for the electronics communities, and is a basic quality to be characterized. Large-scale flakes can be grown epitaxially [3–5] or exfoliated [6,7], but reliable characterization of the pristine electronic band gap remains problematic.

Optical measurements are influenced by the large exciton binding energy of ML-MoS_2. Standard angle-resolved photoemission spectroscopy (ARPES) has no access to the conduction band unless it is shifted below the Fermi energy E_F through heavy doping. This, however, also leads to band distortion and band-gap renormalization due to the change in dielectric environment [8–11]. Pump-probe ARPES can measure the electronic band gap [12], but suffers from poor energy resolution.

Scanning tunneling spectroscopy (STS) can directly access the electronic density of states above and below E_F, and it has indeed been performed on ML-MoS_2 on a variety of substrates. However, the substrates—metallic by necessity—tend to screen, gate, and/or mechanically strain the MoS_2. This leads to the predicted freestanding band gap of $E_g \approx 2.8$ eV [13–16] being considerably reduced. For example the band gap measured by constant height STS is $E_g = 1.74$ eV on an Au substrate [17], 2.01 eV on graphene/SiC [18], 2.17 eV on quartz [19], 2.20 eV on graphene/Au [20], and variously 1.9 eV [21], 2.15 eV [22], or 2.40 eV [23] on graphite. In addition to simply reducing the band-gap size, substrate coupling will affect each band differently: due to the differing planar nature of the Mo and S orbitals, the band structure is distorted inhomogeneously across the MoS_2 Brillouin zone (BZ) [17]. Large band gaps of $E_g \approx 2.65$ eV [24] and ≈ 2.7 eV [25] have been reported, but only in locations where the ML-MoS_2 is locally decoupled from an inhomogeneous substrate. On top of all this, practical difficulties due to sulfur's relatively high vapor pressure had, until recently [3], hindered molecular beam epitaxy (MBE) synthesis of MoS_2. Thus close-to-freestanding MoS_2 flakes of sufficient size, quality, and cleanness on STS-permitting substrates have remained elusive.

Additional to the complications caused by the metallic substrates on which it is performed, there are shortcomings in the typical practice of STS. It has recently been shown by Zhang *et al.* [26] that constant height STS alone is insufficient for accurate band-gap determination, as states from the edge of the BZ can go undetected due to their reduced decay length. Therefore it remains an open question how accurately the constant height STS measured band gaps represent the magnitude of the ML-MoS_2 direct gap. In contrast, constant current STS allows the tip to move closer to the sample to give access to these weaker signals, while κ mode STS (explained below) allows identification of the states' location within the BZ.

In this work we present high-quality ML-, bilayer (BL-), and trilayer (TL-)MoS_2 which is well decoupled from its graphene/Ir(111) substrate. Following the approach of Zhang *et al.* [26], we use "comprehensive STS" (constant height, constant current, and κ modes together) to identify not only the band gaps but also various critical-point energies (CPEs), i.e., local extrema in the band structure. These measured

---

[*] murray@ph2.uni-koeln.de

energies compare favorably with those of theoretical calculations for the freestanding materials, evidencing this system as an opportunity to study the inherent characteristics of mono- or few-layer MoS_2 without obtrusive substrate effects.

Moreover, our analysis makes plain that standard constant height STS fails to detect both the valence band maximum and conduction band minimum, and thus does not measure the band gap of ML-MoS_2. This has implications for the interpretation of STS data of ML-MoS_2, and indeed other materials with extremal points forming the band gap at large parallel momenta. Comprehensive STS is not only more sensitive, but enables also the determination of the CPEs making up the tunneling spectrum. As shall be demonstrated here, this can prevent the false assignment of a band edge. It is thus a vital tool in the determination of the electronic structure of the semiconducting TMDCs. The technique and its associated analysis have only seen a few instances of usage [26–28], so a broader implementation is desirable.

II. METHODS

The sample is prepared *in situ* at pressures $p < 5 \times 10^{-10}$ mbar. The Ir(111) single crystal is cleaned by Ar^+ ion sputtering and annealing at temperatures $T \approx 1500$ K. As described in Ref. [29], a closed monolayer of graphene (Gr) is grown on Ir(111) via temperature programmed growth and chemical vapor deposition (CVD) at $T \approx 1370$ K. ML- to few-layer MoS_2 is subsequently grown on the Gr/Ir(111) substrate by van der Waals MBE, according to the methods developed in Ref. [3]. Mo is evaporated from an *e*-beam evaporator and S from FeS_2 granules in a Knudsen cell. Specifically, we evaporate Mo in a S background pressure of 5×10^{-9} mbar onto the room temperature substrate, and then anneal the system to 1050 K in the same S background pressure. The process of coevaporation then annealing can be repeated in cycles, in order to promote well-oriented, multiple-layer growth.

Scanning tunneling microscopy (STM) and STS are performed at $T = 5$ K and $p < 10^{-11}$ mbar with a tungsten tip. For STS we use a lock-in amplifier with modulation frequency 777 Hz and modulation amplitudes $V_{\text{mod}} = 4\text{–}8\ \text{mV}_{\text{rms}}$, together with thermal broadening this yields experimental resolution of $\Delta E \approx \sqrt{(3.3k_{\text{B}}T)^2 + (2.5eV_{\text{mod}})^2} \approx 20$ meV or better [30]. We perform comprehensive STS comprised of three different modes: constant height [recording $(dI/dV)_Z$], constant current [$(dI/dV)_I$], and κ [$(dI/dZ)_I$], where I is the tunneling current, V the bias voltage and Z the tip-to-sample distance or "height." The principles of these three modes shall be discussed.

For both constant height and constant current STS we measure the dI/dV signal while V is ramped, giving information on the local density of states of the sample [31]. Though constant height STS allows both valence and conduction bands to be measured in a single spectrum, certain states may go undetected if Z is too large. Constant current STS does not permit ramping across E_F but offers greater dynamic range: the tip can move towards the sample and thereby detect some suppressed signals missed in constant height mode. This suppression can be due to the fact that a state with finite parallel momentum $k_\parallel$ will decay into the vacuum with an inverse decay length:

$$\kappa = [(2m\bar{\phi}/\hbar^2) + k_\parallel^2]^{1/2}, \tag{1}$$

where m is the free electron mass and $\bar{\phi} = (\phi_t + \phi_s - e|V|)/2$ is the bias-dependent tunneling barrier between tip and sample with work functions ϕ_t and ϕ_s respectively [32,33]. Thus, states at the edge of the BZ decay more quickly into the vacuum than those at the center. This necessitates the tip moving closer to detect them, especially if stabilization was performed at a voltage (energy) where Γ-point states dominate.

We indirectly measure κ and thus $k_\parallel$ through $(dI/dZ)_I$ mode STS. Here the lock-in modulates the height ($Z_{\text{mod}} = 4\text{–}8$ pm) while V is ramped at constant $I = I_0$ as before. Considering a tunneling current $I \propto e^{-2\kappa Z}$ [34], one finds

$$\left.\frac{dI}{dZ}\right|_{I_0} \propto -2\kappa e^{-2\kappa Z} = -2\kappa I_0; \tag{2}$$

we measure this and thereby extract an effective tunneling decay constant. Through comparison with the spectra obtained via the two other modes, one can assign features of the STS spectra to particular critical points in the BZ. Thus, a degree of k-space resolution has been added to the traditional STS. We note that inside the MoS_2 band gap, when the tip moves very close to the sample, the "thick barrier" limit implicitly assumed in Eq. (2) does not necessarily hold and Gr states may contribute to the tunneling current. Therefore we do not draw inferences from κ values within the band gap.

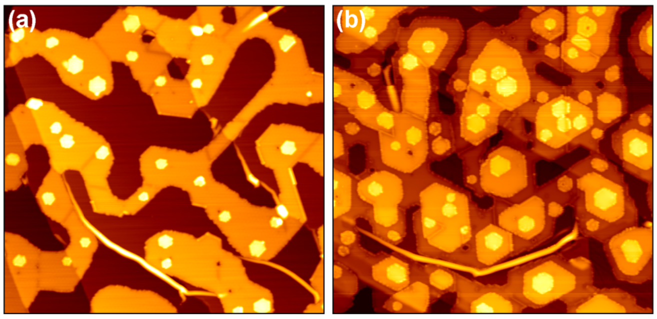

FIG. 1. Constant current STM topographs of MoS_2 on Gr/Ir(111). (a) MoS_2 coverage of 0.6 layers. (b) MoS_2 coverage of 1.4 layers. Small areas of exposed Gr are visible. The TL forms islands of ≈20 nm diameter. Gr wrinkles are visible in the lower section in both topographs. STM parameters: (a) $V = 1.5$ V, $I = 0.01$ nA; (b) $V = 1.0$ V, $I = 0.08$ nA; each image size is $200 \times 190\ \text{nm}^2$.

III. EXPERIMENTAL RESULTS

STM topographs of two typical MoS_2 samples are shown in Fig. 1. In (a) an MoS_2 coverage of around 0.6 layers yields a network of ML-MoS_2 extending over the Gr/Ir(111) substrate, crossing several Ir step edges. It is decorated by small BL islands of ≈10 nm diameter. The cleanness and low defect density of the MoS_2, reported previously [3], were verified with STM here. Grain boundaries are visible between ML flakes of different orientation. The majority of these are mirror twin boundaries (MTBs), the properties of which are discussed in Ref. [35]. In the lower section of the topograph a Gr wrinkle can be seen, resulting from the CVD growth.

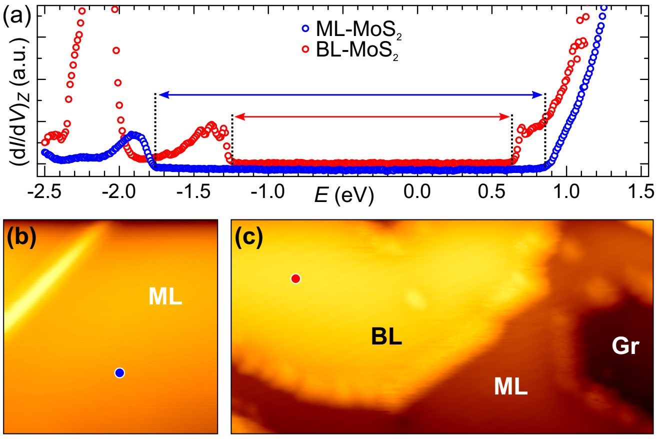

FIG. 2. (a) Constant height spectra of ML- and BL-MoS$_2$ (in blue and red respectively). Assignment of the band gaps based only on this STS method is shown. The spectra were taken at the points marked in topographs (b) and (c). The different areas of each sample are indicated for clarity. In (b) a MTB is seen in the top-left corner. STS/M parameters (with stabilization voltage V_{st}, stabilization current I_{st}): (a) $V_{st} = 1.5$ V; ML $I_{st} = 0.1$ nA, BL $I_{st} = 1.0$ nA; (b) $V = 0.9$ V, $I = 0.10$ nA, image size 10×10 nm^2; (c) $V = 1.0$ V, $I = 0.08$ nA, image size 28×14 nm^2.

With a higher coverage of approximately 1.4 layers, shown in Fig. 1(b), the sample exhibits ML-, BL-, and TL-MoS$_2$ islands in coexistence. Small areas of exposed Gr are visible below the nearly closed ML. Large, well-oriented BL and ≈20 nm diameter TL islands form on top. MTBs are seen to also occur in the BL.

A. Constant height STS of mono- and bilayer MoS$_2$

For illustrative purposes we first determine the band gaps of ML- and BL-MoS$_2$ using constant height STS only, as is typically done in the literature for this and other TMDCs. Figure 2(a) shows two exemplary constant height spectra of ML- and BL-MoS$_2$. Topographs in Figs. 2(b) and 2(c) show where the respective spectra were obtained. Note that all spectra in this work were recorded at locations at least 5 nm from any defects—e.g., edges, MTBs, or point defects—to avoid any perturbation or confinement effects which these may cause. As is common in the literature, we here define the band edges to be where the dI/dV signal becomes clearly discernible from background noise levels. Through this approach, we find the valence band maximum (VBM) to be located at −1.77 eV and the conduction band minimum (CBM) to be at 0.86 eV for ML-MoS$_2$. Similarly for the BL, the corresponding band edges are found to be at −1.24 and 0.63 eV. This would yield band-gap estimates of 2.63 and 1.87 eV for ML- and BL-MoS$_2$ respectively. However, it shall be demonstrated that these band-gap determinations for MoS$_2$ are unreliable.

We briefly consider the band structures of ML- and BL-MoS$_2$ close to E_F, to guide proceeding STS analysis. The band structures sketched in Fig. 3 are based on previous density functional theory (DFT) calculations [13–15,36]. As seen in Fig. 3(a), the ML has a direct band gap located at the K point. The VB is split by ≈145 meV at K due to spin-orbit coupling, and a maximum at Γ lies close in energy [9,13–15,37]. In contrast, the BL (b) has a smaller and indirect band gap, with the VBM located at the Γ point and the CBM at the Q point. The critical points at K and Q in the CB lie close in energy however, and so the true location of the CBM is debated in the literature [38,39]. The VB is split at the Γ point due to interlayer hopping [40].

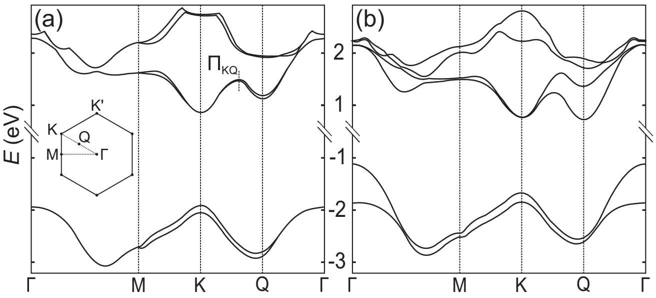

FIG. 3. Sketched band structures of freestanding (a) ML- and (b) BL-MoS$_2$. Redrawn after Ref. [13] and adapted to reflect comparison with other DFT calculations [14,15,36], the figure should serve only as a generic outline. The first BZ is shown as an inset, with the high-symmetry points and Q point marked. Also indicated is a local maximum between the K and Q points in the ML CB, labeled here Π_{KQ}. For ease of reference the entire band structures have been rigidly shifted to approximately match our energies, rather than fixing 0 eV at the VBM as is typical in DFT.

B. Comprehensive STS of monolayer MoS$_2$

In Fig. 4 exemplary sets of comprehensive STS on ML- and BL-MoS$_2$ are shown. The three different STS modes are considered together and for both the ML and BL are compared across at least five sets of spectra, taken on various islands and with different STM tips. Through this, some critical points in the respective band structures can be assigned.

Beginning with the VB of the ML, Fig. 4(a) shows the same constant height spectrum as in Fig. 2(a), now plotted logarithmically. In (b) constant current STS yields a main peak at −1.87 eV with a slight shoulder towards larger binding energies. In (d) the corresponding κ measurement shows a dip, also at −1.87 eV. This dip to 0.93Å^{-1} indicates a sudden drop in the effective tunneling decay constant of the states there, i.e., states with less $k_\parallel$. (A discussion of the actual $k_\parallel$ values extracted from κ follows in Sec. IV). Considering the drop in κ and with reference to the band structure of ML-MoS$_2$ [Fig. 3(a)], we must assume this feature to be due to the Γ point. Though the VBM is expected to be the upper of the spin-split bands at the K point, we can expect the spectrum to be totally dominated by states from Γ. First, the states at K decay faster into the vacuum due to their high $k_\parallel$. Furthermore, calculation has shown that the orbital character at the Γ point is predominantly Mo-d_{z^2}, while at K it is predominantly Mo-d_{xy}, $d_{x^2-y^2}$, i.e., mostly out of plane and mostly in plane respectively [41–43]. Thus, if the bands at K and Γ lie sufficiently close in energy, we would expect the Γ band to mask the K band in our STS signal. Indeed in *ab initio* calculations the separation between the upper K band ($K_\uparrow$) and the band at Γ is found variously to be around $\Delta\Gamma K_\uparrow = 0.04$ [13], 0.05 [37], 0.12 [15], or 0.19 eV [14].

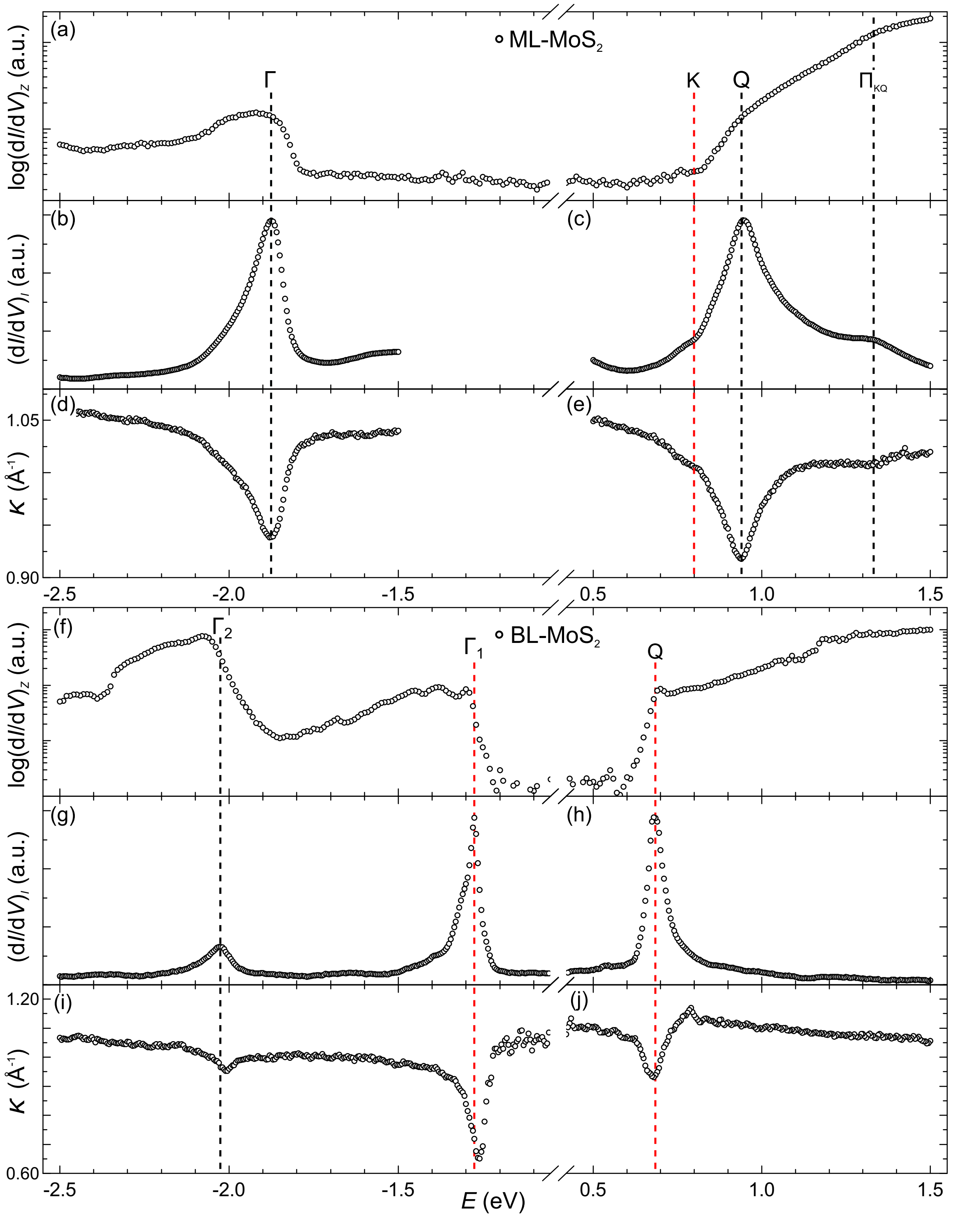

FIG. 4. Comprehensive STS of (a–e) ML- and (f–j) BL-MoS$_2$. The spectra were obtained at the locations shown in Figs. 2(b) and 2(c); note that panels (a) and (f) show the same spectra as Fig. 2(a), here plotted on a logarithmic intensity scale. (a,f) Constant height $(dI/dV)_Z$ STS spectra. (b,c,g,h) Constant current $(dI/dV)_I$ STS spectra performed over the VB and CB edges of the respective systems. (d,e,i,j) κ [recording $(dI/dZ)_I$] STS spectra performed over the VB and CB edges. (a–j) Assigned critical point energies are marked by dashed black lines; those critical points which constitute a VBM or CBM are dashed red. STS parameters: (a,c,e,f,h,j) $V_{\mathrm{st}} = 1.5$ V, (b,d,g,i) $V_{\mathrm{st}} = -2.5$ V; (a-e) $I_{\mathrm{st}} = 0.10$ nA, (f) $I_{\mathrm{st}} = 1.00$ nA, (g-j) $I_{\mathrm{st}} = 0.05$ nA.

We conclude that both branches of the spin-split band at K are masked by Γ states. An estimate for the position of $K_\uparrow$ (i.e. the VBM) can nonetheless be made. In ARPES experiments on ML-MoS$_2$ grown on Gr/Ir(111) by the same method as in this work, a separation between Γ and $K_\uparrow$ of $\Delta\Gamma K_\uparrow = 0.11$ eV was found [9,44]. This energy separation would locate $K_\uparrow$ at -1.76 eV in our case. We consider lower and upper bounds based on the aforementioned DFT calculations

TABLE I. CPEs (eV) identified in ML-MoS$_2$ using comprehensive STS averaged over multiple sets, and the estimated CPE at $K_\uparrow$.

Γ	$(K_\uparrow)$	K	Q	Π_{KQ}
-1.87 ± 0.02	(-1.76 ± 0.08)	0.77 ± 0.02	0.90 ± 0.05	1.30 ± 0.02

to be $\Delta\Gamma K_\uparrow = 0.04$ eV [13] and $\Delta\Gamma K_\uparrow = 0.19$ eV [14] respectively, i.e. for $K_\uparrow$ to lie between -1.83 eV and -1.68 eV. Taking these bounds as a conservative uncertainty, we estimate the VBM of our ML-MoS$_2$ system to be located at -1.76 ± 0.08 eV.

The CB of ML-MoS$_2$ also shows various features in constant current STS, Fig. 4(c). A main peak at 0.94 eV is flanked by a small shoulder at 0.80 eV and, towards higher energies, a broad hump at 1.32 eV. In (e), κ shows a clear dip to 0.91 Å^{-1} at 0.94 eV. Consulting the theoretical band structure [Fig. 3(a)], a local minimum close to the CB edge is expected at the Q point, and any Γ states are much further from the Fermi level, thus this feature must be assigned to the Q point. Across our sets this peak tended to take one of two values—either 0.86 or 0.95 eV approximately—and typically has a broad shape suggestive of more than one contributing state. We find no correlation of the Q-point peak value to the lateral position in the MoS$_2$ layer. The properties could be due to the spin-splitting of the band at the Q point, predicted to be of magnitude 0.03–0.08 eV [13–15,37]. The faint shoulder at 0.80 eV has no obvious corresponding feature in (e) here, though a small peak was occasionally seen at this energy in κ spectra. The feature was practically undetectable in constant height STS, suggesting that it originates from states of large $k_\parallel$ and/or of mostly in-plane orbital nature. This fact, combined with a small peak sometimes seen in κ and with consultation of the ML-MoS$_2$ band structure, compels assigning this feature to states at the K point. This represents the CBM of ML-MoS$_2$, found at 0.77 ± 0.02 eV across the measured sets. This K-point extremum being detectable, in contrast to the K point of the VB, can be explained by its orbital character. The K point at the CBM is dominated by out-of-plane Mo-d_{z^2} orbitals; at the VBM it is dominated by in-plane Mo-d_{xy}, $d_{x^2-y^2}$ orbitals [41–43]. Finally, we assign the broad hump at 1.32 eV to the local maximum lying roughly halfway between the K and Q points, which we term Π_{KQ}. The (average) assigned CPEs for the ML are summarized in Table I.

It should be noted that the CPEs constituting band edges have alternatively been defined by Zhang *et al.* [26] to be at the midpoint of the transition from TMDC to substrate states in the STS signal. This is practically equivalent to us taking the energy at FWHM of the peaks closest to E_F; for example in Fig. 4(c), with Gaussians fitted to the various features including the K-point shoulder, this would yield a CBM at 0.75 eV rather than 0.80 eV. However, due to ambiguities of peak fitting in our spectra and for simplicity, we chose instead to define the band edges at the peak centers in constant current STS.

C. Comprehensive STS of bilayer MoS$_2$

In constant height STS of the BL-MoS$_2$, Fig. 4(f), two sharp rises in intensity are seen in the VB. These are accompanied by clear peaks in constant current and clear dips in κ measurements, (g) and (i) respectively. Based on their nature and with consideration of the generic BL band structure [Fig. 3(b)], we can confidently assign the features marked at -1.28 and -2.03 eV to the split bands at the Γ point, labeled Γ_1 and Γ_2 respectively. The signal from Γ_2 is much weaker in constant current and κ STS because in the midst of the VB states the feedback loop has taken the tip further away from the sample, making it less sensitive to the onset of the Γ_2 band. Also for this reason, and considering their faster decay into the vacuum, it is wholly unsurprising that the K-point states expected close to -2 eV were not reliably detected.

Similarly in the CB a sharp rise in constant height [Fig. 4(f)] coincides with a peak in constant current (h) and dip in κ (j). The last of these indicates states from near the center of the BZ. Consultation of Fig. 3(b) shows that Γ states lie deep in the CB, and thus we assign this feature at 0.68 eV to the Q point representing the CBM. The small peak in κ at around 0.79 eV in (j) could possibly be due to the K-point minimum, but this feature was not observed consistently enough with different tips to allow an unambiguous deconvolution. Considering the Q-point states' energetic proximity, their location at the band edge, and their smaller $k_\parallel$, they could be expected to mask the K-point states in STS. Indeed this issue is nontrivial; there is debate in the literature as to whether the CBM of BL-MoS$_2$ lies at the K point [13,45] or at the Q point [38,40,46], a matter of relevance due to the lack of symmetry at the latter. The (average) assigned CPEs for the BL are summarized in Table II.

With the band extrema identified in Tables I and II we determine band gaps of $E_\text{g}^\text{ML} = 2.53 \pm 0.08$ eV and $E_\text{g}^\text{BL} = 1.96 \pm 0.05$ eV. For the specific sets shown in Fig. 4 the band gaps are 2.56 and 1.96 eV respectively.

D. Comprehensive STS of trilayer MoS$_2$

Figure 5 shows comprehensive STS of TL-MoS$_2$, together with a BL set for comparison. The small size of the TL islands—for example ≈15 nm diameter in Fig. 5—means that interfering quantum confinement effects cannot be ruled out. Nonetheless, some qualitative features are obvious from the spectroscopic data. Namely, a third branch in the VB has appeared due to further splitting of the band at Γ, while the CB edge remains mostly unchanged, in line with theoretical calculations [43,47]. This is discussed further in Sec. IV. A band gap of $E_\text{g}^\text{TL} = 1.77$ eV is estimated based on Fig. 5, though

TABLE II. CPEs (eV) identified in BL-MoS$_2$ using comprehensive STS averaged over multiple sets.

Γ_2	Γ_1	Q
-2.05 ± 0.04	-1.27 ± 0.04	0.69 ± 0.03

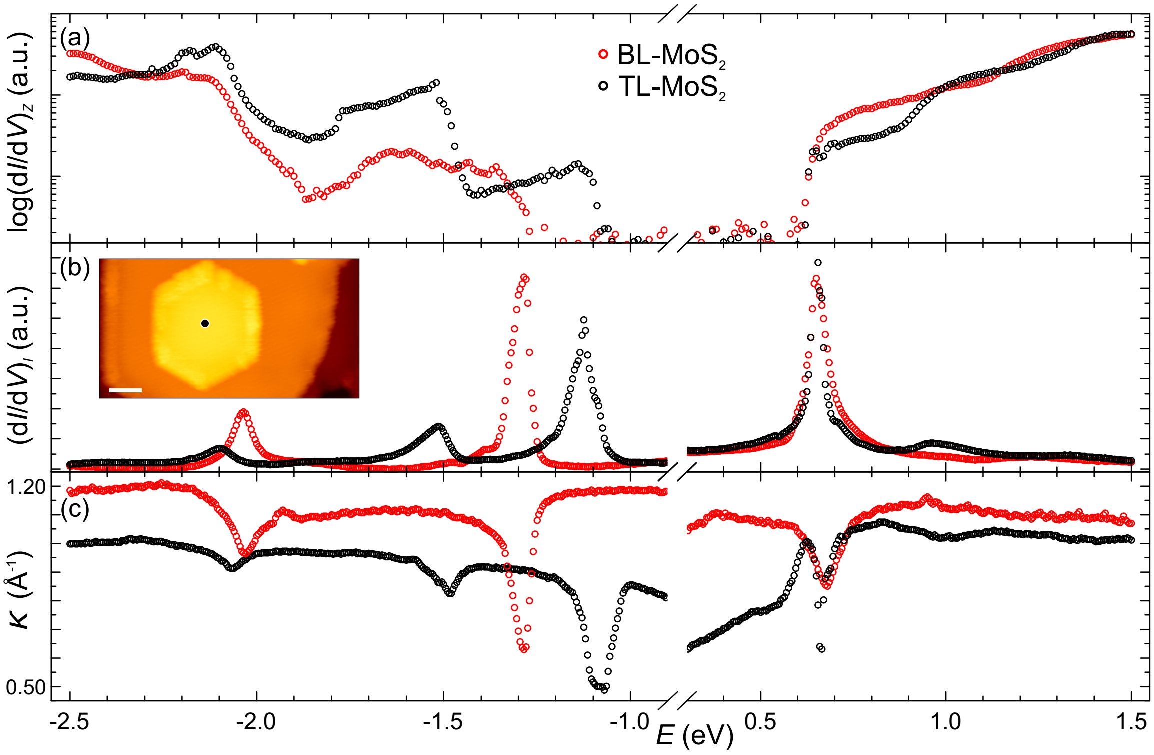

FIG. 5. Comprehensive STS of TL-MoS$_2$ (black), with BL-MoS$_2$ (red) for comparison. The TL spectra were obtained at the location shown in the inset STM topograph; the BL spectra elsewhere on the same sample. Note that this is a different BL set from that shown in Figs. 2 and 4, to give an idea of deviation within the spectroscopic data. STS parameters: (a) $V_{\rm st} = 1.5$ V, $I_{\rm st} = 1.0$ nA; (b,c) $V_{\rm st} = -2.5$ V and 1.5 V (for VB and CB respectively), $I_{\rm st} = 0.1$ nA; TL and BL spectra both obtained with the same parameters. STM (inset): $V = 1.0$ V, $I = 0.07$ nA, scale bar 5 nm.

we provide this value tentatively due to limited statistics. Additionally, although investigations of such islands did not show lateral confinement, the aforementioned quantum-size issue should be noted.

IV. DISCUSSION

We find that using constant height STS alone would lead to a 0.10 eV overestimation of $E_{\rm g}^{\rm ML}$ (when compared with comprehensive STS analysis) because the measured states are not actually those at the respective band edges. In constant height STS both band extrema go undetected. In comprehensive STS the CBM at K is detected. The VBM is not detected but, importantly, a false assignment of the VBM is prevented through κ measurements. One could wrongly assume that the peak in Figs. 4(a) and 4(b) is due to the VBM (at the K point), but the drop in κ rules this out. Put simply, comprehensive STS sees more states, and when it is blind to certain states then it can tell us that this is the case.

The benefits of the more thorough technique are further illustrated by accurate observation of layer-dependent phenomena in the MoS$_2$. It is known from the literature that the band-gap reduction with increasing thickness is due to the VBM—specifically the Γ point—shifting to smaller binding energies, while the CBM does not change significantly in energy [43,47,48]. Using only constant height STS the CBM appears to shift by 0.23 eV towards $E_{\rm F}$ upon addition of a second MoS$_2$ layer, whereas the shift is indeed much less drastic (0.08 eV) in comprehensive STS. The continuation of these trends—a static CBM and an up-shifting VBM—is visible as the thickness is increased from BL to TL (Fig. 5). Additionally, the well-documented lifting of degeneracy in the Γ band and its consequent splitting from one (ML) to two (BL) to three (TL) branches is clearly visible across the data sets. Thereby the coupling of each newly added MoS$_2$ layer to those underneath is seen through comprehensive STS.

The technique has its limitations, of course. As discussed, we could not unambiguously detect the K-point states which represent the VBM of ML-MoS$_2$, presumably due to their short decay length, in-plane orbital character, and proximity to the dominating Γ point. States being hidden due to a combination of these factors is an issue; previous comprehensive STS investigations of ML-MoS$_2$ have also failed to identify the VBM [28]. The K-point VBM was clearly detected in ML-MoSe$_2$ and ML-WSe$_2$, presumably because in these cases it is separated from the Γ point by large energies of 0.39 and 0.64 eV respectively [26]. However, the CBs of these materials and their sulfide analogues exhibit a trend: the K-point STS signal becomes less and less prominent as it moves energetically closer to the Q point [26].

Measuring κ helps reveal a state's location in the BZ, but extracting the corresponding values of $k_\parallel$ proves nontrivial. In Eq. (1) the only unknown variable is the energy barrier $(\phi_t + \phi_s)/2$. We can set this (to 2.5 eV) to obtain reasonable $k_\parallel$ values for most CPEs. However, this is an *ad hoc* adjustment and it fails for some CPEs regardless. Similar problems arise in κ measurements in the literature [26,28]. The values of κ given here remain valid; we additionally take $I(Z)$ spectra at various bias voltages, to which $I(Z) \propto e^{-2\kappa Z}$ is then fitted, showing excellent agreement with $(dI/dZ)_I$ spectra. We suggest the difficulty in translating κ into actual $k_\parallel$ values is due to an oversimplified picture of the tunneling that forms the basis of Eq. (1). Nonetheless, κ serves as a useful qualitative measure of a state's position in the BZ relative to states energetically nearby.

A more puzzling issue is an apparent mismatch between STS and ARPES studies. Specifically, the Γ point in the VBM of ML-MoS_2 on Gr/Ir(111) is found to be -1.87 eV in STS (this work) but -1.61 eV in ARPES [9,44]. The Γ points in BL-MoS_2 on the same substrate coincide, however: -2.05 eV and -1.27 eV in STS (this work) compared with -1.98 eV and -1.33 eV in ARPES [9,44]. In collaborative STS [17] and ARPES [8] investigation of ML-MoS_2 on Au(111), discrepancies of 0.10 eV and 0.15 eV were found for the Γ and K points respectively. Comprehensive STS on the same system showed further disagreement [28]. A comparative study of comprehensive STS and ARPES (performed on the same sample in the same UHV chamber) would present a considerable experimental challenge, but would be worthwhile if the community is to address these problems of inconsistency.

Despite the discussed experimental uncertainties, it is clear that ML-MoS_2 on Gr/Ir(111) is a very well decoupled system. Our conservative estimate $E_g^{ML} = 2.53 \pm 0.08$ eV represents the largest STS-measured band gap of ML-MoS_2 on a homogeneous substrate. This value comes much closer to the freestanding $E_g \approx 2.8$ eV predicted by DFT [13–16] than those of ML-MoS_2 measured on other substrates, such as graphite ($E_g = 2.40$ eV [23]). If we would instead take the band-gap size of 2.63 eV based on constant height STS alone—as is done in the literature with which we compare this work—our system would appear even better decoupled. ML-MoS_2 nanopatches suspended over Au(111) vacancy islands of roughly 3 nm diameter have shown an apparent band gap of $\approx$2.7 eV, indicating that they are quasifreestanding [25], but their small size leaves them liable to lateral quantum confinement effects. An apparent band gap of $\approx$2.65 eV has been reported for water-intercalated areas of ML-MoS_2 on graphite [24]. However, the interfacial water layer and defects resultant from the wet transfer process have competing doping effects and leave the MoS_2 inhomogeneous.

The freestanding nature of our system is further apparent upon closer examination of the measured CPE values. In Table III the energy separations of ML- and BL-MoS_2 CPEs can be compared with those of various DFT calculations. Taking into account that there is considerable discrepancy within the DFT results themselves, the measured CPEs agree reasonably with calculation. The band gap $E_g^{BL} = 1.96 \pm 0.04$ eV also compares well with values 1.89 eV [13] and 1.83 eV [40] from the literature.

TABLE III. Comparison of CPE separations measured in ML- and BL-MoS_2/Gr/Ir(111) here with those of freestanding MoS_2 as calculated by various DFT approaches. In the ΔKQ column the energies of both spin orientations in the split band at Q are given.

Ref.	ML CB ΔKQ (eV)	ML CB $\Delta K\Pi_{KQ}$ (eV)	BL VB $\Delta\Gamma_{1,2}$ (eV)
this work	0.13 ± 0.05	0.53 ± 0.03	0.78 ± 0.06
[13]	$_\uparrow 0.44$, $_\downarrow 0.51$	0.71	0.75
[14]	$_\uparrow 0.19$, $_\downarrow 0.25$	0.48	
[15,36]	$_\uparrow 0.08$, $_\downarrow 0.12$	0.30	0.69
[37]	$_\uparrow 0.13$, $_\downarrow 0.17$	0.27	
[40]			0.76

Previous experiments on ML-MoS_2 on Gr/Ir(111) suggest weak substrate interaction also. MoS_2 islands are mobile enough to be moved laterally on the surface using the STM tip [3]. Additional evidence of weak interaction was seen in photoluminescence spectroscopy, x-ray photoemission spectroscopy, temperature dependent Raman spectroscopy, and ARPES [9]. For example, comparing Raman measurements at room temperature and at 4 K showed that the ML-MoS_2 does not follow the thermal expansion of its substrate. Instead its expansion resembles that of a freestanding layer, meaning that it is not strained by the substrate. In ARPES, no hybridization of Gr and MoS_2 bands was seen [9].

V. CONCLUSION

We have characterized the electronic structure of quasifreestanding ML-, BL-, and TL-MoS_2 on Gr/Ir(111) with high-precision STS analysis, whereby the band gaps have been determined, various CPEs close to E_F identified, and layer-dependent phenomena observed. The measured band-gap sizes are close to those of the freestanding material, showing that MoS_2 is well decoupled from this substrate. The measured CPEs can be cross-referenced with those predicted by DFT calculations from the literature, further corroborating this. Thus Gr/Ir(111) represents a substrate for STS investigations of the inherent properties of two-dimensional TMDCs, with minimal interference from gating, band-rehybridization, or strain effects.

This work implores the use of comprehensive STS where possible. The technique gives access to states otherwise undetectable, for example the CBM of ML-MoS_2 here. Moreover, it adds a degree of k-space resolution, allowing identification of band structure features and preventing false assignments, for example of the VBM of ML-MoS_2 here. Thus the supplementary constant current and κ STS modes are crucial for accurately determining the band gap of ML-MoS_2, or of similar semiconductors with band edges located near the BZ boundary.

ACKNOWLEDGMENTS

This work was funded by the Deutsche Forschungsgemeinschaft (DFG, German Research Foundation), Project No. 277146847–CRC 1238 (subprojects A01 and B06). W.J. acknowledges financial support from the Bonn-Cologne Graduate School of Physics and Astronomy (BCGS).

[1] R. Ganatra and Q. Zhang, ACS Nano **8**, 4074 (2014).
[2] S. Manzeli, D. Ovchinnikov, D. Pasquier, O. V. Yazyev, and A. Kis, Nat. Rev. Mater. **2**, 17033 (2017).
[3] J. Hall, B. Pielić, C. Murray, W. Jolie, T. Wekking, C. Busse, M. Kralj, and T. Michely, 2D Mater. **5**, 025005 (2018).
[4] S. Najmaei, Z. Liu, W. Zhou, X. Zou, G. Shi, S. Lei, B. I. Yakobson, J. C. Idrobo, P. M. Ajayan, and J. Lou, Nat. Mater. **12**, 754 (2013).
[5] H. Li, Y. Li, A. Aljarb, Y. Shi, and L.-J. Li, Chem. Rev. **118**, 6134 (2018).
[6] K. S. Novoselov, D. Jiang, F. Schedin, T. J. Booth, V. V. Khotkevich, S. V. Morozov, and A. K. Geim, Proc. Natl. Acad. Sci. USA **102**, 10451 (2005).
[7] B. Radisavljevic, A. Radenovic, J. Brivio, V. Giacometti, and A. Kis, Nat. Nanotechnol. **6**, 147 (2011).
[8] J. A. Miwa, S. Ulstrup, S. G. Sørensen, M. Dendzik, A. G. Čabo, M. Bianchi, J. V. Lauritsen, and P. Hofmann, Phys. Rev. Lett. **114**, 046802 (2015).
[9] N. Ehlen, J. Hall, B. V. Senkovskiy, M. Hell, J. Li, A. Herman, D. Smirnov, A. Fedorov, V. Yu Voroshnin, G. Di Santo, L. Petaccia, T. Michely, and A. Grüneis, 2D Mater. **6**, 011006 (2018).
[10] Y. Liang and L. Yang, Phys. Rev. Lett. **114**, 063001 (2015).
[11] D. Erben, A. Steinhoff, C. Gies, G. Schönhoff, T. O. Wehling, and F. Jahnke, Phys. Rev. B **98**, 035434 (2018).
[12] A. Grubišić Čabo, J. A. Miwa, S. S. Grønborg, J. M. Riley, J. C. Johannsen, C. Cacho, O. Alexander, R. T. Chapman, E. Springate, M. Grioni, J. V. Lauritsen, P. D. King, P. Hofmann, and S. Ulstrup, Nano Lett. **15**, 5883 (2015).
[13] T. Cheiwchanchamnangij and W. R. L. Lambrecht, Phys. Rev. B **85**, 205302 (2012).
[14] D. Y. Qiu, F. H. da Jornada, and S. G. Louie, Phys. Rev. Lett. **111**, 216805 (2013).
[15] A. Ramasubramaniam, Phys. Rev. B **86**, 115409 (2012).
[16] H. Shi, H. Pan, Y.-W. Zhang, and B. I. Yakobson, Phys. Rev. B **87**, 155304 (2013).
[17] A. Bruix, J. A. Miwa, N. Hauptmann, D. Wegner, S. Ulstrup, S. S. Grønborg, C. E. Sanders, M. Dendzik, A. Grubišić Čabo, M. Bianchi, J. V. Lauritsen, A. A. Khajetoorians, B. Hammer, and P. Hofmann, Phys. Rev. B **93**, 165422 (2016).
[18] X. Liu, I. Balla, H. Bergeron, G. P. Campbell, M. J. Bedzyk, and M. C. Hersam, ACS Nano **10**, 1067 (2016).
[19] A. F. Rigosi, H. M. Hill, K. T. Rim, G. W. Flynn, and T. F. Heinz, Phys. Rev. B **94**, 075440 (2016).
[20] J. Shi, X. Zhou, G.-F. Han, M. Liu, D. Ma, J. Sun, C. Li, Q. Ji, Y. Zhang, X. Song, X.-Y. Lang, Q. Jiang, Z. Liu, and Y. Zhang, Adv. Mater. Int. **3**, 1600332 (2016).
[21] C.-I. Lu, C. J. Butler, J.-K. Huang, C.-R. Hsing, H.-H. Yang, Y.-H. Chu, C.-H. Luo, Y.-C. Sun, S.-H. Hsu, K.-H. O. Yang, C.-M. Wei, L.-J. Li, and M.-T. Lin, Appl. Phys. Lett. **106**, 181904 (2015).
[22] C. Zhang, A. Johnson, C.-L. Hsu, L.-J. Li, and C.-K. Shih, Nano Lett. **14**, 2443 (2014).
[23] Y. L. Huang, Y. Chen, W. Zhang, S. Y. Quek, C.-H. Chen, L.-J. Li, W.-T. Hsu, W.-H. Chang, Y. J. Zheng, W. Chen, and A. T. S. Wee, Nat. Commun. **6**, 6298 (2015).
[24] M. Hong, P. Yang, X. Zhou, S. Zhao, C. Xie, J. Shi, Z. Zhang, Q. Fu, and Y. Zhang, Adv. Mater. Int. **5**, 1800641 (2018).
[25] N. Krane, C. Lotze, J. M. Läger, G. Reecht, and K. J. Franke, Nano Lett. **16**, 5163 (2016).
[26] C. Zhang, Y. Chen, A. Johnson, M.-Y. Li, L.-J. Li, P. C. Mende, R. M. Feenstra, and C.-K. Shih, Nano Lett. **15**, 6494 (2015).
[27] C. Zhang, C.-P. Chuu, X. Ren, M.-Y. Li, L.-J. Li, C. Jin, M.-Y. Chou, and C.-K. Shih, Sci. Adv. **3**, e1601459 (2017).
[28] N. Krane, C. Lotze, and K. J. Franke, Surf. Sci. **678**, 136 (2018).
[29] J. Coraux, A. T. N'Diaye, M. Engler, C. Busse, D. Wall, N. Buckanie, F. J. Meyer zu Heringdorf, R. van Gastel, B. Poelsema, and T. Michely, New J. Phys. **11**, 039801 (2009).
[30] M. Morgenstern, Surf. Rev. Lett. **10**, 933 (2003).
[31] J. A. Stroscio, R. M. Feenstra, and A. P. Fein, Phys. Rev. Lett. **57**, 2579 (1986).
[32] R. M. Feenstra, J. A. Stroscio, and A. P. Fein, Surf. Sci. **181**, 295 (1987).
[33] J. Tersoff and D. R. Hamann, Phys. Rev. Lett. **50**, 1998 (1983).
[34] J. Tersoff and D. R. Hamann, Phys. Rev. B **31**, 805 (1985).
[35] W. Jolie, C. Murray, P. S. Weiß, J. Hall, F. Portner, N. Atodiresei, A. V. Krasheninnikov, C. Busse, H.-P. Komsa, A. Rosch, and T. Michely, Phys. Rev. X (to be published) (2019).
[36] A. Ramasubramaniam, D. Naveh, and E. Towe, Phys. Rev. B **84**, 205325 (2011).
[37] Z. Y. Zhu, Y. C. Cheng, and U. Schwingenschlögl, Phys. Rev. B **84**, 153402 (2011).
[38] L. Du, T. Zhang, M. Liao, G. Liu, S. Wang, R. He, Z. Ye, H. Yu, R. Yang, D. Shi, Y. Yao, and G. Zhang, Phys. Rev. B **97**, 165410 (2018).
[39] G.-B. Liu, D. Xiao, Y. Yao, X. Xu, and W. Yao, Chem. Soc. Rev. **44**, 2643 (2015).
[40] L. Debbichi, O. Eriksson, and S. Lebègue, Phys. Rev. B **89**, 205311 (2014).
[41] H.-P. Komsa and A. V. Krasheninnikov, Phys. Rev. B **88**, 085318 (2013).
[42] E. Cappelluti, R. Roldán, J. A. Silva-Guillén, P. Ordejón, and F. Guinea, Phys. Rev. B **88**, 075409 (2013).
[43] J. E. Padilha, H. Peelaers, A. Janotti, and C. G. Van de Walle, Phys. Rev. B **90**, 205420 (2014).
[44] N. Ehlen (private communication).
[45] T. Chu, H. Ilatikhameneh, G. Klimeck, R. Rahman, and Z. Chen, Nano Lett. **15**, 8000 (2015).
[46] K. F. Mak, C. Lee, J. Hone, J. Shan, and T. F. Heinz, Phys. Rev. Lett. **105**, 136805 (2010).
[47] D. J. Trainer, A. V. Putilov, C. Di Giorgio, T. Saari, B. Wang, M. Wolak, R. U. Chandrasena, C. Lane, T.-R. Chang, H.-T. Jeng, H. Lin, F. Kronast, A. X. Gray, X. X. Xi, J. Nieminen, A. Bansil, and M. Iavarone, Sci. Rep. **7**, 40559 (2017).
[48] A. J. Bradley, M. M. Ugeda, F. H. Da Jornada, D. Y. Qiu, W. Ruan, Y. Zhang, S. Wickenburg, A. Riss, J. Lu, S. K. Mo, Z. Hussain, Z. X. Shen, S. G. Louie, and M. F. Crommie, Nano Lett. **15**, 2594 (2015).

CHAPTER 6

Manuscript [2]: Tomonaga-Luttinger Liquid in a Box: Electrons Confined within MoS_2 Mirror-Twin Boundaries

This chapter wholly consists of the above-named publication, published in Physical Review X *on 28th March 2019, available online.*

The experiments were proposed by W. Jolie, C. Murray, C. Busse, H.-P. Komsa, A. Rosch and T. Michely. All sample growth was performed at $_{\mathrm{T}}$STM, *by W. Jolie and C. Murray with advice given by J. Hall; the singular exception is the room temperature sample (Fig. 7) grown and imaged at* TuMAII *by J. Hall. The STM and STS measurements were carried out by C. Murray and W. Jolie. W. Jolie performed most of the initial measurements before eventually C. Murray took over responsibility of measurement. The STM and STS data were analysed by W. Jolie and C. Murray. W. Jolie took on the main burden of analysis, especially in the final stages. Amongst other things, C. Murray analysed the energy gaps* E_{gap} *and the MTB lengths* L, *determining the* E_{gap}-1/L *relationship of the 1D states. On a practical level, C. Murray developed a method for processing the vast amounts of data recorded during STS linescans, considerably expediting the workflow for this and future investigations using linescans.*

Theoretical modelling of the TLL was performed by P. S. Weiß, with supervision from A. Rosch. F. Portner provided theoretical modelling during the early stages of the project. H.-P. Komsa performed DFT calculations of the electronic structure of both MTB types and simulated STS maps thereof; advice was given by A. Krasheninnikov and N. Atodiresei.

The interpretation of the results was discussed at length by W. Jolie, C. Murray, P. S. Weiß, C. Busse, H.-P. Komsa, A. Rosch and T. Michely. W. Jolie wrote the manuscript and finalised it in close collaboration with C. Murray, P. S. Weiß, H.-P. Komsa, A. Rosch and T. Michely.

Some of the results shown in this Chapter can be found in the doctoral thesis of W. Jolie [225]. At that time the findings were mistakenly ascribed to 1D CDW order. After further measurement and analysis this interpretation was revised to that given here.

PHYSICAL REVIEW X **9**, 011055 (2019)

Tomonaga-Luttinger Liquid in a Box: Electrons Confined within MoS_2 Mirror-Twin Boundaries

Wouter Jolie,[1,2,*] Clifford Murray,[1] Philipp S. Weiß,[3] Joshua Hall,[1] Fabian Portner,[3] Nicolae Atodiresei,[4]
Arkady V. Krasheninnikov,[5,6] Carsten Busse,[1,2,7] Hannu-Pekka Komsa,[6] Achim Rosch,[3] and Thomas Michely[1]
[1]*II. Physikalisches Institut, Universität zu Köln, Zülpicher Straße 77, 50937 Köln, Germany*
[2]*Institut für Materialphysik, Westfälische Wilhelms-Universität Münster,*
Wilhelm-Klemm-Straße 10, 48149 Münster, Germany
[3]*Institut für Theoretische Physik, Universität zu Köln, Zülpicher Straße 77, 50937 Köln, Germany*
[4]*Peter Grünberg Institute and Institute for Advanced Simulation,*
Forschungszentrum, 52428 Jülich, Germany
[5]*Institute of Ion Beam Physics and Materials Research, Helmholtz-Zentrum Dresden-Rossendorf,*
01328 Dresden, Germany
[6]*Department of Applied Physics, Aalto University School of Science,*
PO Box 11100, FI-00076 Aalto, Finland
[7]*Department Physik, Universität Siegen, 57068 Siegen, Germany*

(Received 1 November 2018; published 28 March 2019)

Two- or three-dimensional metals are usually well described by weakly interacting, fermionic quasiparticles. This concept breaks down in one dimension due to strong Coulomb interactions. There, low-energy electronic excitations are expected to be bosonic collective modes, which fractionalize into independent spin- and charge-density waves. Experimental research on one-dimensional metals is still hampered by their difficult realization, their limited accessibility to measurements, and by competing or obscuring effects such as Peierls distortions or zero bias anomalies. Here we overcome these difficulties by constructing a well-isolated, one-dimensional metal of finite length present in MoS_2 mirror-twin boundaries. Using scanning tunneling spectroscopy we measure the single-particle density of the interacting electron system as a function of energy and position in the 1D box. Comparison to theoretical modeling provides unambiguous evidence that we are observing spin-charge separation in real space.

DOI: 10.1103/PhysRevX.9.011055 Subject Areas: Condensed Matter Physics, Nanophysics

I. INTRODUCTION

While long thought to remain a theorist's dream [1,2], a few realizations of one-dimensional metals suitable for the investigation of low-energy excitations as described by the Tomonaga-Luttinger liquid (TLL) theory [1–3] are now available. Among them are metallic carbon nanotubes [4,5], GaAs/AlGaAs-based wire devices [6–8], quasi-1D bulk materials [9,10], and self-assembled atomic wires on semiconductor surfaces [11–18].

According to TLL theory [1–3], fingerprints of TLL behavior in 1D metals are power laws for the suppression of the density of states near the Fermi energy E_F [4,5,9–12,14] and—most significantly—the different dispersions of spin and charge excitations with velocities v_s and v_c [6–8,19]. Their experimental detection is primarily conducted by transport and tunneling transport measurements [4,6–8], angle-resolved photoemission electron spectroscopy (ARPES) [5,9,11,12,14,19], and scanning tunneling spectroscopy (STS) [10,12,19].

The difficulties in pinpointing TLL behavior, specifically in self-assembled systems, become apparent by considering the case of self-organized Au wires on Ge(001): From the 1D appearance of the Au adatom chains and power-law scaling of the density of states observed by STM and ARPES, TLL behavior was concluded [12]. In subsequent work [13,17,18] TLL behavior was questioned and even excluded; e.g., the 1D character of the system was rejected [13,17] and the suppression of the density of states was linked to disorder [17].

These remarks make plain that, in order to gain high-quality data enabling advancement of theory, well-defined 1D systems and new tools to identify TLL behavior are highly desirable. One such new tool is the use of quantum simulators to emulate and explore TLL behavior [20]. As shown below, our approach is the design of an extremely

---

[*] wjolie@ph2.uni-koeln.de

well-defined 1D system of finite length giving rise to a discrete excitation spectrum, accessible by STS.

In recent years an exciting realization of a 1D metal was discovered, namely, mirror-twin boundaries (MTBs) in semiconducting transition-metal dichalcogenide monolayers. Their structures were unambiguously determined by transmission electron microscopy [21–23], and density-functional theory (DFT) invariably predicted the MTBs to host one-dimensional, metallic states [24–27] that are protected through the large band gap of approximately 2 eV in the surrounding 2D layer. Intense research yielded partially conflicting results regarding the electronic structure of a specific MTB in a monolayer of $\mathrm{MoSe_2}$ resting on a van der Waals substrate [19,28,29], namely, the $4|4P$ MTB consisting of fourfold rings sharing a point at the chalcogene site [24,30]. By using room-temperature as well as low-temperature (4 K) STM and STS, Liu *et al.* [28] found a quantum well state emerging from the finite length of the interpenetrating MTBs. Barja *et al.* [29] proposed a Peierls type charge-density wave (CDW) at 4.5 K, but disregarded quantization effects in their MTBs of finite length. By avoiding the CDW regime through room-temperature ARPES measurements, Ma *et al.* [19] found indications of TLL behavior by observing a suppression of the density of states near E_F and by successfully fitting their spectrum to a Hubbard model with long-ranged interactions.

We go beyond this work and focus on a structurally different MTB in a monolayer of $\mathrm{MoS_2}$. For this MTB no CDW transition occurs, thus allowing us to observe TLL physics down to lowest temperatures. By making 1D wires well isolated from the environment, of high perfection and well-defined length, we are able to observe spin-charge separation in real space through the unique local spectroscopic capabilities of low-temperature STM and STS. This technique can directly probe the probability distribution and energy of discrete TLL excitations in a 1D box. The interpretation of our data is based on the work of Fabrizio and Gogolin [31] as well as Anfuso and Eggert [32], who demonstrated that for a TLL in a box the local distribution of the single-particle spectral weight—determining the probability to inject or extract an electron in a tunneling experiment—visualizes its fundamental properties.

II. RESULTS

A. Design of a 1D box in $\mathrm{MoS_2}$ and quantization effects

To construct our 1D box we grow $\mathrm{MoS_2}$ islands epitaxially on the van der Waals substrate graphene on Ir(111) [33]; see Appendix A. The lower C_3 symmetry of $\mathrm{MoS_2}$ compared to the C_6 symmetry of the substrate leads to two equivalent mirror orientations of $\mathrm{MoS_2}$ islands despite epitaxial alignment. These islands coalescence and reshape during synthesis, resulting in straight MTBs. A white arrow highlights such a MTB in the STM topograph shown in Fig. 1(a). It appears higher than its surroundings when the bias voltage is set close to or within the band gap of $\mathrm{MoS_2}$ [33], consistent with an electronic structure markedly different from the $\mathrm{MoS_2}$ layer. All MTBs have well-defined lengths, as they terminate at the island edges. Atomic resolution topographs of MTBs are provided in Appendix A.

Two types of MTBs are found in our experiments. As shown in Fig. 1(b), one type displays two parallel lines (double line) of dots in an empty state STS map, as has been observed in previous work on MTBs in $\mathrm{MoSe_2}$. This MTB has been identified as a $4|4P$ MTB [19,28,29]. Depending on the preparation conditions, the $4|4P$ MTBs make up 5%–30% of all MTBs. Their frequency of occurrence reduces with increasing growth temperature, and they are often pinned to defects. This indicates that they are energetically less favorable than the second type of MTB, which is predominant in our $\mathrm{MoS_2}$ samples. This second type of MTB displays in a STS map a single line of dots as visualized in Fig. 1(c). The dot periodicity along the line scatters from MTB to MTB, but is close to $3a$ for the double line and close to $2a$ for the single line MTB, where $a = 3.15$ Å is the lattice parameter of $\mathrm{MoS_2}$. In the present paper, we focus on the single line MTB, while the double line MTB is discussed in Appendixes A and B, where it is shown to be in fact of $4|4P$ structure.

The local density of states (LDOS) $A(E,x)$ present along MTBs is directly accessible with STS, since $dI/dV \propto A(E,x)$. Figure 1(d) shows dI/dV as a function of the bias voltage V (converted to an energy $E = eV$), measured at the position marked by a red dot in Fig. 1(c). The spectrum reveals a finite density of states throughout the measured energy range, except for a narrow gap E_{gap} of the order of 100 meV located at E_F ($E = 0$). All states visible in the spectrum lie within the 2.5 eV band gap of the surrouding $\mathrm{MoS_2}$ [33], and hence, are strongly confined within the MTB.

Figure 1(e) displays a STM topograph of a single line MTB of 20-nm length with terminations formed by the $\mathrm{MoS_2}$ island edges, whereas Figs. 1(f) and 1(g) are corresponding constant-height STS maps of the dashed box in Fig. 1(e). Both maps are measured at the peak energies of the lowest unoccupied and highest occupied state, respectively. As follows from the careful comparison of the two patterns, the number of maxima increases by one when moving from the lowest unoccupied state to the highest occupied state. The uniform spacing of the maxima and their in-phase relation at the box edges imply an antiphase relation in the middle of the MTB, as seen best in the corresponding line scans shown in Fig. 1(h).

This pattern is exactly what is expected for noninteracting particles (holes) in a box of size L: the wave number

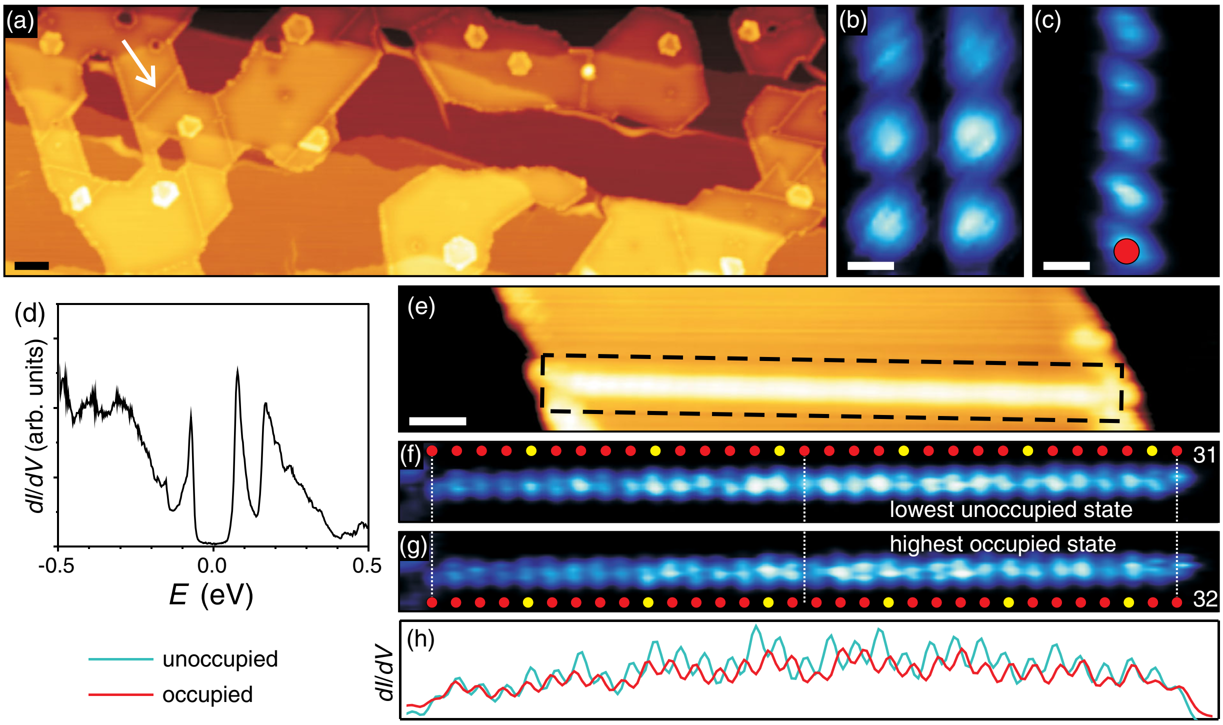

FIG. 1. 1D states in MoS_2 mirror-twin boundaries. (a) Constant-current STM topograph ($U = 0.9$ V, $I = 0.03$ nA, scale bar 10 nm) of a partial MoS_2 monolayer grown by reactive molecular beam epitaxy on graphene. The latter is fully covering and conformal to the Ir(111) substrate. The MoS_2 layer islands extend over several substrate steps and carry small hexagonally shaped second layer MoS_2 islands. In consequence of island coalescence and reshaping during the annealing step of the synthesis, straight MTBs are formed along the three dense-packed directions of MoS_2. They are visible as bright lines, of which one is highlighted by a white arrow. (b) Constant-height STS map of a double line $4|4P$ MTB ($U = 0.1$ V, scale bar 0.5 nm). (c) Constant-height STS map of a single line MTB ($U = 0.1$ V, scale bar 0.5 nm). (d) dI/dV spectrum measured at the red dot position in (c) ($U_{\text{stab}} = 0.5$ V, $I_{\text{stab}} = 0.1$ nA). (e) STM topograph of a single line MTB ($U = 0.5$ V, $I = 0.1$ nA, scale bar 2 nm). (f) Constant-height STS map of the dashed box area in (e) at the energy of the lowest unoccupied state ($U = 0.033$ V). (g) Constant-height STS map of the dashed box area in (e) at the energy of the highest occupied state ($U = -0.048$ V). The dots marking the maxima in the LDOS patterns make plain that there is one maximum less in the lowest unoccupied state of the MTB. From the thin vertical lines in (f) and (g) it becomes apparent that the LDOS maxima are in phase at the edges of the 1D box, but in antiphase in the center. (h) Line profiles along the MTB, showing the entire phase relation between lowest occupied and highest unoccupied state.

k of the highest occupied and lowest unoccupied state differs by π/L, leading to an extra maximum in the resulting probability distribution $A(E,x) \sim \sin^2(kx)$. In the following, we first show that DFT calculations reproduce both the shape and phase relation of the bound-state wave functions near E_F. Then we discuss the role of interaction effects which are mandatory to accurately reproduce our findings.

B. Density-functional theory calculations

We propose the single line MTB to possess the $4|4E$ structure, i.e., to consist of fourfold rings which share an edge, as schematically depicted in the ball-and-stick model of Fig. 2(a). The DFT calculated band structure for the ribbon geometry of Fig. 2(a) is displayed in Fig. 2(b). Apparent is a holelike band localized at the $4|4E$ MTB, with its maximum at $k = 0$ and crossing E_F at $k = k_F \approx (\pi/2a)$. The wave functions related to this band at $k = (\pi/2a)$ are illustrated by the partial charge-density isosurface plots in Fig. 2(a), and show clear localization to Mo and S atoms around the MTB. Furthermore, the angular momentum projections evidence that they have purely Mo-d and S-p character, as illustrated in the projected DOS in Fig. 2(c). From the partial charge-density plots in Fig. 2(a), it is also obvious that the tunneling current stems primarily form the S-p orbitals localized at the S atoms, as these orbitals extend farthest into the vacuum. We note that DFT calculations including spin-orbit coupling show the metallic MTB band unchanged and spin degenerate. For an inversion domain supercell bounded by three $4|4E$ MTB segments, as shown in Fig. 2(d), the simulated LDOS maps for the lowest unoccupied [Fig. 2(e)] and highest occupied [Fig. 2(f)] states match in appearance and periodicity precisely with the dI/dV maps in Figs. 1(c), 1(f), and 1(g). It is noteworthy that also the number of LDOS maxima

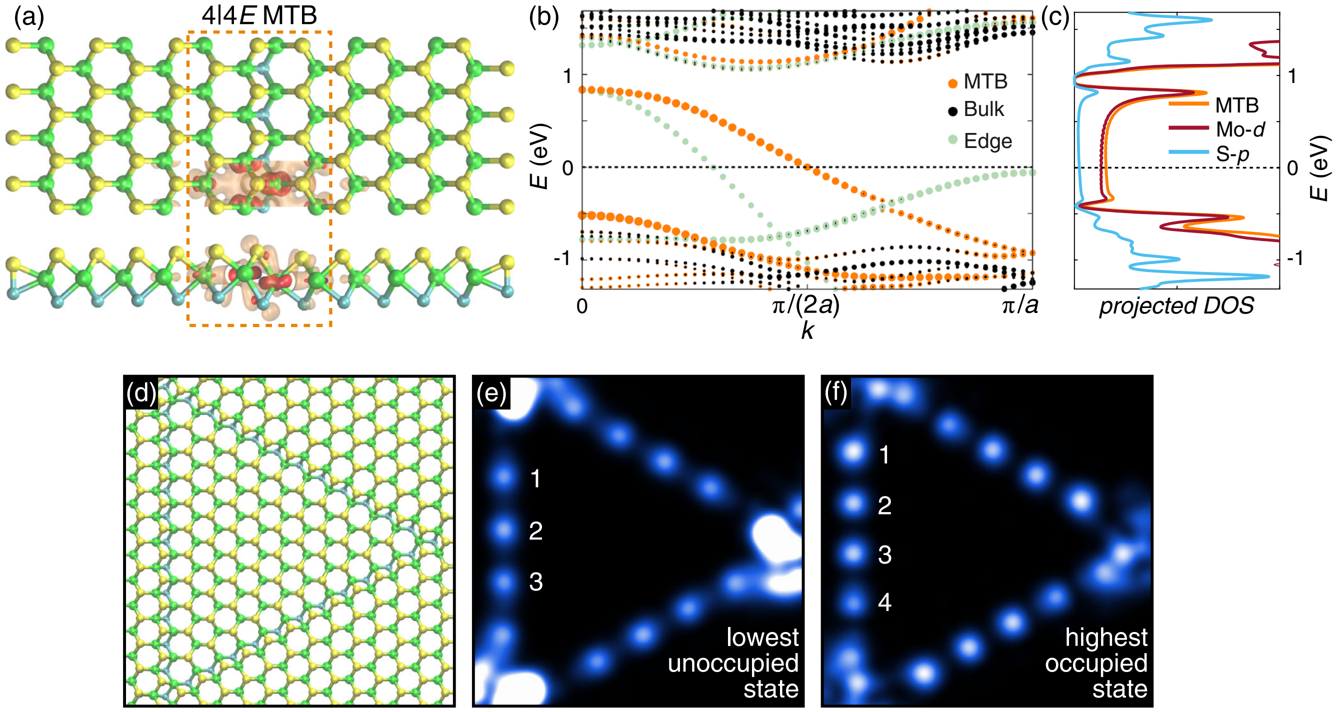

FIG. 2. DFT calculations for 4|4*E* mirror-twin boundaries in $\mathrm{MoS_2}$. (a) Top and side view of a ball-and-stick model. Mo atoms, green; S atoms, yellow (top layer) and cyan (bottom layer). (b) Band structure calculated for the ribbon geometry of (a) with periodic boundary conditions in the direction along the MTB. Horizontal dashed line denotes the position of E_F at $E = 0$. The holelike band present at the 4|4*E* MTB is colored orange and crosses E_F at $k \approx (\pi/2a)$. The partial charge density of the MTB band wave functions at $k = \pi/(2a)$ is shown in (a) with two different isosurface values in red and light red. Bulk bands are colored black and bands located at the ribbon edges specific to the finite-sized supercell are colored green. (c) Projected density of states (orange) of the atoms around the MTB within the red dashed box in (a) corresponding to the metallic MTB band in (b), and its Mo-*d* (dark red) and S-*p* (light blue) contributions. (d) Geometry of triangular inversion domain enclosed by three 4|4*E* MTB segments. (e),(f) LDOS maps (simulated STS maps) for the supercell shown in (d) at a height of 2.8 Å. Discrete states with wave vector just below [above] k_F corresponding to lowest unoccupied [highest occupied] state are shown in (e) [(*f*)]. E_F was adjusted to match $k_F = (\pi/2a)$. From comparison of (e) and (f) it is apparent that the number of maxima on a 4|4*E* MTB segment increases by one when moving from the lowest unoccupied state to the highest occupied state. Note that the features in the corners of the LDOS maps in (e) and (f) are due to the interactions of the triangle corners in the DFT supercell.

increases by one upon moving from the lowest unoccupied to the highest occupied state. Our assignment of the single line being a 4|4*E* MTB is backed up by the fact that DFT calculations also reproduce STS maps of the 4|4*P* double line MTB as documented in Appendix B.

C. Failure of the free particle in a 1D box picture

While our DFT calculations seem to suggest a free particle (hole) in a 1D box picture, as schematically sketched on the left-hand side of Fig. 3(a), this model fails in reproducing the quantized electronic structure in our spectra. A sequence of STS spectra along the 4|4*E* MTB (measurement path is indicated by a dotted line) shown in Fig. 3(b) reveals in the color plot of Fig. 3(c) the presence of additional, well-separated quantized states above the lowest unoccupied state and below the highest occupied state.

In Fig. 3(d), we show the corresponding pattern expected for noninteracting holes confined to a 1D box of the same length using the band structure from DFT. Several discrepancies are present compared to Fig. 3(c): In the experiment (i) the energy gap E_{gap} between the highest occupied and the lowest unoccupied state is much larger compared to the neighboring energy level spacings; (ii) there is a higher number of energy levels and the level spacing is not approximately equidistant; (iii) most striking, some states adjacent in energy display the same number of maxima, and hence, are in phase throughout the entire MTB [compare states highlighted by arrows in Fig. 3(c)]. In the following, we argue that these observations can be explained by the TLL theory.

D. Tomonaga-Luttinger liquid in a 1D box

TLL theory is an effective field theory describing the low-energy excitations of an interacting 1D metal. The low-energy excitations are not Fermi liquid quasiparticles but instead spin- and charge-density waves which travel with two different velocities, v_s and v_c, giving rise to two

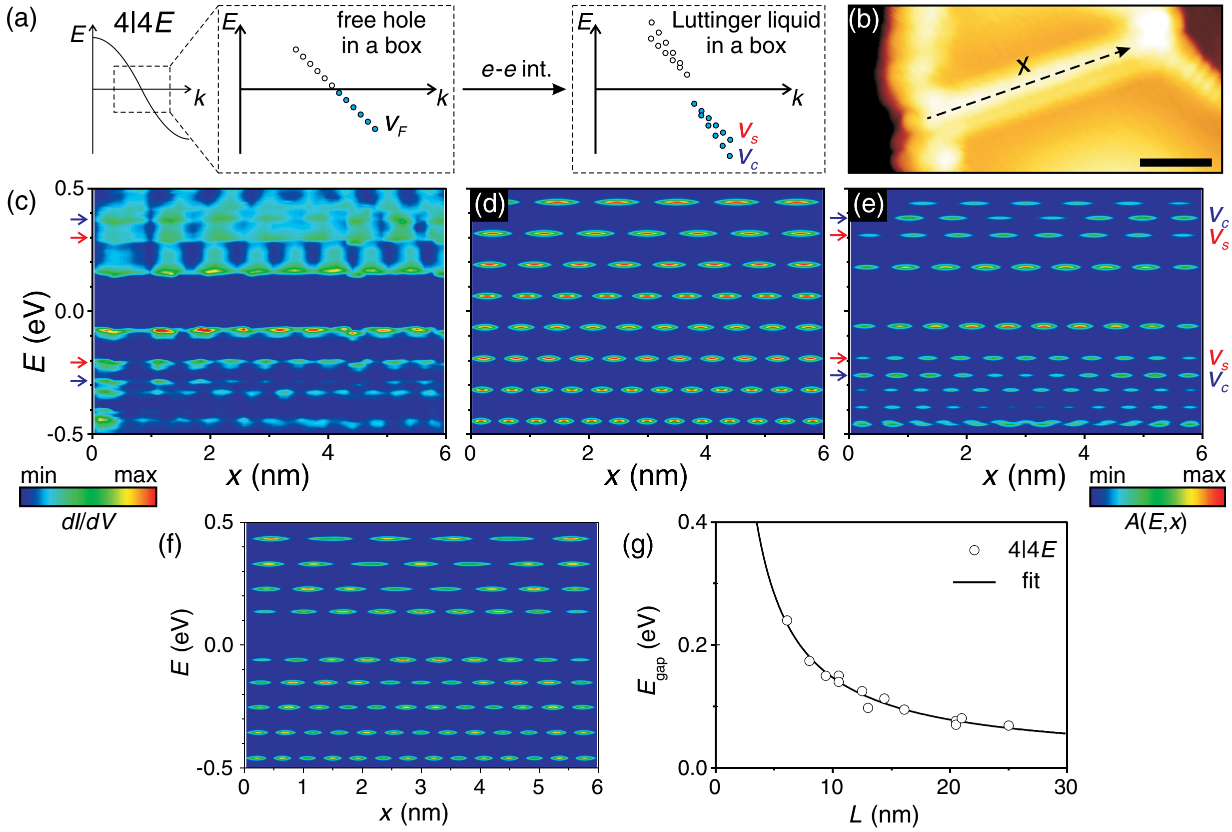

FIG. 3. Confined quasiparticles in MoS_2 MTBs. (a) Sketch of the TLL model. The holelike band of the $4|4E$ MTB is first linearized, then quantized. Filled states are occupied. Including electron-electron interactions increases the gap at the chemical potential and lifts the degeneracy of the charge and spin quasiparticles. (b) STM topograph of a $4|4E$ MTB ($U = 1$ V, $I = 0.2$ nA, scale bar 2 nm). Dotted line shows the path of the tip during STS data acquisition. (c) Corresponding dI/dV signal as a function of energy and position ($U_{\mathrm{stab}} = 0.8$ V, $I_{\mathrm{stab}} = 1$ nA). Arrows denote states which have the same number of maxima and are in phase throughout the MTB. Color scale ranges from dark blue for zero dI/dV signal to red for maximum dI/dV. Same color scale is used in (d)–(f) for the simulated LDOS. (d) Simulated LDOS assuming noninteracting holes confined to a 1D box using the band structure from DFT. (e) Simulated LDOS using the TLL model ($v_c = 0.38$ nm eV, $v_s = 0.25$ nm eV, $K_c = 0.5$). First spin and charge excitations with velocities v_s and v_c are highlighted by arrows. They display identical number of maxima and in-phase behavior over the entire MTB length, as observed experimentally. (f) Simulated LDOS assuming a CDW with an interaction strength matched to fit the experimentally observed gap. (g) Dependence of E_{gap} as a function of $4|4E$ MTB length L, supporting our TLL interpretation.

different dispersions, as schematically sketched in Fig. 3(a). When an electron is injected into the system, it fractionalizes: it creates a multitude of spin and charge excitations. In a finite-size system these excitations are standing waves with discrete energies which provide characteristic fingerprints in a STM experiment.

At low energies, the Hamiltonian of the Luttinger liquid in the finite system of length L can be written as

$$H = \frac{(N - N_0)^2}{2cL} + \frac{\pi v_s S_z^2}{K_s L} + \sum_{m>0} (v_s q_m b_{s,m}^\dagger b_{s,m} + v_c q_m b_{c,m}^\dagger b_{c,m}), \qquad (1)$$

where $b_{s,m}^\dagger$ and $b_{c,m}^\dagger$ are the creation operators of a spin and charge excitation with quantum number $m \in \mathbb{N}$ and c the capacitance per length of the wire. Because of the finite size of the system, the excitations have discrete energies $v_s q_m$ and $v_c q_m$, where $q_m = (\pi/L)m$ is the discrete momentum which is defined to be positive. The relation of the bosonic field to the fermionic operators depends on two Luttinger parameters, K_s and K_c, which encode the effects of interactions. Note that in the finite-size system, positive and negative momenta (and left and right movers) are always coupled by the boundary conditions.

An important ingredient of the Luttinger liquid theory is the first two terms in Eq. (1), which describe the so-called zero modes. The first term is simply the charging energy, N is the total charge in the box, and N_0 is a background charge parametrizing the chemical potential. This Coulomb-blockade barrier determines E_{gap}. It contains contributions from the finite-size level spacing, the local interaction, and the long-ranged Coulomb interaction. In standard TLL (a theory with purely local interactions), the capacitance per length c is fixed by the Luttinger liquid parameter K_c, $c = 2K_c/(\pi v_c)$. We consider the capacitance of the grain boundary as an independent fitting parameter arising from the long-ranged Coulomb interaction [34]. The second term is a similar contribution in the spin sector, where we assume that the ground state has zero spin. In our calculations we set $K_s = 1$ (assuming spin-rotation invariance).

In order to compare to experiment we calculate the LDOS of the Luttinger liquid:

$$A(E,x) = \sum_\sigma \int_{-\infty}^{\infty} \frac{dt}{2\pi} e^{iEt} \langle \{\Psi_\sigma(x,t), \Psi_\sigma^\dagger(x,0)\}\rangle, \qquad (2)$$

where Ψ_σ are the fermionic field operators. $\{\cdot,\cdot\}$ denotes the anticommutator, and $\langle\cdots\rangle$ is the expectation with respect to the N_0-fermion ground state, i.e., a state without bosonic excitations; see Appendix C for details.

The spectrum predicted by TLL is shown as a color plot in Fig. 3(e) for parameters matching the experimental findings in Fig. 3(c). Our Luttinger liquid in a box overcomes all discrepancies mentioned above, yielding (i) the proper $E_{\rm gap}$, (ii) the increased number of levels with nonequidistant spacings, and (iii) adjacent states with the same number of maxima and an in-phase relation of the maxima throughout the entire MTB length. These states, highlighted by arrows in Fig. 3(e), result from the different velocities v_s and v_c of the first spin and charge excitations, which are well separated in energy.

E. Absence of a Peierls-type charge-density wave

Our data cannot be explained by a Peierls-type CDW suggested for the $4|4P$ MTB in $\mathrm{MoSe_2}$ [19,29]. A calculated spectrum for the MTB with a CDW matched to reproduce $E_{\rm gap}$ is represented in Fig. 3(f) (see Appendix D). It is obvious that the discrepancies (ii) and (iii) remain. Moreover, we find that $E_{\rm gap}$ decreases with $1/L$ consistent with TLL theory, where $E_{\rm gap} = [(1/c) + (\pi v_s/2)](1/L)$, but not with a CDW scenario, where $E_{\rm gap} = \text{const}$. A fit to $E_{\rm gap}(L) = A/L + B$ [Fig. 3(g)] leads to a tiny extrapolated gap $E_{\rm gap}(\infty) = (10 \pm 6)$ meV. Assumption of a Peierls-type CDW gap would be inconsistent with our room-temperature observation of the beating pattern; see Appendix D. The value of $A = (1.37 \pm 0.07)$ eV nm is consistent with the estimate $A = (\pi v_s/2) + (\pi v_c/2K_c) = (1.6 \pm 0.3)$ eV nm; see Sec. II D.

F. Spin-charge separation in reciprocal space

Additional insight and support for the TLL picture is provided by the analysis of the dI/dV spectra taken along longer $4|4E$ MTBs. Figures 4(a) and 4(b) present a color plot of the MTB of Fig. 1(d) together with its Fourier transform (FT). The latter is considerably more instructive, since it directly reveals the dispersion of the confined states [35]. Corresponding simulations using TLL theory are shown in Figs. 4(c) and 4(d).

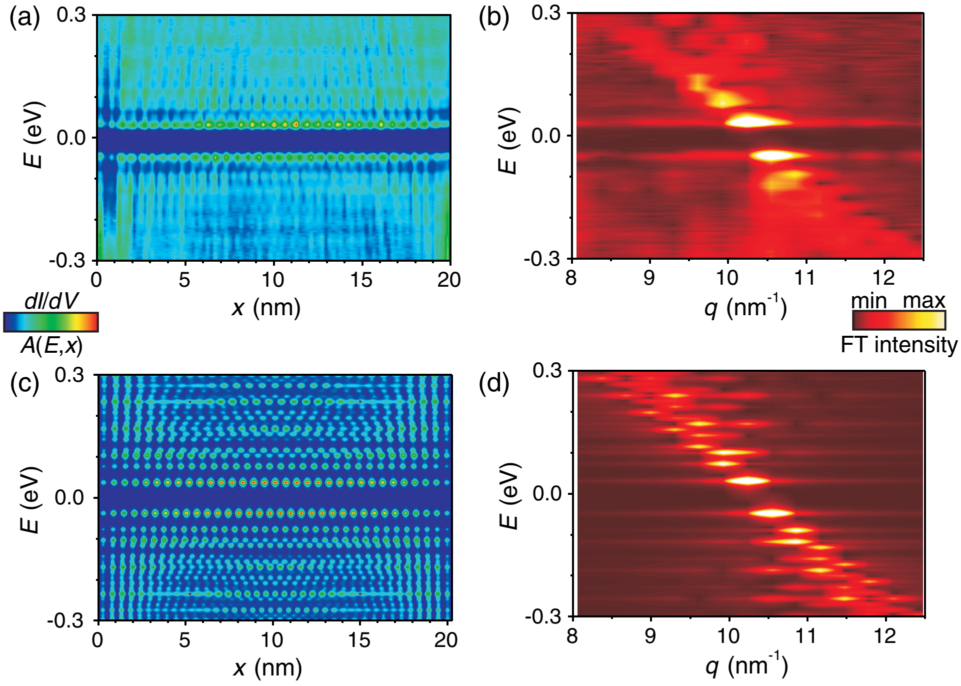

FIG. 4. Dispersion of confined quasiparticles in $\mathrm{MoS_2}$ MTBs. (a) Color plot of the dI/dV signal along the MTB displayed in Fig. 1(e) as a function of energy and position ($U_{\rm stab} = 0.5$ V, $I_{\rm stab} = 0.1$ nA). (b) FT of the experimental data, revealing the dispersion of the confined quasiparticles. (c) Simulated LDOS using our TLL model ($v_c = 0.45$ nm eV, $v_s = 0.27$ nm eV, $K_c = 0.5$). Same color scale as used in (a). (d) FT of the simulated LDOS in (c) with the same color scale as in (b).

The strongest peaks in the simulated FT of Fig. 4(d) are located at the energies $\pm(E_{\mathrm{gap}}/2)$ of the highest occupied and lowest unoccupied states. Their corresponding momenta are $2k_F^{\mp}$, where k_F^- is the momentum of the highest occupied state and $k_F^+ = k_F^- + (\pi/L)$ is the momentum of the lowest unoccupied state. They describe excitations where only the fermion number (zero modes of the TLL) changes and no spin or charge modes are excited. A series of prominent peaks is located at momenta $2(k_F^{\pm} \pm q_m)$, $q_m = (\pi/L)m$, $m > 0$, with energies $\mp[(E_{\mathrm{gap}}/2) + v_s q_m]$, $\mp[(E_{\mathrm{gap}}/2) + v_c q_m]$ describing a situation where the injected electron produces a pure spin or a pure charge excitation. Fitting these peaks can be used to determine the charge and spin velocities, v_c and v_s, assuming that $v_s < v_c$, as expected for repulsive interactions. This situation is depicted in Fig. 3(a).

It is also possible that spin and charge excitations are present simultaneously. When several modes with momenta $q_1, q_2, \ldots, q_n > 0$ are excited, this leads to peaks at the momenta $2(k_F^{\pm} \pm \sum_i \sigma_i q_i)$ with arbitrary signs $\sigma_i = \pm 1$. The associated energies are $\mp[(E_{\mathrm{gap}}/2) + \sum_i v_\nu q_{i_\nu}]$, with $\nu = c, s$ for a charge or spin excitation, respectively. These extra peaks are, however, only activated when one of the Luttinger liquid parameters K_c and K_s deviates from 1, where 1 corresponds to the noninteracting case. In our simulations, $K_c = 0.5$ and $K_s = 1$. The smaller the Luttinger parameters are, the more weight is transferred from the primary peaks to the side peaks giving rise to a more symmetrical spectrum with an accumulation of weight below and above the two strongest peaks. Our data do not allow a determination of K_c with high precision; we estimate $K_c = 0.5 \pm 0.1$ (see Appendix E for spectra with different values of K_c).

Comparing the simulated FT plot of Fig. 4(d) to the corresponding experimental FT plot of Fig. 4(b) makes plain that in the experimental data, though more blurred, the spectral weight is not only aligned along a simple curve $v_F k$, in contrast to the noninteracting case. Clear indications for the presence of a second velocity are visible. Furthermore, extra weight is accumulated above and below the central peaks, in coincidence with the theoretical modeling.

III. DISCUSSION AND CONCLUSIONS

While we find a good qualitative agreement between experiment and theory, there are also discrepancies. Most prominently, the theory is by construction exactly particle-hole symmetric, while in the experiment both the position of the peaks and their width differ for positive and negative energies. In Fig. 3(c), the peaks at positive energies are strongly broadened. The coupling to electrons in the substrate is the prime candidate for this effect. One further effect has been neglected in our theoretical analysis: backscattering in the spin channel, which cannot be treated exactly within TLL theory. While backscattering is formally irrelevant and vanishes for $L \to \infty$, it is only logarithmically suppressed as function of L for spin-rotation symmetry. It is therefore expected to affect the finite-size spectrum, possibly explaining some of the discrepancies in peak positions.

The insight obtained here for the $4|4E$ MTBs in $\mathrm{MoS_2}$ also sheds some light on the controversial results for the $4|4P$ MTB in $\mathrm{MoSe_2}$. Quantum confinement effects, as detected by Liu *et al.* [28], are a necessary consequence of a finite MTB wire length. Thus, for a finite length MTB with a metallic band crossing E_F around $k = \pi/3a$ (as for the $4|4P$ MTB in $\mathrm{MoSe_2}$ [30]), the observations of a gap around E_F, of an approximate period tripling, and an antiphase relation between the highest occupied and lowest unoccupied state in the center of the wire are to be expected, and do not constitute evidence for the presence of a CDW as proposed by Barja *et al.* [29]. Based on the similarity of the $4|4P$ and $4|4E$ MTBs and our clear-cut evidence for the presence of a TLL in the $4|4E$ MTB in $\mathrm{MoS_2}$, it appears likely that indeed a TLL is also present in the $4|4P$ MTB in the monolayer of $\mathrm{MoSe_2}$, as proposed by Ma *et al.* [19].

When comparing previous results on the $4|4P$ MTB in $\mathrm{MoSe_2}$ to ours on the $4|4E$ MTB in $\mathrm{MoS_2}$, it turns out that the Luttinger parameter K_c in the range of 0.20–0.21 obtained by Ma *et al.* [19] is much lower than our estimate $K_c = 0.5 \pm 0.1$. One possible reason for this discrepancy is that Ma *et al.* deduce K_c from a power-law fit to the density of states near E_F by averaging over a dense network of 1D subsystems. This analysis does not take into account the finite wire length between crossing points (of the order of 10 nm). The finite wire length implies an extra suppression of the density of states both due to finite-size gaps [see our Fig. 3(g)] and due to an extra suppression of the density of states close to defects and walls predicted by Luttinger liquid theory [36]. This extra suppression of the density of states may lead to an estimate of K_c which is systematically too small.

In conclusion, STS spectral maps along MTBs and their FTs show clear evidence for spin-charge separation, characteristic for a quantum confined TLL. We envision that higher resolution data could be obtained by further decoupling the 1D metal from its environment and by lowering the temperature, enabling a quantitative comparison to TLL theory. Moreover, chemical gating and defect engineering of the MTBs might enable one to modify the correlation strength in the TLL or even create new exotic phases.

ACKNOWLEDGMENTS

W. J., C. M., P. S. W., J. H., N. A., A. R., and T. M. gratefully acknowledge funding by the Deutsche Forschungsgemeinschaft (DFG, German Research Foundation)-Project No. 277146847-CRC 1238 (subprojects A01, B06, C01, and C02). W. J. acknowledges support from the Bonn-Cologne Graduate School for Physics and Astronomy. This work is also supported by the University of Cologne via the Advanced Postdoc Grant "2D materials beyond graphene." Support from the Academy of Finland is acknowledged under Projects No. 286279 (A. V. K. and H.-P. K.) and No. 311058 (H.-P. K.). We also thank CSC-IT Center for Science Ltd. and generous grants of computer time and PRACE for awarding us access to Hazel Hen at High Performance Computing Center, University of Stuttgart, Germany. We acknowledge useful discussions with J. Sirker and S. Trebst.

APPENDIX A: EXPERIMENTAL METHODS AND HIGH-RESOLUTION IMAGES OF MoS_2

1. Sample preparation

The synthesis of MoS_2 on the substrate graphene on Ir(111) is conducted in a two-step process [33]. During the first step, Mo is evaporated from a rod with a rate of 0.125 monolayers/ min on the graphene surface at room temperature in a S pressure of $p \approx 5 \times 10^{-9}$ mbar.

During the second step, the sample is annealed for 5 min at $T = 1050$ K in a S pressure of $p \approx 5 \times 10^{-9}$ mbar. This leads to large, flat monolayer MoS_2 islands with small second layer islands on top.

2. Scanning tunneling microscopy

All STM and STS experiments were conducted at $T = 5$ K. For STS, we measure the dI/dV signal using the lock-in technique (modulation voltage $V_{\mathrm{mod}} = 4$ mV, frequency $f = 777$ Hz). For our color plots, we use a linear interpolation of the discrete data.

3. Identifying mirror-twin boundaries

Atomically resolved STM images of MTBs in monolayer MoS_2/graphene/Ir(111) are shown in Fig. 5. In Fig. 5(a), one finds two islands separated by a line defect. The dense-packed rows in both islands have the same orientation—visualized with white lines in Fig. 5(a). Hence, this line defect must be a MTB. Together with its electronic signatures, which are described in the main text, the MTB can be attributed to a $4|4E$ MTB.

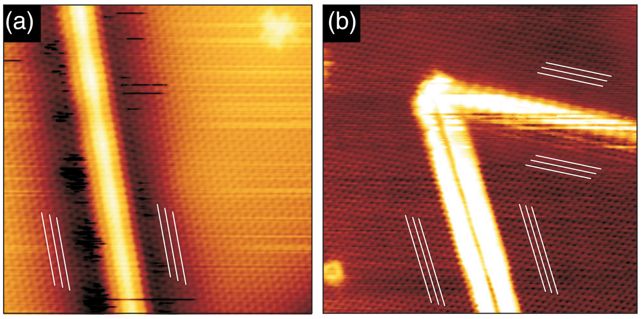

FIG. 5. MTBs in monolayer MoS_2. (a) Constant-current STM image of a $4|4E$ MTB in MoS_2/graphene/Ir(111) [$U = 0.9$ V, $I = 0.5$ nA, image size (12×12) nm^2]. The white lines show that both grains are perfectly aligned. (b) Constant-current STM image of a grain boundary forming both a $4|4E$ and a $4|4P$ MTB [$U = 0.4$ V, $I = 1$ nA, image size (15×15) nm^2].

Another atomically resolved STM image is shown in Fig. 5(b). It displays a boundary containing two different line defects which meet at an angle. One has a single line structure as in Fig. 5(a), while the other exhibits a double structure. It is this double line feature, together with a periodic beating of approximately $3a$ (not visible here), which clearly distinguishes this boundary. The orientation of the atomic rows on both sides of the double line is identical. Hence, both boundaries must be MTBs. The MTB with double lines is attributed to a $4|4P$ MTB.

APPENDIX B: DENSITY-FUNCTIONAL THEORY

1. Density-functional theory calculations

All density-functional theory calculations were carried out within the plane-wave basis and the projector augmented wave framework as implemented in VASP [37,38]. The exchange-correlation effects are treated with the functional proposed by Perdew, Burke, and Ernzerhof [39]. The atomic models in the ribbon calculations consist of tetragonal cells with sizes of about $6\sqrt{(3)} \times 1 \times 1$ and periodic only along the MTB with vacuum claddings in the other two directions. The $4|4E$ or $4|4P$ MTB are located symmetrically in the middle, while the ribbon edges are of the S_2-passivated Mo-zigzag type. The k-point sampling of $1 \times 12 \times 1$ and the plane-wave cutoff of 500 eV guarantee converged total energies. For MTBs of finite length, we adopted models where triangular MTB loops are embedded within a 16×16 supercell. In this case, Γ-point sampling and reduced plane-wave cutoff are adopted. The STS images are obtained within the Tersoff-Hamann approximation [40].

2. $4|4P$ mirror-twin boundaries

We propose that the double line MTB possesses the $4|4P$ structure, i.e., consists of fourfold rings which share a point, as schematically depicted in the ball-and-stick model of Fig. 6(a). The DFT calculated band structure for the ribbon geometry of Fig. 6(a) is displayed in Fig. 6(b). Apparent is an electronlike band localized at the $4|4P$ MTB, with its minimum at $k = 0$ and crossing E_F at $k = k_F \approx \pi/(3a)$. For an inversion domain supercell bounded by three $4|4P$ MTB segments as shown in Fig. 6(c), the simulated LDOS maps for the lowest unoccupied [Fig. 6(d)] and highest occupied [Fig. 6(e)] state match in appearance and periodicity precisely with the STS maps of the $4|4P$ MTBs. Also to be noted is that the number of LDOS maxima decreases by one upon moving from the lowest unoccupied to the highest occupied state. Our assignment of the double line being a $4|4P$ MTB is in agreement with literature [19,28,29].

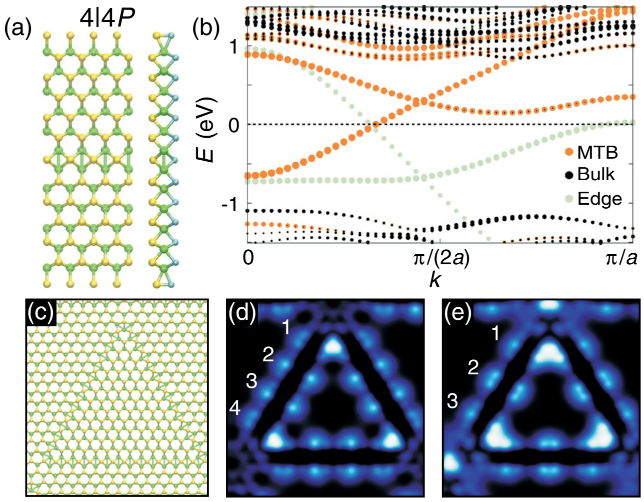

FIG. 6. DFT calculations for 4|4P mirror-twin boundaries in MoS$_2$. (a) Top and side view of a ball-and-stick model. Mo atoms, green; S atoms, yellow (top layer) and cyan (bottom layer). (b) Band structure calculated for the ribbon geometry of (a) with periodic boundary conditions in direction along MTB. Horizontal dashed line denotes the position of E_F at $E = 0$. The electronlike band present at the 4|4P MTB is colored orange and crosses E_F at $k \approx \pi/(3a)$. A second band appears above E_F. Bulk bands are colored black and bands located at the ribbon edges specific to the finite-sized supercell are colored green. (c) Geometry of triangular inversion domain enclosed by three 4|4P MTB segments. (d),(e) LDOS maps (simulated STS maps) for the supercell shown in (c) at a height of 2.8 Å. Discrete states with wave vector just above [below] k_F corresponding to lowest unoccupied [highest occupied] state are shown in (d) [(e)]. E_F was adjusted to match $k_F = \pi/(3a)$.

APPENDIX C: TOMONAGA-LUTTINGER LIQUID THEORY IN A 1D BOX

To describe a Luttinger liquid in a system of finite length [31,32], the electron operator is first split into a left-moving and a right-moving part:

$$\Psi_\sigma(x) = e^{-ik_F x}\Psi_{\sigma,L}(x) + e^{ik_F x}\Psi_{\sigma,R}(x). \tag{C1}$$

At the two boundaries, a right-moving electron is scattered into a left-moving one. It is therefore useful to define a new field $\tilde{\Psi}_\sigma(x)$, which is $\Psi_{\sigma,R}(x)$ for $0 \le x \le L$ and $-\Psi_{\sigma,L}(-x)$ for $-L \le x \le 0$. This new field has simple periodic boundary conditions $\tilde{\Psi}_\sigma(-L) = \tilde{\Psi}_\sigma(L)$ and naturally incorporates the physics at the boundary.

The electron operator is obtained from the bosonization identity:

$$\tilde{\Psi}_\sigma(x,t) = \frac{F_\sigma(x,t)}{\sqrt{2\pi a}} e^{i\Phi_c(x,t)} e^{i\sigma\Phi_s(x,t)}, \tag{C2}$$

$$\Phi_\nu(x,t) = \sum_{m=1}^{\infty} \frac{1}{\sqrt{m}} [\chi_{\nu,m}(x) e^{-iv_\nu q_m t} b_{\nu,m} + \text{H.c.}], \tag{C3}$$

$$F_\sigma(x,t) = F_\sigma e^{i(E_{\text{gap}}/2)t} e^{i[(\pi/L)x - E_{\text{gap}}t](N_\sigma - N_{0,\sigma})}, \tag{C4}$$

with Klein factors F_σ and $\chi_{\nu,k}(x) = (\alpha_\nu e^{iq_{m_\nu}x} - \beta_\nu e^{-iq_{m_\nu}x})/\sqrt{2}$ and $\alpha_\nu = (K_\nu^{1/2} + K_\nu^{-1/2})/2$, $\beta_\nu = (K_\nu^{1/2} - K_\nu^{-1/2})/2$ $(\nu = c,\, s)$.

In order to evaluate the LDOS [Eq. (2)], we use the bosonization identity Eq. (C2) and obtain

$$A(E,x) = \sum_{\pm} \sum_{m_c,m_s>0} A^{(\pm)}_{m_c,m_s}(x)\delta(E \mp \omega_{m_c,m_s}), \tag{C5}$$

with the spectrum of charge and spin excitations,

$$\omega_{m_c,m_s} = \frac{E_{\text{gap}}}{2} + v_c q_{m_c} + v_s q_{m_s}, \tag{C6}$$

and the spectral weights,

$$A^{(\pm)}_{m_c,m_s}(x) = C\left|\sin\left(\frac{\pi}{L}x\right)\right|^{-\sum_\nu \alpha_\nu\beta_\nu} \left(2I^{x,-x}_{m_c,m_s} - e^{i2k_F^{\pm}x} I^{\pm x,\pm x}_{m_c,m_s} - e^{-i2k_F^{\pm}x} I^{\mp x,\mp x}_{m_c,m_s}\right). \tag{C7}$$

The remaining integrations,

$$I^{x,y}_{m_c,m_s} = \sum_{\nu=c,s} \int_0^{T_\nu} \frac{dt}{T_\nu} e^{iv_\nu q_{m_\nu} t} \exp\left[\sum_{k=1}^{m_\nu} \chi_{\nu,k}(x)\chi_{\nu,k}(y) e^{-iv_\nu q_k t}\right], \tag{C8}$$

are performed numerically. Here, $T_\nu = 2L/v_\nu$ is the travel time of charge- and spin-density waves. C is a cutoff-dependent prefactor.

APPENDIX D: CHARGE-DENSITY WAVE

1. Charge-density wave model

To calculate the LDOS for a CDW we use standard mean-field theory assuming a local interaction U in a continuum model. We solve the Schrödinger equation in a box self-consistently,

$$[-iv_F\partial_x + Un(x)]\psi_n(x) = E_n\psi_n(x), \tag{D1}$$

with the Fermi velocity v_F and the electron density,

$$n(x) = \sum_{n=1}^{N_0} |\psi_n(x)|^2. \tag{D2}$$

The LDOS of the interacting electrons is then given by

$$A(E, x) = \sum_{n\in\mathbb{N}} |\psi_n(x)|^2 \delta(E - E_n). \tag{D3}$$

The CDW gap opens between the highest occupied E_{N_0} and the lowest empty hole state E_{N_0+1} for attractive interactions $U < 0$. To produce Fig. 3(f) we take the value of v_F from the DFT calculation and we fit the interaction constant U to the experimental size of the gap E_{gap}. Note that a negative U is needed to obtain a CDW. The attractive interaction mimics the effect of optical phonons giving rise to an attractive interaction at momenta $2k_F$.

2. Room-temperature STM measurements

Our room-temperature measurements of $4|4E$ MTBs (Fig. 7) reveal that the characteristic beating pattern observed at low temperature persists also at room temperature. Based on the fit of Fig. 3(g), a CDW gap could only be of the order of 10 meV. For a Peierls-type CDW this would result in a transition temperature $T_C = 33$ K [41], inconsistent with our room-temperature observation. Note that the observation of the beating pattern does not imply the presence of a TLL at room temperature, but it does imply that at least quantization effects resulting from the finite length of the metallic wire persist up to room temperature.

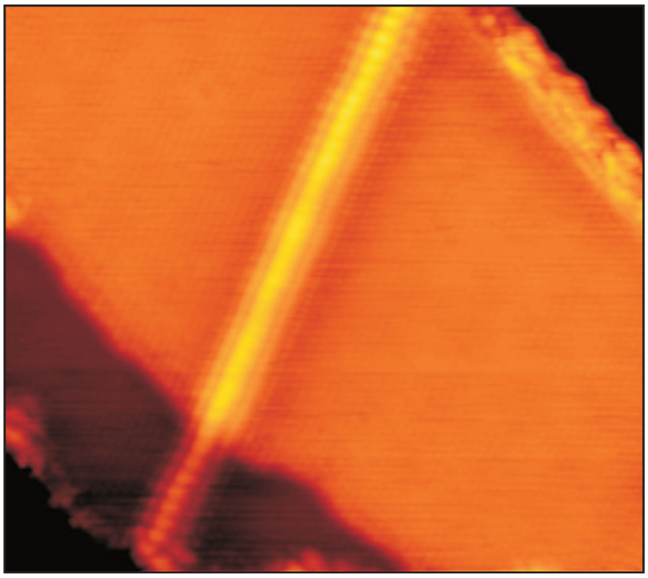

FIG. 7. Room-temperature STM measurements of a MTB in $\mathrm{MoS_2}$ crossing a substrate step. STM image of a $4|4E$ MTB [$U = -0.51$ V, $I = 0.056$ nA, image size (20×18) nm^2]. The periodic beating pattern of approximately $2a$ is observed best close to the ends of the MTB.

APPENDIX E: FOURIER SPECTRA OF THE LOCAL DENSITY OF STATES

1. Fourier transformation of experimental and theoretical spectra

We apply a standard Fourier transformation to our experimental and theoretical spectra and calculate the modulus of the Fourier mode. This procedure leads to discrete peaks at momenta $2\pi n/L$. Note, however, that the resulting picture depends on the precise choice of the width L of the real-space window used for the Fourier transform. As L determines the discretization in momentum space, this potentially leads to an error of the order of $\pm 2\pi/L$ in the position and width of the peaks. We have included only spectra in our Fourier transformation which show a signal clearly associated to the MTB. For our plots, we use a linear interpolation of the discrete data.

2. Comparison of Fourier spectra of different TLL parameters K_c and of a charge-density wave

In the generic interacting case, $K_c < 1$, Fourier modes at $2(k_F^+ \pm q_n)$ and $2(k_F^- \pm q_n)$ with $0 \le n \le m_c$ contribute at a given energy level labeled by the quantum number m_c. From this selection rule alone, one could expect a symmetric distribution of intensity centered around $2k_F^\pm$. The weights of the Fourier modes, however, are determined by the TLL parameter K_c. We discuss their dependence on K_c for a wire containing the same number of holes as in Fig. 4 (main text). In Fig. 8(a) we show the real-space image of the LDOS for $K_c = 0.5$. Its Fourier transform Fig. 8(b) reveals which Fourier modes are activated by K_c, and to what extent.

In order to make the effect of $K_c < 1$ more transparent, we also show the Fourier spectra for the nominally noninteracting case, $K_c = 1$ [see Fig. 8(c)], and for strong interactions, $K_c = 0.2$ [see Fig. 8(d)]. Note that we use a fixed ratio $v_s/v_c = 0.6$ and a fixed value of $E_{\mathrm{gap}} = 0.08$ eV in all plots, as our main goal is to demonstrate the role of matrix elements controlled by K_c. In reality, a noninteracting system is characterized by $v_s/v_c = 1$ and the ratio generically shrinks when interactions get stronger. For $K_c = 1$, only Fourier modes $2[k_F^\pm \pm (q_{m_c} + q_{m_s})]$ with quantum numbers (m_c, m_s) have nonzero weight. As a consequence, the Fourier spectrum displays the linear dispersion of charge and spin excitations, $\mp [(E_{\mathrm{gap}}/2) + v_c(k_F^\pm \pm q_{m_c}) + v_s(k_F^\pm \pm q_{m_s})]$.

The most pronounced peaks in Fig. 8(c) correspond to "pure" excitations, e.g., $(m_c = 1, m_s = 0)$. The remaining intensity is distributed among "mixed" excitations, e.g., $(m_c = 1, m_s = 1)$. For strong interactions ($K_c = 0.2$), a larger number of Fourier modes is activated and the charge peaks are transformed to a more symmetric distribution (as expected from the selection rule). In this scenario, the most pronounced peaks are found at $2k_F^\pm$. (The number of

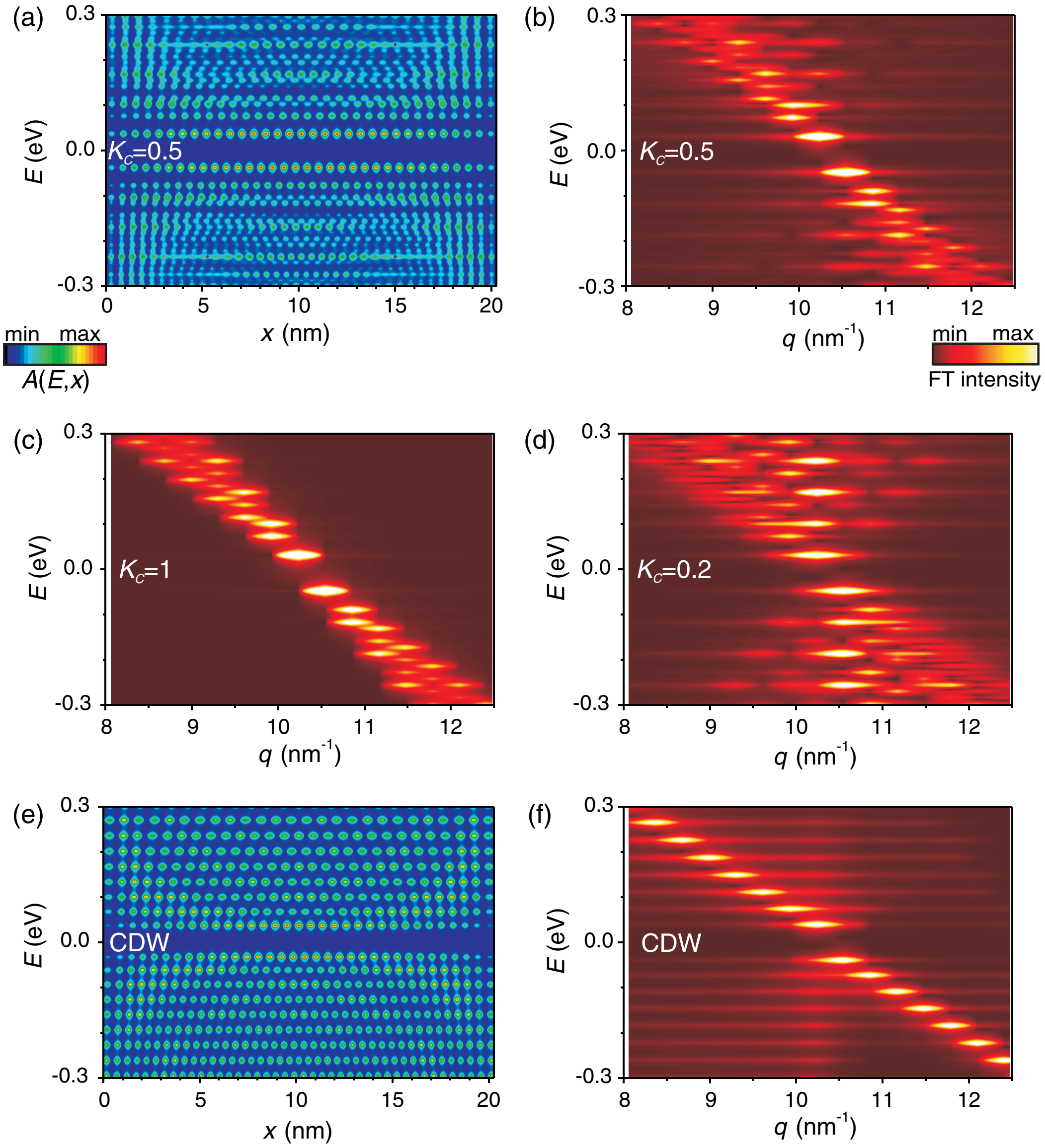

FIG. 8. Comparison between various interaction parameters K_C and CDW scenario. (a) TLL simulation using $K_C = 0.5$ as discussed in the main text ($v_c = 0.45$ nm eV, $v_s = 0.27$ nm eV, $E_{\text{gap}} = 0.08$ eV). (b) Corresponding FT. (c) FT of a TLL simulation with $K_C = 1$ (nominally noninteracting). (d) FT of a TLL simulation with $K_C = 0.2$ (strong interaction). (e) CDW simulation using a potential that reproduces the gap $E_{\text{gap}} = 0.08$ eV ($v_F = 0.25$ nm eV). (f) Corresponding FT.

pure spin peaks does not change since we set $K_s = 1$.) Comparison between experimental and theoretical Fourier spectra allows us to roughly estimate K_c from the number of activated Fourier modes and from the presence or absence of symmetry in the distribution.

In Fig. 8(e) we show the LDOS of the wire in a CDW state [with the same number of holes and the same value of E_{gap} as used for the TLL plots, Figs. 8(a)–8(d)]. There are three clear differences when compared to the TLL Fourier spectra, Figs. 8(b)–8(d). (i) The main peaks in its Fourier spectrum Fig. 8(f) form a single dispersing band since there is no spin-charge separation. (ii) The side peaks are only located at $2k_F^-$. These indicate the $2k_F^-$ scattering processes which lead to the opening of the gap. (iii) The band slightly curves in the vicinity of the gap while in TLL the bands are strictly linear.

[1] S.-I. Tomonaga, *Remarks on Bloch's Method of Sound Waves Applied to Many-Fermion Problems*, Prog. Theor. Phys. **5**, 544 (1950).
[2] J. M. Luttinger, *An Exactly Soluble Model of a Many-Fermion System*, J. Math. Phys. (N.Y.) **4**, 1154 (1963).
[3] F. D. M. Haldane, *"Luttinger Liquid Theory" of One-Dimensional Quantum Fluids. I. Properties of the Luttinger*

Model and Their Extension to the General 1D Interacting Spinless Fermi Gas, J. Phys. C **14**, 2585 (1981).

[4] M. Bockrath, D. H. Cobden, J. Lu, A. G. Rinzler, R. E. Smalley, L. Balents, and P. L. McEuen, *Luttinger-Liquid Behaviour in Carbon Nanotubes*, Nature (London) **397**, 598 (1999).

[5] H. Ishii, H. Kataura, H. Shiozawa, H. Yoshioka, H. Otsubo, Y. Takayama, T. Miyahara, S. Suzuki, Y. Achiba, M. Nakatake, T. Narimura, M. Higashiguchi, K. Shimada, H. Namatame, and M. Taniguchi, *Direct Observation of Tomonaga-Luttinger-Liquid State in Carbon Nanotubes at Low Temperatures*, Nature (London) **426**, 540 (2003).

[6] O. M. Auslaender, H. Steinberg, A. Yacoby, Y. Tserkovnyak, B. I. Halperin, K. W. Baldwin, L. N. Pfeiffer, and K. W. West, *Spin-Charge Separation and Localization in One Dimension*, Science **308**, 88 (2005).

[7] Y. Jompol, C. J. B. Ford, J. P. Griffiths, I. Farrer, G. A. C. Jones, D. Anderson, D. A. Ritchie, T. W. Silk, and A. J. Schofield, *Probing Spin-Charge Separation in a Tomonaga-Luttinger Liquid*, Science **325**, 597 (2009).

[8] M. Hashisaka, N. Hiyama, T. Akiho, K. Muraki, and T. Fujisawa, *Waveform Measurement of Charge- and Spin-Density Wavepackets in a Chiral Tomonaga-Luttinger Liquid*, Nat. Phys. **13**, 559 (2017).

[9] R. Claessen, M. Sing, U. Schwingenschlögl, P. Blaha, M. Dressel, and C. S. Jacobsen, *Spectroscopic Signatures of Spin-Charge Separation in the Quasi-One-Dimensional Organic Conductor TTF-TCNQ*, Phys. Rev. Lett. **88**, 096402 (2002).

[10] J. Hager, R. Matzdorf, J. He, R. Jin, D. Mandrus, M. A. Cazalilla, and E. W. Plummer, *Non-Fermi-Liquid Behavior in Quasi-One-Dimensional* $\mathrm{Li_{0.9}Mo_6O_{17}}$, Phys. Rev. Lett. **95**, 186402 (2005).

[11] P. Segovia, D. Purdie, M. Hengsberger, and Y. Baer, *Observation of Spin and Charge Collective Modes in One-Dimensional Metallic Chains*, Nature (London) **402**, 504 (1999).

[12] C. Blumenstein, J. Schäfer, S. Mietke, S. Meyer, A. Dollinger, M. Lochner, X. Y. Cui, L. Patthey, R. Matzdorf, and R. Claessen, *Atomically Controlled Quantum Chains Hosting a Tomonaga-Luttinger Liquid*, Nat. Phys. **7**, 776 (2011).

[13] K. Nakatsuji and F. Komori, *Debate Over Dispersion Direction in a Tomonaga-Luttinger-Liquid System*, Nat. Phys. **8**, 174 (2012).

[14] Y. Ohtsubo, J.-I. Kishi, K. Hagiwara, P. Le Fèvre, F. Bertran, A. Taleb-Ibrahimi, H. Yamane, S.-I. Ideta, M. Matsunami, K. Tanaka, and S.-I. Kimura, *Surface Tomonaga-Luttinger-Liquid State on Bi/InSb(001)*, Phys. Rev. Lett. **115**, 256404 (2015).

[15] P. C. Snijders and H. H. Weitering, *Colloquium: Electronic Instabilities in Self-Assembled Atom Wires*, Rev. Mod. Phys. **82**, 307 (2010).

[16] E. H. Do and H. W. Yeom, *Electron Quantization in Broken Atomic Wires*, Phys. Rev. Lett. **115**, 266803 (2015).

[17] N. de Jong, R. Heimbuch, S. Eliëns, S. Smit, E. Frantzeskakis, J.-S. Caux, H. J. W. Zandvliet, and M. S. Golden, *Gold-Induced Nanowires on the Ge(100) Surface Yield a 2D and Not a 1D Electronic Structure*, Phys. Rev. B **93**, 235444 (2016).

[18] L. Dudy, J. Aulbach, T. Wagner, J. Schäfer, and R. Claessen, *One-Dimensional Quantum Matter: Gold-Induced Nanowires on Semiconductor Surfaces*, J. Phys. Condens. Matter **29**, 433001 (2017).

[19] Y. Ma, H. C. Diaz, J. Avila, C. Chen, V. Kalappattil, R. Das, M.-H. Phan, T. Čadež, J. M. P. Carmelo, M. C. Asensio, and M. Batzill, *Angle Resolved Photoemission Spectroscopy Reveals Spin Charge Separation in Metallic* $\mathrm{MoSe_2}$ *Grain Boundary*, Nat. Commun. **8**, 14231 (2017).

[20] A. Anthore, Z. Iftikhar, E. Boulat, F. D. Parmentier, A. Cavanna, A. Ouerghi, U. Gennser, and F. Pierre, *Circuit Quantum Simulation of a Tomonaga-Luttinger Liquid with an Impurity*, Phys. Rev. X **8**, 031075 (2018).

[21] W. Zhou, X. Zou, S. Najmaei, Z. Liu, Y. Shi, J. Kong, J. Lou, P. M. Ajayan, B. I. Yakobson, and J. C. Idrobo, *Intrinsic Structural Defects in Monolayer Molybdenum Disulfide*, Nano Lett. **13**, 2615 (2013).

[22] J. Lin, S. T. Pantelides, and W. Zhou, *Vacancy-Induced Formation and Growth of Inversion Domains in Transition-Metal Dichalcogenide Monolayer*, ACS Nano **9**, 5189 (2015).

[23] S. Wang, G. D. Lee, S. Lee, E. Yoon, and J. H. Warner, *Detailed Atomic Reconstruction of Extended Line Defects in Monolayer* $\mathrm{MoS_2}$, ACS Nano **10**, 5419 (2016).

[24] X. Zou, Y. Liu, and B. I. Yakobson, *Predicting Dislocations and Grain Boundaries in Two-Dimensional Metal-Disulfides from the First Principles*, Nano Lett. **13**, 253 (2013).

[25] D. Le and T. S. Rahman, *Joined Edges in* $\mathrm{MoS_2}$*: Metallic and Half-Metallic Wires*, J. Phys. Condens. Matter **25**, 312201 (2013).

[26] M. Gibertini and N. Marzari, *Emergence of One-Dimensional Wires of Free Carriers in Transition-Metal-Dichalcogenide Nanostructures*, Nano Lett. **15**, 6229 (2015).

[27] M. Farmanbar, T. Amlaki, and G. Brocks, *Green's Function Approach to Edge States in Transition Metal Dichalcogenides*, Phys. Rev. B **93**, 205444 (2016).

[28] H. Liu, L. Jiao, F. Yang, Y. Cai, X. Wu, W. Ho, C. Gao, J. Jia, N. Wang, H. Fan, W. Yao, and M. Xie, *Dense Network of One-Dimensional Midgap Metallic Modes in Monolayer* $\mathrm{MoSe_2}$ *and Their Spatial Undulations*, Phys. Rev. Lett. **113**, 066105 (2014).

[29] S. Barja, S. Wickenburg, Z.-F. Liu, Y. Zhang, H. Ryu, M. M. Ugeda, Z. Hussain, Z.-X. Shen, S.-K. Mo, E. Wong, M. B. Salmeron, F. Wang, M. F. Crommie, D. F. Ogletree, J. B. Neaton, and A. Weber-Bargioni, *Charge Density Wave Order in 1D Mirror Twin Boundaries of Single-Layer* $\mathrm{MoSe_2}$, Nat. Phys. **12**, 751 (2016).

[30] H.-P. Komsa and A. V. Krasheninnikov, *Engineering the Electronic Properties of Two-Dimensional Transition Metal Dichalcogenides by Introducing Mirror Twin Boundaries*, Adv. Electron. Mater. **3**, 1600468 (2017).

[31] M. Fabrizio and A. O. Gogolin, *Interacting One-Dimensional Electron Gas with Open Boundaries*, Phys. Rev. B **51**, 17827 (1995).

[32] F. Anfuso and S. Eggert, *Luttinger Liquid in a Finite One-Dimensional Wire with Box-like Boundary Conditions*, Phys. Rev. B **68**, 241301 (2003).

[33] J. Hall, B. Pielić, C. Murray, W. Jolie, T. Wekking, C. Busse, M. Kralj, and T. Michely, *Molecular Beam Epitaxy of Quasi-*

Freestanding Transition Metal Disulphide Monolayers on van der Waals Substrates: A Growth Study, 2D Mater. **5**, 025005 (2018).

[34] D. Boese, M. Governale, A. Rosch, and U. Zülicke, *Mesoscopic Effects in Tunneling between Parallel Quantum Wires*, Phys. Rev. B **64**, 085315 (2001).

[35] C. Meyer, J. Klijn, M. Morgenstern, and R. Wiesendanger, *Direct Measurement of the Local Density of States of a Disordered One-Dimensional Conductor*, Phys. Rev. Lett. **91**, 076803 (2003).

[36] V. Meden, W. Metzner, U. Schollwöck, O. Schneider, T. Stauber, and K. Schönhammer, *Luttinger Liquids with Boundaries: Power-Laws and Energy Scales*, Eur. Phys. J. B **16**, 631 (2000).

[37] G. Kresse and J. Hafner, *Ab Initio Molecular Dynamics for Liquid Metals*, Phys. Rev. B **47**, 558 (1993).

[38] G. Kresse and J. Furthmüller, *Efficiency of Ab-Initio Total Energy Calculations for Metals and Semiconductors Using a Plane-Wave Basis Set*, Comput. Mater. Sci. **6**, 15 (1996).

[39] J. P. Perdew, K. Burke, and M. Ernzerhof, *Generalized Gradient Approximation Made Simple*, Phys. Rev. Lett. **77**, 3865 (1996).

[40] J. Tersoff and D. R. Hamann, *Theory of the Scanning Tunneling Microscope*, Phys. Rev. B **31**, 805 (1985).

[41] K. Rossnagel, *On the Origin of Charge-Density Waves in Select Layered Transition-Metal Dichalcogenides*, J. Phys. Condens. Matter **23**, 213001 (2011).

CHAPTER 7

Manuscript [3]: Band Bending and Valence Band Quantization at Line Defects in MoS_2

This chapter wholly consists of the above-named manuscript and its supplement, published in ACS Nano *on 30th June 2020.* Reprinted with permission from ACS Nano 2020, 14, 7, 9176–9187. Copyright 2020 American Chemical Society.

The experiments were proposed by C. Murray, W. Jolie, C. van Efferen and T. Michely. All sample growth and measurement was performed at $_{\mathrm{T}}$STM. *The samples were grown by C. Murray, W. Jolie and C. van Efferen with advice given by J. Hall. The STM and STS measurements were carried out by C. Murray and C. van Efferen, with assistance from J. A. Fischer. The STM/S data analysis was performed principally by C. Murray, with assistance from C. van Efferen. DFT calculations were performed by H.-P. Komsa in Helsinki, with advice from A. Krashenninikov. The electrostatic continuum model was developed by C. van Efferen and C. Murray, with guidance from A. Rosch and T. Michely. The interpretation of the results was discussed in depth by C. Murray, C. van Efferen, A. Rosch, A. Krashenninikov, H.-P. Komsa and T. Michely.*

C. Murray wrote the manuscript and finalised it in close collaboration with H.-P. Komsa and T. Michely.

Some of the results shown in this Chapter can be found in the Master's thesis of C. van Efferen and, to a minor extent, the doctoral thesis of W. Jolie [225].

ACS NANO

www.acsnano.org

ARTICLE

Band Bending and Valence Band Quantization at Line Defects in MoS$_2$

Clifford Murray,* Camiel van Efferen, Wouter Jolie, Jeison Antonio Fischer, Joshua Hall, Achim Rosch, Arkady V. Krasheninnikov, Hannu-Pekka Komsa, and Thomas Michely

Cite This: *ACS Nano* 2020, 14, 9176−9187

ABSTRACT: **The variation of the electronic structure normal to 1D defects in quasi-freestanding MoS$_2$, grown by molecular beam epitaxy, is investigated through high resolution scanning tunneling spectroscopy at 5 K. Strong upward bending of valence and conduction bands toward the line defects is found for the 4|4E mirror twin boundary and island edges but not for the 4|4P mirror twin boundary. Quantized energy levels in the valence band are observed wherever upward band bending takes place. Focusing on the common 4|4E mirror twin boundary, density functional theory calculations give an estimate of its charging, which agrees well with electrostatic modeling. We show that the line charge can also be assessed from the filling of the boundary-localized electronic band, whereby we provide a measurement of the theoretically predicted quantized polarization charge at MoS$_2$ mirror twin boundaries. These calculations elucidate the origin of band bending and charging at these 1D defects in MoS$_2$. The 4|4E mirror twin boundary not only impairs charge transport of electrons and holes due to band bending, but holes are additionally subject to a potential barrier, which is inferred from the independence of the quantized energy landscape on either side of the boundary.**

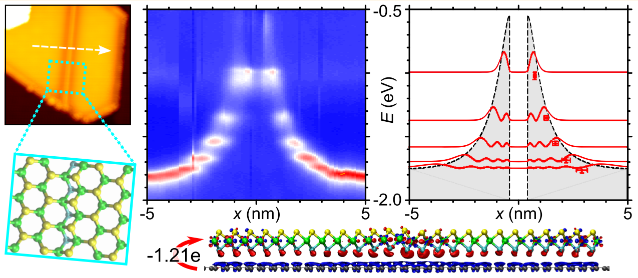

KEYWORDS: *band bending, scanning tunnelling spectroscopy, MoS$_2$, polarization charge, mirror twin boundary*

Coupled to the rise of MoS$_2$ and other transition metal dichalcogenide (TMDC) semiconductors as prospective two-dimensional (2D) device materials came the need to investigate their one-dimensional (1D) defect structures, *e.g.*, grain boundaries (GBs). Depending on their structure, GBs impair device performance to differing degrees when positioned in the channel of a single layer MoS$_2$ field effect transistor.[1−4] It is thus evident that control of the type and concentration of GBs is of importance for device fabrication. Besides satisfying scientific curiosity, it therefore pays to understand their effect on band structure and charge carrier transport. The lowest energy GBs are those hardest to avoid during growth, as the energy penalty associated with their introduction is marginal. In the three-dimensional (3D) world, these low energy GBs are 2D stacking faults or twin planes. For the case of SiC devices, such defects cause increased leakage current, reduced blocking voltage, and the degradation of bipolar devices.[5,6] In the world of 2D materials, the analogue to twin planes is 1D mirror twin boundaries (MTBs). These structural defects have some surprising effects on the band structure of monolayer MoS$_2$, to be investigated in this article.

GBs in MoS$_2$ layers have already been intensively investigated. Experimentally, scanning tunneling microscopy (STM) and spectroscopy (STS) are the ideal tools to identify and characterize MoS$_2$ GBs electronically.[7−11] Despite large variations in magnitude, typically an upward shift of the valence band (VB) and often also of the conduction band (CB) is observed at the GB.[7−12] The magnitude of the reported shifts range from 0.15 to 1.0 eV for the VB, depending on substrate and GB type. CB shifts may be of the same magnitude but are usually smaller. The spatial extension of the band bending is on the order of 5 nm away from the GB. Similar band bending effects were also described for MoS$_2$,[12] MoSe$_2$, and WSe$_2$ edges,[13,14] as well as for lateral heterojunctions, *e.g.*, of MoS$_2$ with WS$_2$ or WSe$_2$.[15,16] As an explanation for the observed band bending strain,[7,8,16,17] charge transfer into in-gap states,[4,12,18] or a combination of both were invoked.[9,10,15] Despite the technological importance

Received: June 14, 2020
Accepted: June 30, 2020
Published: June 30, 2020

https://dx.doi.org/10.1021/acsnano.0c04945

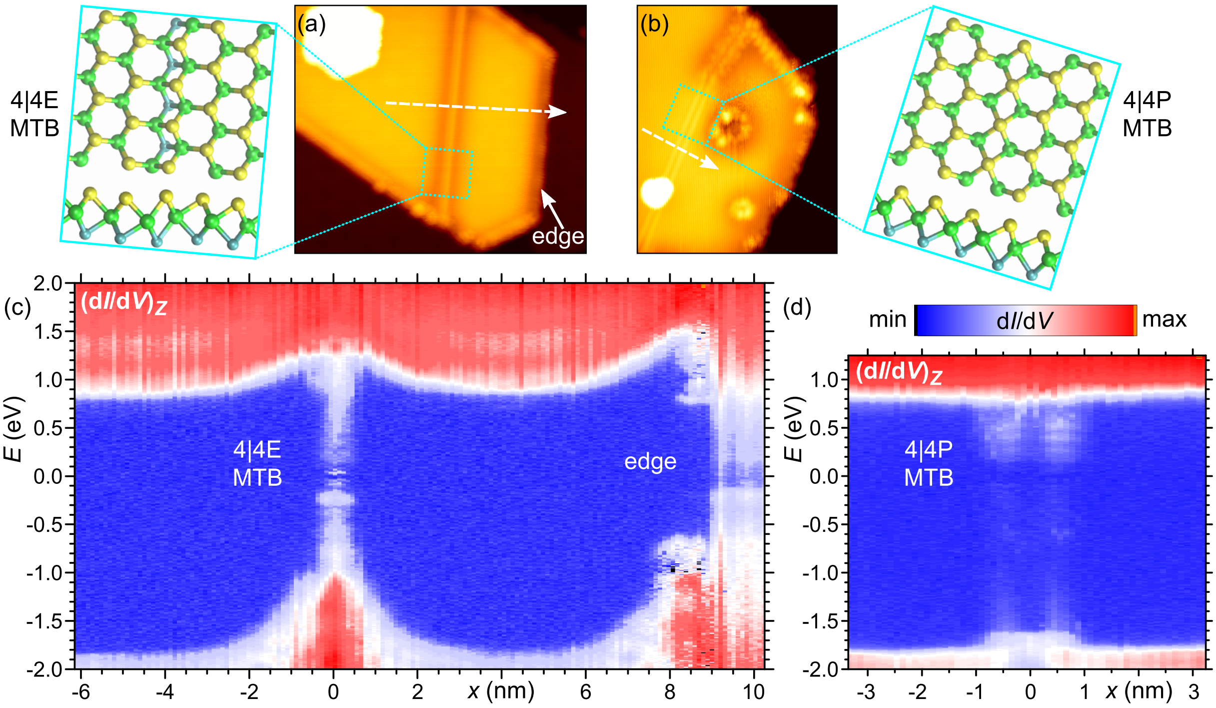

Figure 1. STS linescans across 1D defects in ML-MoS$_2$ on Gr/Ir(111). (a,b) Constant current STM topographs showing ML-MoS$_2$ islands; Gr appears as a dark background. In (a) *a* a roughly 20 nm long 4|4E-type MTB runs near-vertically down the center of the image, with a straight island edge parallel to it. In the top-left of the image a small BL-MoS$_2$ island is seen. In (b) a 4|4P-type MTB is present. At the top of the image the MTB terminates and an irregular GB begins, while bottom-left, a bright object (probably a Mo cluster) lies on top of the MTB. Ball-and-stick models of the 4|4E and 4|4P MTBs, in top and side views, are shown according to their topograph orientation in (a) and (b), respectively. Mo atoms are green, S atoms are yellow (top layer) or cyan (bottom layer). (c,d) Constant height STS linescans acquired along the dashed white arrows shown in (a) and (b), respectively. The recorded $(dI/dV)_Z$ signal is plotted as a function of energy E and position x, according to the shown (logarithmic) color scale with arbitrary units. STM/STS parameters: (a) $V = 1.2$ V, $I = 50$ pA, image size 27 × 23 nm^2; (b) $V = 1.0$ V, $I = 100$ pA, image size 19 × 15 nm^2; (c) stabilization voltage $V_{st} = 2.00$ V, stabilization current $I_{st} = 800$ pA; (d) $V_{st} = 1.25$ V, $I_{st} = 50$ pA.

of the band bending, modifications of the electronic structure around GBs are still poorly understood.

Here, for the investigation of 1D line defects in MoS$_2$, we take an approach different from previous work. Molecular beam epitaxy (MBE),[19] rather than the typical chemical vapor deposition, is employed for the growth of the MoS$_2$ layer to be investigated by STM and STS. The advantage is that the MoS$_2$ layer is grown under ultrahigh vacuum conditions and remains thereunder for spectroscopic investigation. Thereby the MoS$_2$ and the potentially reactive 1D defects remain clean of adsorbates. Inert, single-crystal graphene (Gr) on Ir(111) is used as a substrate.[20] Consequently, high-resolution STS is facilitated and ambiguities in the comparison of the data to density functional theory (DFT) calculation, which could result from adsorption or an inhomogeneous environment, are avoided. We discover that band bending over a distance of 5 nm, and the associated confinement normal to the 1D line defect renders the MoS$_2$ VB quantized. Although we focus our investigation on the most frequent and presumably lowest energy MTBs,[21,22] we find the same phenomenon for the edges of monolayer (ML) and bilayer (BL) MoS$_2$ islands, as well as for less symmetric, higher energy GBs. From the comparison between the experimental and calculated results, we establish that the band bending is not caused by strain but by charge on the line defects. Using DFT and measuring the Fermi wave vectors of MTB states, we decompose the net charge on the line defects into contributions from polarization and in-gap states of the 1D line defects. Charge transfer from Gr into in-gap defect bands is of decisive importance for band bending and the formation of the hole confining potential in the VB, meaning that this effect is substrate-tunable.

RESULTS AND DISCUSSION

Scanning Tunneling Spectroscopy. The STM topographs in Figure 1a,b show the 1D defects typical for MBE-grown ML-MoS$_2$ islands, in our case on Gr/Ir(111) (see Methods). 4|4E- and a 4|4P-type MTBs are visible in parts a and b of Figure 1, respectively; their atomic structures are depicted, illustrating that they form between 180° misoriented domains. 4|4E- or 4|4P-type MTBs appear in topographs as bright single- or double-tracks, respectively (see ref 22 for details). The MTBs host 1D metallic states and consist of 4-fold rings sharing an edge along a Mo−S bond (hence named 4|4E) or sharing a point at S-dimer sites (hence named 4|4P).[22−25] In MoSe$_2$ and MoTe$_2$, the 4|4P-type MTB is energetically most favorable, while in MoS$_2$, both 4|4P- and 4|4E types are stable.[21,26] In our samples, 4|4E-type MTBs are about 5 times more common and typically longer than 4|4P-type. An atomically straight zigzag island edge, parallel to the MTB, is also indicated in Figure 1a.

We perform high-resolution, constant height STS linescans orthogonally across the 1D defects; in Figure 1c over the 4|4E MTB and continuing over the island edge, in Figure 1d over the 4|4P MTB. The meV, Å resolution of the linescans leaves no data interpolation or filtering necessary (see Methods). In the color plot, blue represents a low or zero signal intensity (*i.e.*, in the band gap), while the red end of the scale signifies a finite density of states. The unperturbed or "bulk" ML-MoS$_2$ band structure is measured when sufficiently far from defects, for example, in Figure 1c at $x = -6$ nm: at ≈0.8 eV the onset of the CB and at ≈−1.8 eV that of the VB are seen by STS.[27]

Scanning orthogonally over the 4|4E MTB, defined to lie at 0 nm in Figure 1c, both the VB and CB bend several hundred meV upward (*i.e.*, toward higher energies). This bending occurs in a range of ≈5 nm on both sides of the MTB. No band bending of significance could be detected beyond this range.[28] States are detected throughout the band gap at the location of the MTB. They are derived from the 1D metallic MTB bands in the band gap of the 2D MoS$_2$.[22] Their quantization and Coulomb-blockade energy gap, associated with the Tomonaga−Luttinger liquid hosted along the finite-length MTB,[22] are visible close to E_F. Toward the island edge (located at ≈8.5 nm) similar upward bending and in-gap states are observed. Finally, the relatively featureless spectra of Gr on Ir(111) are recorded for $x > 9$ nm. In Figure 1d, the 4|4P-type MTB is located at 0 nm. The double-track structure of the 1D metallic states[22] is faintly visible. In contrast to the 4|4E MTBs and edges, the 4|4P MTB does not cause significant band bending. Further measurements confirming this are available in the Supporting Information, Figure S1.

We focus on the large band bending seen at 4|4E MTBs and obtain additional information via constant current STS; exemplary linescans are shown in Figure 2a,b. Constant current STS is of higher sensitivity to the variations at the band edges, *i.e.*, to abrupt increases of the LDOS due to van Hove singularities and thus can better resolve the subtle features at the edges, while features within the bands are hardly visible.[29,30] We note that similar band edge resolution with an inferior signal-to-noise ratio can be achieved by constant height STS after normalizing to the tunneling current (compare Supporting Information, Figure S2).

The 1D MTB band is metallic and was visible at $x = 0$ in the constant height STS of Figure 1c. However, with increasing magnitude of bias voltage, no abrupt increase of the LDOS takes place in the investigated ranges of Figure 2(a,b), and so the 1D MTB band is not visible in constant current STS. Well-visible in the constant current STS are the conduction and the valence band edges in parts a and b of Figure 2, respectively, through a sudden intensity rise.

In the CB, Figure 2a, far from the MTB, we see the Q-point edge states at ≈0.9 eV and, faintly, the K-point edge states at ≈0.7 eV.[27] The latter is the CB minimum of ML-MoS$_2$ and is barely visible in constant height STS due to its large parallel momentum, but constant current STS allows the tip to move closer to the sample to detect this weak signal.[27,29] Toward the MTB, the bands are bent smoothly up to roughly 1.3 eV. The K-point edge appears to bend slightly more than the Q-point edge, until their signals merge around 2 nm from the MTB. Bending of higher energy band edges is also faintly visible.

In the VB, Figure 2b, the dominating Γ-point edge begins at around −1.8 eV and bends upward to −1.0 eV at the MTB, thus undergoing larger bending than the CB. The VB bending occurs stepwise in increasing energy intervals. The discrete energies are near identical on either side of the MTB and were approximately the same across dozens of such MTBs of various lengths, see Figure 2c.

We consider a simple explanation for these discrete energies: the bending of the VB creates a potential well as sketched in Figure 3a. This confinement quantizes the VB energy levels

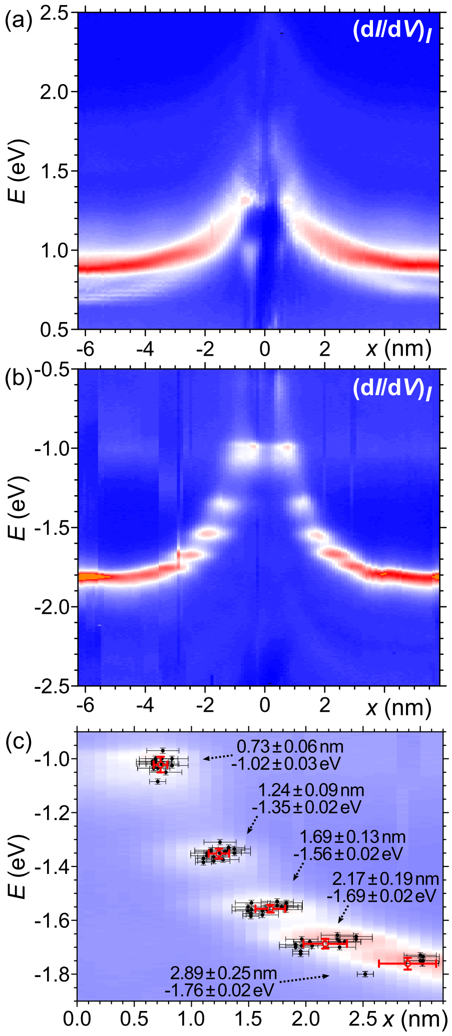

Figure 2. (a,b) Constant current STS linescans over a 4|4E MTB in ML-MoS$_2$ within the energy ranges of the CB and VB extrema, respectively. The recorded $(dI/dV)_I$ signal is plotted as in Figure 1d, but on a linear color scale. See Supporting Information, Figure S2, for a topograph of the MTB and a constant height STS scan in the same location. (c) Statistical distribution of quantized VB states at 4|4E MTBs. Black points show the energies E and positions x of the STS maxima from 20 different sets of states, mean values are in red and are stated. See Supporting Information for further details. For comparison, the right-hand side states of (b) are shown in the background. STS parameters: (a) $V_{st} = 2.5$ V; (b) $V_{st} = -2.5$ V; (a,b) $I_{st} = 50$ pA.

perpendicular to the MTB, whereas electrons excited to the CB are not confined. The energy levels and the maxima of the squared wave functions at the edge of the potential are reasonably well reproduced by solving the 1D Schrödinger equation for holes in the shown potential. The strongest probability density maxima of the quantized states are located close to the bent VB edge, with additional small peaks closer to the MTB. These smaller peaks are invisible to constant current STS (compare Figure 2b), while constant height STS shows featureless intensity below the band edge next to the MTB (compare Figure 1c). To understand this, it is important to note that the states represented in Figure 3a are 1D solutions of the Schrödinger equation for a 1D potential *normal* to the MTB. In reality, they mark the van Hove singularities of confined states that disperse *parallel* to the MTB. Their hole

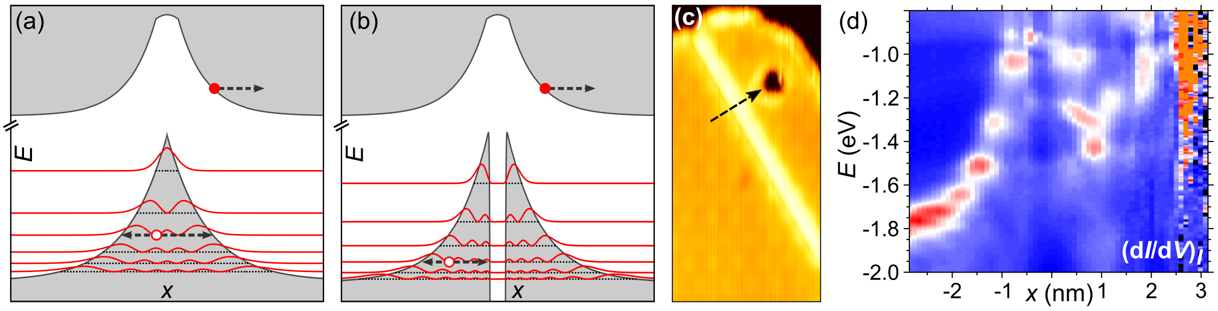

Figure 3. (a) Schematic sketch of hypothetical band bending at the 4|4E MTB, not to scale. Gray shaded areas represent the VB and CB. Also shown are energy levels (black dotted lines) and probability densities (red, arbitrary scale) obtained by solving the 1D Schrödinger equation for holes in this confining potential. (b) As (a), but assuming that the MTB gives rise to an additional repulsive potential, bisectioning the potential of (a) into two mirror-symmetric confining potentials. (c) Constant current STM topograph in which a small hole in the ML-MoS_2 island can be seen close to a 4|4E MTB. (d) Constant current STS linescan acquired along the black dashed arrow shown in (c). Linear color scale as Figure 2. STM/STS parameters: (c) $V = -2.0$ V, $I = 100$ pA, image size 30 × 15 nm^2; (d) $V_{st} = -2.0$ V, $I_{st} = 100$ pA.

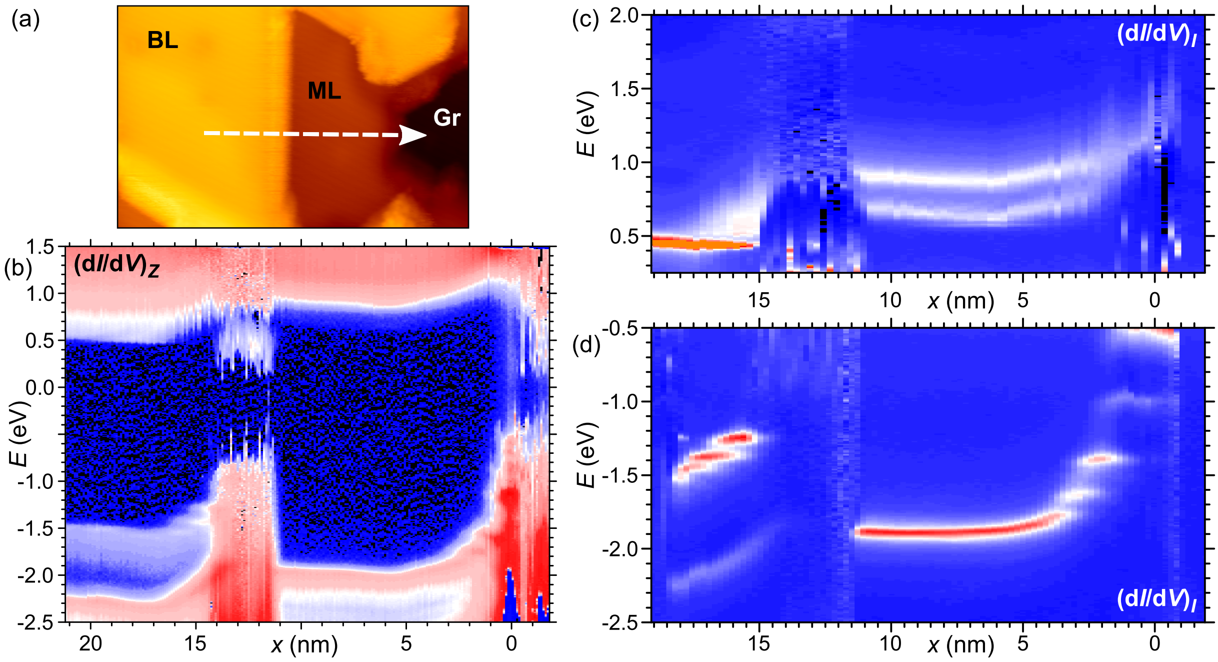

Figure 4. Band bending at edges of BL- and ML-MoS_2 islands. (a) Constant current STM topograph showing BL-MoS_2, ML-MoS_2, and Gr as indicated. The dashed white arrow marks where STS linescans were performed. (b) Constant height STS linescan, logarithmic color scale as Figure 1d. (c,d) Constant current STS linescans of the conduction and valence band extrema, respectively. Linear color scales as Figure 2. $x = 0$ nm defines the ML-MoS_2 edge in each scan. STM/STS parameters: (a) $V = 1.0$ V, $I = 80$ pA, image size 40 × 25 nm^2; (b) $V_{st} = 1.5$ V, $I_{st} = 90$ pA; (c) $V_{st} = 2.25$ V; (d) $V_{st} = -2.50$ V; (c,d) $I_{st} = 80$ pA.

dispersion along the MTB is characterized by downward, open parabolas which overlap throughout below the band edge, but not at the band edge. Thus, the edge-sensitive constant current STS mode measures only the dominant van Hove singularities, while constant height STS measures a featureless LDOS below the bent VB edge due to overlapping states.

An alternative scenario to the single potential well consists of two independent wells, left and right of the MTB, with the MTB acting as a repulsive barrier. It allows one to recreate the observed peaks as well, as suggested by Figure 3b. We note that distinction of these two situations is relevant, as hole transport through the MTB will be strongly impaired if the MTB acts as a repulsive potential for holes.

Experimentally, it is straightforward to distinguish these two situations. Figure 3c shows a MoS_2 island which features a small vacancy island directly next to a 4|4E MTB. An STS linescan from the complete side of the MTB to the broken side is displayed in Figure 3d. On the complete side, the quantized energy levels of the VB are like that at a "pristine" MTB, compare Figure 2c. On the other side, however, the quantized states are strongly modified due to the changed potential energy landscape. The eigenenergies and eigenstates on the complete side are not perturbed by the environment on the broken side, making plain that the two sides are independent; the MTB is a barrier to holes, confirming the scenario of Figure 3b.

Does the VB bending at a MoS_2 island edge, as visible in Figure 1c, cause quantization similar to that at a MTB? And does such band bending also occur at BL-MoS_2 island edges? To answer these questions, we performed STS linescans along the path marked in Figure 4a, from a BL-island via BL- and ML-MoS_2 edges down to the Gr level. In constant height STS,

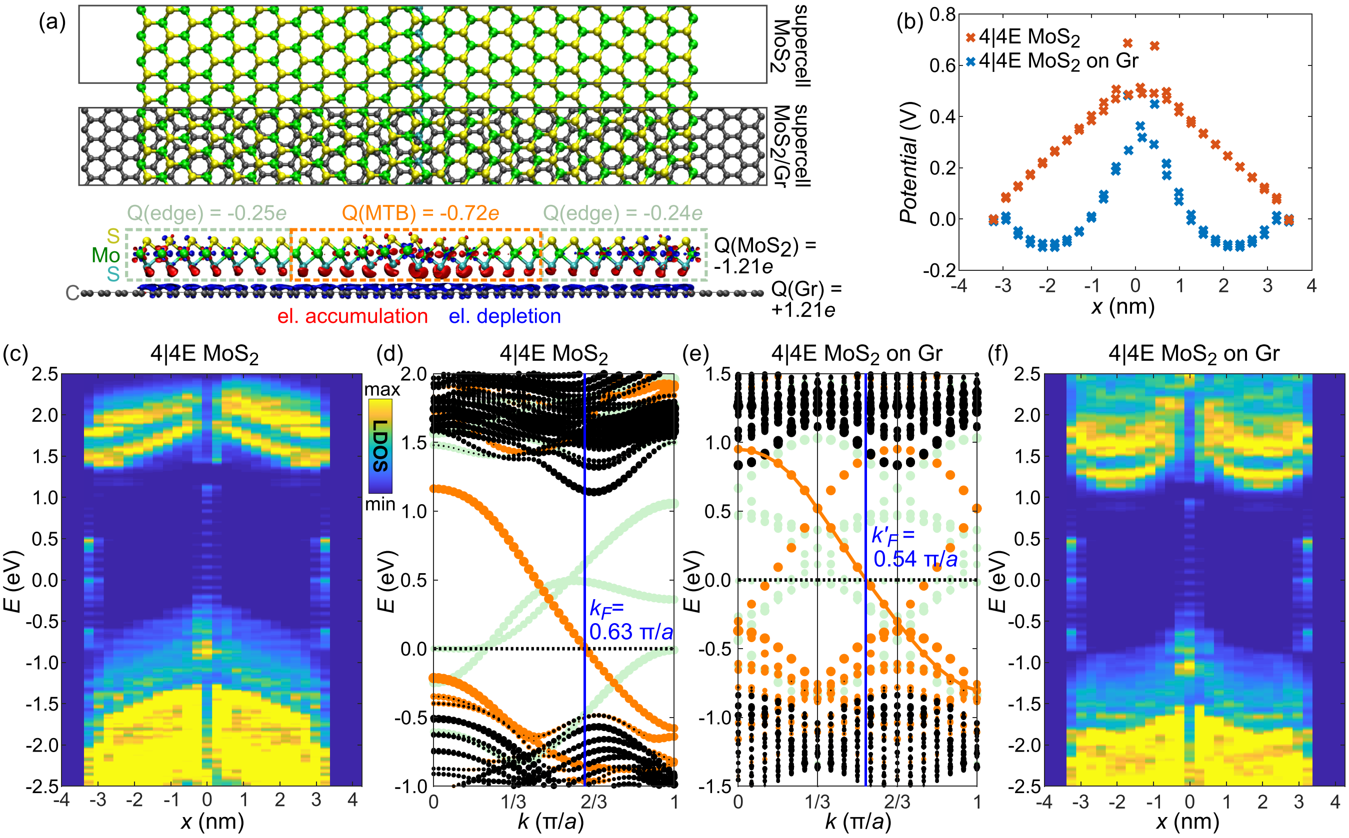

Figure 5. DFT calculations of band bending at 4|4E MTBs in ML-MoS$_2$, freestanding or on Gr. (a) DFT geometry of a 4|4E MTB centered in a ribbon of pristine MoS$_2$ (top view of upper unit cell) and on Gr (top view of lower unit cell). The side view below illustrates the charge transfer from Gr to the MoS$_2$ ribbon by plotting charge difference isosurfaces corresponding to a charge density gain (loss) of 0.002 e/Å^3 in red (blue). Charge gain or loss is indicated for different sections of the geometry. (b) S atom core potentials perpendicular to the 4|4E MTB in the freestanding MoS$_2$ ribbon, red crosses; for the ribbon on Gr, blue crosses. S atom core potential is set to 0 V at the edges in each case. (c) Projected LDOS for S atoms perpendicular to the 4|4E MTB in the freestanding MoS$_2$ ribbon. LDOS on an arbitrary color scale as indicated. (d) Band structure of freestanding MoS$_2$ ribbon with 4|4E MTB, with different regions highlighted by different colors (MTB, orange; edges, light green; bulk, black). (e) Band structure of MoS$_2$ ribbon on Gr with 4|4E MTB, with different regions highlighted by different colors [as in (d)]. The supercell construction leads to band folding, which is circumvented by using the periodic zone scheme and manually highlighting the MTB band. Fermi-level is set to zero in (d,e), and its crossing of the MTB band marked by a vertical blue line. (f) Projected LDOS for S atoms perpendicular to the 4|4E in the MoS$_2$ ribbon on Gr. Color scale as in (c).

Figure 4b, it is seen that also the BL-MoS$_2$ bands undergo upward bending at the island edge, similar to in the ML. Both of the BLs split Γ-point bands (at ≈−1.4 eV and ≈−2.2 eV at x = 20 nm) are bent upward at the edge. More information is gathered from constant current STS of the CB and VB energy ranges shown in parts c and d of Figures 4, respectively. The BL CB edge appears to bend ≈0.3 eV upward, while in the ML bending of the K- and Q-point states (with slightly different curvatures) bears a resemblance to that at 4|4E MTBs (Figure 2a) and is of the order of 0.5 eV. Although STS at MoS$_2$ edges is typically affected by tip instabilities like those visible in Figure 4d, quantization of the VB is unambiguous next to both the BL- and ML-MoS$_2$ island edges. While the discrete VB energy values were approximately the same for other ML island edges, the characteristic energies differ from those observed at 4|4E MTBs (Figure 2b,c). We have additionally observed VB quantization at some tilt GBs, see Supporting Information, Figure S3.

Density Functional Theory Calculations. Band bending may be caused by charge accumulation or depletion, but charge density is not directly probeable by STM/STS, typically. To uncover the mechanism of charging, we compare our experimental results to DFT calculations. Figure 5a shows the geometry of a ML-MoS$_2$ ribbon containing a 4|4E-type MTB, the Gr substrate, and the size of the two DFT supercells used to calculate the freestanding MoS$_2$ ribbon and the MoS$_2$ ribbon on Gr (see Methods).

We first focus on the freestanding ribbon with a 4|4E MTB. In Figure 5b, the S atom core potential variation perpendicular to the 4|4E MTB is plotted (red crosses). The 4|4E MTB is at a higher potential than the ribbon edges, and they are connected through a near-linear slope. In Figure 5c, the corresponding projected LDOS is displayed. We focus on S atoms because they contribute most to the STS signal, being closest to the STM tip. *Via* STS simulations for pristine MoS$_2$, we verified the S atoms' dominant contribution and note that the LDOS for Mo atoms displays qualitatively the same features. The variation in the band edge positions in Figure 5c reflects that of the core potentials. The near-linear potential gradient can be reproduced by describing the MoS$_2$ ribbon as a sheet of thickness d and effective dielectric constant ϵ (compare ref 31) containing three parallel wires of line charge λ, corresponding to the MTB and the two edges. See Supporting Information, Figure S4 for details. Through comparison with our DFT, we estimate λ_{MTB} = −0.05 e/a at the MTB and λ_{edge} = +0.025 e/a at each edge. Here e is the

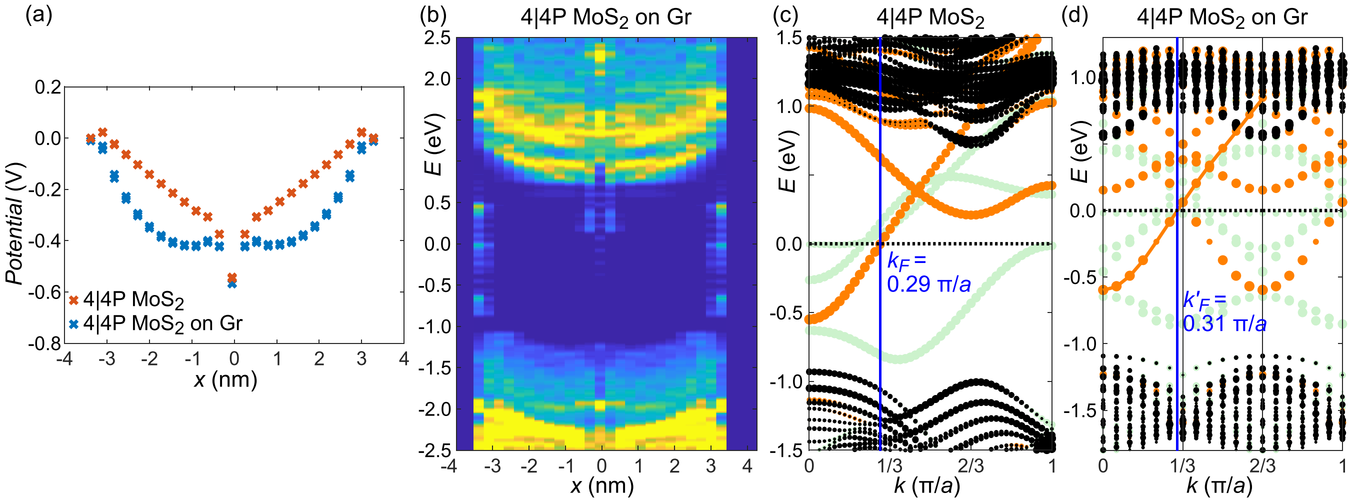

Figure 6. DFT calculations of band bending at 4|4P MTBs in ML-MoS$_2$, freestanding or on Gr. Geometry equivalent to that shown in Figure 5a. (a) S atom core potentials perpendicular to the 4|4P MTB in the freestanding MoS$_2$ ribbon, red crosses; for the ribbon on Gr, blue crosses. S atom core potential is set to 0 V at the edges in each case. (b) Projected LDOS for S atoms perpendicular to a 4|4P MTB in a MoS$_2$ ribbon on Gr. Color scale as in Figure 5c. (c) Band structure for freestanding MoS$_2$ ribbon with 4|4P MTB. (d) Band structure for MoS$_2$ ribbon on Gr with 4|4P MTB, shown within the periodic zone scheme and manually highlighting the MTB band. Fermi-level is set to zero in (c,d); color scheme as in Figure 5d.

elementary charge and a = 3.15 Å the primitive translation of MoS$_2$ along the line.

The net line charge $\lambda_{\text{MTB}} = -0.05\ e/a$ is composed of two contributions: (i) the 1D MTB band carries a charge defined by the Fermi wavevector k_{F}. The band structure of a freestanding ribbon is shown in Figure 5d, with MTB and edge bands found inside the bulk gap. Corresponding in-gap states are visible at the MTB and edges in Figure 5c. For the MTB band, k_{F} is located at $0.63\frac{\pi}{a}$ and, because the band is hole-like, its filling is 0.37. Therefore, the MTB band carries a band charge $\lambda_{\text{MTB}}^{\text{band}} = -\frac{2e}{\pi}(1 - k_{\text{F}}) = -0.74\ e/a$ (cf. $-2\ e/a$ for a full band). (ii) Evidently, there must be an additional positive charge contribution to the MTB in order to reach the much smaller net line charge of $\lambda_{\text{MTB}} = -0.05\ e/a$. The ribbon is composed of two MoS$_2$ domains of opposite orientation and opposite formal polarization $\pm\mathbf{P}$.[32,33] At the MTB, the abrupt change in polarization ΔP induces a polarization charge $\lambda_{\text{MTB}}^{\text{pol}}$ (discussed in more detail below). As $\lambda_{\text{MTB}} = \lambda_{\text{MTB}}^{\text{band}} + \lambda_{\text{MTB}}^{\text{pol}}$, we deduce $\lambda_{\text{MTB}}^{\text{pol}} = +0.69\ e/a$ on the MTB. The nearly complete compensation of band and polarization charge can be rationalized as follows: the electrostatic energy created by the polarization of the MoS$_2$ drives the filling of the 1D MTB and edge bands in order to minimize system energy.[33] In fact, in the limit of infinite ribbon width, λ_{MTB} is exactly zero, as otherwise the energy of the electrostatic field would diverge ("the polar catastrophe").[33]

When the MoS$_2$ ribbon is placed on Gr, a total charge of $-1.21e$ is depleted from the Gr layer and added to the MoS$_2$ ribbon, as determined from Bader charges[34] and illustrated by the charge density difference in the side view of Figure 5a. Most of this charge is located at the MTB and ribbon edges, with less in the "bulk" regions between. Dividing the MoS$_2$ ribbon into MTB and edge regions, we estimate an excess of $-0.72e$ located at the MTB and $-0.25e$ at each edge. Considering the $3a$ breadth of the supercell, this equates to linear charge densities of $-0.24\ e/a$ and $-0.08\ e/a$ at MTB and edge, respectively. These transfer charge densities should be added to those of the freestanding MoS$_2$ ribbon, *i.e.*, a total of $\lambda_{\text{MTB}} = -0.29\ e/a$ is predicted at the 4|4E MTB in MoS$_2$ on Gr. Note that, unlike in the MoS$_2$ ribbon, the charge distribution in Gr is relatively uniform (compare Figure 5a and Supporting Information, Figure S5), indicating a rather large screening length in Gr.

The origin of charge transfer from Gr to the MoS$_2$ is the work function difference between Gr and ML-MoS$_2$. According to DFT and in agreement with experiment, the work function of Gr is lower than the work function of MoS$_2$. DFT (experimental) values are around 4.5 eV (4.6 eV) for Gr and 5.1 eV (5.2 eV) for ML-MoS$_2$.[35−38] Consequently, when MoS$_2$ is placed on Gr, the Fermi levels will align through charge transfer. The charge transfer will thus decrease the chemical potential in Gr and increase the chemical potential in MoS$_2$. If our model for determining λ is valid, one should also be able to extract the charge transfer from the change in filling of the MTB band. The band structure from the MoS$_2$/Gr supercell is shown in Figure 5e. Note that due to the incommensurate unit cells of MoS$_2$ and Gr, the supercell construction must be used, resulting in band folding. This is then displayed in the periodic zone scheme with the MTB band highlighted. We extract the Fermi wavevector of the 1D MTB band $k_{\text{F}}' = 0.54\frac{\pi}{a}$ (where $'$ denotes the presence of Gr). This corresponds to the filling of the hole-like band being increased from 0.37 to 0.46, *i.e.*, the 1D band charge is increased by $\Delta\lambda_{\text{MTB}}^{\text{band}} = -\frac{2e}{\pi}(k_{\text{F}} - k_{\text{F}}') = -0.18e/a$, in decent agreement with our Bader charge transfer analysis above ($-0.24\ e/a$). In experiment, we measure standing waves along the 4|4E MTB of periodicity (2.01 ± 0.04) a corresponding to a Fermi wavevector $(0.50 \pm 0.01)\frac{\pi}{a}$ (see ref 22), in agreement with the DFT value $k_{\text{F}}' = 0.54\frac{\pi}{a}$. Our conclusions here are in line with Kaneko et al.,[18] who speculated that the accumulation of charge transferred from the substrate into 1D MTB bands could be the origin of a substantial band bending at MoS$_2$ MTBs.

Figure 5f shows the projected LDOS of the S atoms perpendicular to the 4|4E MTB for the ribbon on Gr. Large upward band bending occurs at the MTB and edges in the CBs and VBs, in qualitative agreement with experiment and consistent with the negative line charges on them. Because of the limited cell size the band bending is smaller in magnitude than in experiment; the MoS_2 band structure does not reach its "bulk" state between the MTB and the edges (compare to the case of an asymmetrically positioned MTB in Supporting Information, Figure S6). The S atom core potentials for the ribbon with a 4|4E MTB on Gr are plotted in Figure 5b as blue crosses. They reproduce the variation of the band edge energy with the spatial coordinate.

Corresponding results for the 4|4P-type MTB are shown in Figure 6. The S atom core potentials for the freestanding ribbon, shown in Figure 6a, indicate that the MTB is positively charged. The ribbon on Gr, on the other hand, shows hardly any band bending in the core potentials or in the projected LDOS (Figure 6b), as also observed in experiment. Again, charge transfer from Gr to MoS_2 takes place when the layers are brought into contact (compare band structures Figure 6c,d) but results in a nearly neutral net line charge. This implies that polarization charge and 1D band charge compensate fully ($\lambda_{\mathrm{MTB}}^{\mathrm{pol}} \approx -\lambda_{\mathrm{MTB}}^{\mathrm{band}}$), and indeed this conforms with our understanding of the system. Assuming the same polarization charge as for the 4|4E MTB would result in an estimate of $\lambda_{\mathrm{MTB}}^{\mathrm{band}} = -0.69\ e/a$. For the electron-like 1D MTB band ($\lambda_{\mathrm{MTB}}^{\mathrm{band}} = -\frac{2e}{\pi}k_{\mathrm{F}}$), this corresponds to a Fermi wavevector of $k_{\mathrm{F}}' = 0.345\frac{\pi}{a}$. This is in excellent agreement with our calculated DFT value $k_{\mathrm{F}}' = 0.31\frac{\pi}{a}$ (Figure 6d) and our experimental measurement of $(0.33 \pm 0.01)\frac{\pi}{a}$ [based on $(3.00 \pm 0.04)\ a$ standing wave periodicity in 4|4P MTBs, see ref 22].

Rephrased, because the charge transfer from Gr fortuitously results in $\lambda_{\mathrm{MTB}} = 0$ for our 4|4P MTB, the measurement of the Fermi wavevector of the 1D MTB band implies a measurement of the polarization charge $\lambda_{\mathrm{MTB}}^{\mathrm{pol}}$. To the authors' best knowledge, this is the first direct measurement of a polarization charge. The measured value $\lambda_{\mathrm{MTB}}^{\mathrm{pol}} = +0.66\ e/a$ exactly matches $\lambda_{\mathrm{MTB}}^{\mathrm{pol}} = +\frac{2}{3}e/a$ predicted by Gibertini and Marzari[33] for 4|4P MTBs. More strictly, we are referring here to the "bound charge", which is the sum of λ^{pol} and a correction for the changed stochiometry of the interface. The 4|4E MTB was not calculated in ref 33, but, considering the MoS_2 lattice symmetry and the boundaries' shared Mo_2S_2 stochiometry, the 4|4E MTB must possess the same quantized bound and polarization charge as its 4|4P counterpart.

We note that placing MoS_2 on Gr as acharge reservoir already captures the essence of the processes; the Ir(111) substrate, omitted due to computational limitations, does not change the picture qualitatively. We attribute this to the circumstance that Gr on Ir(111) is almost undoped (Dirac point only 0.1 eV above E_{F}). However, because Gr offers poor lateral screening, the Ir substrate will affect the lateral screening substantially.

In our DFT calculations, we see no significant lattice strain ($\epsilon < 0.5\%$) in the bulk due to MTBs or island edges, ruling out its relevance for band bending. This is consistent with DFT calculations showing that MTBs induce strain only within ≈0.5 nm normal to their axis,[39,40] *i.e.*, on a length scale ten times smaller than that of our bending. In previous works, TMDC band bending was ascribed to strain at the 1D interfaces,[8,16,17,40] or a combination of charging and strain.[7,9,10,15] This may be meaningful for low-symmetry tilt GBs composed of arrays of point dislocations, giving rise to large local strains[7] or lateral heterostructures with mismatch strain[16] but not for the present case of perfect 4|4E MTBs and straight edges.

Continuum Modeling. The potential used in Figure 3b to reproduce the quantization at the 4|4E MTB was fitted "by hand" and not based on a physical origin. In the following, we will use the 4|4E MTB linear charge density $\lambda_{\mathrm{MTB}} = -0.29\ e/a$ as derived from DFT and physically meaningful system parameters in a simplistic model, in an effort to reproduce the band bending potential and the resultant dominant probability density maxima in E and x, as visible in experiment.

The band bending in the MoS_2 ribbon on Gr/Ir(111) is modeled by a screened electrostatic potential due to an infinite line of charge located at the MTB, sandwiched between vacuum and a perfect metal substrate, as sketched in Figure 7a. Following the work of Le Quang et al.,[14] the MTB charge "generates" image charges in the vacuum and the metal, which themselves generate additional image charges, and so on to the nth order. The potential at the MoS_2 surface at a lateral distance x is then:

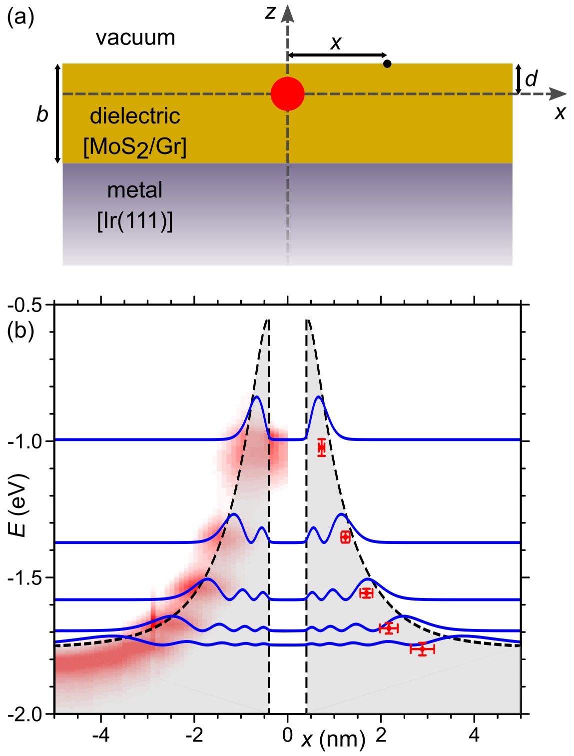

Figure 7. Modeling the VB bending and quantization at a 4|4E MTB (a) Cross-sectional sketch of the model calculating the potential due to a screened, infinite line of charge, see eq 1. *b* is the thickness of the MoS_2/Gr layer and *d* the "depth" of the charge below the vacuum interface. $V(x)$ is calculated for a point on the surface, *x* being the orthogonal distance from the axis of the MTB. (b) Model potential (black) and resulting quantized states (blue) obtained using the values given in the text. The quantized state energy eigenvalues (baselines) are added to their probability densities (displayed as maxima of arbitrary height). For visual comparison, the STS linescan of Figure 2b (color filtered) and the mean experimental maxima values are shown in red on the left- and right-hand sides, respectively.

$$V(x) = \frac{4k_e\lambda}{\epsilon_{\rm di} + \epsilon_{\rm vac}}\left\{\ln\frac{d}{\sqrt{x^2+d^2}} + \sum_{n=1}^{\infty}(-1)^n\gamma^{n-1}\left[\ln\frac{2nb-d}{\sqrt{x^2+(2nb-d)^2}} + \gamma\ln\frac{2nb+d}{\sqrt{x^2+(2nb+d)^2}}\right]\right\} + C \qquad (1)$$

where $k_e = (4\pi\epsilon_0)^{-1}$, $\gamma = \frac{\epsilon_{\rm di}-\epsilon_{\rm vac}}{\epsilon_{\rm di}+\epsilon_{\rm vac}}$, $\epsilon_{\rm di}$, and $\epsilon_{\rm vac} = 1$ are the dielectric constants of the dielectric layer and vacuum respectively, λ is the linear charge density at the MTB, b and d are as defined in Figure 7a, and C is a potential energy offset (as any potential energy is only defined relative to another). The first term in eq 1 corresponds to self-screening by the dielectric only, while the second term in eq 1, the summation of potentials due to image charges to the nth order is due to metal screening. Finally, at the location of the MTB, we add a potential barrier of depth −5 eV and width 0.8 nm by hand. We solve the Schrödinger equation for positive charge carriers of effective mass m_h^* in the resultant potential.

As it is the Γ-point which is detected in STS in the VB, we use an effective hole mass $m_h^* = 2.7m_e$.[41,42] We consider the charge to be located in the center of the ML-MoS_2 layer, thus $d = 0.31$ nm. For simplicity, we model the MoS_2 and Gr (and their van der Waals gaps) together as a single dielectric layer of thickness $b = 1.2$ nm. Gr is only slightly doped in this configuration[43,44] and thus expected to screen rather weakly, consistent with the nearly uniform charge distribution in Gr in Figure 5a. Indeed, considering Gr to be part of the perfect metal substrate leads to an overestimation of the screening.[14] The dielectric constant of ML-MoS_2 is anisotropic and nontrivial[31,45] and is complicated further by combination with Gr in our model. It is typically in the range $\epsilon_{\rm di} = 5-10$, with similar values predicted for a ML-MoS_2/Gr heterostructure.[46]

Setting $\lambda_{\rm MTB} = -0.29\ e/a$, and with only $\epsilon_{\rm di}$ and C as variables, we find that values of $\epsilon_{\rm di} = 6.2$ and $C = -0.55$ eV yield a very good fit, Figure 7b. The potential reproduces the lateral positions of the main probability density maxima and the energy level positions with error less of than 0.03 eV, see Table S1 in Supporting Information.

This continuum modeling neglects the atomistic details of the system, the anisotropy of its screening, and simplifies its layered structure. Nevertheless, it captures the system's essentials. Using literature-based estimates for b, d, $\epsilon_{\rm di}$, m_h^*, and the linear charge density $\lambda_{\rm MTB} = -0.29\ e/a$ obtained by DFT, the modeling reproduces eigenenergies and spatial positions of the quantized VB states at 4|4E MTBs.

DISCUSSION

On the basis of literature reports, band bending of the VB and the CB at 1D defects appears to be the rule rather than the exception in TMDC semiconductors.[7−16] Our results are in line with this general finding, although the 4|4P MTB does not show band bending. Specifically, at 4|4E MTBs, both charge carrier types face a significant potential barrier, with obvious negative implications for the conductivity of the MoS_2. Electrons face a barrier of at least 0.6 eV, while holes become trapped in an even deeper potential well.

A key point emerging from our DFT calculations is that the band bending depends heavily on the substrate, as the substrate's electronic properties, specifically its work function, determine the amount of charge transferred. For our case of slightly p-doped Gr (Dirac point 0.1 eV above E_F[44]), electron transfer from the substrate to the 1D defects prevails, causing an upward shift of the bands next to 4|4E MTBs and layer edges. By strong n- or p-doping of Gr, its work function,[47,48] thus the charge transfer, and consequently the amount of band bending at each 1D line defect, is likely to be changed. This could for instance cause upward or downward bending also at the 4|4P MTB, for which we consider the absence of band bending in our measurements to be coincidental and related to the specific amount of charge transferred to the system. The sensitive dependence of the band bending on the environment could also partly explain why the measured band bending for MoS_2 GBs with similar tilt angles differs vastly.[4,7,9,11]

If the nature of the substrate or chemical gating are able to affect band bending, electrostatic gating will do so as well. Thus, the magnitude of band bending at a 1D defect is not a fixed quantity but will change during device operation. On one hand, this will make the effect of 1D defects on charge carrier transport harder to predict. On the other, it could mean that the transport through MTBs and the carrier trapping at MTBs/edges can be controlled or switched via gating.

For hole transport through 4|4E MTBs, perhaps an even greater hurdle than bent bands is the repulsive barrier, which is obvious from the complete independence of the quantized VB states on either side of the MTB. Although tunneling transport is likely to take place (in our modeling the barrier width was set to 0.8 nm), the transmission will be strongly diminished by the barrier. The barrier is a natural consequence of the broken crystal symmetry at the location of the MTB, causing backscattering. We speculate that it is likely that similar barriers for holes exist also for other grain boundaries, *e.g.*, at the 4|4P MTB. It thus seems that hole transmission across MTBs is not only suppressed in the energy range of the spin−orbit splitting of the VB due to spin−valley locking, as described by Pulkin and Yazyev,[49] but is globally impaired due to a barrier at the location of the MTB causing backscattering. Indeed, Park et al.[50] have noted a strong suppression of transmission deep within the VB at 4|4P MTBs. Considering these results, it appears rewarding to investigate hole transport across 4|4E and 4|4P MTBs in more detail, for example, with a 4-probe STM.

In our work, quantization in the VB next to line defects was found whenever a substantial upward shift of several hundred meV was observed: at 4|4E MTBs, at ML and BL edges, as well as at low symmetry GBs (see Supporting Information). It is evident that such quantization effects should also be present in other, similar systems which display band bending. Consequently, the question arises: why has such quantization not been noted in the past? First, we remark that the constant height STS linescan of a BL-$MoSe_2$ edge by Zhang et al.[13] (compare Figure 3b of ref 13) indeed displays step-like features in the upper VB edge, which could be interpreted as signatures of VB quantization in view of the current findings. Next, we note that the VB states were made clearly visible only by constant current STS (or equivalently normalized constant height STS, see Figure S2), conducted with sufficient resolution and at low temperature.

On the basis of our DFT calculations we obtain the net line charge $\lambda_{\rm MTB} = -0.29\ e/a$ on the 4|4E MTB in MoS_2 on Gr.

Because of the marginal doping of Gr on Ir(111), this is also expected to be a reasonable estimate for that on Gr/Ir(111). Using this line charge and realistic system parameters, we were able to fit energy and location of the confined states in the VB accurately with a simple electrostatic model.[14] Although imperfect, the agreement is reasonable and substantiates a net line charge of $\lambda_{\mathrm{MTB}} \approx -0.29\ e/a$. Our result is similar to those obtained by Le Quang et al.,[14] with $\lambda = -0.27\ e/a$ for the edge of a trilayer WSe_2 flake, while Kobayashi et al.[15] obtained linear charge densities an order of magnitude larger for a MoS_2−WS_2 1D heterojunction interface.

The 2D interfaces of insulating oxide heterostructures can be electrically conductive, in contrast to their bulk constituents. The origin of this conductivity is a matter of debate; a proposed mechanism is the formation of polarization charge at the interface to avoid a so-called "polar catastrophe".[51] The study of analogous polar discontinuities at the 1D interfaces of 2D materials is an emerging field.[52−54] To the best of our knowledge, the quantitative verification of the polarization charge at the MTBs here represents the first experimental measurement of such interface polarization charge. Considering the complications due to defects and intermixing at 3D heterointerfaces,[55,56] the pristine interfaces of MoS_2 MTBs may act as a reduced-dimensionality testing ground for polar-charging models.

The well-defined band bending and localization of charges at 4|4E MTBs, and edges could find application in optics and optoelectronics. The asymmetry of the bending means a decreasing exciton energy profile toward the defect, possibly leading to an exciton funneling effect as has been achieved through strain-induced bending,[57,58] it might also be possible to control the funneling via the aforementioned electrostatic gating. In analogy to TMDC semiconductor point defects having bound excitons[59,60] and serving as single photon emitters,[61] the quantized VB states next to 1D defects in MoS_2 could also be utilized.

CONCLUSIONS

In summary, we have investigated the electronic landscape perpendicular to line defects in MoS_2 islands with high-resolution STS. Band bending occurs in a 5 nm range at MTBs and ML- as well as BL-island edges, as a result of charge on these 1D defects. Our experiments and DFT calculations develop a fully consistent picture of the defect charging, which is in agreement with literature predictions.[18,33] Namely, the net line charge on MTBs in MoS_2 is the result of polarization charge, its compensation by 1D MTB band-filling, and additional charge transfer into these in-gap bands due to the substrate's different work function. Our work shows that STS is a viable tool to investigate the charging of domain boundaries. For the 4|4P MTB, the absence of band bending implies the net absence of charge on the MTB. Therefore, via the STS measurement of the 1D band charge on the MTB, a first direct confirmation of the quantized polarization charge on MTBs was possible, precisely confirming the value of $+\frac{2}{3}e/a$ predicted by Gibertini and Marzari.[33] For the 4|4E MTB, the knowledge of the quantized polarization charge together with the measurement of the 1D band charge allows us to estimate the net charge on the MTB, which is in excellent agreement with the prediction of the DFT calculation.

The large (≈0.8 eV) VB bending normal to the 4|4E-type MTBs on Gr/Ir(111) leads to VB quantization next to it, with a barrier at the MTB creating two independent confining potentials for holes to its left and right. Therefore, hole transport through these MTBs is suppressed. Using a simplistic electrostatic model, with realistic system parameters and the DFT-derived line charge $\lambda_{\mathrm{MTB}} = -0.29\ e/a$, the resulting screened potential reproduces band bending accurately. Solving the 1D Schrödinger equation for this potential reproduces the eigenenergies and spatial position of the dominant peaks in the probability density. The CB next to 4|4E MTBs displays band bending too, thus CB electron transport is also substantially impaired. Hence this MTB is a considerable barrier to both charge-carrier types. On the basis of our findings, band bending of the VB and CB normal to the 1D line defects is proposed to be tunable through chemical or electrostatic gating.

METHODS

Samples were grown *in situ* in a preparation chamber with a base pressure $<5 \times 10^{-10}$ mbar connected to a 5 K bath cryostat STM system. Ir(111) was cleaned by cycles of 1.5 keV Ar^+ ion erosion and flash annealing to 1550 K. Gr was grown on top by room temperature ethylene exposure until saturation and subsequent thermal decomposition at 1370 K. The resulting well-oriented Gr islands were grown to a complete single crystal Gr layer through exposure to 2000 L ethylene at 1370 K.[62] MoS_2 was grown at 300 K on Gr/Ir(111) by Mo deposition with a flux of about 5×10^{15} atoms $m^{-2}\ s^{-1}$ in a background elemental sulfur pressure of about 1×10^{-8} mbar. Subsequently, the sample is annealed for 300 s at 1050 K in a S pressure of the same magnitude. Compare ref 10.

STM and STS measurements were performed at 5 K and pressures $<5 \times 10^{-11}$ mbar. STS was carried out with the lock-in technique, using a modulation frequency 777 Hz and modulation voltage $V_{\mathrm{mod}} = 4\ \mathrm{mV_{rms}}$. This yields an experimental resolution of ≈10 meV or better.[63] We used both constant height [recording $(\mathrm{d}I/\mathrm{d}V)_Z$] and constant current [$(\mathrm{d}I/\mathrm{d}V)_I$] STS, where I is the tunneling current, V the bias voltage, and Z the height of the tip above the sample. In both modes, $\mathrm{d}I/\mathrm{d}V$ is recorded while V is ramped. For further explanation, see ref 27. A linescan consists of a sequence of spectra taken at most 1 Å apart along a straight line. In each spectrum, data points are taken every 5−20 meV depending on the desired resolution. The path of the linescan may not be perfectly normal to the 1D defect, but the resulting error in x can be neglected; in the scan of Figure 1c, for example, this amounts to a factor $\cos(1.9°) = 0.999$. The color plots of the linescans show raw data; no interpolation or smoothing is involved.

All density functional theory calculations were carried out using the Vienna *Ab Initio* Simulation Package (VASP).[64,65] The plane wave cutoff was set to 400 eV throughout. The atomic structure for the ML-MoS_2 ribbon with MTB and unpassivated Mo-edges on Gr, as shown in Figure 5, was constructed as follows. While the strain in the direction perpendicular to the MTB ($\mathbf{a}_1$) is naturally released in the ribbon geometry, a suitable supercell needs to be constructed to release strain in the direction parallel to the MTB ($\mathbf{a}_2$). Because $3a$ of MoS_2 fairly closely matches with $4a$ of Gr, we used a MoS_2 layer consisting of $3 \times (12 + 12)$ unit cells (12 units in each side of the MTB) and a Gr layer consisting of 4×40 unit cells. The supercell is hexagonal, and thus the distance between the MTB and the edge of the ribbon is $6\sqrt{3}\,a \approx 33.3$ Å. The lattice constant of MoS_2 along $\mathbf{a}_2$ is fixed to that of pristine ML-MoS_2, which yields a Gr lattice constant 2.385 Å, not very far from the optimized value of 2.468 Å. The lattice constant of Gr along $\mathbf{a}_1$ is fixed to that of pristine Gr. The carbon atom z-coordinates are fixed to prevent buckling. We used the exchange-correlation functional of Perdew, Burke, and Ernzerhof (PBE),[66] augmented with Grimme's corrections (−D2) for the van der Waals interactions.[67] A $4 \times 1 \times 1$ k-point mesh was used during ionic relaxation. The density of states is evaluated with a 12×1 mesh, *i.e.*, corresponding to a 36×1 mesh for MoS_2 ribbon and 48×40 for Gr.

ASSOCIATED CONTENT

Supporting Information

The Supporting Information is available free of charge at https://pubs.acs.org/doi/10.1021/acsnano.0c04945.

> Supplementary STM/STS measurements of 4|4P and 4|4E MTBs, an explanation of the analysis of quantized state locations, an example of VB quantization occurring at a tilt-angle GB, charged wire modeling used to estimate the net linear charge of 1D defects in a freestanding MoS_2 layer, additional DFT calculations of the 4|4E MTB, and fit values resulting from the electrostatic continuum model (PDF)

AUTHOR INFORMATION

Corresponding Author

Clifford Murray − *II. Physikalisches Institut, Universität zu Köln, Cologne D-50937, Germany;* orcid.org/0000-0002-5618-0915; Email: murray@ph2.uni-koeln.de

Authors

Camiel van Efferen − *II. Physikalisches Institut, Universität zu Köln, Cologne D-50937, Germany*

Wouter Jolie − *II. Physikalisches Institut, Universität zu Köln, Cologne D-50937, Germany; Institut für Materialphysik, Westfälische Wilhelms-Universität Münster, Münster D-48149, Germany*

Jeison Antonio Fischer − *II. Physikalisches Institut, Universität zu Köln, Cologne D-50937, Germany*

Joshua Hall − *II. Physikalisches Institut, Universität zu Köln, Cologne D-50937, Germany;* orcid.org/0000-0002-7009-5602

Achim Rosch − *Institut für Theoretische Physik, Universität zu Köln, Cologne D-50937, Germany*

Arkady V. Krasheninnikov − *Institute of Ion Beam Physics and Materials Research, Helmholtz-Zentrum Dresden-Rossendorf, Dresden D-01328, Germany; Department of Applied Physics, Aalto University School of Science, Aalto FI-00076, Finland;* orcid.org/0000-0003-0074-7588

Hannu-Pekka Komsa − *Department of Applied Physics, Aalto University School of Science, Aalto FI-00076, Finland; Microelectronics Research Unit, University of Oulu, Oulu FI-90014, Finland;* orcid.org/0000-0002-0970-0957

Thomas Michely − *II. Physikalisches Institut, Universität zu Köln, Cologne D-50937, Germany*

Complete contact information is available at:
https://pubs.acs.org/10.1021/acsnano.0c04945

Notes

The authors declare no competing financial interest.

ACKNOWLEDGMENTS

This work was funded by the Deutsche Forschungsgemeinschaft (DFG, German Research Foundation), CRC 1238 (project no. 277146847, subprojects A01, B06, and C02). Support from the German Academic Exchange Service DAAD via PPP Finland "MODEST", project ID 57458732 is gratefully acknowledged. H.P.K. acknowledges financial support from the Academy of Finland through project no. 311058 and CSC-IT Center for Science Ltd. for generous grants of computer time. A.V.K. acknowledges funding from DFG through project KR 48661-2 (406129719). We thank Carsten Busse and Mahdi Ghorbani-Asl for useful discussions.

REFERENCES

(1) Van Der Zande, A. M.; Huang, P. Y.; Chenet, D. A.; Berkelbach, T. C.; You, Y.; Lee, G. H.; Heinz, T. F.; Reichman, D. R.; Muller, D. A.; Hone, J. C. Grains and Grain Boundaries in Highly Crystalline Monolayer Molybdenum Disulphide. *Nat. Mater.* **2013**, *12*, 554−561.

(2) Najmaei, S.; Amani, M.; Chin, M. L.; Liu, Z.; Birdwell, A. G.; O'Regan, T. P.; Ajayan, P. M.; Dubey, M.; Lou, J. Electrical Transport Properties of Polycrystalline Monolayer Molybdenum Disulfide. *ACS Nano* **2014**, *8*, 7930−7937.

(3) Du, L.; Yu, H.; Xie, L.; Wu, S.; Wang, S.; Lu, X.; Liao, M.; Meng, J.; Zhao, J.; Zhang, J.; Zhu, J.; Chen, P.; Wang, G.; Yang, R.; Shi, D.; Zhang, G. The Effect of Twin Grain Boundary Tuned by Temperature on the Electrical Transport Properties of Monolayer MoS_2. *Crystals* **2016**, *6*, 115.

(4) Ly, T. H.; Perello, D. J.; Zhao, J.; Deng, Q.; Kim, H.; Han, G. H.; Chae, S. H.; Jeong, H. Y.; Lee, Y. H. Misorientation-Angle-Dependent Electrical Transport across Molybdenum Disulfide Grain Boundaries. *Nat. Commun.* **2016**, *7*, 10426.

(5) Kimoto, T. Material Science and Device Physics in SiC Technology for High-Voltage Power Devices. *Jpn. J. Appl. Phys.* **2015**, *54*, 040103.

(6) Skowronski, M.; Ha, S. Degradation of Hexagonal Silicon-Carbide-Based Bipolar Devices. *J. Appl. Phys.* **2006**, *99*, 011101.

(7) Huang, Y. L.; Chen, Y.; Zhang, W.; Quek, S. Y.; Chen, C.-H.; Li, L.-J.; Hsu, W.-T.; Chang, W.-H.; Zheng, Y. J.; Chen, W.; Wee, A. T. S. Bandgap Tunability at Single-Layer Molybdenum Disulphide Grain Boundaries. *Nat. Commun.* **2015**, *6*, 6298.

(8) Wang, D.; Yu, H.; Tao, L.; Xiao, W.; Fan, P.; Zhang, T.; Liao, M.; Guo, W.; Shi, D.; Du, S.; Zhang, G.; Gao, H. Bandgap Broadening at Grain Boundaries in Single-Layer MoS_2. *Nano Res.* **2018**, *11*, 6102−6109.

(9) Yan, C.; Dong, X.; Li, C. H.; Li, L. Charging Effect at Grain Boundaries of MoS_2. *Nanotechnology* **2018**, *29*, 195704.

(10) Liu, X.; Balla, I.; Bergeron, H.; Hersam, M. C. Point Defects and Grain Boundaries in Rotationally Commensurate MoS_2 on Epitaxial Graphene. *J. Phys. Chem. C* **2016**, *120*, 20798−20805.

(11) Precner, M.; Polaković, T.; Qiao, Q.; Trainer, D. J.; Putilov, A. V.; Di Giorgio, C.; Cone, I.; Zhu, Y.; Xi, X. X.; Iavarone, M.; Karapetrov, G. Evolution of Metastable Defects and Its Effect on the Electronic Properties of MoS_2 Films. *Sci. Rep.* **2018**, *8*, 6724.

(12) Zhang, C.; Johnson, A.; Hsu, C.-L.; Li, L..-.; Yao, W..; Tersoff, J..; Shih, C.-K. Direct Imaging of Band Profile in Single Layer MoS_2 on Graphite: Quasiparticle Energy Gap, Metallic Edge States, and Edge Band Bending. *Nano Lett.* **2014**, *14*, 2443−2447.

(13) Zhang, C.; Chen, Y.; Huang, J.-K.; Wu, X.; Li, L.-J.; Yao, W.; Tersoff, J.; Shih, C.-K. Visualizing Band Offsets and Edge States in Bilayer-Monolayer Transition Metal Dichalcogenides Lateral Heterojunction. *Nat. Commun.* **2016**, *7*, 10349.

(14) Le Quang, T.; Nogajewski, K.; Potemski, M.; Dau, M. T.; Jamet, M.; Mallet, P.; Veuillen, J.-Y. Band-Bending Induced by Charged Defects and Edges of Atomically Thin Transition Metal Dichalcogenide Films. *2D Mater.* **2018**, *5*, 035034.

(15) Kobayashi, Y.; Yoshida, S.; Sakurada, R.; Takashima, K.; Yamamoto, T.; Saito, T.; Konabe, S.; Taniguchi, T.; Watanabe, K.; Maniwa, Y.; Takeuchi, O.; Shigekawa, H.; Miyata, Y. Modulation of Electrical Potential and Conductivity in an Atomic-Layer Semiconductor Heterojunction. *Sci. Rep.* **2016**, *6*, 31223.

(16) Zhang, C.; Li, M.-Y.; Tersoff, J.; Han, Y.; Su, Y.; Li, L.-J.; Muller, D. A.; Shih, C.-K. Strain Distributions and Their Influence on Electronic Structures of WSe_2-MoS_2 Laterally Strained Heterojunctions. *Nat. Nanotechnol.* **2018**, *13*, 152−158.

(17) Ma, Y.; Kolekar, S.; Coy Diaz, H.; Aprojanz, J.; Miccoli, I.; Tegenkamp, C.; Batzill, M. Metallic Twin Grain Boundaries Embedded in $MoSe_2$ Monolayers Grown by Molecular Beam Epitaxy. *ACS Nano* **2017**, *11*, 5130−5139.

(18) Kaneko, T.; Saito, R. Origin of Band Bending at Domain Boundaries of MoS_2: First-Principles Study. *Jpn. J. Appl. Phys.* **2018**, *57*, 04FP09.

(19) Hall, J.; Pielić, B.; Murray, C.; Jolie, W.; Wekking, T.; Busse, C.; Kralj, M.; Michely, T. Molecular Beam Epitaxy of Quasi-Freestanding Transition Metal Disulphide Monolayers on van der Waals Substrates: A Growth Study. *2D Mater.* **2018**, *5*, 025005.

(20) Coraux, J.; N'Diaye, A. T.; Busse, C.; Michely, T. Structural Coherency of Graphene on Ir(111). *Nano Lett.* **2008**, *8*, 565−570.

(21) Komsa, H.-P.; Krasheninnikov, A. V. Engineering the Electronic Properties of Two-Dimensional Transition Metal Dichalcogenides by Introducing Mirror Twin Boundaries. *Adv. Electron. Mater.* **2017**, *3*, 1600468.

(22) Jolie, W.; Murray, C.; Weiß, P. S.; Hall, J.; Portner, F.; Atodiresei, N.; Krasheninnikov, A. V.; Busse, C.; Komsa, H.-P.; Rosch, A.; Michely, T. Tomonaga-Luttinger Liquid in a Box: Electrons Confined within MoS_2 Mirror-Twin Boundaries. *Phys. Rev. X* **2019**, *9*, 011055.

(23) Zhou, W.; Zou, X.; Najmaei, S.; Liu, Z.; Shi, Y.; Kong, J.; Lou, J.; Ajayan, P. M.; Yakobson, B. I.; Idrobo, J.-C. Intrinsic Structural Defects in Monolayer Molybdenum Disulfide. *Nano Lett.* **2013**, *13*, 2615−2622.

(24) Zou, X.; Liu, Y.; Yakobson, B. I. Predicting Dislocations and Grain Boundaries in Two-Dimensional Metal-Disulfides from the First Principles. *Nano Lett.* **2013**, *13*, 253−258.

(25) Zou, X.; Yakobson, B. I. Metallic High-Angle Grain Boundaries in Monolayer Polycrystalline WS_2. *Small* **2015**, *11*, 4503−4507.

(26) Batzill, M. Mirror Twin Grain Boundaries in Molybdenum Dichalcogenides. *J. Phys.: Condens. Matter* **2018**, *30*, 493001.

(27) Murray, C.; Jolie, W.; Fischer, J. A.; Hall, J.; van Efferen, C.; Ehlen, N.; Grüneis, A.; Busse, C.; Michely, T. Comprehensive Tunneling Spectroscopy of Quasifreestanding MoS_2 on Graphene on Ir(111). *Phys. Rev. B: Condens. Matter Mater. Phys.* **2019**, *99*, 115434.

(28) Yu, H.; Kutana, A.; Yakobson, B. I. Carrier Delocalization in Two-Dimensional Coplanar *p-n* Junctions of Graphene and Metal Dichalcogenides. *Nano Lett.* **2016**, *16*, 5032−5036.

(29) Zhang, C.; Chen, Y.; Johnson, A.; Li, M.-Y.; Li, L.-J.; Mende, P. C.; Feenstra, R. M.; Shih, C.-K. Probing Critical Point Energies of Transition Metal Dichalcogenides: Surprising Indirect Gap of Single Layer WSe_2. *Nano Lett.* **2015**, *15*, 6494−6500.

(30) Stroscio, J. A.; Kaiser, W. J. *Scanning Tunneling Microscopy*, 27th ed.; Academic Press: San Diego, 1993; pp 102−147.

(31) Zhang, C.; Wang, H.; Chan, W.; Manolatou, C.; Rana, F. Absorption of Light by Excitons and Trions in Monolayers of Metal Dichalcogenide MoS_2: Experiments and Theory. *Phys. Rev. B: Condens. Matter Mater. Phys.* **2014**, *89*, 205436.

(32) Vanderbilt, D.; King-Smith, R. D. Electric Polarization as a Bulk Quantity and Its Relation to Surface Charge. *Phys. Rev. B: Condens. Matter Mater. Phys.* **1993**, *48*, 4442−4455.

(33) Gibertini, M.; Marzari, N. Emergence of One-Dimensional Wires of Free Carriers in Transition-Metal-Dichalcogenide Nanostructures. *Nano Lett.* **2015**, *15*, 6229−6238.

(34) Henkelman, G.; Arnaldsson, A.; Jónsson, H. A Fast and Robust Algorithm for Bader Decomposition of Charge Density. *Comput. Mater. Sci.* **2006**, *36*, 354−360.

(35) Khomyakov, P. A.; Giovannetti, G.; Rusu, P. C.; Brocks, G.; van den Brink, J.; Kelly, P. J. First-Principles Study of the Interaction and Charge Transfer between Graphene and Metals. *Phys. Rev. B: Condens. Matter Mater. Phys.* **2009**, *79*, 195425.

(36) Yu, Y.-J.; Zhao, Y.; Ryu, S.; Brus, L. E.; Kim, K. S.; Kim, P. Tuning the Graphene Work Function by Electric Field Effect. *Nano Lett.* **2009**, *9*, 3430−3434.

(37) Zhong, H.; Quhe, R.; Wang, Y.; Ni, Z.; Ye, M.; Song, Z.; Pan, Y.; Yang, J.; Yang, L.; Lei, M.; Shi, J.; Lu, J. Interfacial Properties of Monolayer and Bilayer MoS_2 Contacts with Metals: Beyond the Energy Band Calculations. *Sci. Rep.* **2016**, *6*, 21786.

(38) Choi, S.; Shaolin, Z.; Yang, W. Layer-Number-Dependent Work Function of MoS_2 Nanoflakes. *J. Korean Phys. Soc.* **2014**, *64*, 1550−1555.

(39) Zhao, X.; Ding, Z.; Chen, J.; Dan, J.; Poh, S. M.; Fu, W.; Pennycook, S. J.; Zhou, W.; Loh, K. P. Strain Modulation by van der Waals Coupling in Bilayer Transition Metal Dichalcogenide. *ACS Nano* **2018**, *12*, 1940−1948.

(40) Nalin Mehta, A.; Mo, J.; Pourtois, G.; Dabral, A.; Groven, B.; Bender, H.; Favia, P.; Caymax, M.; Vandervorst, W. Grain-Boundary-Induced Strain and Distortion in Epitaxial Bilayer MoS_2 Lattice. *J. Phys. Chem. C* **2020**, *124*, 6472−6478.

(41) Peelaers, H.; Van de Walle, C. G. Effects of Strain on Band Structure and Effective Masses in MoS_2. *Phys. Rev. B: Condens. Matter Mater. Phys.* **2012**, *86*, 241401.

(42) Yu, S.; Xiong, H. D.; Eshun, K.; Yuan, H.; Li, Q. Phase Transition, Effective Mass and Carrier Mobility of MoS_2 Monolayer under Tensile Strain. *Appl. Surf. Sci.* **2015**, *325*, 27−32.

(43) Ehlen, N.; Hall, J.; Senkovskiy, B. V.; Hell, M.; Li, J.; Herman, A.; Smirnov, D.; Fedorov, A.; Yu Voroshnin, V.; Di Santo, G.; Petaccia, L.; Michely, T.; Grüneis, A. Narrow Photoluminescence and Raman Peaks of Epitaxial MoS_2 on Graphene/Ir(111). *2D Mater.* **2019**, *6*, 011006.

(44) Pletikosić, I.; Kralj, M.; Pervan, P.; Brako, R.; Coraux, J.; N'Diaye, A. T.; Busse, C.; Michely, T. Dirac Cones and Minigaps for Graphene on Ir(111). *Phys. Rev. Lett.* **2009**, *102*, 056808.

(45) Laturia, A.; Van de Put, M. L.; Vandenberghe, W. G. Dielectric Properties of Hexagonal Boron Nitride and Transition Metal Dichalcogenides: From Monolayer to Bulk. *npj 2D Mater. Appl.* **2018**, *2*, 6.

(46) Qiu, B.; Zhao, X.; Hu, G.; Yue, W.; Ren, J.; Yuan, X. Optical Properties of Graphene/MoS_2 Heterostructure: First Principles Calculations. *Nanomaterials* **2018**, *8*, 962.

(47) Schumacher, S.; Wehling, T. O.; Lazić, P.; Runte, S.; Förster, D. F.; Busse, C.; Petrović, M.; Kralj, M.; Blügel, S.; Atodiresei, N.; Caciuc, V.; Michely, T. The Backside of Graphene: Manipulating Adsorption by Intercalation. *Nano Lett.* **2013**, *13*, 5013−5019.

(48) Schröder, U. A.; Petrović, M.; Gerber, T.; Martínez-Galera, A. J.; GrÅnäs, E.; Arman, M. A.; Herbig, C.; Schnadt, J.; Kralj, M.; Knudsen, J.; Michely, T. Core Level Shifts of Intercalated Graphene. *2D Mater.* **2017**, *4*, 015013.

(49) Pulkin, A.; Yazyev, O. V. Spin- and Valley-Polarized Transport across Line Defects in Monolayer MoS_2. *Phys. Rev. B: Condens. Matter Mater. Phys.* **2016**, *93*, 041419.

(50) Park, J.; Xue, K.-H.; Mouis, M.; Triozon, F.; Cresti, A. Electron Transport Properties of Mirror Twin Grain Boundaries in Molybdenum Disulfide: Impact of Disorder. *Phys. Rev. B: Condens. Matter Mater. Phys.* **2019**, *100*, 235403.

(51) Ohtomo, A.; Hwang, H. Y. A High-Mobility Electron Gas at the $LaAlO_3/SrTiO_3$ Heterointerface. *Nature* **2004**, *427*, 423−426.

(52) Gibertini, M.; Pizzi, G.; Marzari, N. Engineering Polar Discontinuities in Honeycomb Lattices. *Nat. Commun.* **2014**, *5*, 5157.

(53) Martinez-Gordillo, R.; Pruneda, M. Polar Discontinuities and 1D Interfaces in Monolayered Materials. *Prog. Surf. Sci.* **2015**, *90*, 444−463.

(54) Park, J.; Lee, J.; Liu, L.; Clark, K. W.; Durand, C.; Park, C.; Sumpter, B. G.; Baddorf, A. P.; Mohsin, A.; Yoon, M.; Gu, G.; Li, A.-P. Spatially Resolved One-Dimensional Boundary States in Graphene-Hexagonal Boron Nitride Planar Heterostructures. *Nat. Commun.* **2014**, *5*, 5403.

(55) Mannhart, J.; Schlom, D. G. Oxide Interfaces - An Opportunity for Electronics. *Science* **2010**, *327*, 1607−1611.

(56) Pai, Y.-Y.; Tylan-Tyler, A.; Irvin, P.; Levy, J. Physics of $SrTiO_3$-Based Heterostructures and Nanostructures: A Review. *Rep. Prog. Phys.* **2018**, *81*, 036503.

(57) Feng, J.; Qian, X.; Huang, C. W.; Li, J. Strain-Engineered Artificial Atom as a Broad-Spectrum Solar Energy Funnel. *Nat. Photonics* **2012**, *6*, 866−872.

(58) Branny, A.; Kumar, S.; Proux, R.; Gerardot, B. D. Deterministic Strain-Induced Arrays of Quantum Emitters in a Two-Dimensional Semiconductor. *Nat. Commun.* **2017**, *8*, 15053.

(59) Carozo, V.; Wang, Y.; Fujisawa, K.; Carvalho, B. R.; McCreary, A.; Feng, S.; Lin, Z.; Zhou, C.; Perea-López, N.; Elías, A. L.; Kabius, B.; Crespi, V. H.; Terrones, M. Optical Identification of Sulfur

Vacancies: Bound Excitons at the Edges of Monolayer Tungsten Disulfide. *Sci. Adv.* **2017**, *3*, No. e1602813.

(60) Dubey, S.; Lisi, S.; Nayak, G.; Herziger, F.; Nguyen, V. D.; Le Quang, T.; Cherkez, V.; González, C.; Dappe, Y. J.; Watanabe, K.; Taniguchi, T.; Magaud, L.; Mallet, P.; Veuillen, J. Y.; Arenal, R.; Marty, L.; Renard, J.; Bendiab, N.; Coraux, J.; Bouchiat, V. Weakly Trapped, Charged, and Free Excitons in Single-Layer MoS_2 in the Presence of Defects, Strain, and Charged Impurities. *ACS Nano* **2017**, *11*, 11206−11216.

(61) Zheng, Y. J.; Chen, Y.; Huang, Y. L.; Gogoi, P. K.; Li, M. Y.; Li, L. J.; Trevisanutto, P. E.; Wang, Q.; Pennycook, S. J.; Wee, A. T.; Quek, S. Y. Point Defects and Localized Excitons in 2D WSe_2. *ACS Nano* **2019**, *13*, 6050−6059.

(62) van Gastel, R.; N'Diaye, A. T.; Wall, D.; Coraux, J.; Busse, C.; Buckanie, N. M.; Meyer zu Heringdorf, F.-J.; Horn von Hoegen, M.; Michely, T.; Poelsema, B. Selecting a Single Orientation for Millimeter Sized Graphene Sheets. *Appl. Phys. Lett.* **2009**, *95*, 121901.

(63) Morgenstern, M. Probing the Local Density of States of Dilute Electron Systems in Different Dimensions. *Surf. Rev. Lett.* **2003**, *10*, 933−962.

(64) Kresse, G.; Hafner, J. *Ab Initio* Molecular Dynamics for Open-Shell Transition Metals. *Phys. Rev. B: Condens. Matter Mater. Phys.* **1993**, *48*, 13115−13118.

(65) Kresse, G.; Furthmüller, J. Efficiency of *Ab-Initio* Total Energy Calculations for Metals and Semiconductors Using a Plane-Wave Basis Set. *Comput. Mater. Sci.* **1996**, *6*, 15−50.

(66) Perdew, J. P.; Burke, K.; Ernzerhof, M. Generalized Gradient Approximation Made Simple. *Phys. Rev. Lett.* **1996**, *77*, 3865−3868.

(67) Grimme, S. Semiempirical GGA-Type Density Functional Constructed with a Long-Range Dispersion Correction. *J. Comput. Chem.* **2006**, *27*, 1787−1799.

7.1 Manuscript 3: Supporting Information

Supporting Information: Band Bending and Valence Band Quantization at Line Defects in MoS_2

Clifford Murray,[*,†] Camiel van Efferen,[†] Wouter Jolie,[†,‡] Jeison Antonio Fischer,[†] Joshua Hall,[†] Achim Rosch,[¶] Arkady V. Krasheninnikov,[§,‖] Hannu-Pekka Komsa,[‖,⊥] and Thomas Michely[†]

†*II. Physikalisches Institut, Universität zu Köln, Cologne D-50937, Germany*

‡*Institut für Materialphysik, Westfälische Wilhelms-Universität Münster, Münster D-48149, Germany*

¶*Institut für Theoretische Physik, Universität zu Köln, Cologne D-50937, Germany*

§*Institute of Ion Beam Physics and Materials Research, Helmholtz-Zentrum Dresden-Rossendorf, Dresden D-01328, Germany*

‖*Department of Applied Physics, Aalto University School of Science, Aalto FI-00076, Finland*

⊥*Microelectronics Research Unit, University of Oulu, Oulu FI-90014, Finland*

E-mail: murray@ph2.uni-koeln.de

Supporting Information Available

The Supporting Information includes supplementary scanning tunneling microscopy/spectroscopy (STM/STS) measurements of 4|4P and 4|4E mirror twin boundaries (MTBs), an explanation of the analysis of quantized state locations, an example of valence band (VB) quantization occurring at a tilt-angle grain boundary (GB), charged wire modeling used to estimate the net linear charge of 1D defects in a freestanding MoS_2 layer, additional density functional theory (DFT) calculations of the 4|4E MTB, and fit values resulting from the electrostatic continuum model.

Supplement to Fig. 1d

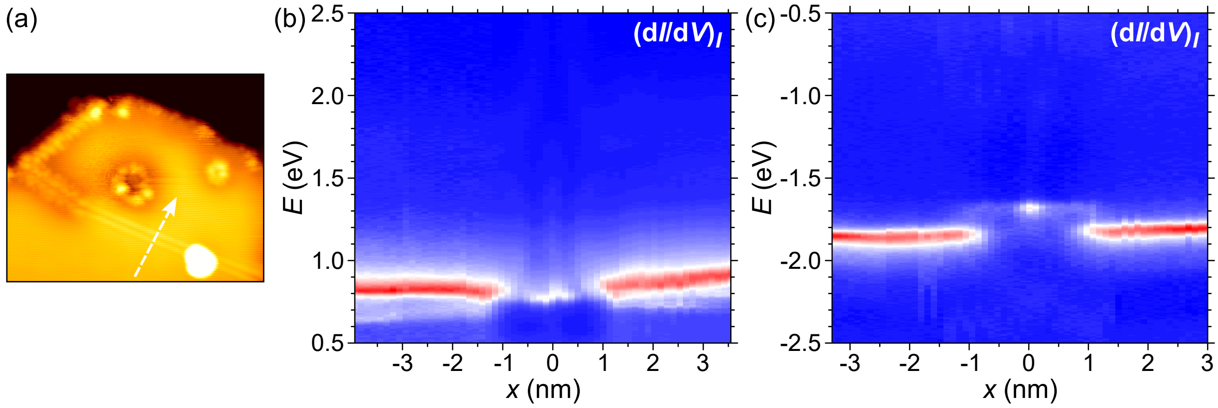

Figure S1: Supplementary linescans of the 4|4P-type MTB shown in Figure 1 of the main text. (a) Constant current STM topograph of 4|4P MTB as described in main text. (b,c) Constant current STS linescans of the conduction and valence bands, respectively, acquired orthogonal to the 4|4P MTB as indicated by the dashed white arrow of (a). Linear color scale as in Figure 2. STM/STS parameters: (a) $V = 1.0\,\mathrm{V}$, $I = 100\,\mathrm{pA}$, image size $19 \times 15\,\mathrm{nm}^2$; (b) $V_{\mathrm{st}} = 2.5\,\mathrm{V}$; (c) $V_{\mathrm{st}} = -2.5\,\mathrm{V}$; (b,c) $I_{\mathrm{st}} = 50\,\mathrm{pA}$.

Figure S1 shows that very little band bending is observed at 4|4P MTBs in constant current STS linescans, as in constant height STS (Figure 1d main text). At the right-hand extreme of the linescans ($x \approx 3\,\mathrm{nm}$) some upwards bending occurs due to the edges of a nearby hole in the MoS_2 island. In Figure S1c an in-gap occupied state is observed at the 4|4P MTB. It should be noted that performing STS linescans over 4|4P-type MTBs was far more challenging than over 4|4E MTBs, and often resulted in disruptive changes to the tip apex directly over the MTB. The reasons for this are not clear.

Supplement to Fig. 2

Supplementary STM/STS

Figure S2 shows the location topograph and accompanying constant height STS linescan to Figure 2a,b of the main text. The measured 4|4E-type MTB ends in a kink, after which another 4|4E MTB begins. Note that by normalizing constant height STS linescans we obtain something similar to what is obtained in constant current STS,[S1] and the VB quantization at the MTB can be made visible.

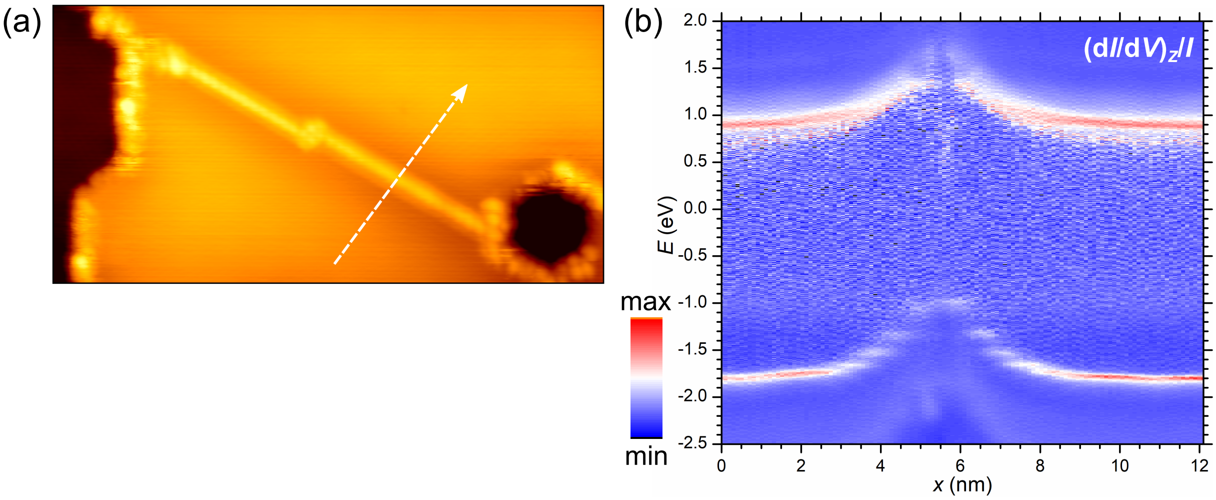

Figure S2: Supplementary data to Figure 2a,b of the main text. (a) Constant current STM topograph showing the 4|4E-type MTB in ML-MoS_2 on Gr/Ir(111), across which the linescans of Figure 2a,b (main text) were performed. The path of the linescans is indicated by a dashed white arrow. (b) Constant height STS linescan acquired along the dashed white arrow of (a). Linear color scale as in Figure 2. For demonstrative purposes, the linescan spectra have been normalized through division by the simultaneously recorded tunneling current. STM/STS parameters: (a) $V = 0.9\,\mathrm{V}$, $I = 80\,\mathrm{pA}$, image size $30 \times 15\,\mathrm{nm}^2$; (b) $V_{\mathrm{st}} = -2.5\,\mathrm{V}$, $I_{\mathrm{st}} = 200\,\mathrm{pA}$.

Statistical distribution of quantized VB states at 4|4E MTBs

Figure 2c (main text) shows the distribution (in E and x) of 20 sets of quantized VB states at 4|4E MTBs, measured with various tips and tunneling conditions, with mean values and associated errors of each state given. These values are tested against the model in the main text, see Figure 7. Consider a VB constant current STS scan over a 4|4E MTB (*e.g.*

Figure 2b). The E of the intensity maxima can simply be read off. The MTB itself is not visible however, making x difficult to define. Therefore we assume the MTB to be midway between the each maxima pair on either side. For this reason we obtain only 10 sets of x values from 20 sets of states. A larger error is associated with the $n = 4, 5$ states because they tend to 'smear' into each other and the relaxed band edge.

Valence band quantization at a tilt grain boundary

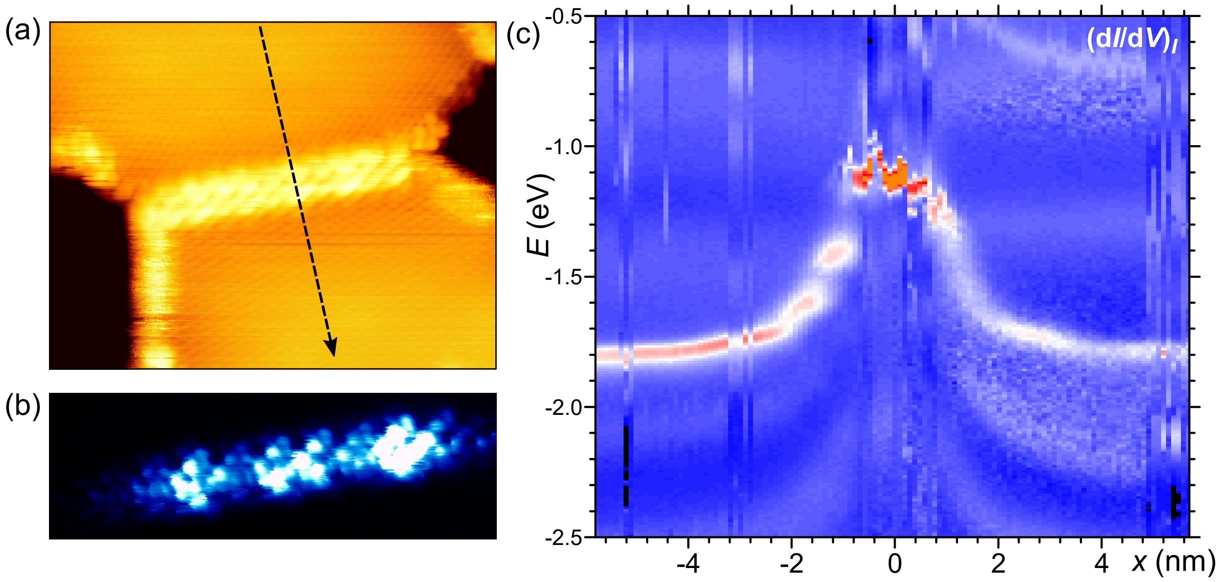

Figure S3: Band bending at a tilt GB in ML-MoS$_2$. (a) Constant current STM topograph showing a $\sim 21°$-tilt GB. (b) Constant height STM topograph of the same GB showing its (unoccupied) in-gap states. (c) Constant current STS linescan of the VB, acquired along the dashed white arrow in (a). Linear color scale as in Figure 2. STM/STS parameters: (a) $V = 0.9\,\mathrm{V}$, $I = 100\,\mathrm{pA}$, image size $15 \times 12\,\mathrm{nm}^2$; (b) $V = 0.3\,\mathrm{V}$, $I = 50\,\mathrm{pA}$, image size $9 \times 3\,\mathrm{nm}^2$; (c) $V_{\mathrm{st}} = -2.5\,\mathrm{V}$, $I_{\mathrm{st}} = 50\,\mathrm{pA}$.

In the STM topograph of Figure S3a a tilt grain boundary (GB) in ML-MoS$_2$ is shown. Atomic resolution is faintly visible; through examination of topographs in which it is better visible, a misorientation angle of $\sim 21°$ between the grains is found. A constant height STM topograph is recorded over the tilt GB, Figure S3b, at a voltage (energy) inside the 'bulk' ML-MoS$_2$ band gap. The boundary's in-gap states are different to those of 4|4E or 4|4P MTBs,[S2] confirming that this is indeed another type of boundary. A constant current STS scan performed orthogonal to the GB, Figure S3c, shows large bending of the VB similar to that seen at 4|4E MTBs and island edges. Although the STS tip is unstable, quantized VB states are evident at $\approx -1.41\,\text{eV}$ and $\approx -1.60\,\text{eV}$ on one side of the GB. On the other side, the bending does not appear discretized; it is rather smooth. We would surmise that the different bending behaviours are due to the respective misorientations either side of the GB. The charge carriers impinging normal to the GB will be of different wavevector and thus scatter differently at the GB.

Defect charge in freestanding 4|4E ribbon

The charges at the 4|4E MTB and at the edges of a freestanding ML-MoS$_2$ ribbon are extracted using a simple electrostatic model. Following Ref. S3, the MoS$_2$ layer is described by a sheet of thickness d and effective dielectric constant $\epsilon_2 = \sqrt{\epsilon_\perp \epsilon_{||}}$, where $d = 6.22$ Å, $\epsilon_\perp = 6.17$, and $\epsilon_{||} = 15.28$ are extracted from a DFT calculation at the PBE level. The sheet is embedded from above and below by media described by dielectric constants ϵ_1 and ϵ_3. The potential at the center of the sheet can be solved easily in Fourier space from $V(q) = \frac{2\pi e}{|q|\epsilon(q)}\rho(q)$, where $\rho(q)$ is the Fourier transform of the model charge distribution and $\epsilon(q)$ is given in Eq. (A1) of Ref. S3. We use a 2D grid with the dimensions extracted from the DFT supercell calculation and grid spacing of about $0.5a_0$. The charge distribution is modeled using three wires, infinite along the ribbon and Gaussian distribution of variance $2a_0$ in the direction perpendicular to the MTB. These wire charges are varied until the potential matches that from the DFT calculation (as shown in Figure 5b).

Figure S4a shows the potentials from DFT and from the 'three wire model'. Good agreement between the two is obtained when the MTB charge is $\lambda \approx 0.05\,e/a$, shown in Figure S4b. The edge charges are $-\lambda/2$, which yields a charge neutral cell. It is also worth noting that the potential is very straight, *i.e.*, there is little bending. The results are not sensitive to the thickness of the sheet as long the dielectric constant is renormalized properly.

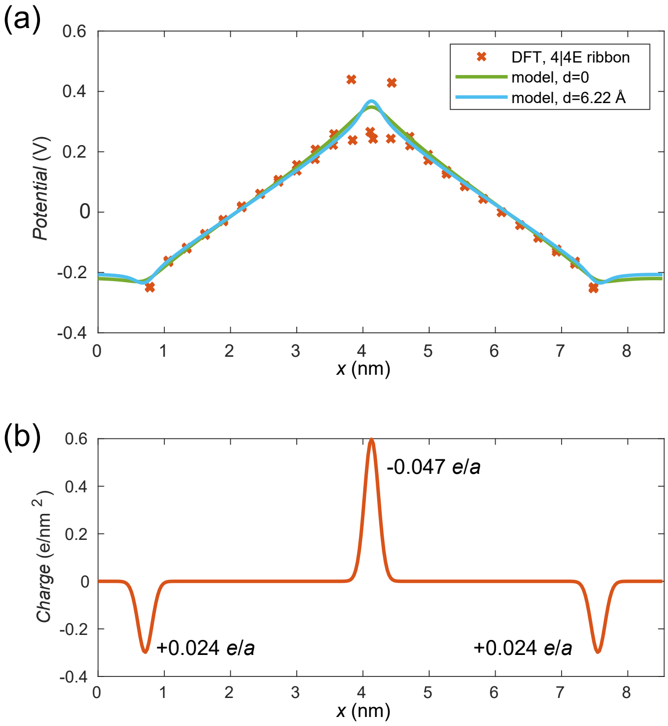

Figure S4: Estimating the charge of 4|4E MTB and edges in freestanding ML-MoS$_2$. (a) S-atom core potentials from DFT [Figure 5b] compared with the potential due to three parallel wires placed at the locations corresponding to edge, 4|4E MTB, and edge for a purely 2D model (green) or for a model with finite sheet thickness $d = 6.22\,\text{Å}$ (blue). (b) The areal charge density corresponding to (a). Linear charge densities λ, *i.e.* integrated over each wire, are also indicated.

Supplementary DFT ribbon calculations to Fig. 5

Graphene LDOS

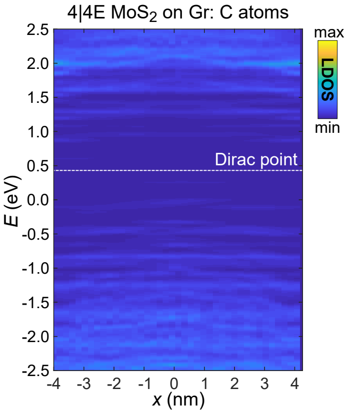

Figure S5: Additional to DFT calculation of band bending at 4|4E MTBs in ML-MoS$_2$ on Gr: projected LDOS of C atoms (in the Gr ribbon) perpendicular to the 4|4E MTB plane. See geometry in Figure 5a of main text. The energy of the Gr Dirac point in this configuration is indicated.

Figure S5 shows the projected LDOS of the underlying C atoms in the 4|4E MoS$_2$/Gr DFT geometry (Figure 5a). The Gr LDOS shows very little variation, indicating that the MoS$_2$ band bending is not due to a spatially varying substrate potential. The indicated Dirac point position is $\approx 0.4\,\mathrm{eV}$ above the Fermi level. The Dirac point of freestanding Gr is at $0\,\mathrm{eV}$ in our DFT calculation. Thus the addition of ML-MoS$_2$ represents p-doping of Gr, consistent with charge transfer to the MoS$_2$.

Asymmetrically-positioned 4|4E MTB

Figure S6 shows additional DFT calculations, similar to Figure 5 of the main text but with the 4|4E MTB placed to one side of the supercell, as seen in Figure S6a. Due to the supercell's limited length in x, the 'bulk' MoS$_2$ region is never far away enough ($\approx 5\,\mathrm{nm}$) from a 1D defect to completely negate its bending effect. Here the situation is improved on the left side of the cell. Comparing the projected LDOS of states for S atoms in this configuration (Figure S6b) with those of the centred MTB (Figure 5f), we see that the bending is indeed

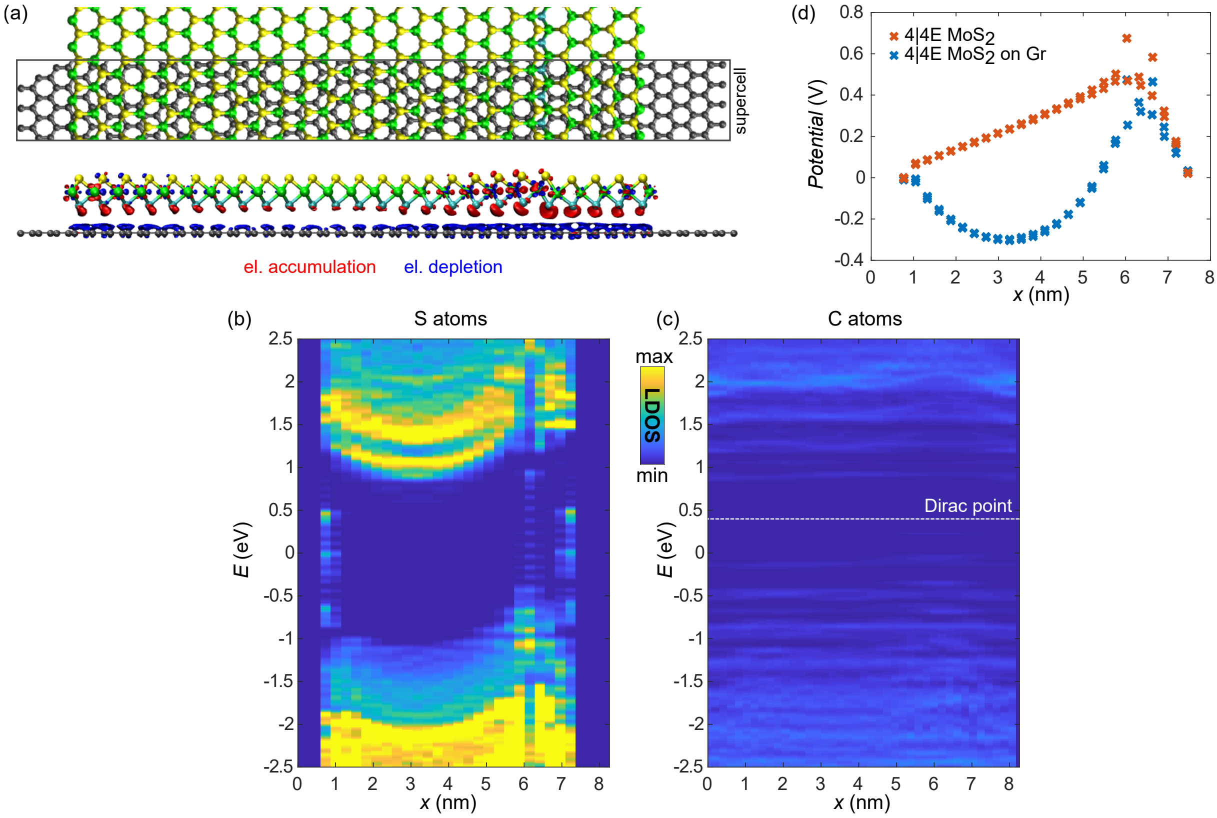

Figure S6: DFT calculation of band bending at a 4|4E MTB placed off-centre in the ML-MoS_2 on Gr supercell, compare Figure 5 of main text. (a) DFT geometry in top and side view. In top view the MoS_2 section is also shown isolated, for clarity only. In the side view charge distribution isosurfaces are shown (b,c) Projected LDOS for S and C atoms, respectively, perpendicular to the 4|4E MTB in the geometry of (a). (d) Atomic potentials for S atoms perpendicular to the 4|4E MTB in the geometry of (a), blue crosses, and for a freestanding MoS_2 ribbon [otherwise identical to (a)], red crosses.

larger here. Note that the bands do not bend up to a higher absolute energy, but rather the 'bulk' ML-MoS_2 bands reach a lower energy in between, as they are further from the charged defects. To the right of the MTB the electronic behaviour is totally different, due to the very close proximity of charged MTB and edge regions. This can be compared conceptually to the scenario in Figure 2a,b, in which the VB states were strongly perturbed by a vacancy island on one side of the MTB only. Figure S6c again confirms that there is little variation in the Gr bands. In the S-atom core potentials for the MoS_2/Gr geometry, blue crosses of Figure S6d, the larger absolute bending is evident. In the freestanding MoS_2 ribbon, red crosses, it is apparent that the inter-defect charge exchange is not distance dependent.

Values from screened electrostatic modeling

Table S1 compares the energy levels and spatial locations of the quantized VB maxima at 4|4E MTBs from experiment (as given in Figure 2c) and from our screened electrostatic continuum model (Figure 7). The potential is created with the physically realistic parameters $\epsilon_{\mathrm{di}} = 6.2$, $b = 1.2\,\mathrm{nm}$, $d = 0.31\,\mathrm{nm}$ $\lambda_{\mathrm{MTB}} = -0.29\,e/a = -0.92\,e/\mathrm{nm}$, and $C = -0.55\,\mathrm{eV}$, with a 0.8 nm-wide potential barrier at the MTB added by hand. The 1D Schrödinger equation is then solved for holes of effective mass $m_{\mathrm{h}}^{*} = 2.7m_{\mathrm{e}}$ in this potential. Table S1 shows that the quantized state maxima differ in energy by at most 0.03 eV, while considerable spatial discrepancies only begin to appear near the base of the exponentially widening potential ($n = 4, 5$).

Table S1: VB state maxima at ML-MoS_2 4|4E MTBs, obtained from experiment (see Figure 2c) and modeling (see Figure 7).

	measured		fit	
n	E (eV)	x (nm)	E (eV)	x (nm)
1	−1.02	0.73	−0.99	0.67
2	−1.35	1.24	−1.37	1.15
3	−1.56	1.69	−1.58	1.72
4	−1.69	2.17	−1.69	2.47
5	−1.76	2.89	−1.75	3.78

References

(S1) Pronschinske, A.; Mardit, D. J.; Dougherty, D. B. Modeling the Constant-Current Distance-Voltage Mode of Scanning Tunneling Spectroscopy. *Phys. Rev. B* **2011**, *84*, 205427.

(S2) Jolie, W.; Murray, C.; Weiß, P. S.; Hall, J.; Portner, F.; Atodiresei, N.; Krasheninnikov, A. V.; Busse, C.; Komsa, H.-P.; Rosch, A.; Michely, T. Tomonaga-Luttinger Liquid in a Box: Electrons Confined within MoS_2 Mirror-Twin Boundaries. *Phys. Rev. X* **2019**, *9*, 011055.

(S3) Zhang, C.; Wang, H.; Chan, W.; Manolatou, C.; Rana, F. Absorption of Light by Excitons and Trions in Monolayers of Metal Dichalcogenide MoS_2: Experiments and Theory. *Phys. Rev. B* **2014**, *89*, 205436.

CHAPTER 8

Manuscript 4: Manipulating MoS_2 and its 1D phenomena via substrate screening and charge

This chapter wholly consists of the above-named manuscript and its supplement.

The experiments were proposed by C. Murray, C. van Efferen, J. A. Fischer, W. Jolie and T. Michely. The Eu-intercalated sample was grown and measured by C. Murray and C. van Efferen; other Eu-intercalated samples were grown and measured with J. A. Fischer and W. Jolie. The O-intercalated sample was grown by C. van Efferen and measured by him and C. Murray. Advice on MoS_2 *growth was provided by J. Hall. All experiments were performed at* $_{\mathrm{T}}$STM. *The LEED, STM and STS data analysis was performed principally by C. Murray and C. van Efferen, with assistance from J. A. Fischer and W. Jolie.*

The interpretation of the results was discussed in depth by C. Murray, C. van Efferen, J. A. Fischer and T. Michely. This work builds upon that carried out in Publications 1, 2 and 3 and so the efforts of the respective co-authors should also be considered [1–3].

C. Murray wrote the manuscript, with advice and corrections from C. van Efferen, J. A. Fischer and T. Michely.

Some of the results shown in this Chapter can be found in the Master's thesis of C. van Efferen and, to a minor extent, the doctoral thesis of W. Jolie [225].

Manipulating MoS_2 and its 1D phenomena via substrate screening and charge

Clifford Murray,[1, *] Camiel van Efferen,[1] Wouter Jolie,[1, 2] Joshua Hall,[1] Jeison A. Fischer,[1] and Thomas Michely[1]
[1] *II. Physikalisches Institut, Universität zu Köln, Zülpicher Straße 77, 50937 Köln, Germany*
[2] *Institut für Materialphysik, Westfälische Wilhelms-Universität Münster,*
Wilhelm-Klemm-Straße 10, 48149 Münster, Germany

(Dated: July 2, 2020)

Much effort has been made to modify the properties of transition metal dichalcogenide layers via their environment, both as a means of testing and as a route to new functionalization. However, it remains a challenge to induce large electronic changes without chemically altering the layer or compromising its two-dimensionality. Here, a giant band gap reduction of up to 0.67 eV is achieved in MoS_2 by a non-invasive technique: the introduction of foreign atomic species to the backside of its graphene substrate. With Eu and O as example intercalants, we are able to n- and p-gate MoS_2 via charge carrier donation to graphene, which remains a well-decoupled, 2D substrate. Scanning tunnelling spectroscopy disentangles renormalization and Fermi-level pinning effects on the MoS_2 band structure. The MoS_2 hosts 1D states confined in and around mirror-twin boundary defects. The charging of these defects and their consequent screening by the changed substrate are revealed by the response of the 1D states.

I. INTRODUCTION

Modification and control of the electrostatic environment remains at the forefront of research into atomically thin transition metal dichalcogenides (TMDCs). Their 2D nature makes them extremely sensitive to any changes in their surroundings [1–4], in part due to their greatly reduced screening efficiency, with electric field lines which protrude out of the layer [5]. Thus a careful choice of dielectric environment can be used to tune their electronic and optical band gap [6, 7], control quasi-particle dynamics [8], and is of paramount importance for TMDC-based devices such as field-effect transistors [9]. Also of relevance to devices is the electronic interaction between TMDCs and metallic layers such as graphene (Gr). The latter is promising as a contact electrode owing to, amongst other things, its unique band structure which allows easy tuning of its Fermi level [9–11]. To this end, the Schottky barrier, charge transfer and interface dynamics of TMDC-Gr heterostructures under various conditions must be investigated [12].

The electronic environment of TMDC semiconductors can been tuned in a variety of ways. Foreign species can be adsorbed on the layer surface or intercalated [13–17]. Strong doping can be achieved this way, but it is invariably associated with a chemical change to the layer, the distribution of adatoms can be irregular, and it is not always reversible. Another method is to test TMDCs in back-gated devices based, for example, on Gr [18, 19], wherein the charge carrier concentration in Gr and thereby the dielectric screening experienced by the TMDC layer can be altered. While this technique offers excellent tunability, it is limited in the carrier concentrations that can be achieved before breakdown occurs.

Another way in which the environmental response of TMDCs is investigated is – almost by necessity – through the use of different substrates [6, 20–26]. Direct comparison between systems can difficult, however, due to the specifics of the substrate-layer interaction and the varied quality of the 2D layer from case to case. As an example, the electronic band gap of monolayer MoS_2 differs by some 0.9 eV over a range of substrates as measured by scanning tunnelling spectroscopy [27–32], and this cannot solely by attributed to one effect such as dielectric screening. Moreover, it must be possible to actually grow the TMDC layer in high quality in the first place, which is not always possible on strongly-interacting substrates.

Here, we non-invasively alter the electronic environment of monolayer MoS_2 *in situ*, by doping its Gr substrate from the backside. This is done through the use of intercalants, taking Eu and O as n- and p-dopants respectively, to create high quality MoS_2/Gr/(Eu or O)/Ir(111) layered configurations. Thereby the MoS_2 layer is essentially n- or p-gated via the Gr. With Eu, the charge carrier density of Gr is increased beyond what is possible in traditional device setups. The n-gating effect is so drastic that the MoS_2 band gap is reduced by 0.67 eV and the conduction band edge is brought close to the Fermi level. The increased metallicity of Gr results in stronger interaction with MoS_2 but it remains reasonably well decoupled, as evidenced by the survival of 1D defect states. By contrast, O-intercalation results in weak p-gating and a decoupling from the Ir substrate. Changes to the MoS_2 band structure in both cases are investigated by comprehensive scanning tunnelling spectroscopy (STS).

We have previous documented 1D electronic phenomena in MoS_2 on Gr/Ir(111), namely states confined along 4|4E mirror twin boundaries (MTBs) [33] and valence band states quantized by band bending normal to 4|4E MTBs [34]. The characteristic 1D states change in response to the substrate modifications, and are used to learn more about the charge transfer, screening and interlayer interaction of the MoS_2-Gr heterostructures. Moreover, the extreme gating due to Eu forces the Fermi wavevector of the 1D states to shift from $k_\mathrm{F} \approx \frac{\pi}{2a}$

---

[*] murray@ph2.uni-koeln.de

to $\frac{\pi}{2.69a}$. This marks a departure from previous experiments in which MoS_2 and $MoSe_2$ MTB states were commensurate with the lattice [33, 35, 36], and is an opportunity to study the interaction between 1D correlated-electrons and their lattice.

II. METHODS

The samples were grown *in situ* in a preparation chamber with base pressure $p < 5 \times 10^{-10}$ mbar. Ir(111) is cleaned by 1.5 keV Ar^+ ion erosion and annealing to temperatures $T \approx 1550$ K. Gr is grown on Ir(111) by two steps. First, room temperature ethylene exposure till saturation followed by 1370 K thermal decomposition gives well-oriented Gr islands. Second, exposure to 2000 L ethylene at 1370 K for 10 mins yields a complete single-crystal Gr layer; for the O-intercalated sample limiting this step to 1 min yields an incomplete layer. Compare Ref. 37. ML- and BL-MoS_2 are grown by van der Waals MBE, see Ref. 38. Mo is deposited in a background elemental S pressure of 1×10^{-8} mbar onto the room temperature Gr substrate. The system is then annealed to 1050 K in the same S background pressure. The Eu-intercalated sample is prepared in the order: Gr growth; Eu intercalation; MoS_2 growth. Eu is evaporated from a Knudsen cell onto the 720 K Gr/Ir(111) crystal for 10 mins. Intercalation is confirmed by low-energy electron diffraction (LEED), see Refs. 39, 40. The sample is flash annealed to 1050 K to remove residual Eu before subsequent MoS_2 growth. The O-intercalated sample is prepared in the order: Gr growth; MoS_2 growth, O intercalation. O-intercalation is achieved by exposing the 530 K MoS_2/Gr/Ir(111) crystal to 2×10^4 L of O_2. Molecular oxygen dissociates on the Ir surface; atomic O then diffuses under the Gr islands. See Refs. 41, 42.

STM and STS are carried out in the $T = 5$ K bath cryostat system after *in situ* transfer from the preparation chamber. STS is performed with the lock-in technique, at modulation frequency 777 Hz and modulation voltage $V_{\mathrm{mod}} = 4\,\mathrm{mV_{rms}}$, with an experimental resolution of ≈ 10 meV or better [43]. We employ constant height [recording $(\mathrm{d}I/\mathrm{d}V)_Z$] and constant current [$(\mathrm{d}I/\mathrm{d}V)_I$] STS modes, where I is the tunneling current, V the bias voltage, and Z the tip-sample distance or 'height'. In both modes $\mathrm{d}I/\mathrm{d}V$ is recorded while V is ramped; see Ref. 32 for further explanation. Field emission resonance (FER) spectroscopy is performed in constant current mode [44, 45].

III. EXPERIMENTAL RESULTS

A. Substrate modification

Large-scale STM topographs of the three samples under investigation are shown in Figs. 1(a-c). In the unmodified, 'control' sample, (a), a coverage of roughly 0.6 layers of ML-MoS_2 extends across the Gr/Ir(111) substrate, including a few Ir step edges. Small BL-MoS_2 islands are seen. Also faintly visible are dark, straight lines intersecting the MoS_2 network – these are 4|4E and 4|4P type mirror twin boundaries (MTBs) [33, 46], to be discussed later. The apparent heights of various features are shown in the line profile Fig. 1(d): an Ir step edge under Gr is about 0.22 nm; ML-MoS_2 is 0.65 nm above Gr; BL-MoS_2 an additional 0.55 nm above that, all as expected [37, 38]. A cross-section of the profiled region is sketched.

The Eu-modified sample and accompanying line profile are shown in Figs. 1(b,e). Large intercalation patches and 'stripes' of apparent height 0.25 nm are visible, similar to previous Gr/Eu/Ir(111) samples [39]. As in (a), MoS_2 islands have grown together to form a network. From the varied directions and irregularity of the island edges [and from LEED, see Supporting Information (SI) Fig. S1] it is apparent that MoS_2 is now less epitaxially aligned with the substrate. All investigated MoS_2 islands had an apparent height of around 1.0 nm relative to the lower [darker in (b)] patches of Gr. We thus infer that ML-MoS_2 is only found on top of Eu-intercalated Gr, *i.e.* it preferentially grows there. Despite a similar total MoS_2 coverage to the sample in (a), no BL islands have formed. This is another indication that MoS_2 has an enhanced wettability on Eu-intercalated Gr. A further indication of changed growth dynamics is the complete absence of 4|4P-type MTBs in this sample; typically they make up 5%−30% of MTBs in MBE-grown MoS_2 on Gr/Ir(111) [33]. The Eu intercalation structure will be discussed in more detail below.

The O-modified sample is shown in Figs. 1(c,f). An incomplete Gr layer was grown to allow for O_2 dissociation on exposed Ir; the edge of the Gr flake is seen in the lower left of the topograph, while the exposed Ir is decorated with adsorbates, presumably Mo, S, O or some combination thereof. No macroscopic O-intercalation structures are visible, but there are numerous indications that the Gr is intercalated everywhere, to be discussed in the next section. A relatively well-oriented network of ML-MoS_2 is seen, with small BL islands on top.

In Fig. 2 we identify the intercalation superstructures on the atomic scale. For purpose of comparison, Fig. 2(a) shows a topograph of Gr/Ir(111), and in the inset the Fourier transform (FT) of the topograph. The Gr lattice and the moiré it forms with Ir(111), of unit lengths 0.245 nm and 2.53 nm respectively, are visible in real space. In reciprocal space the brightest outer spots correspond to Gr (white circles), and they are surrounded by satellites due to the moiré

The topograph in Fig. 2(b) shows an area of Gr/Eu/Ir. A rectangular lattice covers most of the image, with small trenches of presumably lower (or zero) Eu density in between. The FT of the topograph, inset, reveals that the Gr/Ir(111) moiré is still present to some extent. The Eu superstructure (green circles) is measured to have unit lengths (0.426 ± 0.07) nm and (0.495 ± 0.06) nm, corre-

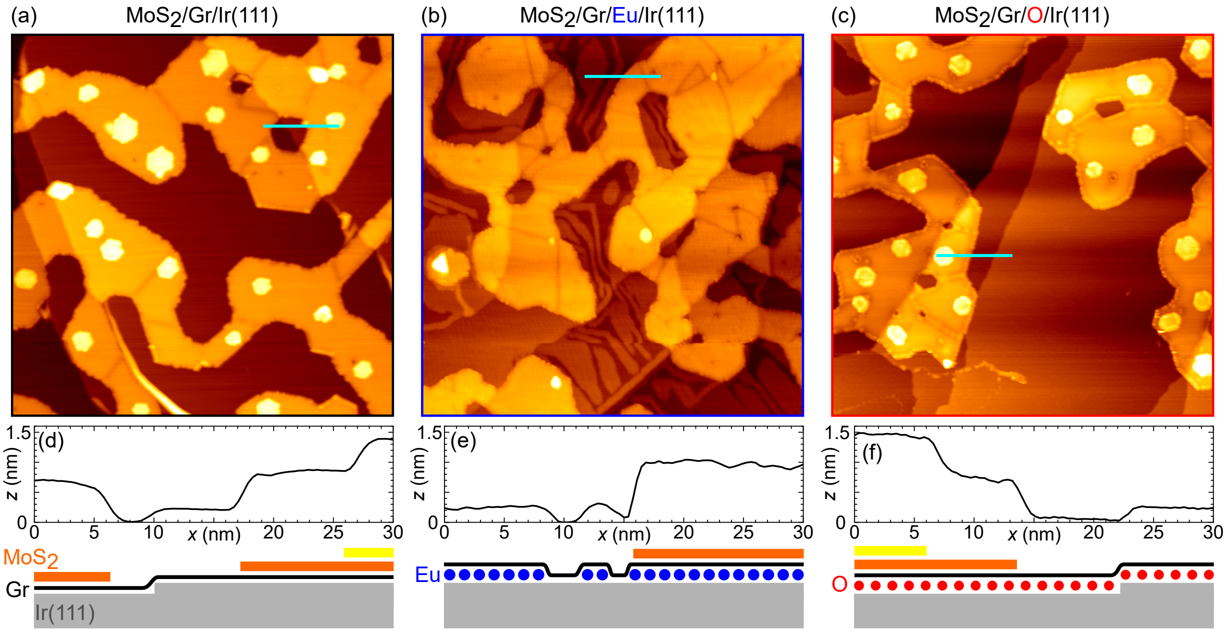

FIG. 1. Constant current STM overview topographs of the different samples: (a) MoS_2/Gr/Ir(111); (b) MoS_2/Gr/Eu/Ir(111); (c) MoS_2/Gr/O/Ir(111). In each of (a-c) the path of a 30 nm line profile is marked in cyan; these are shown in (d-f) respectively, accompanied by a sketch of the sample cross-section along the line. STM parameters (V, I): (a) 1.5 V, 0.01 nA; (b) 1.0 V, 0.10 nA; (c) 1.0 V, 0.05 nA; (a-c) image size $150 \times 150\,\mathrm{nm}^2$.

sponding to a c(4×2) with respect to Gr. The superstructure spots also have satellites of the Gr/Ir(111) moiré unit length, and there are additional spots (pink circle), each resulting from the summation of vectors analogous to multiple scattering in LEED. Note that another of the three possible c(4 × 2) domains is visible in the lower right of the topograph, though it is too small to cause a considerable reciprocal intensity.

Eu is known to form various hexagonally symmetric superstructures under Gr on Ir(111) [39, 40, 48]. The c(4 × 2) phase has not been reported previously, but we note that it has precisely the same density as the well-documented (2 × 2) phase, namely 25% with respect to the Gr lattice; see SI for further discussion. Using field emission resonance (FER) spectroscopy we can determine the change in the Gr work function due to the Eu intercalation layer [47, 49]. As shown in Fig. 2(c), resonant states (Gundlach oscillations) are measured on Gr/Ir and on Gr/Eu/Ir. In accordance with the method described by Lin *et al.* [47], each state can be assigned an order n, and an approximately linear energy shift between same-order states is observed, inset. This indicates a work function reduction $\Delta\Phi_{\mathrm{Gr}} = (-1.4 \pm 0.1)$ eV on Eu-intercalated Gr. Assuming a rigid shift of the Dirac cone, this would mean a new Dirac point of −1.3 eV, compared to its value of 0.1 eV for Gr/Ir(111) [50]. This is in line with the ARPES-measured Dirac point of −1.36 eV for Gr/(2 × 2)-Eu/Ir(111) [40], and represents strong n-doping of Gr. We find that the Eu-intercalated islands are near-uniformly doped, see Fig. S2.

An equivalent topographic image of Gr/O/Ir(111) is shown in Fig. 2(d). It appears inhomogeneous, with no obvious intercalation superstructure. The Gr/Ir(111) moiré is not seen clearly. In the FT image the Gr lattice and some moiré spots are visible, but it must be noted that the contrast has been greatly increased in comparison to (a,b). A hazy superstructure resembling a $(\sqrt{3} \times \sqrt{3})$R30° can be seen. O adopts various coverage-dependent superlattices under Gr on Ir(111), one of which is a $(\sqrt{3} \times \sqrt{3})$R30° with respect to Ir [42, 51, 52]. It is known to decouple Gr from Ir, thereby weakening the moiré interaction as is observed here. The decoupling of Gr is further proven by quasi-particle interference (see Fig. S3), as reported previously for O-intercalated Gr flakes on Ir(111) [52].

The lack of a clear O superstructure matching those known from literature suggests that there may be a poorly-ordered mixture of intercalants. It is possible that some Mo- or S-intercalation already occurred during the MoS_2 growth step because the Gr layer was not fully closed [38, 53]. As there are no patches of non-intercalated Gr, it is not possible to extract the work function change as in Fig. 2(c). However, we can determine that the work function is roughly the same throughout the sample (see Fig. S4), indicating that the interlayer uniformly dopes the Gr, whatever its precise composition. For sake of simplicity, we henceforth refer to this substrate as Gr/O/Ir(111) regardless. Additionally, for brevity, we henceforth drop ML- from ML-MoS_2 and (111) from Ir(111), except where necessary to avoid confusion.

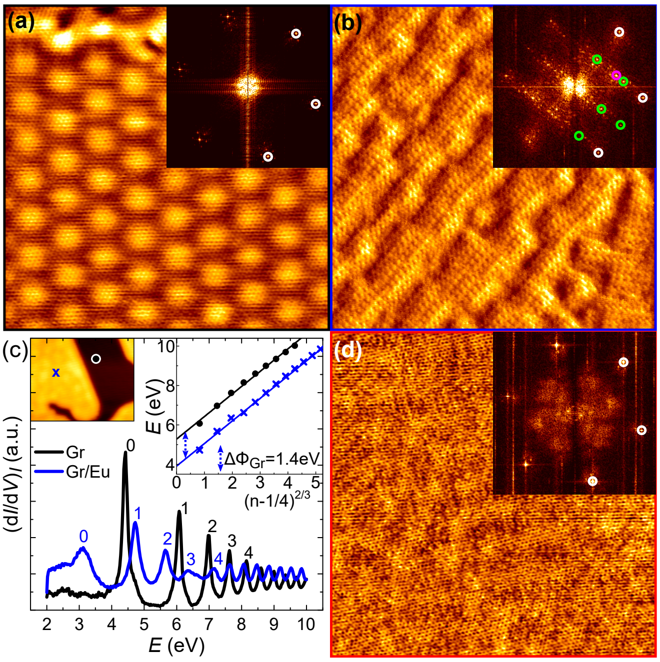

FIG. 2. Constant current STM close-up topographs of Gr for the samples (a) MoS_2/Gr/Ir(111), (b) MoS_2/Gr/Eu/Ir(111), (d) MoS_2/Gr/O/Ir(111). Note that areas of exposed Gr have been chosen; there is no MoS_2 visible in the topograhps. Insets (a,b,d) show the Fourier transform (FT) of each image, spots corresponding to Gr (white) circled. (c) Field emission resonance (FER) spectroscopy recorded on Gr/Ir(111) (black) and Gr/Eu/Ir(111) (blue) at the locations shown in the inset (left). Resonant states are numbered n, and in the inset (right) plotted E against $(n-\frac{1}{4})^{\frac{2}{3}}$, see Ref. 47. The energy shift in the corresponding lines of best fit gives the difference in Gr work function $\Delta\Phi_{\mathrm{Gr}} = (-1.4 \pm 0.1)\,\mathrm{eV}$. STM parameters (V, I): (a) -0.15 V, 8.0 nA; (b) 0.30 V, 0.4 nA; (d) 0.05 V, 0.1 nA; (a,b,d) image size $20 \times 20\,\mathrm{nm}^2$, insets $11 \times 11\,\mathrm{nm}^{-2}$. In (b,d) current and height images have been merged to make the superstructure more visible. (c) FER spectroscopy stabilization voltage $V_{\mathrm{st}} = 2$ V; inset left: $20 \times 16\,\mathrm{nm}^2$, 1.0 V, 0.04 nA.

B. Altered bandstructure of MoS_2

We use ‘comprehensive’ STS to investigate how the band structure of MoS_2 is altered by the modified substrates. Fig. 3 shows typical spectra recorded on MoS_2 on each substrate. Spectra are always taken far away ($>$ 6 nm) from any defects, island edges or substrate step edges. Fig. 3(a) shows constant height STS, which gives a rough idea of the band gap size and location [32, 54]. For example, for MoS_2 on Gr/Ir the valence band (VB) and conduction band (CB) edges are close to -1.8 eV and 0.9 eV, respectively. We see immediately that by intercalating the Gr we have indeed altered the macroscopic electronic properties of the MoS_2 on top. The Eu-interlayer has caused both band edges to shift downwards (that is, towards lower energies), with the effect being much stronger in the CB. This represents n-gating of MoS_2. The O-interlayer, on the other hand, has caused a small upwards shift of the bands, representing slight p-gating of MoS_2. Note that in both intercalated samples, the STS-measured band structure was uniform throughout the bulk of the MoS_2 layer, despite the small-scale inhomogeneities in the Eu- and O-interlayers.

To get a more precise view of the respective band structures, we also perform constant current STS, Fig. 3(b). In a previous work we analysed ML-MoS_2/Gr/Ir with this method supplemented by a third STS mode, allowing the identification of critical points in the band structure, see Ref. 32. In the VB the Γ-point band edge states cause a large peak. The VB maximum at the K-point is not detected because of its large parallel momentum and in-plane orbital character. The CB minimum at the K-point, however, is dominated by out-of-plane orbitals and thus shows up as a small shoulder. States from the CB Q-point edge cause a larger peak. The average energies of these critical points are given Table I.

This prior knowledge can be used to identify critical points in the spectra of MoS_2 on intercalated Gr. Beginning with MoS_2 on Gr/Eu/Ir, the Γ-point in the VB is immediately recognisable, and is found at -1.90 eV on average (compare Table I). The CB is more tricky because it is so close to E_{F}. In constant height mode STS the tip moves closer to (and ultimately crashes into) the sample as V_{bias} is ramped towards 0 V. This causes a continuous increase in signal intensity approaching E_{F} (compare Ref. 55). Nonetheless, a peak is clearly visible at 0.20 eV. Based on: the peak’s prominence; comparison with the constant height spectra; and the low tunnelling probability at the K-point, we assume this peak to be from Q-point states. Assuming a rigid shift of bands, this would place the CB minimum at K at 0.07 eV; measuring that close to E_{F} crashes the tip, however.

Inspecting constant current STS of MoS_2 on Gr/O/Ir, Fig. 3(b), we see that the band structure has not been drastically altered. The Γ-point states in the VB and the Q-point states in the CB have been shifted up by an average of 0.05 eV and 0.04 eV respectively, see Table I. A noticeable change is that the K-point states of the CB edge have become much more pronounced. We attribute this to the decoupling effect of the O-interlayer; the MoS_2 is now farther from the Ir. This necessitates the tip being closer to the surface while tunnelling in the band gap. This increases the tunnelling probability for the K-point states at the band gap edge, which have a short decay length into the vacuum [32, 54].

It is worth already discussing how the macroscopic electronic properties of the MoS_2 layer have been changed, beginning with the Eu-modified sample. The band gap of MoS_2/Gr/Ir(111) was established to be $E_{\mathrm{g}}^{\mathrm{Gr}} = 2.53$ eV in Ref. 32. In MoS_2/Gr/Eu/Ir the CB edge at K could not be detected but, for the sake of a rough comparison, we assume that it has shifted rigidly with the Q-point. Thus the Eu-interlayer has significantly reduced the MoS_2 band gap to $E_{\mathrm{g}}^{\mathrm{Eu}} = 1.86$ eV. The band gap has not narrowed symmetrically however;

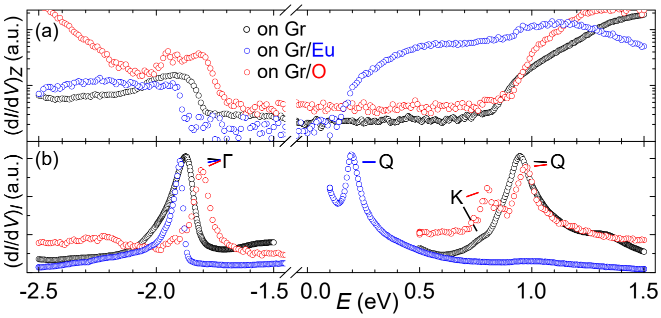

FIG. 3. STS of ML-MoS$_2$ on different substrates, measured in (a) constant height and (b) constant current STS modes. MoS$_2$ on Gr/Ir is shown in black; on Gr/Eu/Ir in blue; on Gr/O/Ir in red. Some critical point energies are identified. The dI/dV is given in arbitrary units; the spectra have been shifted in dI/dV for visual clarity; (a) is shown on a logarithmic scale. STS parameters: (a) all $V_{\mathrm{st}} = 1.5\,\mathrm{V}$; $I_{\mathrm{st}} = 0.2\,\mathrm{nA}$ (black) 0.5 nA (blue) 0.3 nA (red); (b) all $V_{\mathrm{st}} = -2.5\,\mathrm{V}$ or 1.5 V, $I_{\mathrm{st}} = 0.1\,\mathrm{nA}$.

the VB has shifted by $\Delta E^{\mathrm{Eu}}_{\mathrm{VB}} = -0.03\,\mathrm{eV}$ and the CB by $\Delta E^{\mathrm{Eu}}_{\mathrm{CB}} = -0.70\,\mathrm{eV}$.

We attribute this asymmetry as being due to two mechanisms, which compete in the VB but combine additively in the CB. The first mechanism, termed ΔE_{Φ}, is the Schottky-barrier physics of the MoS$_2$-Gr heterojunction, *i.e.* a shift of both bands in the same direction due to the changed work function of Gr [12, 22]. The work function of Gr/Ir is already lower than that of MoS$_2$ [34]; the Eu-interlayer has caused a further reduction $\Delta\Phi_{\mathrm{Gr}} = 1.4\,\mathrm{eV}$ [Fig. 2(c)], necessitating an n-gated shift of MoS$_2$ until its Fermi level is aligned. The second mechanism, ΔE_{rn}, is the band gap renormalization due to increased dielectric screening by Gr. We assume that this affects both VB and CB equally, *i.e.* both bands move symmetrically towards E_{F} [25, 56]. The Eu-interlayer has greatly increased the charge carrier density of Gr [57], improving its screening ability. Combining these contributions, the VB is shifted by $\Delta E^{\mathrm{Eu}}_{\mathrm{VB}} = \Delta E^{\mathrm{Eu}}_{\Phi} - \Delta E^{\mathrm{Eu}}_{\mathrm{rn}}$ and the CB by $\Delta E^{\mathrm{Eu}}_{\mathrm{CB}} = \Delta E^{\mathrm{Eu}}_{\Phi} + \Delta E^{\mathrm{Eu}}_{\mathrm{rn}}$, with $\Delta E^{\mathrm{Eu}}_{\Phi} = -0.365\,\mathrm{eV}$ and $\Delta E^{\mathrm{Eu}}_{\mathrm{rn}} = -0.335\,\mathrm{eV}$. The plausibility and significance of these values will be considered in the discussion, but the effects of the Eu-interlayer are nonetheless clear: it has strongly n-doped the Gr, which in turn n-gates the MoS$_2$ top layer and renormalizes its band gap via screening.

Applying the same analysis to MoS$_2$ modified by the O-interlayer is not meaningful, as the 0.02 eV band gap reduction is within the margin of error; very little renormalization has occurred, if any. This will be addressed in the Discussion.

C. Altered 1D states in MoS$_2$ MTBs

We now investigate how the Eu- and O-interlayers affect 1D states localized at MoS$_2$ line defects. We focus on

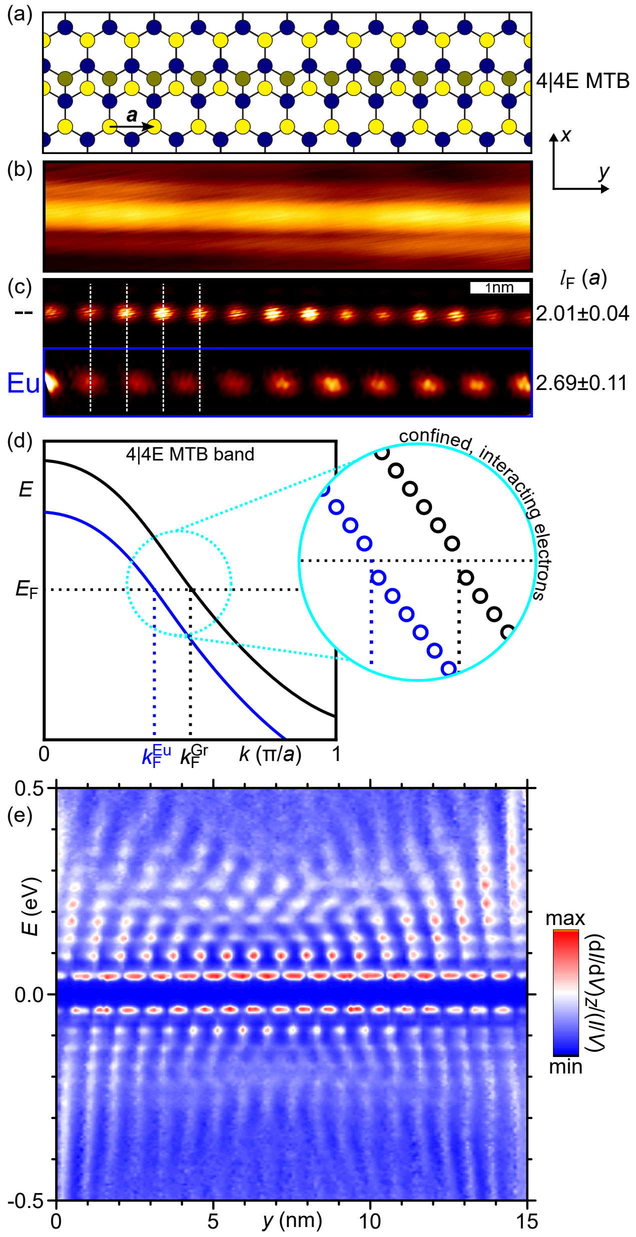

FIG. 4. Confined states along 4|4E MTBs in ML-MoS$_2$ on different substrates. (a) Ball-and-stick model of a 4|4E MTB. Mo atoms are navy, S atoms yellow (top layer) or dark yellow (bottom layer). A MoS$_2$ lattice vector is indicated. (b) Constant current STM topograph of a 4|4E MTB in MoS$_2$ on Gr/Ir. (c) Constant height STM of 4|4E MTBs in MoS$_2$ on Gr/Ir (upper panel) and on Gr/Eu/Ir (lower panel). Vertical white lines are a guide to the eye . Average periodicity $l^{\mathrm{i}}_{\mathrm{F}}$ (i = Gr,Eu) is given for each sample. (d) Schematic of the hole-like 1D band of the 4|4E MTB on both substrates; color-coding as above; not to scale. The inset shows the situation for confined, interacting electrons. (e) Constant height STS linescan along a 4|4E MTB in MoS$_2$/Gr/Eu/Ir (see Fig. S5). The $(\mathrm{d}I/\mathrm{d}V)_Z$ signal is normalized against I/V, and plotted as a function of energy E and position y according to the shown color scale (arbitrary units). STM/S parameters: (b) $V = 1.25\,\mathrm{V}$ $I = 0.02\,\mathrm{nA}$; (c) upper panel $V = 0.10\,\mathrm{V}$, $I_{\mathrm{st}} = 0.5\,\mathrm{nA}$; lower panel $V = 0.20\,\mathrm{V}$, $I_{\mathrm{st}} = 0.05\,\mathrm{nA}$. 1 nm scale bar shown; (e) $V_{\mathrm{st}} = -0.5\,\mathrm{V}$, $I_{\mathrm{st}} = 0.1\,\mathrm{nA}$.

TABLE I. Critical point energies (eV) identified in ML-$\mathrm{MoS_2}$ on different substrates using constant current STS (averaged over multiple data sets), and the corresponding electronic band gap E_g. For more detail on the $\mathrm{MoS_2}$/Gr/Ir data, including the determination of $E_\mathrm{g} = 2.53\,\mathrm{eV}$, see Ref. 32. The larger error on E_g for the Eu case reflects ambiguity in the identification of the CB minimum (see main text).

$\mathrm{MoS_2}$ on	Γ	K	Q	E_g
Gr/Ir	-1.87 ± 0.02	0.77 ± 0.02	0.90 ± 0.05	2.53 ± 0.08
Gr/Eu/Ir	-1.90 ± 0.01	(0.07)	0.20 ± 0.01	1.86 ± 0.13
Gr/O/Ir	-1.82 ± 0.03	0.80 ± 0.04	0.94 ± 0.03	2.51 ± 0.08

the 4|4E mirror twin boundary (MTB), the atomic structure of which is displayed in Fig. 4(a). This 1D defect forms between 180°-misoriented $\mathrm{MoS_2}$ domains [46, 58]. It is the most common MTB type in $\mathrm{MoS_2}$ on Gr/Ir(111); around 10 of them, ranging in length 5−25 nm, are visible in Fig. 1(a).

A close-up of a section of such a 4|4E MTB is shown in Fig. 4(b). We image the same MTB in constant height STM at 0.1 eV, Fig. 4(c) top panel. This reveals states deep inside the $\mathrm{MoS_2}$ band gap, which are quantized along the MTB with a measured period of $2.02\,a$, where $a = 0.315\,\mathrm{nm}$ is the ML-$\mathrm{MoS_2}$ lattice constant. An equivalent measurement on the other side of E_F, at $-0.1\,\mathrm{eV}$, reveals quantization of period $1.99\,a$. Averaging for states above and below E_F and over many such MTBs in $\mathrm{MoS_2}$/Gr/Ir, we find $l_\mathrm{F}^\mathrm{Gr} = (2.01 \pm 0.04)\,a$. We have explained this phenomenon previously [33, 34]. The 4|4E MTB has a 1D hole-like band with Fermi wavevector $k_\mathrm{F}^\mathrm{Gr} \approx \frac{\pi}{2a}$ in this configuration, and hence an approximate period doubling is seen, Fig. 4(d). In fact, the band is quantized and a gap appears at E_F, due to electron-electron interactions along the finite length of the MTB [33] [depicted in the inset of (d)].

We image the 4|4E MTB in $\mathrm{MoS_2}$ on Gr/Eu/Ir similary, Fig. 4(c) middle panel. It also shows confined states, but their periodicity has visibly increased due to the Eu-interlayer; we now find an average of $l_\mathrm{F}^\mathrm{Eu} = (2.69 \pm 0.11)\,a$. As illustrated in the main sketch of Fig. 4(d), this corresponds to a shift of the 1D MTB band relative to E_F (or *vice versa*) so that it crosses at $k_\mathrm{F}^\mathrm{Eu} = (0.37 \pm 0.02)\,\pi/a$. This corresponds to an increased filling of the hole-like band.

In previous work, DFT showed that a 4|4E MTB in a *freestanding* $\mathrm{MoS_2}$ layer is approximately charge neutral. Placing the $\mathrm{MoS_2}$ on Gr caused an increased MTB band filling due to Gr electron donation; comparing Fermi wavevectors before and after showed a changed linear charge density of $\Delta\lambda = -\frac{2e}{\pi}(k_\mathrm{F} - k'_\mathrm{F}) = -0.18\,e/a$ [34], see Table II. We can similarly assess the change in band filling due to the Eu interlayer from experiment; we find $\Delta\lambda = -\frac{2e}{\pi}(k_\mathrm{F}^\mathrm{Gr} - k_\mathrm{F}^\mathrm{Eu}) = -0.26\,e/a$. The Eu-interlayer strongly n-dopes the Gr, which donates some of its excess electrons to the metallic MTB band, causing a shift in k_F. This is visualized by the changed periodicity of the confined MTB states observed in real space.

TABLE II. Fermi wavevectors of the 4|4E MTB band in ML-$\mathrm{MoS_2}$ on different substrates, and the associated line charge on the MTB, $\lambda = -\frac{2e}{\pi}(1 - k_\mathrm{F})$. See Ref.34 for more details.

$\mathrm{MoS_2}$ on	k_F (π/a)	λ (e/a)
freestanding (DFT) [34]	0.63	−0.74
Gr (DFT) [34]	0.54	−0.92
Gr/Ir (STM)	0.50	−1.00
Gr/Eu/Ir (STM)	0.37	−1.26

As mentioned above and depicted in the inset of Fig. 4(d), the situation in $\mathrm{MoS_2}$/Gr/Ir(111) is more complicated than a confined 1D band. The weak screening in 1D leads to strong electron-correlation and the emergence of Tomonaga Luttinger liquid (TLL) behaviour [33]. This is partly evidenced by a Coulomb blockade energy gap at E_F. In Fig. 4(e) we perform a constant height STS linescan – a series of spectra 1 Å apart – along the length of a 4|4E MTB on Gr/Eu/Ir(111). It shows a gap of size $E_\mathrm{gap} = 80\,\mathrm{meV}$ around the Fermi level and many additional quantized states of smaller energy spacing. Measuring other 4|4E MTBs of various lengths L, we find an approximate $E_\mathrm{gap} \propto 1/L$ dependence consistent with a Coulomb blockade, see Fig. S5. A definitive statement on the persistence of the TLL goes beyond the scope of this work. Nonetheless, the Coulomb blockade gap and the many quantized energy levels seen in Fig. 4(e) show that the 4|4E MTB in $\mathrm{MoS_2}$/Gr/Eu/Ir(111) is still highly 1D.

In the $\mathrm{MoS_2}$ on Gr/O/Ir sample the 4|4E MTB type was rare, and so a reliable estimate of l_F^O cannot be made. Conversely the 4|4P-type MTB was more common in this sample, and so it could be used as a check for any substrate-induce shifts effects instead, see Fig. S6. The 4|4P MTB shows a $l_\mathrm{F}^\mathrm{Gr} = (3.00 \pm 0.04)\,a$ beating pattern in $\mathrm{MoS_2}$ on Gr/Ir [33]; in $\mathrm{MoS_2}$ on Gr/O/Ir we find an average value of $(3.07 \pm 0.09)\,a$. Thus the O-interlayer has not significantly changed the filling of the electron-like band of the 4|4P MTB.

D. Altered band bending at $\mathrm{MoS_2}$ MTBs

In Fig. 5 we investigate the electronic landscape directly surrounding the 4|4E MTB on each substrate. In Figs. 5(a,b) we take constant current STS linescans orthogonally crossing the 4|4E MTB. While (a) captures the behaviour of the CB edge, (b) captures that of the VB. Far away from the MTB, at $|x| = 5\,\mathrm{nm}$, the unperturbed band structure of $\mathrm{MoS_2}$ on Gr/Ir is observed; the dominant Q-point and faint K-point states around 0.90 eV and 0.77 eV respectively in (a), and the sharp Γ-point around −1.87 eV in (b). Approaching the MTB at $x = 0\,\mathrm{nm}$, both CB and VB are seen to bend upwards by at least 0.5 eV. The bending is smooth in the CB but occurs stepwise at characteristic energies in the VB. These VB energies are well-defined for the system, being approximately the same at dozens of 4|4E MTB with a standard deviation $< 0.03\,\mathrm{eV}$.

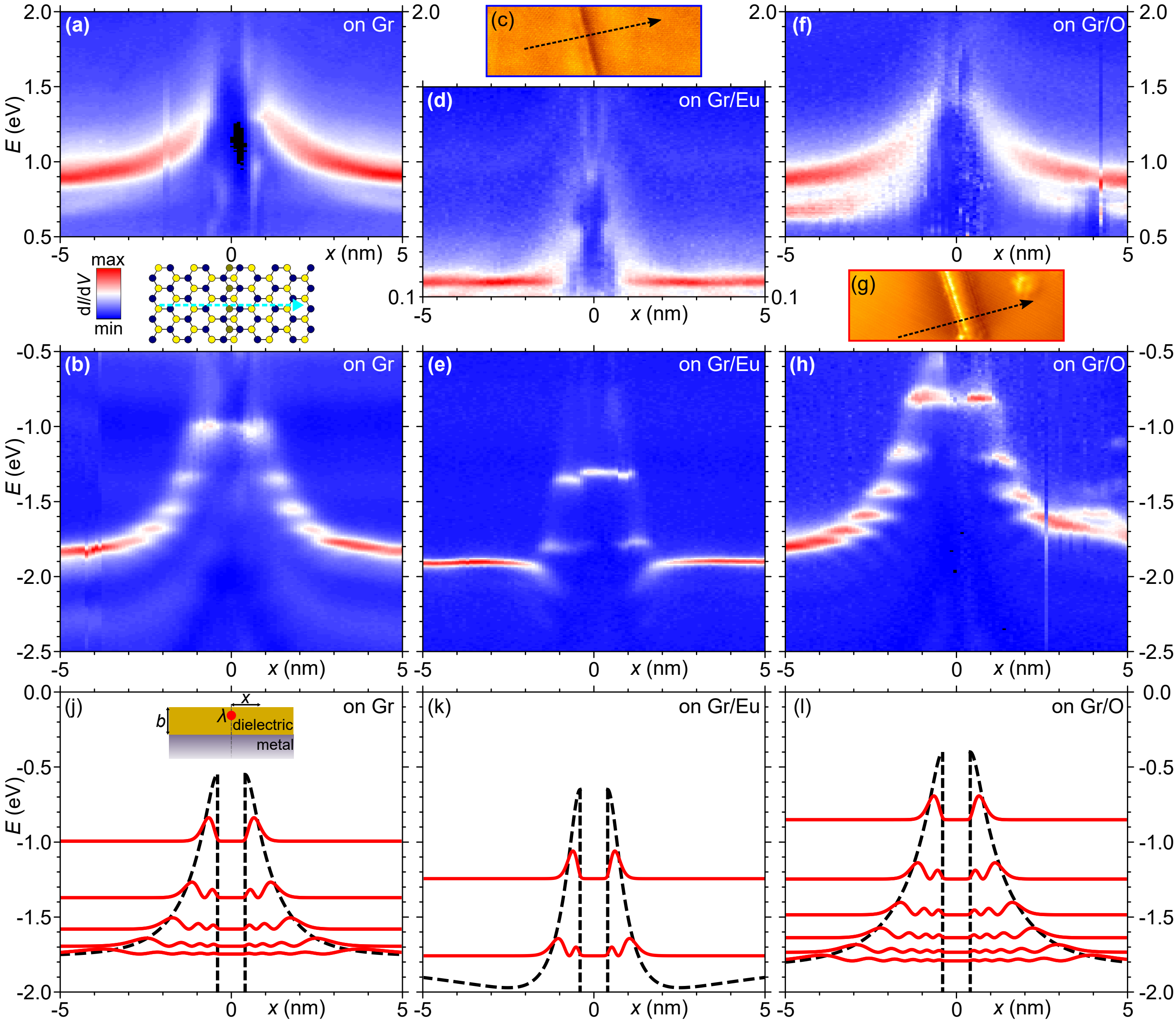

FIG. 5. Band bending at 4|4E MTBs in ML-MoS$_2$ on different substrates: (a-b) on Gr/Ir; (c-e) on Gr/Eu/Ir; (f-h) on Gr/O/Ir; (j-l) and electrostatic modelling thereof. Constant current STS linescans are taken in the energy ranges of the CB (a,d,f) and VB (b,e,h) extrema. (See Fig. S7 for constant height STS linescans). The recorded $(dI/dV)_I$ signal is plotted as a function of energy E and position x according to the color scale shown in (a), in arbitrary units. In (a) the path of a linescan over a 4|4E MTB is shown schematically by an arrow, not to scale. In (c) the path of the linescans (d,e) over an MTB on Gr/Eu/Ir is shown in a STM topograph. Similarly in (g) for linescans (f,h). In (g) a point defect is visible in the upper right. (j-l) show the output of electrostatic continuum modelling, with model potential (black) and resultant quantized states (red); see main text and Ref. 34. Inset of (j) shows a cross-sectional sketch of the model geometry. STS parameters: (a,b) $V_{\mathrm{st}} = \pm 2.5$ V, $I_{\mathrm{st}} = 0.05$ nA (d) $V_{\mathrm{st}} = 1.5$ V; (e) $V_{\mathrm{st}} = 2.0$ V; (f,h) $V_{\mathrm{st}} = -2.5$ V; (d,e,f,h) $I_{\mathrm{st}} = 0.10$ nA; STM parameters: (c) $V = 1.5$ V; (g) $V = 1.0$ V; (c,g) image size $15 \times 5\,\mathrm{nm}^2$, $I = 0.1$ nA.

We analysed this behaviour in detail in Ref. 34. Excess negative charge on the 4|4E MTB creates an electrostatic potential, which bends the surrounding MoS$_2$ semiconductor bands upwards. In the VB a potential well for holes is created, confining them normal to the MTB and quantizing the VB in that direction. Additionally, it was experimentally shown that the MTB is itself a barrier to holes and so there is an independent well on either side of the MTB.

A 4|4E MTB in MoS$_2$ on Gr/Eu/Ir, Fig. 5(c), is investigated by constant current STS linescans in the same manner, Figs. 5(d,e). The band bending behaviour is strikingly different. It occurs in a much smaller range of 2 nm on either side of the MTB, compared to 5 nm in (a,b). In (e) there are fewer quantized VB levels – only two – and their energy spacing is larger. The highest quantized state occurs at around $-1.3\,\mathrm{eV}$ instead of $-1.0\,\mathrm{eV}$. Additionally, the VB bends down slightly at $|x| \approx 1.5\,\mathrm{nm}$ before bending up steeply; this is also clearly visible in constant height STS, see Fig. S7. Note that in the CB, Fig. 5(d), the sharp bending of the bands leaves the states confined along the MTB length [Fig. 5(e)] electronically protected.

In Figs. 5(f-h) the band bending at a 4|4E MTB in MoS_2 on Gr/O/Ir is probed. In the STM topograph, (g), a point defect is visible on the right-hand side of the MTB. In constant current STS (f,h), the point defect can be seen to weakly perturb the electronic landscape on that side of the MTB. As was shown in Ref. 34, the two sides are largely independent, and so the behaviour seen from $x = -5$ to $0\,\mathrm{nm}$ should not be affected. The bending in the CB, (f), has not changed significantly due to the O-interlayer. The only marked change is the increased tunnelling probability into the K-point states at the band minimum due to decoupling from the substrate, as in Fig. 3. The quantized bending of the VB, (h), displays more changes due to the O-interlayer. The highest quantized state occurs at a higher energy ($-0.80\,\mathrm{eV}$), there now are now 6 quantized states visible instead of 5, and the bending now occurs over a slightly longer range. All of these changes point towards a wider potential well.

The quantized VB bending in MoS_2/Gr/Ir can be accurately reproduced using a simple electrostatic continuum model, as shown in Fig. 5(j). A line of charge density λ is embedded in a 2D dielectric layer of relative permittivity ϵ and thickness b, atop a semi-infinite metal substrate (see Ref. [34] for further details). Note that Gr was considered to be part of the dielectric layer; for low charge carrier concentration the Thomas-Fermi screening radius of Gr is larger than the thickness of the MoS_2/Gr heterostructure, and thus it cannot screen effectively [19]. From the model a screened potential [black lines in (j)] is calculated by a method of image charges [59], with the barrier at the MTB added by hand. The 1D Schrödinger equation is solved for holes in the potential, and the resultant squared wavefunctions plotted at their eigenenergies (red lines); the probability maxima at the band edge closely reproduce those seen in experiment. Our investigation showed that, to a large extent, this band bending is governed by the substrate: the substrate donates the MTB's excess charge, and the substrate is mostly responsible for the screening of this charge.

We make some simplified but meaningful changes to our model, in order to qualitatively reproduce the substrate-modified band bending and aid understanding. In the case of MoS_2 on Gr/Eu/Ir three changes are made. First, $-0.26\,e/a$ is added to the line charge λ, to reflect the extra charge donation by Eu as determined in Table II. Secondly, we reduce the thickness of the dielectric layer, from $b = 1.2\,\mathrm{nm}$ to $0.7\,\mathrm{nm}$. Judging by the work function change $\Delta\Phi_{\mathrm{Gr}} = -1.4\,\mathrm{eV}$ due to the Eu-interlayer [Fig. 2(c)], the charge concentration in Gr has increased by at least an order of magnitude [57], its screening radius has decreased accordingly [19], and Gr is now able to screen effectively. This is evidenced also by the band structure analysis, Section III B. Thus we include Gr in the metal substrate instead of the dielectric, by reducing the latter's thickness b.

The third modification to the model is manually simulated 'over-screening'. We give the screening contribution due to image charges a 110% weight, essentially making the substrate a better-than-perfect metal. This is the only way to recreate a slight dip in the potential before it rises, the effect of which is seen in the bands in (e). An interpretation of this over-screening is given in the Discussion. After these three modifications to the model, the new potential and the resultant VB states are shown in Fig. 5(k). Thinning the dielectric layer brings the line charge (fixed at $0.31\,\mathrm{nm}$ from the vacuum interface) closer to the substrate which, together with the third modification, leads to increased screening by the metal substrate. This results in a much narrower potential well, and successfully counteracts the increased MTB line charge λ. The narrower well leads to fewer confined eigenenergies in the model, qualitatively reproducing the experimental observations in (e).

The O-modified situation in the VB is modelled in Fig. 5(l). Compared to the model for MoS_2 on Gr/Ir, (c), there is only one meaningful change to the parameters: the width of the dielectric b is increased by $0.4\,\mathrm{nm}$. This is a crude attempt to replicate the increased Mo/Gr-Ir separation due to the decoupling O-interlayer. Thus the line charge is brought further away from the metal substrate and its image charges their, and the screening is reduced. The results in a wider potential well and recreates the smaller energetic spacing of the quantized VB states as seen in (h).

IV. DISCUSSION

A. Macroscopic effects

In Section III B the band structure of MoS_2 was altered by intercalants under the Gr layer. The effect is most drastic in the case of Eu, which strongly n-dopes the Gr. We first consider the band realignment due to the reduction in the Gr work function $\Delta\Phi_{\mathrm{Gr}} = -1.4\,\mathrm{eV}$, and what this tells us about the MoS_2-Gr interlayer interaction. Extracting the change in MoS_2 Schottky barrier height $\Delta\Phi_{\mathrm{b}}$ is not trivial because the bands are also renormalized, but we can take the rigid shift $\Delta E_{\Phi}^{\mathrm{Eu}} = -0.365\,\mathrm{eV}$ and the change in electron affinity $\Delta E_{\mathrm{CB}}^{\mathrm{Eu}} = -0.70\,\mathrm{eV}$ as lower and upper bounds, respectively. The Schottky barrier response of our semiconductor-metal junction is characterized by the pinning factor $S = \Delta\Phi_{\mathrm{b}}/\Delta\Phi_{\mathrm{Gr}}$. In the Schottky-Mott limit $S = 1$; in the limit of perfect Fermi level pinning (FLP) $S \approx 0$ [60, 61]. We find a pinning factor in the range $S = 0.26 - 0.50$ using the bounds given above.

This represents weaker FLP than the values $S \sim 0.1$

seen for MoS_2-3D metal junctions [62], where metal-induced gap states [63] or interface defects [64, 65] pin the Fermi level. The former has been refuted for van der Waals heterostructures [12] and we see no gap states in STS (Fig. 3). The latter is equally unlikely judging by the high crystalline quality of both MoS_2 and Gr in STM. A possible explanation for FLP in our system is an interface dipole, formed due to charge redistribution between MoS_2 and Gr, which causes a shift in energies [12, 56, 66, 67].

The moderate FLP here contrasts with similar TMDC-Gr van der Waals heterostructures where pinning factors close to $S \approx 1$ were reported [22, 23]. This could be explained by the fact that in Refs. 22 and 23 the substrate work function change was only around 0.15 eV, whereas in our the case the heavy doping of Gr may induce a much more significant interface dipole across the van der Waals gap [68]. A strengthened electronic interaction between MoS_2 and Gr is in agreement with the growth morphology changes discussed in Section III A.

The other significant change to the MoS_2 band structure on Gr/Eu/Ir is a band gap reduction of $\Delta E_\mathrm{g} = (0.67 \pm 0.15)$ eV compared to Gr/Ir. This would represent a huge band gap renormalization due to dielectric screening. Comparing this value to similar 2D TMDC-Gr heterostructures: $MoSe_2$ underwent a STS-measured renormalization of 0.24 eV on bilayer-Gr/SiC as compared to HOPG [6]. ReS_2 underwent a renormalization of 0.22 eV when a 108 V gate voltage was applied to its Gr substrate, amounting to a $\Delta n = 7.7 \times 10^{12}\,\mathrm{cm}^{-2}$ charge carrier increase in Gr [19]. In a somewhat different device configuration, a 0.40 eV renormalization was seen in WSe_2 in response to $\Delta n = 1.5 \times 10^{13}\,\mathrm{cm}^{-2}$ gate doping [18]. Meanwhile, *GW* calculations of a MoS_2-Gr heterostructure found that shifting the Gr Fermi level by 0.8 eV would cause a 0.3 eV renormalization in MoS_2, but upon further gating the effect apparently levels off [69].

In our case, the Eu-interlayer results in a Gr charge carrier density of $n \approx 1 \times 10^{14}\,\mathrm{cm}^{-2}$ [57]. This level of gating goes beyond what is capable in standard field-effect transistors [70]. Thus the $\Delta E_\mathrm{g} = (0.67 \pm 0.15)$ eV band gap reduction may represent a much larger band gap renormalization than is typically reported for dielectrically screened 2D TMDC semiconductors in literature. On the other hand, the fact that it is considerably larger than theoretical predictions [69, 71] suggests that the band gap reduction is not soley due to increased dielectric screening by Gr. It is possible that the increased MoS_2-Gr interaction, discussed above, will lead to other effects such as increased orbital coupling between the layers [72], hybridization of bands [20, 73], or ‘pseudodoping’ [70].

We have assumed that the screening-induced band gap renormalization occurs symmetrically [25, 56]. However, other studies of dielectric screening predicted asymmetry, with most of the shift occuring in the VB [74]. Furthermore, the renormalization is dependent on the effective mass of each band [71], and so we can expect slightly stronger renormalization at the Q-point than the K-point [75], for example. Further theoretical investigation of the free-particle TMDC bandstructure's response to strong dielectric screening could be wished [56]. Studies typically focus on excitation-induced renormalization [76–79], perhaps because the optical band gap of TMDCs is more experimentally accessible.

In Section III B we observed that the O-interlayer causes a slight upwards shift of MoS_2 bands, presumably through its p-doping of Gr. No significant band gap renormalization was detected. It perhaps seems contradictory that there is an increased charge carrier density in Gr but negligible increase in dielectric screening. However, with only weak doping the Gr may still be incapable of effective screening (large Thomas-Fermi screening radius). Meanwhile, the aforementioned decoupling effect of the O-interlayer will have reduced the screening contribution from the Ir substrate, offsetting any increased screening contribution from Gr.

B. Charged defects

In Section III C we observed that the filling of 4|4E MTB bands is altered by the Eu-interlayer, the clear explanation being that the n-doped Gr can donate extra charge to the metallic defect band. This is directly visible in STM and STS, where the periodicity of the confined states shows a change from $l_\mathrm{F}^\mathrm{Gr} = 2.01\,a$ to $l_\mathrm{F}^\mathrm{Eu} = 2.69\,a$. This shows that Eu-interlayer can strongly perturb the MoS_2 electronically. At the same time, the Eu-interlayer has not disturbed the MoS_2 chemically or structurally, and so the one-dimensionality of the confined MTB states is preserved, as demonstrated in Fig. 4(e).

An interesting outcome of the results is that, despite some amount of p-gating by the O-interlayer, we do not see the expected increase in l_F for the electron-like band of the 4|4P MTB, see Fig. S6. Moreover, the 4|4P MTB has now shown an approximate $3a$ beating in monolayers of MoS_2 or $MoSe_2$ on a multitude of substrates: Gr/Ir(111) [33], Gr/O/Ir(111), bulk MoS_2 [36], graphite [80], bilayer Gr on SiC(0001) [35]. These substrates have a wide range of work functions. This, in tandem with our results here, suggests that the Fermi wavevector in 4|4P MTBs locks into $k_\mathrm{F} = \frac{\pi}{3a}$, i.e. that it prefers to be commensurate with the lattice. This points towards strong electron-phonon coupling in 4|4P-type MTBs. Thus the incommensurate $l_\mathrm{F}^\mathrm{Eu} = 2.69\,a$ periodicity observed in 4|4E MTB in MoS_2/Gr/Eu/Ir(111) represents something unique.

In Section III D the band bending at 4|4E MTBs, and in particular the quantization of the VB, was affected by the changed charge and screening environments. Through some rather crude changes to our previously used electrostatic model [34], we could qualitatively recreate the effects of the Eu- and O-interlayers. In the case of the former, we incorporated the additional net MTB charge of $\lambda = -0.26\,e/a$ inferred from the changed band filling. The increased screening effectiveness of the heavily doped Gr layer was also taken into account, giving a much narrower potential well and thus steeper band bending and fewer quantized states.

A peculiar observation from the band bending at in MoS_2/Gr/Eu/Ir is the slight dip in the bands before their steep rise, see Figs.5(e) and S6(b). This effect was recreated in modelling by making the metal substrate 'over-screen', in essence making positive images of greater charge than necessary. This kind of screening overcompensation has parallels to the phenomenon of Friedel oscillations. We tentatively propose this over-screening dip to result from Friedel oscillations normal to the MTB in the Gr layer. This has been predicted to occur in highly doped layers of Gr when there is a charged impurity in an adjacent layer [81]. In our case, the MTB is highly charged and the Gr has a large concentration of free carriers due to the Eu-interlayer. We imagine Friedel oscillations forming in the Gr as it screens the MTB. The low density part of the oscillation is reflected in a slight dip in the potential felt by the MoS_2 layer above. This conjecture must be verified with considerations of the apparent length scale and k_F of the Eu-intercalated Gr.

Another strange aspect of the band bending in MoS_2/Gr/Eu/Ir(111) is the fact that the quantized state at $-1.3\,eV$ appears to penetrate the barrier of the MTB, and has a kink on the left side. (Note that the kink on the right is a tip artefact, evidenced by the abrupt discontinuity; see Fig. S7(b) in which it is absent.) This was seen consistently across many measured 4|4E MTBs. One possible explanation for this is that the increased MoS_2-Gr interaction has caused a tunnelling channel to open up at that energy. This energy coincides with the Dirac point of Gr on Eu/Ir(111), though this may be purely coincidental.

The band bending at 4|4E MTBs in MoS_2/Gr/O/Ir(111) occurs over a slightly wider range and more quantized VB states are visible. This points towards weaker screening by the metal substrate, as recreated in our model. This is consistent with a decoupling effect of the O-interlayer. Despite a slightly increased charge carrier density in Gr, it still fails to screen effectively. It is clear that more sophisticated modelling and theoretical consideration is needed, both of the MoS_2 band structure and of the effects at MTBs.

V. CONCLUSION

We have demonstrated a non-invasive method to modify the electronic environment of ML-MoS_2, applicable also to other TMDCs and van der Waals materials. This was achieved by intercalating the Gr upon which MoS_2 sits, with Eu or O to n- or p-dope the Gr respectively. This offers a route towards gating TMDC monolayers in UHV without the need for a back-gated device setup. Furthermore, the drastic 0.67 eV band gap reduction of MoS_2 due the introduction of Eu illustrates that this method offers stronger gating than that available in standard heterostructure devices. This backside functionalization of Gr leaves the TMDC top layer chemically pristine, thereby offering advantages over chemical doping or adatom techniques.

As well as changing the ML-MoS_2 band structure, the doped Gr substrate also modified 1D states at MoS_2 line defects. The changed periodicity of the states confined to the 4|4E MTB allow an estimate of the 1D band filling and in turn the additional charge transferred by Gr. The surviving one-dimensionality of the MTB is evidenced by a rich excitation spectrum of confined states. Band bending normal to the MTBs reflected not only the changed defect charge, but also changes to the dielectric screening efficiency of the substrate. The energies of quantized 1D states in the MoS_2 VB could be tuned in this way, and indeed many properties of monolayer TMDCs could be investigated in different charge and screening environments, by using various intercalants such as alkalis [82], other rare earth metals [83] or the p-dopant chlorine [84].

ACKNOWLEDGMENTS

This work was funded by the Deutsche Forschungsgemeinschaft (DFG, German Research Foundation) - Project number 277146847 - CRC 1238 (subprojects A01 and B06).

[1] K. F. Mak, C. Lee, J. Hone, J. Shan, and T. F. Heinz, Phys. Rev. Lett. **105**, 136805 (2010).

[2] A. Chernikov, A. M. van der Zande, H. M. Hill, A. F. Rigosi, A. Velauthapillai, J. Hone, and T. F. Heinz, Phys. Rev. Lett. **115**, 126802 (2015).

[3] D. Costanzo, S. Jo, H. Berger, and A. F. Morpurgo, Nat. Nanotechnol. **11**, 339 (2016).

[4] A. Raja, L. Waldecker, J. Zipfel, Y. Cho, S. Brem, J. D. Ziegler, M. Kulig, T. Taniguchi, K. Watanabe, E. Malic, T. F. Heinz, T. C. Berkelbach, and A. Chernikov, Nat. Nanotechnol. **14**, 832 (2019).

[5] A. Chernikov, T. C. Berkelbach, H. M. Hill, A. Rigosi, Y. Li, O. B. Aslan, D. R. Reichman, M. S. Hybertsen, and T. F. Heinz, Phys. Rev. Lett. **113**, 076802 (2014).

[6] M. M. Ugeda, A. J. Bradley, S. F. Shi, F. H. Da Jornada, Y. Zhang, D. Y. Qiu, W. Ruan, S. K. Mo, Z. Hussain, Z. X. Shen, F. Wang, S. G. Louie, and M. F. Crommie, Nat. Mater. **13**, 1091 (2014).

[7] H.-P. Komsa and A. V. Krasheninnikov, Phys. Rev. B **86**, 241201 (2012).

[8] L. A. Jauregui, A. Y. Joe, K. Pistunova, D. S. Wild, A. A. High, Y. Zhou, G. Scuri, K. De Greve, A. Sushko, C.-H. Yu, T. Taniguchi, K. Watanabe, D. J. Needleman, M. D. Lukin, H. Park, and P. Kim, Science **366**, 870 (2019).

[9] M. E. Beck and M. C. Hersam, ACS Nano **XXX**, acsnano.0c03299 (2020).

[10] A. Rai, H. Movva, A. Roy, D. Taneja, S. Chowdhury, and S. Banerjee, Crystals **8**, 316 (2018).

[11] Y. Liu, H. Wu, H.-C. Cheng, S. Yang, E. Zhu, Q. He, M. Ding, D. Li, J. Guo, N. O. Weiss, Y. Huang, and X. Duan, Nano Lett. **15**, 3030 (2015).

[12] Y. Liu, P. Stradins, and S.-H. Wei, Sci. Adv. **2**, e1600069 (2016).

[13] N. Alidoust, G. Bian, S.-Y. Xu, R. Sankar, M. Neupane, C. Liu, I. Belopolski, D.-X. Qu, J. D. Denlinger, F.-C. Chou, and M. Z. Hasan, Nat. Commun. **5**, 4673 (2014).

[14] Y. Zhang, T.-R. Chang, B. Zhou, Y.-T. Cui, H. Yan, Z. Liu, F. Schmitt, J. Lee, R. Moore, Y. Chen, H. Lin, H.-T. Jeng, S.-K. Mo, Z. Hussain, A. Bansil, and Z.-X. Shen, Nat. Nanotechnol. **9**, 111 (2014).

[15] M. Kang, B. Kim, S. H. Ryu, S. W. Jung, J. Kim, L. Moreschini, C. Jozwiak, E. Rotenberg, A. Bostwick, and K. S. Kim, Nano Lett. **17**, 1610 (2017).

[16] J. Katoch, S. Ulstrup, R. J. Koch, S. Moser, K. M. McCreary, S. Singh, J. Xu, B. T. Jonker, R. K. Kawakami, A. Bostwick, E. Rotenberg, and C. Jozwiak, Nat. Phys. **14**, 355 (2018).

[17] L. Daukiya, M. Nair, M. Cranney, F. Vonau, S. Hajjar-Garreau, D. Aubel, and L. Simon, Prog. Surf. Sci. **94**, 1 (2019).

[18] P. V. Nguyen, N. C. Teutsch, N. P. Wilson, J. Kahn, X. Xia, A. J. Graham, V. Kandyba, A. Giampietri, A. Barinov, G. C. Constantinescu, N. Yeung, N. D. M. Hine, X. Xu, D. H. Cobden, and N. R. Wilson, Nature **572**, 220 (2019).

[19] Z. Qiu, M. Trushin, H. Fang, I. Verzhbitskiy, S. Gao, E. Laksono, M. Yang, P. Lyu, J. Li, J. Su, M. Telychko, K. Watanabe, T. Taniguchi, J. Wu, A. H. C. Neto, L. Yang, G. Eda, S. Adam, and J. Lu, Sci. Adv. **5**, eaaw2347 (2019).

[20] Q. Zhang, Y. Chen, C. Zhang, C.-R. Pan, M.-Y. Chou, C. Zeng, and C.-K. Shih, Nat. Commun. **7**, 13843 (2016).

[21] M. Dendzik, A. Bruix, M. Michiardi, A. S. Ngankeu, M. Bianchi, J. A. Miwa, B. Hammer, P. Hofmann, and C. E. Sanders, Phys. Rev. B **96**, 235440 (2017).

[22] T. Le Quang, V. Cherkez, K. Nogajewski, M. Potemski, M. T. Dau, M. Jamet, P. Mallet, and J.-Y. Veuillen, 2D Mater. **4**, 035019 (2017).

[23] S. Ulstrup, C. E. Giusca, J. A. Miwa, C. E. Sanders, A. Browning, P. Dudin, C. Cacho, O. Kazakova, D. K. Gaskill, R. L. Myers-Ward, T. Zhang, M. Terrones, and P. Hofmann, Nat. Commun. **10**, 3283 (2019).

[24] Y. Pan, S. Fölsch, Y.-C. Lin, B. Jariwala, J. A. Robinson, Y. Nie, K. Cho, and R. M. Feenstra, 2D Mater. **6**, 021001 (2019).

[25] L. Waldecker, A. Raja, M. Rösner, C. Steinke, A. Bostwick, R. J. Koch, C. Jozwiak, T. Taniguchi, K. Watanabe, E. Rotenberg, T. O. Wehling, and T. F. Heinz, Phys. Rev. Lett. **123**, 206403 (2019).

[26] M. I. B. Utama, H. Kleemann, W. Zhao, C. S. Ong, F. H. da Jornada, D. Y. Qiu, H. Cai, H. Li, R. Kou, S. Zhao, S. Wang, K. Watanabe, T. Taniguchi, S. Tongay, A. Zettl, S. G. Louie, and F. Wang, Nat. Electron. **2**, 60 (2019).

[27] A. Bruix, J. A. Miwa, N. Hauptmann, D. Wegner, S. Ulstrup, S. S. Grønborg, C. E. Sanders, M. Dendzik, A. Grubišić Čabo, M. Bianchi, J. V. Lauritsen, A. A. Khajetoorians, B. Hammer, and P. Hofmann, Phys. Rev. B **93**, 165422 (2016).

[28] X. Liu, I. Balla, H. Bergeron, G. P. Campbell, M. J. Bedzyk, and M. C. Hersam, ACS Nano **10**, 1067 (2016).

[29] J. Shi, X. Zhou, G.-F. Han, M. Liu, D. Ma, J. Sun, C. Li, Q. Ji, Y. Zhang, X. Song, X.-Y. Lang, Q. Jiang, Z. Liu, and Y. Zhang, Adv. Mater. Interfaces **3**, 1600332 (2016).

[30] J. Klein, A. Kerelsky, M. Lorke, M. Florian, F. Sigger, J. Kiemle, M. C. Reuter, T. Taniguchi, K. Watanabe, J. J. Finley, A. N. Pasupathy, A. W. Holleitner, F. M. Ross, and U. Wurstbauer, Appl. Phys. Lett. **115**, 261603 (2019).

[31] Y. L. Huang, Y. Chen, W. Zhang, S. Y. Quek, C.-H. Chen, L.-J. Li, W.-T. Hsu, W.-H. Chang, Y. J. Zheng, W. Chen, and A. T. S. Wee, Nat. Commun. **6**, 6298 (2015).

[32] C. Murray, W. Jolie, J. A. Fischer, J. Hall, C. van Efferen, N. Ehlen, A. Grüneis, C. Busse, and T. Michely, Phys. Rev. B **99**, 115434 (2019).

[33] W. Jolie, C. Murray, P. S. Weiß, J. Hall, F. Portner, N. Atodiresei, A. V. Krasheninnikov, C. Busse, H.-P. Komsa, A. Rosch, and T. Michely, Phys. Rev. X **9**, 011055 (2019).

[34] C. Murray, C. V. Efferen, W. Jolie, J. A. Fischer, J. Hall, A. Rosch, A. Krasheninnikov, H.-P. Komsa, and T. Michely, under review , 1 (2020).

[35] S. Barja, S. Wickenburg, Z. F. Liu, Y. Zhang, H. Ryu, M. M. Ugeda, Z. Hussain, Z. X. Shen, S. K. Mo, E. Wong, M. B. Salmeron, F. Wang, M. F. Crommie, D. F. Ogletree, J. B. Neaton, and A. Weber-Bargioni, Nat. Phys. **12**, 751 (2016).

[36] Y. Ma, H. C. Diaz, J. Avila, C. Chen, V. Kalappattil, R. Das, M.-H. Phan, T. Cadez, J. M. P. Carmelo, M. C. Asensio, and M. Batzill, Nat. Commun. **8**, 14231 (2017).

[37] J. Coraux, A. T. N'Diaye, M. Engler, C. Busse, D. Wall, N. Buckanie, F. J. Meyer zu Heringdorf, R. van Gastel, B. Poelsema, and T. Michely, New J. Phys. **11**, 023006 (2009).

[38] J. Hall, B. Pielić, C. Murray, W. Jolie, T. Wekking, C. Busse, M. Kralj, and T. Michely, 2D Mater. **5**, 025005 (2018).

[39] S. Schumacher, D. F. Förster, M. Rösner, T. O. Wehling, and T. Michely, Phys. Rev. Lett. **110**, 086111 (2013).

[40] S. Schumacher, F. Huttmann, M. Petrović, C. Witt, D. F. Förster, C. Vo-Van, J. Coraux, A. J. Martínez-Galera, V. Sessi, I. Vergara, R. Rückamp, M. Grüninger, N. Schleheck, F. Meyer zu Heringdorf, P. Ohresser, M. Kralj, T. O. Wehling, and T. Michely, Phys. Rev. B **90**, 235437 (2014).

[41] E. Grånäs, J. Knudsen, U. A. Schröder, T. Gerber, C. Busse, M. A. Arman, K. Schulte, J. N. Andersen, and T. Michely, ACS Nano **6**, 9951 (2012).

[42] A. J. Martínez-Galera, U. A. Schröder, F. Huttmann, W. Jolie, F. Craes, C. Busse, V. Caciuc, N. Atodiresei, S. Blügel, and T. Michely, Nanoscale **8**, 1932 (2016).

[43] M. Morgenstern, Surf. Rev. Lett. **10**, 933 (2003).

[44] K. H. Gundlach, Solid State Electron. **9**, 949 (1966).

[45] T. Jung, Y. W. Mo, and F. J. Himpsel, Phys. Rev. Lett. **74**, 1641 (1995).

[46] H.-P. Komsa and A. V. Krasheninnikov, Adv. Electron. Mater. **3**, 1600468 (2017).

[47] C. L. Lin, S. M. Lu, W. B. Su, H. T. Shih, B. F. Wu, Y. D. Yao, C. S. Chang, and T. T. Tsong, Phys. Rev. Lett. **99**, 216103 (2007).

[48] D. F. Förster, T. O. Wehling, S. Schumacher, A. Rosch,

and T. Michely, New J. Phys. **14**, 023022 (2012).

[49] S. Schintke, S. Messerli, M. Pivetta, F. Patthey, L. Libioulle, M. Stengel, A. De Vita, and W.-D. Schneider, Phys. Rev. Lett. **87**, 276801 (2001).

[50] I. Pletikosić, M. Kralj, P. Pervan, R. Brako, J. Coraux, A. T. N'Diaye, C. Busse, and T. Michely, Phys. Rev. Lett. **102**, 056808 (2009).

[51] S. Ulstrup, M. Andersen, M. Bianchi, L. Barreto, B. Hammer, L. Hornekær, and P. Hofmann, 2D Mater. **1**, 025002 (2014).

[52] W. Jolie, F. Craes, M. Petrović, N. Atodiresei, V. Caciuc, S. Blügel, M. Kralj, T. Michely, and C. Busse, Phys. Rev. B **89**, 155435 (2014).

[53] B. Pielić, J. Hall, V. Despoja, I. Š. Rakić, M. Petrović, A. Sohani, C. Busse, T. Michely, and M. Kralj, J. Phys. Chem. C **124**, 6659 (2020).

[54] C. Zhang, Y. Chen, A. Johnson, M.-Y. Li, L.-J. Li, P. C. Mende, R. M. Feenstra, and C.-K. Shih, Nano Lett. **15**, 6494 (2015).

[55] N. Krane, C. Lotze, and K. J. Franke, Surf. Sci. **678**, 136 (2018).

[56] Y. Cho and T. C. Berkelbach, Phys. Rev. B **97**, 041409 (2018).

[57] U. A. Schröder, M. Petrović, T. Gerber, A. J. Martínez-Galera, E. Grånäs, M. A. Arman, C. Herbig, J. Schnadt, M. Kralj, J. Knudsen, and T. Michely, 2D Mater. **4**, 015013 (2016).

[58] X. Zou, Y. Liu, and B. I. Yakobson, Nano Lett. **13**, 253 (2013).

[59] T. Le Quang, K. Nogajewski, M. Potemski, M. T. Dau, M. Jamet, P. Mallet, and J.-Y. Veuillen, 2D Mater. **5**, 035034 (2018).

[60] R. T. Tung, Appl. Phys. Rev. **1**, 011304 (2014).

[61] A. Allain, J. Kang, K. Banerjee, and A. Kis, Nat. Mater. **14**, 1195 (2015).

[62] S. Das, H.-Y. Chen, A. V. Penumatcha, and J. Appenzeller, Nano Lett. **13**, 100 (2013).

[63] C. Gong, L. Colombo, R. M. Wallace, and K. Cho, Nano Lett. **14**, 1714 (2014).

[64] P. Bampoulis, R. van Bremen, Q. Yao, B. Poelsema, H. J. W. Zandvliet, and K. Sotthewes, ACS Appl. Mater. Interfaces **9**, 19278 (2017).

[65] K. M. Freedy and S. J. McDonnell, Materials (Basel). **13**, 693 (2020).

[66] R. T. Tung, Phys. Rev. B **64**, 205310 (2001).

[67] Y. J. Dappe, Y. Almadori, M. T. Dau, C. Vergnaud, M. Jamet, C. Paillet, T. Journot, B. Hyot, P. Pochet, and B. Grévin, Nanotechnology **31**, 255709 (2020).

[68] C. Si, Z. Lin, J. Zhou, and Z. Sun, 2D Mater. **4**, 015027 (2017).

[69] A. C. Riis-Jensen, J. Lu, and K. S. Thygesen, Phys. Rev. B **101**, 121110 (2020).

[70] B. Shao, A. Eich, C. Sanders, A. S. Ngankeu, M. Bianchi, P. Hofmann, A. A. Khajetoorians, and T. O. Wehling, Nat. Commun. **10**, 180 (2019).

[71] B. Scharf, D. Van Tuan, I. Žutić, and H. Dery, J. Phys. Condens. Matter **31**, 203001 (2019).

[72] A. J. Bradley, M. M. Ugeda, F. H. Da Jornada, D. Y. Qiu, W. Ruan, Y. Zhang, S. Wickenburg, A. Riss, J. Lu, S. K. Mo, Z. Hussain, Z. X. Shen, S. G. Louie, and M. F. Crommie, Nano Lett. **15**, 2594 (2015).

[73] M. H. Naik and M. Jain, Phys. Rev. Mater. **2**, 084002 (2018).

[74] M. Rösner, C. Steinke, M. Lorke, C. Gies, F. Jahnke, and T. O. Wehling, Nano Lett. **16**, 2322 (2016).

[75] H. Peelaers and C. G. Van de Walle, Phys. Rev. B **86**, 241401 (2012).

[76] Y. Liang and L. Yang, Phys. Rev. Lett. **114**, 063001 (2015).

[77] D. Erben, A. Steinhoff, C. Gies, G. Schönhoff, T. O. Wehling, and F. Jahnke, Phys. Rev. B **98**, 035434 (2018).

[78] S. Gao and L. Yang, Phys. Rev. B **96**, 155410 (2017).

[79] L. Meckbach, T. Stroucken, and S. W. Koch, Appl. Phys. Lett. **112**, 061104 (2018).

[80] H. Liu, L. Jiao, F. Yang, Y. Cai, X. Wu, W. Ho, C. Gao, J. Jia, N. Wang, H. Fan, W. Yao, and M. Xie, Phys. Rev. Lett. **113**, 066105 (2014).

[81] P. B. Visscher and L. M. Falicov, Phys. Rev. B **3**, 2541 (1971).

[82] M. Petrović, I. Šrut Rakić, S. Runte, C. Busse, J. T. Sadowski, P. Lazić, I. Pletikosić, Z.-H. Pan, M. Milun, P. Pervan, N. Atodiresei, R. Brako, D. Šokčević, T. Valla, T. Michely, and M. Kralj, Nat. Commun. **4**, 2772 (2013).

[83] I. Klimovskikh, M. Krivenkov, A. Varykhalov, D. Estyunin, and A. Shikin, Carbon N. Y. **147**, 182 (2019).

[84] N. A. Vinogradov, K. A. Simonov, A. V. Generalov, A. S. Vinogradov, D. V. Vyalikh, C. Laubschat, N. Mårtensson, and A. B. Preobrajenski, J. Phys. Condens. Matter **24**, 314202 (2012).

8.1 Manuscript 4: Supporting Information

Supporting Information: Manipulating MoS_2 and its 1D phenomena via substrate screening and charge

Clifford Murray,[1,*] Camiel van Efferen,[1] Wouter Jolie,[1,2]
Joshua Hall,[1] Jeison A. Fischer,[1] and Thomas Michely[1]

[1]*II. Physikalisches Institut, Universität zu Köln,*
Zülpicher Straße 77, 50937 Köln, Germany
[2]*Institut für Materialphysik, Westfälische Wilhelms-Universität Münster,*
Wilhelm-Klemm-Straße 10, 48149 Münster, Germany

(Dated: November 13, 2020)

---

[*] murray@ph2.uni-koeln.de

The Supporting Information includes: (S1) LEED of the MoS_2/Gr/Eu/Ir(111) sample; (S2) QPI in Gr/O/Ir(111); (S3) FER spectroscopy of Gr/Eu/Ir(111) and (S4) of Gr/O/Ir(111); (S5) constant height STM of the 4|4P MTB confined states in MoS_2/Gr/O/Ir(111); (S6) Supplementary data to the 4|4E MTB confined states in MoS_2/Gr/Eu/Ir(111); (S7) constant height STS linescans over 4|4E MTBs in MoS_2/Gr/Eu/Ir(111) and MoS_2/Gr/O/Ir(111).

S1: LEED of MoS_2/Gr/Eu/Ir(111)

Fig. S1 shows various steps of the MoS_2/Gr/Eu/Ir(111) sample growth process. In (a) the typical pattern of Gr, Ir(111) and their moiré satellite spots are seen. In (b), after dosing Eu onto a hot (720 K) Gr/Ir(111) sample, an apparent (2 × 2)-Eu phase is visible. In (c), after MoS_2 has been grown, the Eu-intercalation superstructure is no longer visible in LEED. This will be partly due to its greatly weakened intensity in this surface-sensitive technique; MoS_2 preferentially grows on the intercalated Gr areas (see main text) and then much of the Eu-interlayer will essentially be under 4 layers of atoms (S-Mo-S-C).

We cannot rule out that the introduction of MoS_2 has changed the Eu-intercalation structure. A plausible explanation is that the slight p-doping of Gr by MoS_2 [4] has changed the binding conditions for Eu. This could explain why a previously unreported c(4 × 2) intercalation superstructure is seen in STM. Alternatively, a symmetry lowering may have occurred upon cooling to 5 K; previous studies of Gr/Eu/Ir(111) did not investigate below 35 K.

Imperfect epitaxial alignment of MoS_2 with respect to Gr/Ir(111) is illustrated by the fact that it forms a ring in LEED, rather than a spot aligned with those of Gr and Ir(111). Compare Fig. 2(c) of Ref. [1] in which MoS_2 is well aligned with the substrate. The ring in Fig. S1(c) nonetheless has its strongest intensity in the Gr and Ir(111) directions, indicating that the epitaxy of the MoS_2 islands is not completely disordered. These observations are in agreement with those from STM, Fig. 2(b).

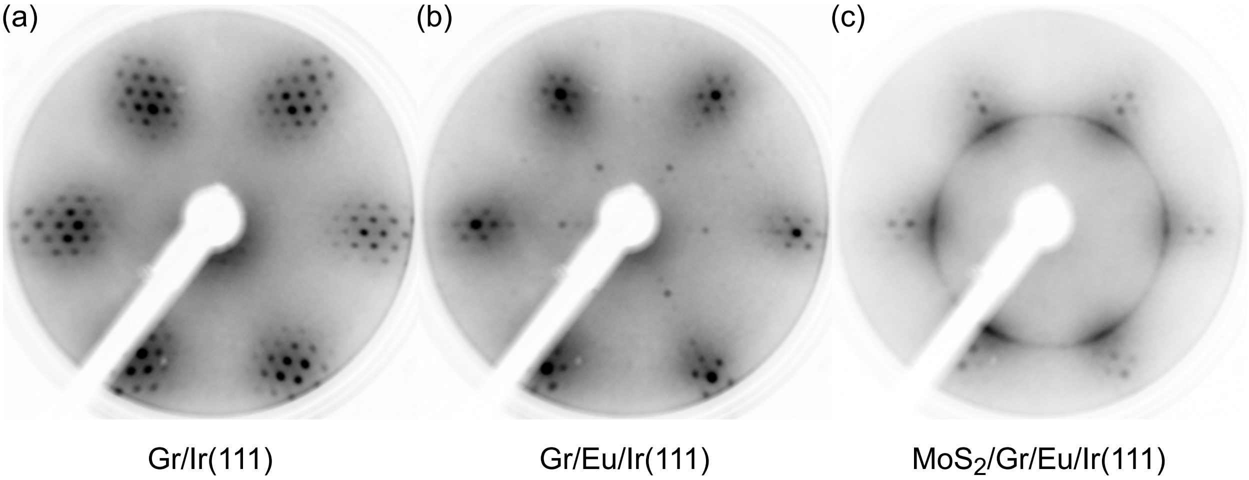

Fig. S1. LEED patterns showing the state of MoS_2/Gr/Eu/Ir(111) sample at various steps; see Methods in main text. (a-c) All with 137 eV electron energy; not corrected for MCP distortion. All recorded with sample at room temperature.

S2: FER spectroscopy of Gr/Eu/Ir(111)

Fig. S2 shows a FER spectroscopy linescan of the MoS_2/Gr/Eu/Ir(111) sample, investigating the effect of the Eu-interlayer on the Gr work function. The shifting of the resonance energies from one region to the other indicates the work function change: it is $\Delta\Phi_{\mathrm{Gr}} = (1.4 \pm 0.1)\,\mathrm{eV}$ lower for Eu-intercalated Gr. Furthermore, the Gr/Eu/Ir(111) region shows some small energy deviations within the island but overall indicates rather uniform gating.

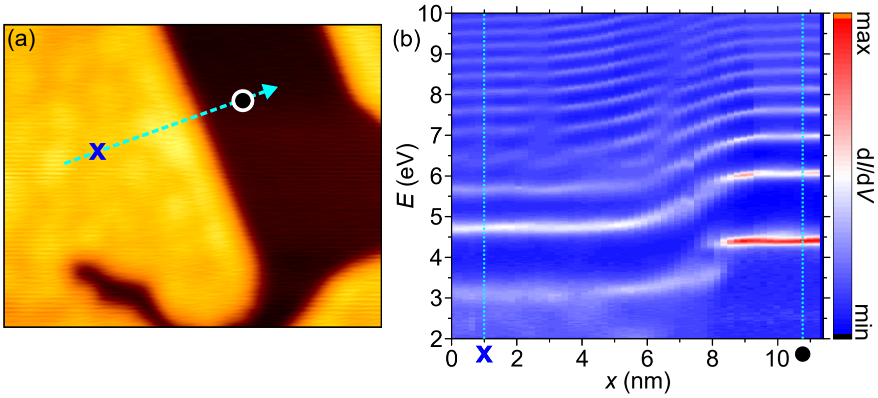

Fig. S2. FER spectroscopy linescan from a region of Gr/Eu/Ir(111) to a region of Gr/Ir(111). (a) Topograph, same as that of the inset in Fig. 2(c) main text. The path of the linescan is indicated by an arrow. (b) The linescan shows field-emission resonances on Gr/Eu/Ir(111) ($x = 0 - 8\,\mathrm{nm}$) and on Gr/Ir(111). The individual spectra shown in Fig. 2(c) of the main text are highlighted by dotted lines and their respective symbols. STM/STS parameters: (a) $20 \times 16\,\mathrm{nm}^2$, $V = 1.0\,\mathrm{V}$, $I = 0.04\,\mathrm{nA}$; (b) $V_{\mathrm{st}} = 2\,\mathrm{V}$, $I_{\mathrm{st}} = 0.1\,\mathrm{nA}$.

S3: QPI in Gr/O/Ir(111)

Fig. S3 shows an STM topograph of a Gr patch from the MoS_2/Gr/O/Ir(111) sample. Outside of the image, to the top left, is the edge of a Gr flake. Standing waves can be made out – this is quasi-particle interference (QPI). In the Fourier transformation of the image, (b), the six Gr spots are seen along with an additional periodicity due to the QPI, highlighted. These are not spots, but rather open circles. These are associated with intervalley scattering in Gr [5, 6], and indicate a decoupling of Gr from Ir(111) by the O-interlayer [7].

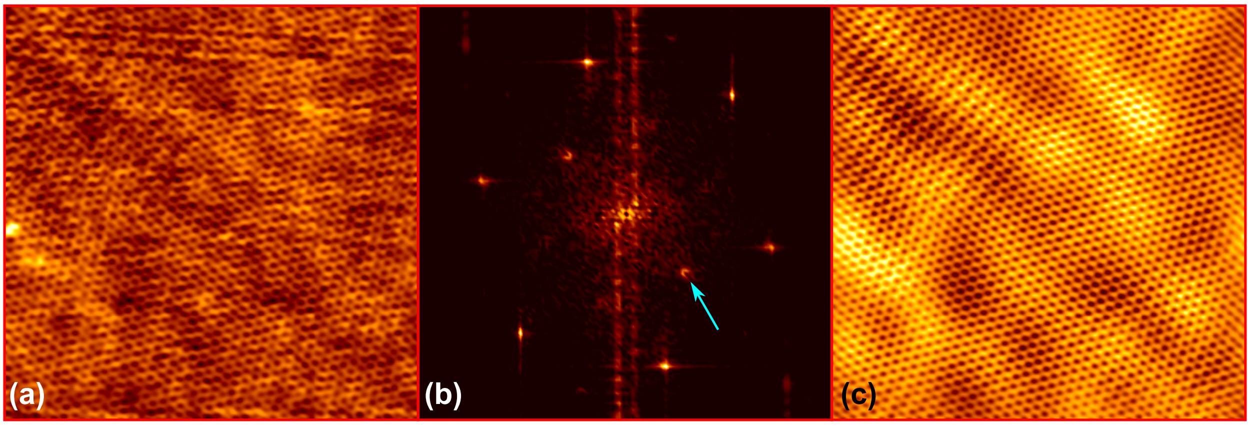

Fig. S3. STM showing standing waves in Gr/O/Ir(111). (a) Constant current STM topograph of Gr, recorded close to the E_F. (b) Fourier transform of (a), with feature indicated. (c) The topograph of (a) filtered to highlight the standing waves coming from the top right corner of the image. STM parameters: $V = 0.010\,\mathrm{V}$, $I = 0.5\,\mathrm{nA}$, image size (a) $10 \times 10\,\mathrm{nm}^2$ (b) $13 \times 13\,\mathrm{nm}^{-2}$.

S4: FER spectroscopy of Gr/O/Ir(111)

Fig. S4 shows a FER spectroscopy linescan of the MoS_2/Gr/O/Ir(111) sample. As noted in the main text, there are no patches of Gr which are not O-intercalated, and so a work function comparison (as above) is not possible. A FER linescan solely over Gr/O/Ir(111) regions is nonetheless instructive. We see that there is some local variation in the resonance energies, presumably due to the inhomogeneity of the O-interlayer. However, particularly in the higher energy resonances (which are more reliable [8]), the work function is more or less constant throughout the Gr layer.

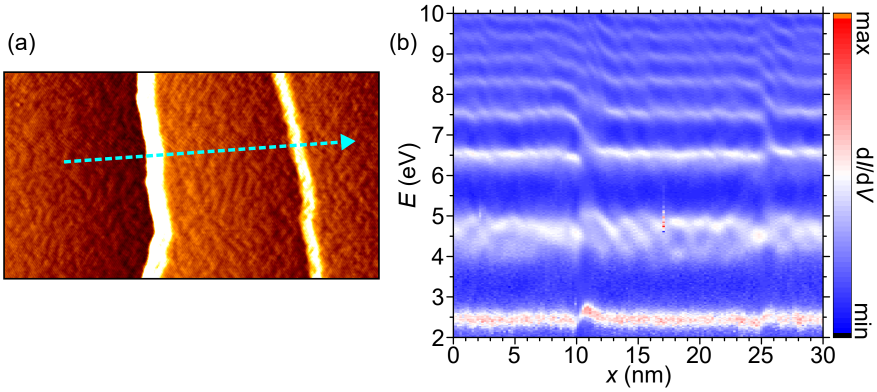

Fig. S4. FER spectroscopy linescan over Gr/O/Ir(111), crossing three Ir(111) step edges. (a) Topograph; from left to right the steps go from low to high. The current and height images have been merged to accentuate the inhomogeneous superstructure due to the O-interlayer. The path of the linescan (b) is indicated by an arrow. STM/STS parameters: (a) $40 \times 22\,\mathrm{nm}^2$, $V = 1.0\,\mathrm{V}$, $I = 0.1\,\mathrm{nA}$; (b) $V_{\mathrm{st}} = 2\,\mathrm{V}$, $I_{\mathrm{st}} = 0.1\,\mathrm{nA}$.

S5: Confined states in 4|4E MTBs in MoS_2/Gr/Eu/Ir(111)

Fig. S5(a) shows the $\approx$ 18 nm long 4|4E MTB in MoS_2/Gr/Eu/Ir(111) at which the linescan of Fig. 4(e) was recorded. In the main text a linear interpolation of the STS data was performed for consistency with Ref. [9]; in (b) the discrete data is displayed. In (c) we plot the measured Fermi level gap size E_{gap} for 4|4E MTBs of various lengths. A line is fitted of form $E_{gap} = A/L + B$, with $A = (1.81 \pm 0.18)$ eV.nm and $B = (-30 \pm 12)$ meV. The latter value is unphysical, but a $E_{gap} \propto 1/L$ relationship with vanishing E_{gap} for large L seems reasonable. This would suggest that the gap at the Fermi level is purely of Coulomb blockade origin, rather than due to charge density wave order.

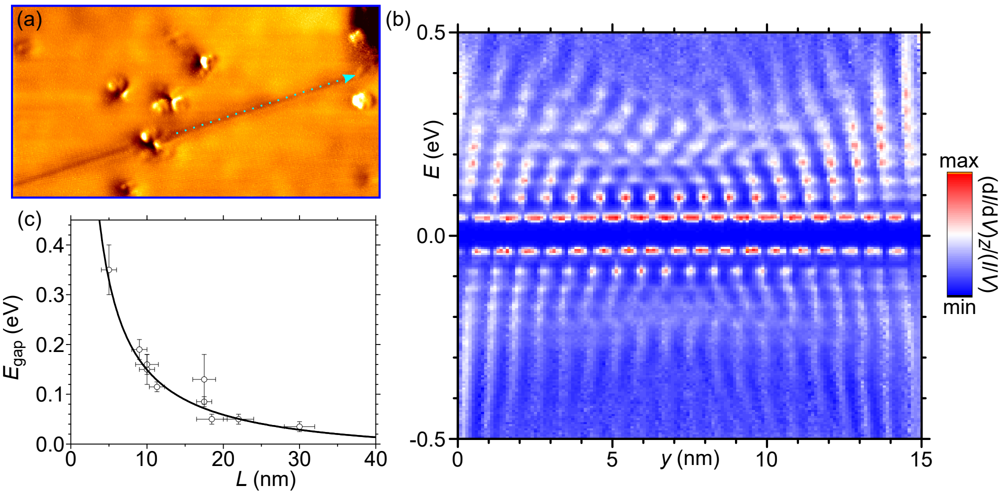

Fig. S5. Supplementary data to 4|4E MTBs confined states in MoS_2/Gr/Eu/Ir(111). (a) Constant current STM topograph showing the location of the STS linescan of Fig. 4(e). The path along the 4|4E MTB is marked by an arrow. (b) The linescan shown as discrete data. (c) A plot of E_{gap} (gap size at Fermi level) against L (MTB length) for numerous 4|4E MTBs. A fitted line is shown in solid black. STM/S parameters: (a) $30 \times 16\,\mathrm{nm}^2$, $V = 1.5$, $I = 0.1$ nA; (b) see main text.

S6: Confined states in 4|4P MTBs in $\mathrm{MoS_2}$/Gr/O/Ir(111)

Figure S6 shows confined states along 4|4P MTBs in the $\mathrm{MoS_2}$/Gr/O/Ir(111) sample; compare Fig. 4 of the main text in which 4|4E MTBs are examined similarly. Averaged above and below the Fermi level and for multiple 4|4P MTBs, we find an average periodicity $l_\mathrm{F}^\mathrm{O} = (3.07 \pm 0.09)a$. The small sample size (and correspondingly large error) makes any conclusion tentative, but this value would be consistent with slight p-gating by the O-interlayer. In $\mathrm{MoS_2}$/Gr/Ir(111) these confined states are found to have an average periodicity $l_\mathrm{F}^\mathrm{Gr} = (3.00 \pm 0.04)a$ [9]. The 4|4P MTB band is electron-like [10], and so p-gating should lead to a larger periodicity. This is depicted in k-space in Fig. S6(c). Also included in the sketch is what one would expect for the Eu-interlayer case – a periodicity shorter than $3a$ – but 4|4P MTBs were not found on that sample.

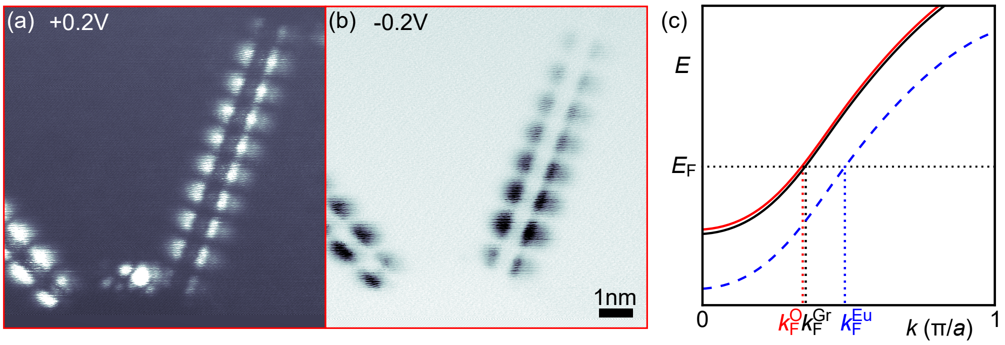

Fig. S6. Constant height STM showing confined states along 4|4P MTBs in $\mathrm{MoS_2}$ on Gr/O/Ir(111), tunneling into (a) unoccupied and (b) occupied states. (c) Schematic showing the expected shift of 1D MTB band and Fermi level relative to each other with gating, analogous to Fig. 4(d) of the main text but for the electron-like band of the 4|4P MTB. STM parameters (V): (a,b) image size $10 \times 10\,\mathrm{nm}^2$, $I_\mathrm{st} = 0.1\,\mathrm{nA}$; (a) $V = 0.2\,\mathrm{V}$; (b) $V = -0.2\,\mathrm{V}$.

S7: Supplementary linescans across in 4|4E MTBs

Fig. S7 shows constant height STS linescans of 4|4E MTBs in MoS_2 on (a,b) Gr/Eu/Ir(111) and (c,d) Gr/Eu/Ir(111), as an accompaniment to Fig. 5. For case of MoS_2 on Gr/Ir(111) see [11]. In (b) and (d) the signal intensity is normalised to the tunnelling current, this allows better visualisation of the data.

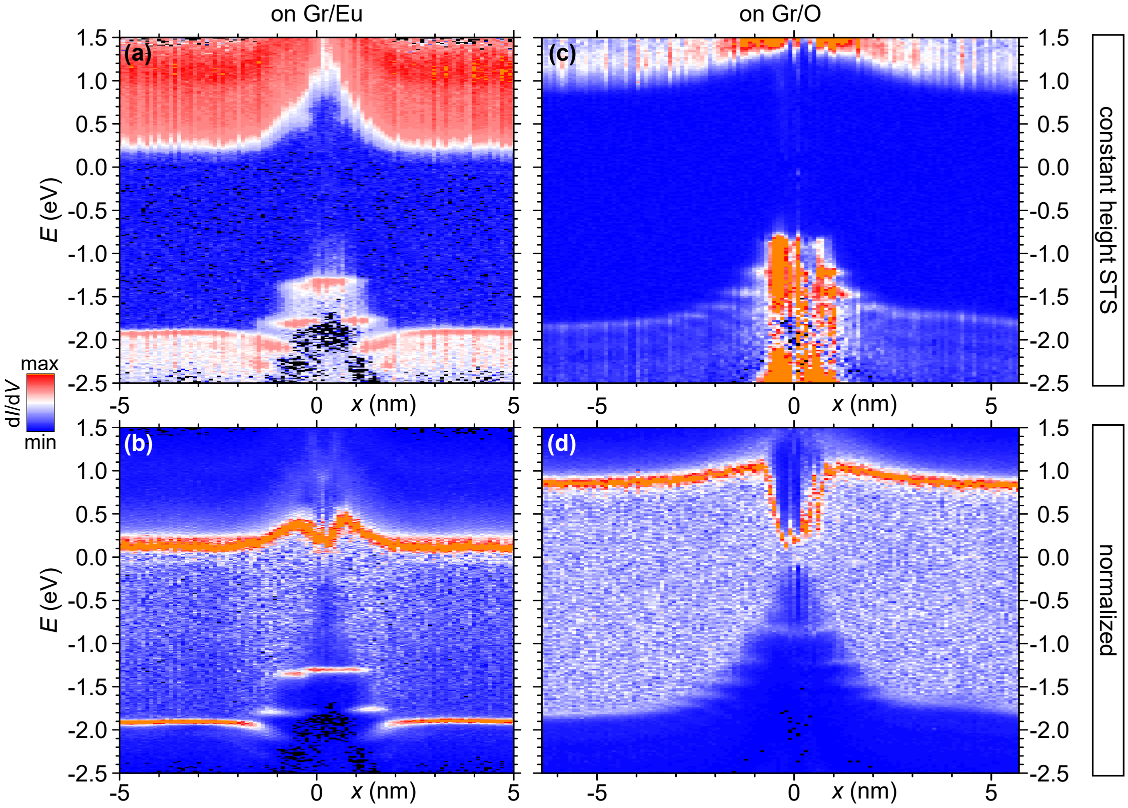

Fig. S7. Constant height STS linescans showing band bending at 4|4E MTBs in MoS_2 on (a,b) Gr/Eu/Ir(111) and (c,d) Gr/O/Ir(111). The linescans follow the paths shown in Figs. 5(c,g) of the main text. (a,c) The recorded $\log(\mathrm{d}I/\mathrm{d}V)_Z$ signal is plotted as a function of energy E and position x according to the color scale shown, in arbitrary units. In (b,d) the respective linescans have been normalized through division by the simultaneously recorded tunnelling current (and plotted on a linear intensity scale). STS parameters: (a-d) $V_{\mathrm{st}} = 1.5\,\mathrm{V}$, $I_{\mathrm{st}} = 0.1\,\mathrm{nA}$.

---

[1] J. Hall, B. Pielić, C. Murray, W. Jolie, T. Wekking, C. Busse, M. Kralj, and T. Michely, 2D Mater. **5**, 025005 (2018).

[2] B. Pielić, J. Hall, V. Despoja, I. Š. Rakić, M. Petrović, A. Sohani, C. Busse, T. Michely, and M. Kralj, J. Phys. Chem. C **124**, 6659 (2020).

[3] F. Zhao, H.-L. Sun, G. Su, and S. Gao, Small **2**, 244 (2006).

[4] N. Ehlen, J. Hall, B. V. Senkovskiy, M. Hell, J. Li, A. Herman, D. Smirnov, A. Fedorov, V. Yu Voroshnin, G. Di Santo, L. Petaccia, T. Michely, and A. Grüneis, 2D Mater. **6**, 011006 (2018).

[5] G. M. Rutter, J. N. Crain, N. P. Guisinger, T. Li, P. N. First, and J. A. Stroscio, Science **317**, 219 (2007).

[6] P. Mallet, I. Brihuega, S. Bose, M. M. Ugeda, J. M. Gómez-Rodríguez, K. Kern, and J. Y. Veuillen, Phys. Rev. B **86**, 045444 (2012).

[7] W. Jolie, F. Craes, M. Petrović, N. Atodiresei, V. Caciuc, S. Blügel, M. Kralj, T. Michely, and C. Busse, Phys. Rev. B **89**, 155435 (2014).

[8] C. L. Lin, S. M. Lu, W. B. Su, H. T. Shih, B. F. Wu, Y. D. Yao, C. S. Chang, and T. T. Tsong, Phys. Rev. Lett. **99**, 216103 (2007).

[9] W. Jolie, C. Murray, P. S. Weiß, J. Hall, F. Portner, N. Atodiresei, A. V. Krasheninnikov, C. Busse, H.-P. Komsa, A. Rosch, and T. Michely, Phys. Rev. X **9**, 011055 (2019).

[10] H.-P. Komsa and A. V. Krasheninnikov, Adv. Electron. Mater. **3**, 1600468 (2017).

[11] C. Murray, C. V. Efferen, W. Jolie, J. A. Fischer, J. Hall, A. Rosch, A. Krasheninnikov, H.-P. Komsa, and T. Michely, under review , 1 (2020).

PART III

Discussion

CHAPTER 9

Summary and Outlook

In this Chapter we briefly summarise the results of each manuscript (Chapters 5-8). We discuss some unanswered questions, and propose future experiments which could answer said questions or generally build on the results. Each manuscript has its own Discussion and Conclusion section (see above), but here we attempt to go somewhat beyond these. Additionally, we consider some relevant, recently published literature, and give a small outlook on a growing field of research – that of well-defined 1D defects in atomically thin TMDC layers. The closing remarks give a perspective on this thesis as a whole.

9.1 Chapter 5: Quasi-freestanding MoS_2 on Gr/Ir(111)

Motivated by our recent advances in the synthesis of 2D transition metal disulfides [85], the electronic properties of mono-, bi- and trilayer MoS_2 on Gr/Ir(111) were investigated using an advanced form of STS; Chapter 5. This 'comprehensive STS', developed by Chendong Zhang *et al.* [41], consists of three different STS modes: constant height STS, constant current STS, and κ-mode STS (whereby a state's inverse decay length and thus its parallel momentum $k_{||}$ are indirectly measured). Each of these modes has their own qualities and, most importantly, they can be cross-referenced with each other and with the computed band structure of the material. Through this, critical point energies at high-symmetry points of the BZ can be assigned to features of the STS data. In essence, STS gains some degree of momentum-space resolution.

Moreover, because constant current STS is much more sensitive to states at the edge of the BZ (that is, with large $k_{||}$), certain states can be detected which would otherwise be missed in constant height STS. This is particularly important in the monolayer TMDC semiconductors, in which the band extrema are at the K-point. Thus, as evidenced by the results of Chapter 5 and by Zhang *et al.* [41], using only constant height STS leads to an incorrect determination of the band gap of these materials. This highlights a problem which the community still must cope with. Most optical methods do not measure the electronic band gap because of the large exciton binding energy of VI-MX_2 monolayers. ARPES does not have access to the unoccupied bands. This leaves STS as a viable candidate for the task, yet in the vast majority of cases only constant height STS mode has been used, and so the band gap size estimates must be taken with a pinch of salt. The work of Chapter 5 shows a wider implementation of comprehensive STS would improve energy gap size estimation, and would generally improve characterisation of the electronic band structure of VI-MX_2 layers.

A particular technical issue was highlighted in Chapter 5 regarding κ-mode STS. The community has attempted to translate the measured κ value into a parallel momentum value $k_{\|}$, *i.e.* to precisely determine a state's location in the BZ [1, 41, 226]. As touched upon in the manuscript, and discussed in detail in the Master's Thesis of C. van Efferen, this routinely fails to give reasonable values of $k_{\|}$. This is due to an oversimplification of the tunnelling barrier within the standard theory of STM. It is common to use literature values for the work function of STM tip (in our case tungsten) and sample (MoS_2). However, it is unreasonable to assume these can be known precisely and that they will stay constant even in the case of small tip-sample separation [227], tip-induced band bending [228], or the presence of image potential states [229], for example. Beyond this, we note that the κ-mode states are much more pronounced in the work of Zhang *et al.* [41] than in our own. Despite using a range of tunnelling currents and modulation voltages, we were generally unable to see peaks (corresponding to K-point states) in various samples. A solution to this should be found, in order to unlock the full potential of this mode.

Aside from the technical conclusions, the main outcome of Chapter 5 is that MoS_2 is more freestanding on Gr/Ir(111) than it is on any other metallic substrate in the literature. This is evidenced by the STS-measured band gap ($E_g = 2.53\,\text{eV}$) and critical point energy spacings being close to predicted values for the intrinsic, freestanding material. In combination with the findings of Hall *et al.* [85] and Ehlen *et al.* [224], this demonstrates that MoS_2 is uniquely close to freestanding on Gr/Ir(111). This set the stage for the work that followed in Chapters 6-8. The weak interaction between MoS_2 and Gr/Ir(111) allows excellent epitaxial alignment, such that the only common defects in the MoS_2 are well-defined, atomically straight defects. These defects would prove to be highly 1D and host interesting electronic properties.

As an outlook, VI-MX_2 layers could be grown on related vdW substrates such as h-BN/Ir(111). Promisingly, it has been shown that vdWE growth of MoS_2/h-BN/Ir(111) is possible and that the sample also host MTBs [85]. A low-temperature electronic characterisation has not yet been performed. This substrate should offer two important features: (i) due to the wide band gap of h-BN, the MoS_2 could be even closer to freestanding in certain regions. (ii) One can expect a periodically varied electronic landscape due to the high corrugation of the h-BN/Ir(111) moiré. As the results of Appendix A.1 show, such a superlattice potential can modulate the MoS_2 band structure in a well-defined manner.

9.2 Chapter 6: Tomonaga-Luttinger liquid confined in MoS_2 MTBs

In Chapter 6 we investigated electronic states along 4|4E mirror twin boundaries (MTBs) in monolayer MoS_2 on Gr/Ir(111) with high-resolution STS at 5 K. Analysis of the spectroscopic data and comparison with theoretical modelling determined the existence of a Tomonaga-Luttinger liquid (TLL) confined by the finite length of the MTBs. Constant height STS linescans along these 1D 'wires' exhibited a sizeable gap around E_F and a multitude of quantised states outside the gap. The electron density of these quantised states undulated along the wire with different energy-dependent wavelengths. The existence of the TLL was evidenced by multiple experimental observations.

Firstly, pairs of quantised states (with different energies) were seen to have similar wavelengths. Translated into momentum space by Fourier transformation (FT), the approximately linear hole-like band of the 4|4E MTB was seen to be split: it had two different dispersions (and some additive combinations thereof). This corresponds to the distinct spin v_s and charge velocities v_c of the TLL, and these could be reproduced by our model Hamiltonian with reasonable Luttinger parameters $K_\mathrm{s} = 1$ and $K_\mathrm{c} = 0.5$. This splitting of spin and charge is the hallmark of TLL theory, as discussed in Section 4.2.

Secondly, the energy gap E_gap around the Fermi-level was found to be dependent on the MTB length L according to the relationship $E_\mathrm{gap} = A/L + B$, in which $A = 1.37\,\mathrm{eV}\cdot\mathrm{nm}$ and $B = 0.01\,\mathrm{eV}$. The former factor was consistent with our model Hamiltonian predictions based on $K_\mathrm{c,s}$ and $v_\mathrm{c,s}$ values as above. The latter factor, being no larger than our experimental resolution, indicated a near-vanishing E_gap in the long-wire limit. This relationship is consistent with a Coulomb blockade energy gap, whereby the energy cost for an electron to tunnel into the wire (and thereby disturb the correlated electrons inside) is inversely proportional to wire length; this marks a departure from Fermi liquid theory. The factor B additionally supports the confined state hypothesis, in that the undulations we observed also at room temperature could not be due to charge density wave (CDW) behaviour: $0.01\,\mathrm{eV}$ would imply a CDW transition temperature of 33 K.

The 1D states contained within VI-MX_2 MTBs (specifically the 4|4P MTB of $MoSe_2$) had been a debated topic, with conflicting ascribed origins: a TMDC-substrate superlattice potential plus confinement [136]; CDW order [126, 230]; TLL plus CDW order [127]. Our experimental observations and system-realistic modelling allowed us to unambiguously exclude substrate effects (see Section 9.1) and CDW behaviour from our interpretation. Furthermore, the high-resolution STS linescans (and FT thereof) allowed a direct view of the independent spin and charge density excitations along the length of the wire. Thereby spin-charge separation – the proverbial smoking gun evidence of the TLL – could be observed in real-space for the first time.

This work shows 4|4E MTBs in MoS_2 on Gr/Ir(111) to be an excellent 'laboratory' in which to study the fascinating physics of electron-electron interactions in the 1D limit. The MTBs are isolated out-of-plane due to the quasi-freestanding nature of MoS_2 on its substrate, and are electronically isolated in the plane due to the low-energy excitations of the TLL lying far from the MoS_2 band edges. Furthermore, we are able to synthesise MoS_2 islands in such a way that these MTB are far from any other 'wires' or defects. This is in contrast to the dense wagon-wheel networks of 4|4P MTBs that seem to be prevalent in $MoSe_2$ and $MoTe_2$ samples [127, 136, 140], and many of the 1D/quasi-1D systems composed of an array of parallel wires [209, 231–233].

The work of Chapter 6 showed that STM/STS is an advantageous technique for the investigation of these 1D systems. An interesting next step is to investigate the spin density wave component of the TLL with spin-polarised STS. Understanding of the TLL behaviour would additionally be helped by measurement at ultra-low temperatures. Reduced thermal broadening would greatly improve the energy resolution of STS spectra. Furthermore, the general stability and reduced lateral drift – the latter being particularly problematic for STS linescans along 1D objects – would facilitate greater spatial resolution.

One of the advantages of studying 1D wires with STM is the local nature of the technique. Specifically, one can investigate individual wires and even monitor their response to local perturbations, in a way that is not possible in ensemble-averaging techniques such as ARPES. A sample configuration could be engineered in which connected MTBs – or even single, long MTBs – traverse different electrostatic environments. The idea of a spatially-dependent Luttinger parameter K_c has been considered theoretically [234], but is obviously challenging to realise in experiment. It could perhaps be achieved via partially intercalated Gr, like in our MoS_2/Gr/Eu/Ir(111) sample (Chapter 8, Fig. 1) but requiring MoS_2 to grow over both Gr regions.

Alternatively, a superlattice potential could be provided by the substrate. In Appendix A.1 we show that the Gr/Ir(111) moiré modulates the MoS_2 band structure by $0.03\,\mathrm{eV}$. That effect may be too small, but a rigid band structure shift of $0.13\,\mathrm{eV}$ has been documented for $MoSe_2$ due to the h-BN/Ru(0001) substrate moiré [235]. Beyond that, work function modulations of $0.4\,\mathrm{eV}$ and $0.5\,\mathrm{eV}$ due to the respective moirés of Gr/Ru(0001) and h-BN/Ir(111) have been reported [236, 237]. We have already proven the latter of these substrates to be suitable for MoS_2 synthesis hosting MTBs [85]. It is also possible to create a moiré superlattice potential through the stacking of TMDC or other vdW layers [238–243], a topic of huge current interest [244]. However, for any of the above cases, it must be noted that a greater electrostatic modulation in the substrate will likely come with a greater corrugation in the MoS_2 layer and locally varying substrate-interaction. It may be challenging to disentangle the electrostatic potential effects from those due to strain, layer-substrate bonding and charge transfer.

In Chapter 8 we pointed out that the 4|4P MTB displays a commensurate band crossing at $k_\mathrm{F} \approx \frac{\pi}{3a}$ on a remarkable range of substrates [2,126,127,136,245], in both MoS_2 and $MoSe_2$. Furthermore, comparing 4|4P MTBs in freestanding MoS_2 and MoS_2/Gr via DFT showed little change between k_F values, both close to $\frac{\pi}{3a}$ (Chapter 7, Fig. 6). At first glance, it appears as though the 4|4P MTB states prefer to lock into commensurability with the lattice – this implies a certain degree of electron-phonon coupling.

By contrast, our work with Eu-gating of 4|4E MTBs shows that an incommensurate crossing at $k_\mathrm{F} \approx \frac{\pi}{2.69a}$ can be achieved through charge donation. DFT-predicted k_F values for 4|4E MTBs in freestanding MoS_2 and MoS_2/Gr also show them to be substrate-sensitive (see Table II of Chapter 8). This begs the question: is the electron-phonon coupling strength much weaker in the 4|4E MTB, and so the 4|4E and 4|4P MTBs show different tendencies regarding commensurability locking? Or, have measurements of the beating periodicity in 4|4P MTBs simply not been precise enough, such that small k_F changes due to different band fillings have been overlooked?

This could be answered by more careful STM measurement of 4|4P MTBs, using high spatial-resolution where possible. Alternatively, a direct test would be to try to gate the MTB into incommensurability, either in a back-gated device setup or by using intercalants as in Chapter 8 (where unfortunately Eu precluded the growth of 4|4P MTBs and O was too weak a dopant). The answer to this question could clear up some of the discrepancies regarding CDW/TLL behaviour in the literature [2, 126, 127]. More importantly, it could improve our understanding of 1D systems, specifically regarding Peierls transitions, TLL behaviour, and their competition.

9.3 Chapter 7: Band bending and quantisation at MTBs and edges

In Chapter 7 we investigated the MoS_2 electronic landscape directly around 4|4E MTBs and other 1D defects: 4|4P MTBs, tilt grain boundaries, monolayer edges, and bilayer edges. STS linescans performed orthogonally to the defects, in both constant height and constant current mode, revealed their effects on the MoS_2 band structure. A considerable bending of bands towards higher energies was observed at all defects except the 4|4P MTB. The bending of the VB creates a hole-confining potential, leading to a quantisation of VB states. Focussing on the 4|4E MTB with careful STS analysis, we found these quantised states to give characteristic intensity maxima, well-defined in energy and location.

STM and STS further showed that if the electrostatic environment on one side of the MTB is perturbed, the quantised energies there are altered. Remarkably, the quantised states on the other side of the MTB are unchanged from their characteristic values. This demonstrates that there are actually two strongly independent potential wells on either side of the MTB, and that the MTB acts as a barrier to holes. The implications of this for charge carrier transport were discussed in the manuscript.

Through DFT and electrostatic modelling a coherent, quantitative picture of the bending and the quantisation was reached. Excess charge on the defects, coming mostly from the substrate (see below), causes an electrostatic potential to be felt by the surrounding semiconductor. This potential is screened by the MoS_2 itself and, more significantly, by the metal substrate. DFT and modelling self-consistently reproduced the experimental observations, using real physical parameters such as the permittivity and thickness of the vdW layer and the linear charge density on the MTB.

One of the main achievements of our work was to unravel the origin of the bending at defects. The answer may at first seem obvious: the defects are metallic, and their charge induces an electrostatic potential. However, the lack of bending at metallic 4|4P MTBs demonstrates that the origin is more complicated than that. With the help of DFT calculations a complete explanation was developed. Namely, each defect has an intrinsic, quantised polarisation charge λ_{pol} which is counteracted by charging of the 1D defect band λ_{band}, see Section 3.4. In the case of an infinitely large, freestanding MoS_2 flake these would compensate perfectly, $\lambda_{\mathrm{pol}} = -\lambda_{\mathrm{band}}$, to prevent divergence of the electrostatic potential. In our case, however, the 1D defect band is additionally filled up by charge from the Gr/Ir(111) substrate leading to a net excess charge density $\lambda = \lambda_{\mathrm{pol}} + \lambda_{\mathrm{band}}$ in most cases. In the 4|4P MTB comparatively less band filling occurs, leading to a negligible net charge excess and no band bending.

In the words of Güller and co-authors [183], "*Aside from special cases of uncompensated polarity, all polar systems in experiments or in numerical simulations are compensated. Recognising polarity signatures is thus not always easy*." In fact, although the so-called ‘modern theory of polarisation’ [167–169] is now almost three decades old, there had been few (perhaps zero) previous instances of its predicted interface polarisation charge being measured experimentally. The recent theoretical interest in polarisation charge at 1D interfaces [165,174,176,183,246] and at VI-MX_2 MTBs in particular [174,247] underlines the significance of our result.

The synthesis [248, 249] and study [157] of TMDC-based lateral heterostructures move forward at a rapid pace (see Section 3.3.1). This includes MoS_2-semiconductor combinations which act as a 2D p-n junction [158, 161, 162], or MoS_2-Gr junctions where the Gr serves as an in-plane contact [250, 251]. The local physics at their atomically sharp, 1D interfaces is of obvious importance and must be well-understood [252–255]. While the MTBs studied here represent something else (a homojunction), many of the relevant phenomena are shared: polarisation charge building at the interface between materials of different formal polarisation; band alignment/bending; backscattering due to the lattice discontinuity. The results of Chapter 7, and the local spectroscopic techniques used to obtain them, should have a wider relevance for the 1D-interface community.

9.4 Chapter 8: Manipulation via substrate screening and charge

In Chapter 8 we altered the substrate of MoS_2 by Eu- and O-intercalation under Gr. This built upon the results of Chapters 5-7. Having thoroughly characterised the MoS_2 band structure and the electronic phenomena at MTBs on Gr/Ir(111), their changes due to the intercalants could be observed and compared with STM and STS. We attempted to disentangle the effects of the changed electronic environment – such as changed screening, band alignment, defect charge transfer, and substrate-wettability.

The Eu-interlayer strongly n-gates the Gr, reducing its work function by around 1.4 eV. On one hand, this shifts both the VB and CB edges of MoS_2 to lower energies. On the other, the increased electron density in Gr leads to much more efficient screening and a corresponding band gap renormalisation in MoS_2; both VB and CB shift towards E_{F}. These complementary/competing shifts are addressed quantitatively with simple assumptions, and the values' implications for Fermi level pinning and dielectric screening are discussed. The influence of the O-interlayer is much less drastic, with its main effect being a decoupling from the Ir(111).

Some of the extra charge carriers available in Gr/Eu/Ir(111) are donated to the 4|4E MTB. This is observed in the characteristic beating pattern being lengthened from $2a$ to $2.69a$. The corresponding change in k_{F} in the 1D defect band is used to quantify this charge transfer, a considerable $\Delta\lambda = -0.26\,e/a$. As discussed in Section 9.2, this represents a significant departure from the tendency of MTB bands to lock into (near-)commensurability with the lattice. The gating effect of the O-interlayer was not strong enough to see a changed filling of 4|4P MTB bands there. It would be interesting to try other intercalants and see to what extent the Fermi wave vector of MTB states can be tuned. One can fantasise about developing a doping-dependent phase diagram of the 1D physics.

The effects of the different substrates are visualised in the band bending at 4|4E MTBs, and understood by qualitative changes to the previously used electrostatic continuum model. In the Eu case much stronger screening results in a steeper, narrower potential well, and thus fewer quantised VB levels. In the O case the opposite is observed: a slightly wider potential well and a greater number of quantised VB levels. We speculate that this is due to increased distance from Ir and the image charges produced there.

Chapter 8 is still very much a work in progress, and there are open questions that need addressed. Firstly, the assumptions that MoS_2 bands shift symmetrically in response to the changed screening is possibly an oversimplification [256]. Theoretical assistance could be wished. However, it will be difficult to accurately simulate the substrate influence, as a DFT calculation including MoS_2, Gr, intercalation layer, *and* the top few layers of Ir(111) is computationally unfeasible [257].

The changes to the band structure, specifically the renormalisation value $\Delta E_{\mathrm{rn}}^{\mathrm{Eu}}$, could be revealed by photoluminescence (PL) and ARPES measurements. As discussed in Section 4.1.3, dielectric screening causes roughly equal reductions in exciton binding energy E_{b} and electronic gap E_{g}, so that the optical gap E_{opt} remains unchanged. PL measurements on our MoS_2/Gr/Ir(111) samples found the value $E_{\mathrm{opt}} = 1.945\,\mathrm{eV}$ [224]. One could similarly detect PL of the MoS_2/Gr/Eu/Ir(111) sample and see if this value is changed. Any change would attributable to non-screening effects such as band hybridisation, which may be observable in ARPES.

The fate of the MoS_2 excitons in the Eu-gated sample is an interesting question. The exciton binding energy $E_{\mathrm{b}}^{\mathrm{Gr}} = 480\,\mathrm{meV}$ for MoS_2/Gr/Ir(111) has been estimated [224]. Assuming our calculated renormalisation of $\Delta E_{\mathrm{rn}}^{\mathrm{Eu}} = -335\,\mathrm{meV}$ to be true would imply a reduced binding energy of $E_{\mathrm{b}}^{\mathrm{Eu}} = 145\,\mathrm{meV}$. This is comparable with the value $E_{\mathrm{b}}^{\mathrm{Eu}} = 90\,\mathrm{meV}$ found for MoS_2/Au(111) [202], where the TMDC layer is strongly screened by (and hybridises with) the metal substrate.

There is undoubtedly an increased MoS_2-Gr interaction due to the Eu-interlayer. This is evidenced by changed growth dynamics and a heavily altered band structure, amongst other things. On the other hand, the rich spectrum of states confined along the 4|4E MTB show that the layer's two-dimensionality is not compromised. If the TLL survives even in this more screened environment it would be quite surprising, and presents an interesting opportunity for research.

Chapter 8 is a preliminary version of a manuscript – written with an eye towards this thesis rather than a journal – and should be viewed as such. In the end, some of the results may need to be reorganised for the sake of a succinct, impactful message. For example, one might focus on the MoS_2/Gr/Eu/Ir(111) sample and how this strongly affects the states at MTBs, representing a testing ground for 1D physics far from equilibrium.

9.5 1D defects in TMDCs: a growing field?

It seems that the study of MTBs in 2D TMDCs is on the rise. Motivated by their technological relevance and advances in synthesis, the last two years have seen a considerable number of papers on TMDC MTBs published or uploaded to *arXiv* [2, 3, 245, 247, 258–275], and even their picture adorning a book cover [276]. In this Section we briefly discuss some recent developments in the MTB literature which are relevant to this thesis. In addition, we look at other 1D defect types in VI-MX$_2$ which have also exhibited TLL physics in the time since Chapter 6 was published [277–279].

While the focus remains on MTBs in MoSe$_2$ and MoS$_2$, more examples have started appearing in their WX$_2$ analogues [264–268]. Wang *et al.* have introduced two MTB types to WSe2 via post-doping with Nb. One of these is the 4|4P MTB while the other, fascinatingly, is the inverse of the 4|4E MTB (that is, with M and X lattice sites swapped). Dappe *et al.* studied WSe$_2$ on Gr/SiC with Kelvin probe force microscopy and observed band bending due to an unidentified MTB-type. A $0.3\,\mathrm{eV}$ drop in the surface potential indicates a negatively charged MTB; the spatial range of the bending could not be accurately determined but is of order $10\,\mathrm{nm}$, consistent with the results of Chapter 7. In MBE-grown VSe$_2$ on MoS$_2$, Chua *et al.* controllably introduced mirror-symmetric, Se-deficient line defects by post-annealing above 400°C [273]. The magnetic properties of the defect patterns were investigated, and show that they cause the onset of ferromagnetism. In another work of note, He *et al.* employed the wagon-wheel pattern of 4|4P MTBs in MoSe$_2$ to create a self-assembled network of organic molecules [260].

Considering the popularity of MoS$_2$ as a material, its MTBs remain under-represented in the literature, presumably due to the challenges faced in its MBE synthesis. Nonetheless, Mehta *et al.* have studied 4|4E and 4|4P MTBs in CVD-grown bilayer MoS$_2$ [262]. They investigate MTB-induced lattice strain via scanning transmission electron microscopy. In the monolayer, the 4|4P MTB imparts tensile strain while the 4|4E MTB imparts compressive strain, but only in a range of around $0.5\,\mathrm{nm}$, consistent with the results of Chapter 7. In the bilayer, a MTB in one layer causes longer-range strain in the other (defect-less) layer due to the stacking misalignment.

In a recent manuscript, Krishnamurthi and Brocks study the electronic structure of 4|4P MTBs in MoS$_2$ and MoSe$_2$ with DFT [247]. Their findings are consistent with a polarisation line charge of $\lambda_{\mathrm{pol}} = +\frac{2}{3}e/a$ at the boundary, and thus are in agreement with the results of Chapter 7 and literature [172]. They additionally consider the implications of the $k_{\mathrm{F}} = \frac{\pi}{3a}$ wave vector for Peierls instabilities, spin density waves, and soliton excitations.

Recent cases of TLL behaviour

The group of Maohai Xie have revisited the 4|4P MTB in MoSe$_2$ in a recently published manuscript [245]. They find evidence for a confined TLL with Luttinger parameter $K_{\mathrm{c}} = 0.28$, in line with the value 0.20 reported by Ma *et al.* [127] for this defect type. Both values suggest a stronger electron-electron interaction than in our 4|4E MTBs ($K_{\mathrm{c}} = 0.5$). They do not observe spin-charge separation, but show other indications of TLL order. Firstly, an $E_{\mathrm{gap}} \propto 1/L$ dependence is observed, consistent with a confined TLL as in our case. Interestingly, they investigate MTBs of length $L > 30\,\mathrm{nm}$ in which the Coulomb blockade gap becomes negligible. This allows a power-law suppression to be observed at zero bias in STS, further evidencing TLL behaviour. They point out another feature in linescans along the MTB: the DOS maxima of the TLL excitations increase with energy at the wire's ends. Specifically, they follow the relationship $E = C/r$, in which r is the distance from the end of the wire and C a constant, in their case equal to $0.49\,\mathrm{eV}\cdot\mathrm{nm}$. This power-law decay of the excitation energy at a scattering boundary has been observed before in carbon nanotubes [280] and is described by the TLL formalism [281].

The same group also detected confined TLL behaviour in Mo_6Se_6 nanowires recently [279]. These are fabricated by 800°C post-annealing of MBE-grown $MoSe_2$ on HOPG or Gr/SiC. The nanowires are connected to the parent $MoSe_2$ sheet by a reconstructed interface. Confined TLL behaviour is demonstrated by characteristics similar to those in the MTBs of Ref. [245]: an $E_{\mathrm{gap}} \propto 1/L$ dependence and a power-law suppression at E_{F} in long wires (with $K_{\mathrm{c}} = 0.21$). Additionally they see quantised states of different energy but similar wavelength, suggesting spin-charge separation. The undulations show a $\approx 3a$ beating pattern, similar to 4|4P MTBs. However, this is not consistent with their DFT-calculated band structure of the nanowire, which predicts a much higher k_{F} close to the BZ edge. They instead assign the beating periodicity to an electronic interference from the nanowire-island interface, which is essentially a $4a$-reconstructed superstructure parallel to the nanowire. Xing Yang *et al.* also investigated Mo_6Se_6 nanowires on Gr/SiC but found contrasting results [278]. They claim their edge-connected nanowires to exhibit CDW behaviour, whereas isolated nanowires (bridging $MoSe_2$ islands) show suppressed CDW order due to a "phason-polaron effect".

Guanhua Yang *et al.* have performed charge transport measurements along the straight metallic edges of exfoliated MoS_2 and WS_2 flakes [277]. The edge conductance shows a power-law relationship with both voltage and temperature, which they consider a sign of "possible" TLL behaviour. They extract Luttinger parameters $K_{\mathrm{c}} = 0.10$ and 0.11 for the MoS_2 and WS_2 flakes respectively, indicating a much stronger electron-correlation than that found in MTBs [2,127,245]. An obvious question would be if the straight edges of MoS_2 on Gr/Ir(111) host a TLL also. However, in our case it is not certain if the edges are fully metallic, and they cause tip instability [see Figs. 1(c) and 4(b) of Chapter 7]. It should be noted that the edges in Ref. [277] are not atomically straight. Signs of TLL behaviour have also been seen recently at the edges of bismuthene, another hexagonal 2D material [282].

9.6 Closing remarks

Interest in TMDC layers, in particular the Group VI semiconductors, shows no signs of abating. As the synthesis of these layers is refined and devices are downsized, atomically perfect 1D defects will become more common and more relevant. This thesis has hopefully shown that the vdW substrate Gr/Ir(111) is an excellent platform on which to study the electronic properties of VI-MX_2 layers and their 1D defects. It allows excellent growth quality, does not heavily interfere with the TMDC layer's intrinsic properties, and can even be modified *in situ*. This vdW substrate is nonetheless metallic, and so it facilitates STM and STS. Armed with the local spectroscopic techniques exhibited in this thesis, much can be learned about the intrinsic properties of the 2D layers, their defects, the role of the substrate, and the complex interplay between them.

PART IV

Appendix

APPENDIX A

Scientific Appendix

This scientific appendix contains contributions from C. Murray, C. van Efferen, and T. Michely.
***A.1** C. Murray and C. van Efferen grew the sample, designed the experiments, carried out the measurements and analysed the data. Some of results can be found in the Master's thesis of C. van Efferen.*
***A.2** On the same sample, C. Murray designed the experiments, carried out the measurements and analysed the data.*
All work was supervised by T. Michely.

A.1 The Gr/Ir(111) moiré superlattice potiental acting on MoS_2

At certain tunnelling voltages, for example -2 V in Figure A.1, the moiré of Gr/Ir(111) is visible in the MoS_2 adlayer in STM. The MoS_2 layer is known to adopt the moiré corrugation [85], though a locally varying DOS would also affect the STM apparent height and such a contribution cannot be ruled out. We presume the circles of higher apparent height to be above the *top*-sites of the moiré. There the Gr is at the high-point of its corrugation; the *hollow*-sites mark the low-points, where a C atom being directly above an Ir atom leads to weak covalent bonding. This is depicted in (b). More information on the moiré is available in Ref. [103].

In a close-up topograph, Fig. A.1(c), the moiré is seen more clearly. As indicated, we perform STS linescans along the high-symmetry directions of the moiré. These are shown in (d-f). In the MoS_2 VB (d,f) there is a clear undulation in the detected band edge at Γ. The amplitude of this is found to be approximately 30 meV. Through comparison with the topograph (c) and the length scale, we can assign different parts of the undulation to regions of the moiré. The band edge is closest to E_F at the top-sites, and farthest at the hollow-sites.[1] This is consistent with the fact that the Gr work function is ≈ 100 meV higher at the top- than at the hollow-sites [283]. The *bridge*-site is energetically intermediate in (d,f), which makes sense considering the registry and corrugation of the moiré [103].

In the CB, Fig. A.1(e), the undulation appears to be weaker. It can only be seen faintly at higher energies, in fact. Disappointingly, the CB behaviour along the top-hollow-hollow-top direction was not successfully recorded. Nonetheless, as can be seen in the VB of (f), the top-bridge-top direction can be expected to show a clear undulation too. The different behaviour of VB and CB could be explained

---

[1] It is not possible to make a distinction between fcc- and hcp-sites here.

by the orbital nature of the respective band edges. As illustrated in Fig. 2.1(f), the Γ point states of the VB have strong out-of-plane character, particularly with S p_z orbitals extending into the vdW gap, making them more sensitive to small electronic variations in the Gr substrate. This would be consistent with the findings of an STS investigation into rotated MoS$_2$ on HOPG [284]. It was concluded that HOPG influences the MoS$_2$ band structure through S p_z orbitals, which mediate indirect coupling of C p_z orbitals to Mo d_{z^2} orbitals. Thus the VB at Γ was sensitive to MoS$_2$-HOPG registry, but the K-point states not. No comment was made about the Q-point states of the CB.

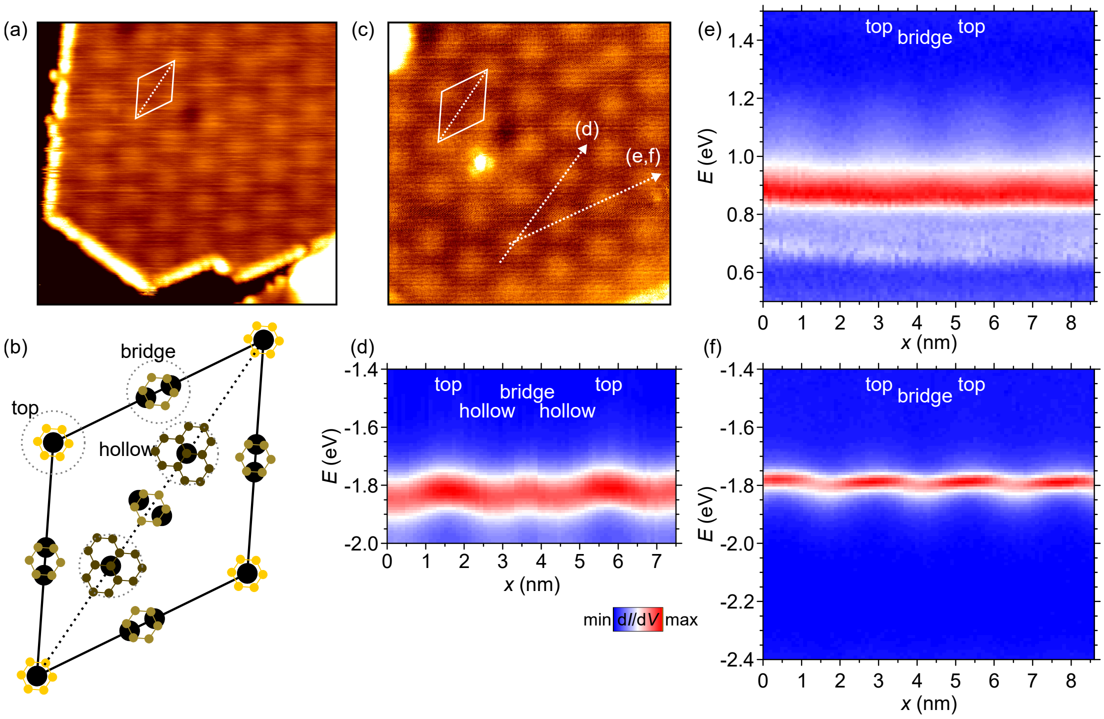

Figure A.1: The Gr/Ir(111) moiré superlattice potenial in ML-MoS$_2$. (a,c) Constant height STM topographs of a ML-MoS$_2$ island on Gr/Ir(111), with moiré unit cell indicated. (b) Schematic of the different moiré unit cell regions; C atoms are coloured from brown to yellow corresponding to their apparent height in the STM topographs; top layer Ir atoms are black. Atoms and bond lengths enlarged for visual clarity. Inequivalence of hollow sites (fcc and hcp) not shown. (d-f) Constant current STS linescans on MoS$_2$ following the (d) top-hollow-hollow-top and (e,f) top-bridge-top directions of the underlying moiré. Paths indicated in (c). STM/S parameters: (a) $(19 \times 18)\,\mathrm{nm}^2$; (c) $(15 \times 15)\,\mathrm{nm}^2$; (a,c) $V = -2\,\mathrm{V}$, $I = 0.08\,\mathrm{nA}$; (d) $V_{\mathrm{st}} = -2.0\,\mathrm{V}$, $I_{\mathrm{st}} = 0.1\,\mathrm{nA}$; (e) $V_{\mathrm{st}} = 1.5\,\mathrm{V}$; $I_{\mathrm{st}} = 0.1\,\mathrm{nA}$; (f) $V_{\mathrm{st}} = -2.4\,\mathrm{V}$, $I_{\mathrm{st}} = 0.1\,\mathrm{nA}$. All measurements performed at 5 K.

Thus an electronic superlattice has been imposed on MoS$_2$ by the periodic potential of the underlying Gr/Ir(111) moiré. This has also been observed in MoSe$_2$ due the moiré of h-BN/Ru(0001) [235]. In contrast to our work, there was almost one-to-one correspondence in the substrate work function modulation (140 meV) and the TMDC band edge modulation (130 meV). Furthermore, both the VB and the CB edge of MoSe$_2$ shifted rigidly in STS. DFT calculations showed that significant interaction between h-BN and Ru in the moiré ‘hole’ region leads to the creation of in-gap states in the h-BN, and these states may lead to extra screening [235]. The moiré of other substrates such as Gr/Ru(0001) [236], h-BN/Ir(111) [237] and h-BN/Cu [285] could also be used as superpotiential templates for TMDC semiconductors.

A.2 Band bending and in-gap states at point defects in MoS_2

In Figure A.2(a) a point defect in an island of ML-MoS_2 is visible in STM. ‘Zooming in’ and changing the bias voltage, (b-d), it becomes clear that there are in fact two defects in close proximity. We name these A- and B-defect types. Moreover, through the dependence of their appearance on bias voltage it is evident that they have very distinct electronic characteristics.

We perform constant height STS linescans directly over the A- and B-defects, shown in Figs. A.2(e) and (f) respectively. The point defects, located at $x = 0$ in each case, show totally different electronic properties. Type A exhibits what appears to be a range of in-gap states both above and below the Fermi level. Type B only shows an in-gap state (or states) just below the CB edge. In the former case, bending is induced in both the CB and VB of the surrounding MoS_2. This is consistent with charging of in-gap states below the Fermi level. At the B-defect no bending is seen, presumably because its in-gap states are unoccupied at $5\,K$.

Additional insight is gained via constant current STS linescans, (g-k). An in-gap state is seen clearly at around $0.35\,eV$ in both A- and B-defects, (g,h). There appear to be additional states above this, which are harder to detect in constant current mode (see Chapter 7). For example, in (h) some states are faintly visible around $0.50\,eV$, whereas in (f) that is where they are most visible. This may point towards differing orbital nature of the in-gap states, such that their detection is dependent on STS-mode (see Chapter 5).

The A-defect shows various intensity maxima below the Fermi level when measured by constant current STS, (j). There is a clear peak at $-0.25\,eV$. It is not fully visible in (j) because the spectra are only recorded up to $-0.30\,eV$; spectra recorded above that were liable to instabilities, seemingly caused by the high tunnelling current at the $-0.25\,eV$ state. We assume that this is a charged defect state. In (j) there are additional intensity maxima below this, in the range $-0.50\,eV$ to $-1.50\,eV$. It is possible that these are quantised VB states, in analogy to Chapter 7. Presumably, the charged in-gap state at $-0.25\,eV$ causes considerable bending, leading to the formation of a hole-confining potential in the VB. In contrast to the quantised states at 4|4E MTBs (Chapter 7 Fig. 2), the states at the A-defect are not symmetric either side of the linescan (j). This can be explained by the simple fact that point defects are 3-fold symmetric, and thus our straight-line scan does not follow a line of symmetry as it does over a MTB.

The B-defect shows no occupied in-gap states in constant current STS, (k). Some slight modulation of the MoS_2 VB edge is seem, presumably due to the Gr/Ir(111) moiré superpotential described in A.1. To briefly summarise, the A-defect has both occupied and unoccupied in-gap states whereas the B-defect has only unoccupied in-gap states; the A-defect causes band bending in MoS_2 whereas the B-defect does not. Taken together, this data suggests that the bending at A-defects is due to an electrostatic potential from charged in-gap states.

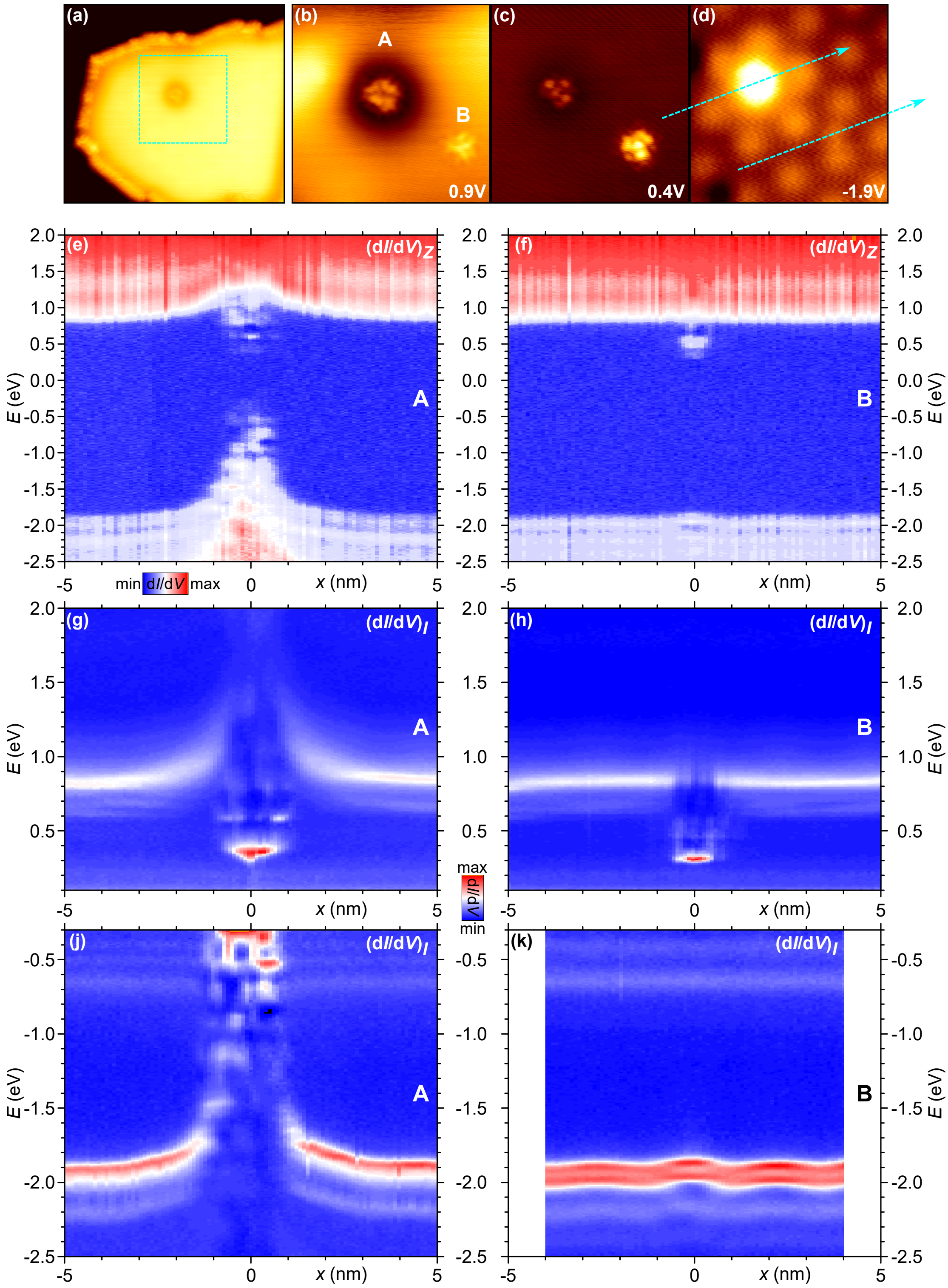

Figure A.2: In-gap states at point defects in ML-MoS$_2$ on Gr/Ir(111). (a-d) Constant height STM topographs showing the location and appearance of two defect types, named A and B. (e,f) Constant height STS linescans over A and B defects respectively. (g-k) Similarly, constant current STS linescans in the energy ranges of the MoS$_2$ CB and VB. Path of all linescans marked in (d). STM parameters: (a) $(25 \times 22)\,\mathrm{nm}^2$, $V = 1.1\,\mathrm{V}$, $I = 0.05\,\mathrm{nA}$; (b-d) $(10 \times 10)\,\mathrm{nm}^2$; (b) $V = 0.9\,\mathrm{V}$, $I = 0.05\,\mathrm{nA}$; (c) $V = 0.4\,\mathrm{V}$, $I = 0.05\,\mathrm{nA}$; (d) $V = -1.9\,\mathrm{V}$, $I = 0.08\,\mathrm{nA}$. STS parameters: (e-h) $V_{\mathrm{st}} = 2.0\,\mathrm{V}$; (j,k) $V_{\mathrm{st}} = -2.5\,\mathrm{V}$; (e) $I_{\mathrm{st}} = 0.5\,\mathrm{nA}$; (f) $I_{\mathrm{st}} = 0.8\,\mathrm{nA}$; (g-k) $I_{\mathrm{st}} = 0.1\,\mathrm{nA}$. All measurements performed at 5 K.

In Figure A.3 we perform a series of constant current STS maps at the two defects. These range from $1.08\,\mathrm{eV}$ (*i.e.*, within the CB of $\mathrm{MoS_2}$) through to $-1.98\,\mathrm{eV}$ (within the VB). The different electronic properties of the A- and B-defects is immediately noticeable again. Although the unoccupied defect states appeared similar in STS linescans [Figs. A.2(g,h)], the maps at energies $0.30\,\mathrm{eV}$ to $0.66\,\mathrm{eV}$ show that they are actually different. The LDOS at the B-defect is especially well-defined, and recreates the 3-fold symmetry of the $\mathrm{MoS_2}$ lattice.

Moving below the Fermi level, the A-defect exhibits clear, well-defined states from around $-0.30\,\mathrm{eV}$ to $-0.54\,\mathrm{eV}$. The activity below this is somewhat unclear, until $-1.14\,\mathrm{eV}$. From that energy until the $\mathrm{MoS_2}$ VB is reached at $-1.86\,\mathrm{eV}$ there is a ring of LDOS which moves radially outward. This is consistent with the VB bending seen in Fig. A.2(j). Notice in Fig. A.2(g) how the $\mathrm{MoS_2}$ CB was bent up from around $0.85\,\mathrm{eV}$ towards higher energies – this is visible in the maps of Fig. A.3 going from $0.84\,\mathrm{eV}$ upwards.

The maps show the B-defect to be electronically 'dead' below E_F, consistent with the previous linescans. Its presence is however evidenced by the local disturbance it causes in the moiré-induced superlattice visible at $-1.86\,\mathrm{eV}$ and $-1.98\,\mathrm{eV}$. At those energies we also notice another disturbance in the bottom left of the image – it is also faintly visible at $-0.06\,\mathrm{eV}$.

The A- and B-defects shown here could be any two of a multitude of point defect types. They could be vacancies or substitutionals, and could exist in each of the three layers of the S-Mo-S structure. Assignment of point defect type is essentially impossible with STM alone [286]. However, we notice similarities between the character of our defect types and some seen in literature. Our B-defect exhibits in-gap states a few hundred meV below the CB edge, but none below E_F – this is consistent with chalcogen vacancies seen in $\mathrm{WS_2}$ [286] and $\mathrm{MoSe_2}$ [261, 287] for example. The A-defect is clearly charged, with filled defects states causing band bending around them. This has been observed in $\mathrm{WS_2}$ on Gr/SiC, where it was tentatively proposed that the charged defects could be carbon-for-sulfur ($\mathrm{C_S}$) or nitrogen-for-sulfur ($\mathrm{N_S}$) substitutionals [288, 289]. Similarly, VB bending was observed at vanadium-for-tungsten ($\mathrm{V_W}$) substitutionals in $\mathrm{WSe_2}$ on Gr/SiC [290]. Mo vacancies are also predicted to produce occupied in-gap states in $\mathrm{MoSe_2}$ [261]. One should expect similar characteristics throughout the VI-$\mathrm{MX_2}$ semiconductors.

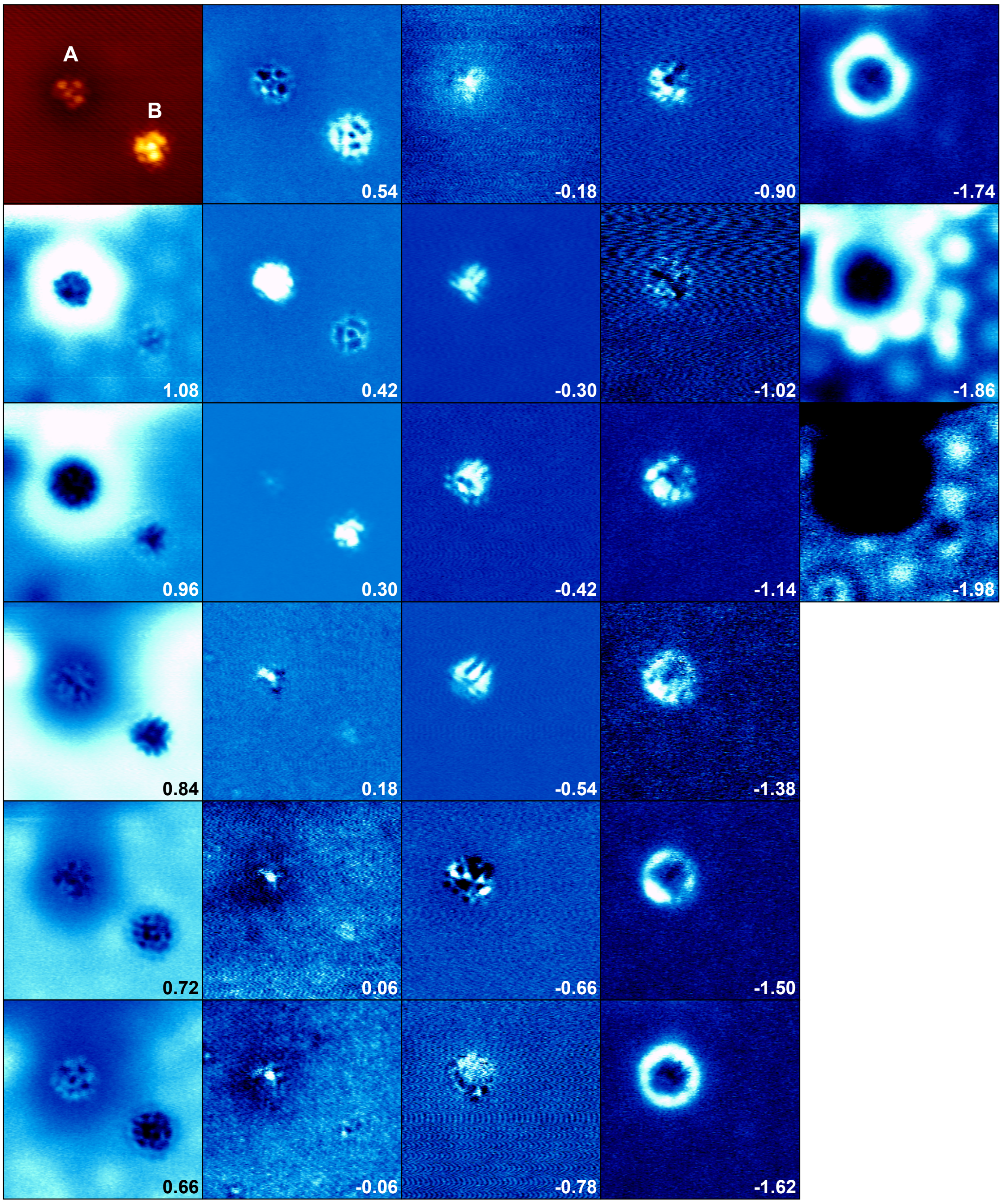

Figure A.3: Constant current STS maps of point defects in ML-$\mathrm{MoS_2}$ on Gr/Ir(111). The energy (eV) is given in the corner of each map. $(\mathrm{d}I/\mathrm{d}V)_Z$ intensity is displayed light (high) to dark (low). Constant current STM topograph in top left panel shown for reference. STM parameters: $V = 0.4\,\mathrm{V}$, $I = 0.05\,\mathrm{nA}$; STS map parameters: $I_{\mathrm{st}} = 0.08\,\mathrm{nA}$, map size $(10 \times 10)\,\mathrm{nm}^2$ or $(256 \times 256)\,\mathrm{px}^2$; time required for each map $\approx 90\,\mathrm{mins}$. All measurements performed at $5\,\mathrm{K}$.

APPENDIX B

List of Publications
(Liste der Teilpublikationen)

The results presented in this thesis can be found in the following publications:
Teile dieser Arbeit wurden als Bestandteil der folgenden Artikel in Fachzeitschriften bereits veröffentlicht:

[1] **C. Murray**, W. Jolie, J. A. Fischer, J. Hall, C. van Efferen, N. Ehlen, A. Grüneis, C. Busse, and T. Michely
Comprehensive tunneling spectroscopy of quasifreestanding MoS_2 on graphene on Ir(111)
Phys. Rev. B, **99**, 115434 (2019)

[2] W. Jolie, **C. Murray**, P. S. Weiß, J. Hall, F. Portner, N. Atodiresei, A. V. Krasheninnikov, C. Busse, H.-P. Komsa, A. Rosch, and T. Michely
Tomonaga-Luttinger Liquid in a Box: Electrons Confined within MoS_2 Mirror-Twin Boundaries
Phys. Rev. X, **9**, 011055 (2019)

[3] **C. Murray**, C. van Efferen, W. Jolie, J. A. Fischer, J. Hall, A. Rosch, A. V. Krasheninnikov, H.-P. Komsa, and T. Michely.
Band Bending and Valence Band Quantization at Line Defects in MoS_2
ACS Nano, **14**, 9176 (2020)

n/a **C. Murray**, C. van Efferen, W. Jolie, J. Hall, J. A. Fischer, and T. Michely.
Manipulating MoS_2 and its 1D phenomena via substrate screening and charge
manuscript, in preparation

Further publications:

Weitere Publikationen:

[85] J. Hall, B. Pielić, **C. Murray**, W. Jolie, T. Wekking, C. Busse, M. Kralj, and T. Michely
Molecular beam epitaxy of quasi-freestanding transition metal disulphide monolayers on van der Waals substrates: a growth study
2D Mater., **5** (2018), 025005

[50] J. Hall, N. Ehlen, J. Berges, E. van Loon, C. van Efferen, **C. Murray**, M. Rösner, J. Li, B. V. Senkovskiy, M. Hell, M. Rolf, T. Heider, M. C. Asensio, J. Avila, L. Plucinski, T. Wehling, A. Grüneis, and T. Michely
Environmental Control of Charge Density Wave Order in Monolayer 2H-TaS_2
ACS Nano, **13** (2019), 10210

n/a D. Dombrowski *et al.*
TaS_2 *on Au(111)*
manuscript, in preparation

Conference contributions as presenting author:

Konferenzbeiträge als präsentierender Autor:

2017 SFB1238 workshop, Maria Lach (DE), *Investigation and manipulation of 1D phenomena in monolayer MoS_2*. Talk

2017 Flatlands beyond Graphene, Lausanne (CH), *Investigation of 1D charge-density waves and quantum confinement in monolayer MoS_2*. Talk

2018 DPG Spring Meeting, Berlin (DE), *Probing the band structure of quasi-freestanding monolayer MoS_2*. Talk

2018 2DSPM (2D Scanning Probe Microscopy) Conference, San Sebastián (ES), *Probing the band structure of quasi-freestanding monolayer MoS_2*. Poster

2018 SFB1238 workshop, Bensberg (DE), *Tomonaga-Luttinger liquid in a box: electrons confined within MoS_2 mirror twin boundaries*. Talk

2019 DPG Spring Meeting, Regensburg (DE), *A one-dimensional hole gas in monolayer MoS_2*. Poster

2019 AS-SIMEX (Atomic structure of nanosystems from first-principles simulations and microscopy experiments), Helsinki (FI), *Band bending in monolayer MoS_2 creating a 1D hole gas*. Poster

2020 EWEG-2D (European Workshop on Epitaxial Graphene and 2D Materials), Sankt Moritz (CH), *Tuning electronic phenomena in MoS_2 via the substrate.* Talk, postponed due to COVID-19.

Academic distinctions:

Akademische Anerkennungen:

- Poster Prize of the 2DSPM Conference, San Sebastián, 2018

Bibliography

[1] C. Murray, W. Jolie, J. A. Fischer, J. Hall, C. van Efferen, N. Ehlen, A. Grüneis, C. Busse and T. Michely, 'Comprehensive tunneling spectroscopy of quasifreestanding MoS_2 on graphene on Ir(111)', *Phys. Rev. B* **99**, 115434 (2019). Cited on page(s) xiv, 31, 79, 106, 123, and 149

[2] W. Jolie, C. Murray, P. S. Weiß, J. Hall, F. Portner, N. Atodiresei, A. V. Krasheninnikov, C. Busse, H.-P. Komsa, A. Rosch and T. Michely, 'Tomonaga-Luttinger Liquid in a Box: Electrons Confined within MoS_2 Mirror-Twin Boundaries', *Phys. Rev. X* **9**, 011055 (2019). Cited on page(s) xiv, 41, 79, 108, 109, 111, 113, 123, and 149

[3] C. Murray, C. van Efferen, W. Jolie, J. A. Fischer, J. Hall, A. Rosch, A. V. Krasheninnikov, H.-P. Komsa and T. Michely, 'Band Bending and Valence Band Quantization at Line Defects in MoS_2', *ACS Nano* **14**, 9176 (2020). Cited on page(s) xiv, 55, 68, 79, 111, 123, and 149

[4] W. Winer, 'Molybdenum disulfide as a lubricant: A review of the fundamental knowledge', *Wear* **10**, 422 (1967). Cited on page(s) 3

[5] M. R. Vazirisereshk, A. Martini, D. A. Strubbe and M. Z. Baykara, 'Solid Lubrication with MoS_2: A Review', *Lubricants* **7**, 57 (2019). Cited on page(s) 3

[6] P. R. Wallace, 'The Band Theory of Graphite', *Phys. Rev.* **71**, 622 (1947). Cited on page(s) 3

[7] K. Novoselov, A. Geim, S. Morozov, D. Jiang, Y. Zhang, S. Dubonos, I. Grigorieva and A. Firsov, 'Electric Field Effect in Atomically Thin Carbon Films', *Science* **306**, 666 (2004). Cited on page(s) 3 and 11

[8] K. S. Novoselov, D. Jiang, F. Schedin, T. J. Booth, V. V. Khotkevich, S. V. Morozov and A. K. Geim, 'Two-dimensional atomic crystals', *Proc. Natl. Acad. Sci.* **102**, 10451 (2005). Cited on page(s) 3 and 11

[9] N. Briggs *et al.*, 'A roadmap for electronic grade 2D materials', *2D Mater.* **6**, 022001 (2019). Cited on page(s) 3, 10, 11, and 15

[10] H. Li, J. Huang, Y. Shi and L. Li, 'Toward the Growth of High Mobility 2D Transition Metal Dichalcogenide Semiconductors', *Adv. Mater. Interfaces* **6**, 1900220 (2019). Cited on page(s) 3, 11, and 15

[11] S. Kang, D. Lee, J. Kim, A. Capasso, H. S. Kang, J.-W. Park, C.-H. Lee and G.-H. Lee, '2D semiconducting materials for electronic and optoelectronic applications: potential and challenge', *2D Mater.* **7**, 022003 (2020). Cited on page(s) 3, 7, 11, and 15

[12] J. Coraux, A. T. N'Diaye, C. Busse and T. Michely, 'Structural Coherency of Graphene on Ir(111)', *Nano Lett.* **8**, 565 (2008). Cited on page(s) 3 and 13

[13] M. Chhowalla, H. S. Shin, G. Eda, L.-J. Li, K. P. Loh and H. Zhang, 'The chemistry of two-dimensional layered transition metal dichalcogenide nanosheets', *Nat. Chem.* **5**, 263 (2013). Cited on page(s) 7

[14] R. Ganatra and Q. Zhang, 'Few-Layer MoS_2: A Promising Layered Semiconductor', *ACS Nano* **8**, 4074 (2014). Cited on page(s) 7 and 11

[15] S. Manzeli, D. Ovchinnikov, D. Pasquier, O. V. Yazyev and A. Kis, '2D transition metal dichalcogenides', *Nat. Rev. Mater.* **2**, 17033 (2017). Cited on page(s) 7 and 8

[16] A. Rai, H. Movva, A. Roy, D. Taneja, S. Chowdhury and S. Banerjee, 'Progress in Contact, Doping and Mobility Engineering of MoS_2: An Atomically Thin 2D Semiconductor', *Crystals* **8**, 316 (2018). Cited on page(s) 7

[17] L. Xiong, K. Wang, D. Li, X. Luo, J. Weng, Z. Liu and H. Zhang, ‘Research progress on the preparations, characterizations and applications of large scale 2D transition metal dichalcogenides films’, *FlatChem* **21**, 100161 (2020). Cited on page(s) 7 and 10

[18] S. Lebègue and O. Eriksson, ‘Electronic structure of two-dimensional crystals from ab initio theory’, *Phys. Rev. B* **79**, 115409 (2009). Cited on page(s) 7

[19] Z. Y. Zhu, Y. C. Cheng and U. Schwingenschlögl, ‘Giant spin-orbit-induced spin splitting in two-dimensional transition-metal dichalcogenide semiconductors’, *Phys. Rev. B* **84**, 153402 (2011). Cited on page(s) 7, 8, and 9

[20] T. Cheiwchanchamnangij and W. R. L. Lambrecht, ‘Quasiparticle band structure calculation of monolayer, bilayer, and bulk MoS_2’, *Phys. Rev. B* **85**, 205302 (2012). Cited on page(s) 7, 8, and 25

[21] A. Ramasubramaniam, ‘Large excitonic effects in monolayers of molybdenum and tungsten dichalcogenides’, *Phys. Rev. B* **86**, 115409 (2012). Cited on page(s) 7, 8, and 25

[22] H.-P. Komsa and A. V. Krasheninnikov, ‘Effects of confinement and environment on the electronic structure and exciton binding energy of MoS_2 from first principles’, *Phys. Rev. B* **86**, 241201 (2012). Cited on page(s) 7

[23] D. Y. Qiu, F. H. da Jornada and S. G. Louie, ‘Optical Spectrum of MoS_2: Many-Body Effects and Diversity of Exciton States’, *Phys. Rev. Lett.* **111**, 216805 (2013). Cited on page(s) 7 and 8

[24] E. Cappelluti, R. Roldán, J. A. Silva-Guillén, P. Ordejón and F. Guinea, ‘Tight-binding model and direct-gap/indirect-gap transition in single-layer and multilayer MoS_2’, *Phys. Rev. B* **88**, 075409 (2013). Cited on page(s) 7, 8, 9, and 10

[25] J. E. Padilha, H. Peelaers, A. Janotti and C. G. Van de Walle, ‘Nature and evolution of the band-edge states in MoS_2: From monolayer to bulk’, *Phys. Rev. B* **90**, 205420 (2014). Cited on page(s) 7, 8, and 9

[26] W. Zhao, R. M. Ribeiro and G. Eda, ‘Electronic Structure and Optical Signatures of Semiconducting Transition Metal Dichalcogenide Nanosheets’, *Acc. Chem. Res.* **48**, 91 (2015). Cited on page(s) 7, 8, and 9

[27] G.-B. Liu, D. Xiao, Y. Yao, X. Xu and W. Yao, ‘Electronic structures and theoretical modelling of two-dimensional group-VIB transition metal dichalcogenides’, *Chem. Soc. Rev.* **44**, 2643 (2015). Cited on page(s) 7, 9, 10, and 25

[28] R. G. Dickinson and L. Pauling, ‘The crystal structure of molybdenite’, *J. Am. Chem. Soc.* **45**, 1466 (1923). Cited on page(s) 7

[29] J. Wilson and A. Yoffe, ‘The transition metal dichalcogenides discussion and interpretation of the observed optical, electrical and structural properties’, *Adv. Phys.* **18**, 193 (1969). Cited on page(s) 7

[30] R. Frindt and A. Yoffe, ‘Physical properties of layer structures: optical properties and photoconductivity of thin crystals of molybdenum disulphide’, *Proc. R. Soc. London. Ser. A. Math. Phys. Sci.* **273**, 69 (1963). Cited on page(s) 7

[31] P. Joensen, R. Frindt and S. Morrison, ‘Single-layer MoS_2’, *Mater. Res. Bull.* **21**, 457 (1986). Cited on page(s) 7

[32] A. K. Geim and K. S. Novoselov, ‘The rise of graphene’, *Nat. Mater.* **6**, 183 (2007). Cited on page(s) 7

[33] X. Zhou, H. Sun and X. Bai, ‘Two-Dimensional Transition Metal Dichalcogenides: Synthesis, Biomedical Applications and Biosafety Evaluation’, *Front. Bioeng. Biotechnol.* **8**, 1 (2020). Cited on page(s) 7

[34] G. H. Han, D. L. Duong, D. H. Keum, S. J. Yun and Y. H. Lee, ‘van der Waals Metallic Transition Metal Dichalcogenides’, *Chem. Rev.* **118**, 6297 (2018). Cited on page(s) 7

[35] Q. Lv and R. Lv, ‘Two-dimensional heterostructures based on graphene and transition metal dichalcogenides: Synthesis, transfer and applications’, *Carbon* **145**, 240 (2019). Cited on page(s) 7 and 18

[36] R. Roldán, L. Chirolli, E. Prada, J. A. Silva-Guillén, P. San-Jose and F. Guinea, 'Theory of 2D crystals: graphene and beyond', **46**, (2017). Cited on page(s) 7

[37] X. Zhang, Z. Lai, Q. Ma and H. Zhang, 'Novel structured transition metal dichalcogenide nanosheets', *Chem. Soc. Rev.* **47**, 3301 (2018). Cited on page(s) 7, 15, and 18

[38] H. H. Huang, X. Fan, D. J. Singh and W. T. Zheng, 'Recent progress of TMD nanomaterials: phase transitions and applications', *Nanoscale* **12**, 1247 (2020). Cited on page(s) 8

[39] J. Hall, Dissertation, University of Cologne, 2019. Cited on page(s) 8, 11, and 12

[40] Z. Fei, T. Palomaki, S. Wu, W. Zhao, X. Cai, B. Sun, P. Nguyen, J. Finney, X. Xu and D. H. Cobden, 'Edge conduction in monolayer WTe_2', *Nat. Phys.* **13**, 677 (2017). Cited on page(s) 8

[41] C. Zhang, Y. Chen, A. Johnson, M.-Y. Li, L.-J. Li, P. C. Mende, R. M. Feenstra and C.-K. Shih, 'Probing Critical Point Energies of Transition Metal Dichalcogenides: Surprising Indirect Gap of Single Layer WSe_2', *Nano Lett.* **15**, 6494 (2015). Cited on page(s) 8, 105, and 106

[42] P. V. Nguyen, N. C. Teutsch, N. P. Wilson, J. Kahn, X. Xia, A. J. Graham, V. Kandyba, A. Giampietri, A. Barinov, G. C. Constantinescu, N. Yeung, N. D. M. Hine, X. Xu, D. H. Cobden and N. R. Wilson, 'Visualizing electrostatic gating effects in two-dimensional heterostructures', *Nature* **572**, 220 (2019). Cited on page(s) 8

[43] C. Ataca, H. Şahin, E. Aktürk and S. Ciraci, 'Mechanical and Electronic Properties of MoS_2 Nanoribbons and Their Defects', *J. Phys. Chem. C* **115**, 3934 (2011). Cited on page(s) 9

[44] C. Ataca, H. Şahin and S. Ciraci, 'Stable, Single-Layer MX_2 Transition-Metal Oxides and Dichalcogenides in a Honeycomb-Like Structure', *J. Phys. Chem. C* **116**, 8983 (2012). Cited on page(s) 9

[45] A. Splendiani, L. Sun, Y. Zhang, T. Li, J. Kim, C. Y. Chim, G. Galli and F. Wang, 'Emerging photoluminescence in monolayer MoS_2', *Nano Lett.* **10**, 1271 (2010). Cited on page(s) 9 and 10

[46] A. J. Bradley, M. M. Ugeda, F. H. Da Jornada, D. Y. Qiu, W. Ruan, Y. Zhang, S. Wickenburg, A. Riss, J. Lu, S. K. Mo, Z. Hussain, Z. X. Shen, S. G. Louie and M. F. Crommie, 'Probing the Role of Interlayer Coupling and Coulomb Interactions on Electronic Structure in Few-Layer $MoSe_2$ Nanostructures', *Nano Lett.* **15**, 2594 (2015). Cited on page(s) 9 and 10

[47] H.-P. Komsa and A. V. Krasheninnikov, 'Electronic structures and optical properties of realistic transition metal dichalcogenide heterostructures from first principles', *Phys. Rev. B* **88**, 085318 (2013). Cited on page(s) 9 and 13

[48] S. C. de la Barrera, M. R. Sinko, D. P. Gopalan, N. Sivadas, K. L. Seyler, K. Watanabe, T. Taniguchi, A. W. Tsen, X. Xu, D. Xiao and B. M. Hunt, 'Tuning Ising superconductivity with layer and spin–orbit coupling in two-dimensional transition-metal dichalcogenides', *Nat. Commun.* **9**, 1427 (2018). Cited on page(s) 10

[49] P. Chen, Y.-H. Chan, M.-H. Wong, X.-Y. Fang, M. Y. Chou, S.-K. Mo, Z. Hussain, A.-V. Fedorov and T.-C. Chiang, 'Dimensional Effects on the Charge Density Waves in Ultrathin Films of $TiSe_2$', *Nano Lett.* **16**, 6331 (2016). Cited on page(s) 10

[50] J. Hall *et al.*, 'Environmental Control of Charge Density Wave Order in Monolayer 2H-TaS_2', *ACS Nano* **13**, 10210 (2019). Cited on page(s) 10 and 124

[51] A. Ciarrocchi, A. Avsar, D. Ovchinnikov and A. Kis, 'Thickness-modulated metal-to-semiconductor transformation in a transition metal dichalcogenide', *Nat. Commun.* **9**, 919 (2018). Cited on page(s) 10

[52] R. A. B. Villaos, C. P. Crisostomo, Z.-Q. Huang, S.-M. Huang, A. A. B. Padama, M. A. Albao, H. Lin and F.-C. Chuang, 'Thickness dependent electronic properties of Pt dichalcogenides', *npj 2D Mater. Appl.* **3**, 2 (2019). Cited on page(s) 10

[53] C. J. Butler, M. Yoshida, T. Hanaguri and Y. Iwasa, 'Mottness versus unit-cell doubling as the driver of the insulating state in 1T-TaS_2', *Nat. Commun.* **11**, 2477 (2020). Cited on page(s) 10

[54] T. Li and G. Galli, 'Electronic Properties of MoS_2 Nanoparticles', *J. Phys. Chem. C* **111**, 16192 (2007). Cited on page(s) 10

[55] D. J. Trainer *et al.*, 'Inter-Layer Coupling Induced Valence Band Edge Shift in Mono- to Few-Layer MoS_2', *Sci. Rep.* **7**, 40559 (2017). Cited on page(s) 10

[56] S. W. Han, H. Kwon, S. K. Kim, S. Ryu, W. S. Yun, D. H. Kim, J. H. Hwang, J.-S. Kang, J. Baik, H. J. Shin and S. C. Hong, 'Band-gap transition induced by interlayer van der Waals interaction in MoS_2', *Phys. Rev. B* **84**, 045409 (2011). Cited on page(s) 10

[57] K. F. Mak, C. Lee, J. Hone, J. Shan and T. F. Heinz, 'Atomically thin MoS_2: A new direct-gap semiconductor', *Phys. Rev. Lett.* **105**, 136805 (2010). Cited on page(s) 10 and 25

[58] J. K. Ellis, M. J. Lucero and G. E. Scuseria, 'The indirect to direct band gap transition in multilayered MoS_2 as predicted by screened hybrid density functional theory', *Appl. Phys. Lett.* **99**, 261908 (2011). Cited on page(s) 10

[59] Y. Zhang *et al.*, 'Direct Observation of the Transition from Indirect to Direct Bandgap in Atomically Thin Epitaxial $MoSe_2$', *Nat. Nanotechnol.* **9**, 111 (2014). Cited on page(s) 10

[60] L. Du, T. Zhang, M. Liao, G. Liu, S. Wang, R. He, Z. Ye, H. Yu, R. Yang, D. Shi, Y. Yao and G. Zhang, 'Temperature-driven evolution of critical points, interlayer coupling, and layer polarization in bilayer MoS_2', *Phys. Rev. B* **97**, 165410 (2018). Cited on page(s) 10

[61] L. Ortenzi, L. Pietronero and E. Cappelluti, 'Zero-point motion and direct-indirect band-gap crossover in layered transition-metal dichalcogenides', *Phys. Rev. B* **98**, 195313 (2018). Cited on page(s) 10

[62] R. Roldán, A. Castellanos-Gomez, E. Cappelluti and F. Guinea, 'Strain engineering in semiconducting two-dimensional crystals', *J. Phys. Condens. Matter* **27**, 313201 (2015). Cited on page(s) 10

[63] Z. Dai, L. Liu and Z. Zhang, 'Strain Engineering of 2D Materials: Issues and Opportunities at the Interface', *Adv. Mater.* **31**, 1805417 (2019). Cited on page(s) 10

[64] C. Backes *et al.*, 'Production and processing of graphene and related materials', *2D Mater.* **7**, 022001 (2020). Cited on page(s) 10 and 11

[65] T. H. Choudhury, X. Zhang, Z. Y. A. Balushi, M. Chubarov and J. M. Redwing, 'Epitaxial Growth of Two-Dimensional Layered Transition Metal Dichalcogenides', *Annu. Rev. Mater. Res.* **50**, (2020). Cited on page(s) 10, 11, and 12

[66] S. J. McDonnell and R. M. Wallace, 'Atomically-thin layered films for device applications based upon 2D TMDC materials', *Thin Solid Films* **616**, 482 (2016). Cited on page(s) 11 and 12

[67] J. Chan, A. Venugopal, A. Pirkle, S. McDonnell, D. Hinojos, C. W. Magnuson, R. S. Ruoff, L. Colombo, R. M. Wallace and E. M. Vogel, 'Reducing Extrinsic Performance-Limiting Factors in Graphene Grown by Chemical Vapor Deposition', *ACS Nano* **6**, 3224 (2012). Cited on page(s) 11

[68] A. Pirkle, J. Chan, A. Venugopal, D. Hinojos, C. W. Magnuson, S. McDonnell, L. Colombo, E. M. Vogel, R. S. Ruoff and R. M. Wallace, 'The effect of chemical residues on the physical and electrical properties of chemical vapor deposited graphene transferred to SiO_2', *Appl. Phys. Lett.* **99**, 122108 (2011). Cited on page(s) 11

[69] W. Zhou, X. Zou, S. Najmaei, Z. Liu, Y. Shi, J. Kong, J. Lou, P. M. Ajayan, B. I. Yakobson and J.-C. Idrobo, 'Intrinsic Structural Defects in Monolayer Molybdenum Disulfide', *Nano Lett.* **13**, 2615 (2013). Cited on page(s) 11, 16, and 17

[70] S. Najmaei, M. Amani, M. L. Chin, Z. Liu, A. G. Birdwell, T. P. O'Regan, P. M. Ajayan, M. Dubey and J. Lou, 'Electrical Transport Properties of Polycrystalline Monolayer Molybdenum Disulfide', *ACS Nano* **8**, 7930 (2014). Cited on page(s) 11

[71] A. Pisoni, J. Jacimovic, R. Gaál, B. Náfrádi, H. Berger, Z. Révay and L. Forró, 'Anisotropic transport properties of tungsten disulfide', *Scr. Mater.* **114**, 48 (2016). Cited on page(s) 11

[72] B. A. Joyce, ‘Molecular beam epitaxy’, *Reports Prog. Phys.* **48**, 1637 (1985). Cited on page(s) 11

[73] L. A. Walsh, R. Addou, R. M. Wallace and C. L. Hinkle, ‘Molecular Beam Epitaxy’ (Elsevier, Amsterdam, 2018), Pages 515–531. Cited on page(s) 11

[74] L. A. Walsh and C. L. Hinkle, ‘van der Waals epitaxy: 2D materials and topological insulators’, *Appl. Mater. Today* **9**, 504 (2017). Cited on page(s) 11

[75] A. Koma, K. Sunouchi and T. Miyajima, ‘Fabrication and characterization of heterostructures with subnanometer thickness’, *Microelectron. Eng.* **2**, 129 (1984). Cited on page(s) 12

[76] P. Tsipas, D. Tsoutsou, J. Marquez-Velasco, K. Aretouli, E. Xenogiannopoulou, E. Vassalou, G. Kordas and A. Dimoulas, ‘Epitaxial $ZrSe_2$/$MoSe_2$ semiconductor v.d. Waals heterostructures on wide band gap AlN substrates’, *Microelectron. Eng.* **147**, 269 (2015). Cited on page(s) 12

[77] R. Yue *et al.*, ‘$HfSe_2$ thin films: 2D transition metal dichalcogenides grown by molecular beam epitaxy’, *ACS Nano* **9**, 474 (2015). Cited on page(s) 12

[78] K. Saiki, K. Ueno, T. Shimada and A. Koma, ‘Application of Van der Waals epitaxy to highly heterogeneous systems’, *J. Cryst. Growth* **95**, 603 (1989). Cited on page(s) 12

[79] M. M. Ugeda, A. J. Bradley, S. F. Shi, F. H. Da Jornada, Y. Zhang, D. Y. Qiu, W. Ruan, S. K. Mo, Z. Hussain, Z. X. Shen, F. Wang, S. G. Louie and M. F. Crommie, ‘Giant bandgap renormalization and excitonic effects in a monolayer transition metal dichalcogenide semiconductor’, *Nat. Mater.* **13**, 1091 (2014). Cited on page(s) 12, 13, and 26

[80] J. H. Park, S. Vishwanath, X. Liu, H. Zhou, S. M. Eichfeld, S. K. Fullerton-Shirey, J. A. Robinson, R. M. Feenstra, J. Furdyna, D. Jena, H. G. Xing and A. C. Kummel, ‘Scanning Tunneling Microscopy and Spectroscopy of Air Exposure Effects on Molecular Beam Epitaxy Grown WSe_2 Monolayers and Bilayers’, *ACS Nano* **10**, 4258 (2016). Cited on page(s) 12

[81] H. C. Diaz, R. Chaghi, Y. Ma and M. Batzill, ‘Molecular beam epitaxy of the van der Waals heterostructure $MoTe_2$ on MoS_2: phase, thermal, and chemical stability’, *2D Mater.* **2**, 044010 (2015). Cited on page(s) 12

[82] W. A. West and A. W. C. Menzies, ‘The Vapor Pressures of Sulphur between 100° and 550° with related Thermal Data’, *J. Phys. Chem.* **33**, 1880 (1929). Cited on page(s) 12

[83] J. A. Miwa, S. Ulstrup, S. G. Sørensen, M. Dendzik, A. Grubišić Čabo, M. Bianchi, J. V. Lauritsen and P. Hofmann, ‘Electronic Structure of Epitaxial Single-Layer MoS_2’, *Phys. Rev. Lett.* **114**, 046802 (2015). Cited on page(s) 12

[84] C. Kreis, M. Traving, R. Adelung, L. Kipp and M. Skibowski, ‘Tracing the valence band maximum during epitaxial growth of HfS_2 on WSe_2’, *Appl. Surf. Sci.* **166**, 17 (2000). Cited on page(s) 12

[85] J. Hall, B. Pielić, C. Murray, W. Jolie, T. Wekking, C. Busse, M. Kralj and T. Michely, ‘Molecular beam epitaxy of quasi-freestanding transition metal disulphide monolayers on van der Waals substrates: a growth study’, *2D Mater.* **5**, 025005 (2018). Cited on page(s) 12, 13, 105, 106, 108, 116, and 124

[86] J. V. Lauritsen, J. Kibsgaard, S. Helveg, H. Topsøe, B. S. Clausen, E. Lægsgaard and F. Besenbacher, ‘Size-dependent structure of MoS_2 nanocrystals’, *Nat. Nanotechnol.* **2**, 53 (2007). Cited on page(s) 12

[87] S. G. Sørensen, H. G. Füchtbauer, A. K. Tuxen, A. S. Walton and J. V. Lauritsen, ‘Structure and Electronic Properties of *In Situ* Synthesized Single-Layer MoS_2 on a Gold Surface’, *ACS Nano* **8**, 6788 (2014). Cited on page(s) 12

[88] H. Bana *et al.*, ‘Epitaxial growth of single-orientation high-quality MoS_2 monolayers’, *2D Mater.* **5**, 035012 (2018). Cited on page(s) 12

[89] A. Bruix, J. A. Miwa, N. Hauptmann, D. Wegner, S. Ulstrup, S. S. Grønborg, C. E. Sanders, M. Dendzik, A. Grubišić Čabo, M. Bianchi, J. V. Lauritsen, A. A. Khajetoorians, B. Hammer and P. Hofmann, ‘Single-layer MoS_2 on Au(111): Band gap renormalization and substrate interaction’, *Phys. Rev. B* **93**, 165422 (2016). Cited on page(s) 12

[90] M. Dendzik, A. Bruix, M. Michiardi, A. S. Ngankeu, M. Bianchi, J. A. Miwa, B. Hammer, P. Hofmann and C. E. Sanders, 'Substrate-induced semiconductor-to-metal transition in monolayer WS_2', *Phys. Rev. B* **96**, 235440 (2017). Cited on page(s) 12

[91] R.-M. Stan, S. K. Mahatha, M. Bianchi, C. E. Sanders, D. Curcio, P. Hofmann and J. A. Miwa, 'Epitaxial single-layer NbS_2 on Au(111): Synthesis, structure, and electronic properties', *Phys. Rev. Mater.* **3**, 044003 (2019). Cited on page(s) 12

[92] H. M. Lefcochilos-Fogelquist, O. R. Albertini and A. Y. Liu, 'Substrate-induced suppression of charge density wave phase in monolayer 1H-TaS_2 on Au(111)', *Phys. Rev. B* **99**, 174113 (2019). Cited on page(s) 12

[93] C. E. Sanders, M. Dendzik, A. S. Ngankeu, A. Eich, A. Bruix, M. Bianchi, J. A. Miwa, B. Hammer, A. A. Khajetoorians and P. Hofmann, 'Crystalline and electronic structure of single-layer TaS_2', *Phys. Rev. B* **94**, 081404 (2016). Cited on page(s) 12

[94] B. Shao, A. Eich, C. Sanders, A. S. Ngankeu, M. Bianchi, P. Hofmann, A. A. Khajetoorians and T. O. Wehling, 'Pseudodoping of a metallic two-dimensional material by the supporting substrate', *Nat. Commun.* **10**, 180 (2019). Cited on page(s) 12

[95] X. Liu, I. Balla, H. Bergeron, G. P. Campbell, M. J. Bedzyk and M. C. Hersam, 'Rotationally commensurate growth of MoS_2 on epitaxial graphene', *ACS Nano* **10**, 1067 (2016). Cited on page(s) 13

[96] J. Shi, X. Zhou, G.-F. Han, M. Liu, D. Ma, J. Sun, C. Li, Q. Ji, Y. Zhang, X. Song, X.-Y. Lang, Q. Jiang, Z. Liu and Y. Zhang, 'Narrow-Gap Quantum Wires Arising from the Edges of Monolayer MoS_2 Synthesized on Graphene', *Adv. Mater. Interfaces* **3**, 1600332 (2016). Cited on page(s) 13

[97] J. Klein, A. Kerelsky, M. Lorke, M. Florian, F. Sigger, J. Kiemle, M. C. Reuter, T. Taniguchi, K. Watanabe, J. J. Finley, A. N. Pasupathy, A. W. Holleitner, F. M. Ross and U. Wurstbauer, 'Impact of substrate induced band tail states on the electronic and optical properties of MoS_2', *Appl. Phys. Lett.* **115**, 261603 (2019). Cited on page(s) 13

[98] Y. L. Huang, Y. Chen, W. Zhang, S. Y. Quek, C.-H. Chen, L.-J. Li, W.-T. Hsu, W.-H. Chang, Y. J. Zheng, W. Chen and A. T. S. Wee, 'Bandgap Tunability at Single-Layer Molybdenum Disulphide Grain Boundaries', *Nat. Commun.* **6**, 6298 (2015). Cited on page(s) 13 and 15

[99] A. K. Geim and I. V. Grigorieva, 'Van der Waals heterostructures', *Nature* **499**, 419 (2013). Cited on page(s) 13

[100] J. Park and M. Yan, 'Covalent Functionalization of Graphene with Reactive Intermediates', *Acc. Chem. Res.* **46**, 181 (2013). Cited on page(s) 13

[101] J. Coraux, A. T. N'Diaye, M. Engler, C. Busse, D. Wall, N. Buckanie, F. J. Meyer zu Heringdorf, R. van Gastel, B. Poelsema and T. Michely, 'Growth of graphene on Ir(111)', *New J. Phys.* **11**, 023006 (2009). Cited on page(s) 13

[102] A. T. N'Diaye, J. Coraux, T. N. Plasa, C. Busse and T. Michely, 'Structure of epitaxial graphene on Ir(111)', *New J. Phys.* **10**, 043033 (2008). Cited on page(s) 13

[103] C. Busse, P. Lazić, R. Djemour, J. Coraux, T. Gerber, N. Atodiresei, V. Caciuc, R. Brako, A. T. N'Diaye, S. Blügel, J. Zegenhagen and T. Michely, 'Graphene on Ir(111): Physisorption with Chemical Modulation', *Phys. Rev. Lett.* **107**, 036101 (2011). Cited on page(s) 13 and 116

[104] I. Pletikosić, M. Kralj, P. Pervan, R. Brako, J. Coraux, A. T. N'Diaye, C. Busse and T. Michely, 'Dirac Cones and Minigaps for Graphene on Ir(111)', *Phys. Rev. Lett.* **102**, 056808 (2009). Cited on page(s) 13

[105] A. H. Castro Neto, F. Guinea, N. M. R. Peres, K. S. Novoselov and A. K. Geim, 'The electronic properties of graphene', *Rev. Mod. Phys.* **81**, 109 (2009). Cited on page(s) 13

[106] U. A. Schröder, M. Petrović, T. Gerber, A. J. Martínez-Galera, E. Grånäs, M. A. Arman, C. Herbig, J. Schnadt, M. Kralj, J. Knudsen and T. Michely, 'Core Level Shifts of Intercalated Graphene', *2D Mater.* **4**, 015013 (2016). Cited on page(s) 13

[107] J. Hong, C. Jin, J. Yuan and Z. Zhang, ‘Atomic Defects in Two-Dimensional Materials: From Single-Atom Spectroscopy to Functionalities in Opto-/Electronics, Nanomagnetism, and Catalysis’, *Adv. Mater.* **29**, 1606434 (2017). Cited on page(s) 15

[108] Z. Hu, Z. Wu, C. Han, J. He, Z. Ni and W. Chen, ‘Two-dimensional transition metal dichalcogenides: interface and defect engineering’, *Chem. Soc. Rev.* **47**, 3100 (2018). Cited on page(s) 15

[109] J. Lin and W. Zhou, ‘Defects in Advanced Electronic Materials and Novel Low Dimensional Structures’ (Elsevier, Amsterdam, 2018), Pages 161–187. Cited on page(s) 15

[110] S. Wang, A. Robertson and J. H. Warner, ‘Atomic structure of defects and dopants in 2D layered transition metal dichalcogenides’, *Chem. Soc. Rev.* **47**, 6764 (2018). Cited on page(s) 15 and 18

[111] M. Batzill, ‘Mirror Twin Grain Boundaries in Molybdenum Dichalcogenides’, *J. Phys. Condens. Matter* **30**, 493001 (2018). Cited on page(s) 15 and 17

[112] R. Siegel, ‘Vacancy concentrations in metals’, *J. Nucl. Mater.* **69-70**, 117 (1978). Cited on page(s) 15

[113] J. Hong *et al.*, ‘Exploring atomic defects in molybdenum disulphide monolayers’, *Nat. Commun.* **6**, 6293 (2015). Cited on page(s) 15

[114] S. Najmaei, Z. Liu, W. Zhou, X. Zou, G. Shi, S. Lei, B. I. Yakobson, J. C. Idrobo, P. M. Ajayan and J. Lou, ‘Vapour phase growth and grain boundary structure of molybdenum disulphide atomic layers’, *Nat. Mater.* **12**, 754 (2013). Cited on page(s) 15 and 16

[115] A. M. Van Der Zande, P. Y. Huang, D. A. Chenet, T. C. Berkelbach, Y. You, G. H. Lee, T. F. Heinz, D. R. Reichman, D. A. Muller and J. C. Hone, ‘Grains and Grain Boundaries in Highly Crystalline Monolayer Molybdenum Disulphide’, *Nat. Mater.* **12**, 554 (2013). Cited on page(s) 15, 16, 17, and 18

[116] A. Azizi, X. Zou, P. Ercius, Z. Zhang, A. L. Elías, N. Perea-López, G. Stone, M. Terrones, B. I. Yakobson and N. Alem, ‘Dislocation motion and grain boundary migration in two-dimensional tungsten disulphide’, *Nat. Commun.* **5**, 4867 (2014). Cited on page(s) 15 and 16

[117] T. H. Ly, D. J. Perello, J. Zhao, Q. Deng, H. Kim, G. H. Han, S. H. Chae, H. Y. Jeong and Y. H. Lee, ‘Misorientation-Angle-Dependent Electrical Transport across Molybdenum Disulfide Grain Boundaries’, *Nat. Commun.* **7**, 10426 (2016). Cited on page(s) 15 and 16

[118] X. Liu, I. Balla, H. Bergeron and M. C. Hersam, ‘Point Defects and Grain Boundaries in Rotationally Commensurate MoS_2 on Epitaxial Graphene’, *J. Phys. Chem. C* **120**, 20798 (2016). Cited on page(s) 15

[119] M. Precner, T. Polaković, Q. Qiao, D. J. Trainer, A. V. Putilov, C. Di Giorgio, I. Cone, Y. Zhu, X. X. Xi, M. Iavarone and G. Karapetrov, ‘Evolution of Metastable Defects and Its Effect on the Electronic Properties of MoS_2 Films’, *Sci. Rep.* **8**, 6724 (2018). Cited on page(s) 15

[120] M. Hong, P. Yang, X. Zhou, S. Zhao, C. Xie, J. Shi, Z. Zhang, Q. Fu and Y. Zhang, ‘Decoupling the Interaction between Wet-Transferred MoS_2 and Graphite Substrate by an Interfacial Water Layer’, *Adv. Mater. Interfaces* **5**, 1800641 (2018). Cited on page(s) 15

[121] Y. L. Huang, Z. Ding, W. Zhang, Y. H. Chang, Y. Shi, L. J. Li, Z. Song, Y. J. Zheng, D. Chi, S. Y. Quek and A. T. Wee, ‘Gap states at low-angle grain boundaries in monolayer tungsten diselenide’, *Nano Lett.* **16**, 3682 (2016). Cited on page(s) 15

[122] H.-P. Komsa and A. V. Krasheninnikov, ‘Engineering the Electronic Properties of Two-Dimensional Transition Metal Dichalcogenides by Introducing Mirror Twin Boundaries’, *Adv. Electron. Mater.* **3**, 1600468 (2017). Cited on page(s) 16 and 17

[123] A. Pulkin and O. V. Yazyev, ‘Spin- and Valley-Polarized Transport across Line Defects in Monolayer MoS_2’, *Phys. Rev. B* **93**, 041419 (2016). Cited on page(s) 16 and 18

[124] X. Zou, Y. Liu and B. I. Yakobson, ‘Predicting Dislocations and Grain Boundaries in Two-Dimensional Metal-Disulfides from the First Principles’, *Nano Lett.* **13**, 253 (2013). Cited on page(s) 16 and 17

[125] D. Le and T. S. Rahman, ‘Joined edges in MoS_2: Metallic and half-metallic wires’, *J. Phys. Condens. Matter* **25**, 4 (2013). Cited on page(s) 16 and 17

[126] S. Barja *et al.*, ‘Charge density wave order in 1D mirror twin boundaries of single-layer $MoSe_2$’, *Nat. Phys.* **12**, 751 (2016). Cited on page(s) 16, 17, 107, 108, and 109

[127] Y. Ma, H. C. Diaz, J. Avila, C. Chen, V. Kalappattil, R. Das, M.-H. Phan, T. Cadez, J. M. P. Carmelo, M. C. Asensio and M. Batzill, ‘Angle resolved photoemission spectroscopy reveals spin charge separation in metallic $MoSe_2$ grain boundary’, *Nat. Commun.* **8**, 14231 (2017). Cited on page(s) 16, 18, 28, 107, 108, 109, 112, and 113

[128] R.-L. Chu, G.-B. Liu, W. Yao, X. Xu, D. Xiao and C. Zhang, ‘Spin-orbit-coupled quantum wires and Majorana fermions on zigzag edges of monolayer transition-metal dichalcogenides’, *Phys. Rev. B* **89**, 155317 (2014). Cited on page(s) 16

[129] K. Hsieh, V. Kochat, X. Zhang, Y. Gong, C. S. Tiwary, P. M. Ajayan and A. Ghosh, ‘Effect of Carrier Localization on Electrical Transport and Noise at Individual Grain Boundaries in Monolayer MoS_2’, *Nano Lett.* **17**, 5452 (2017). Cited on page(s) 16

[130] X. Liu, I. Balla, H. Bergeron and M. C. Hersam, ‘Point Defects and Grain Boundaries in Rotationally Commensurate MoS_2 on Epitaxial Graphene’, *J. Phys. Chem. C* **120**, 20798 (2016). Cited on page(s) 16

[131] C. Yan, X. Dong, C. H. Li and L. Li, ‘Charging Effect at Grain Boundaries of MoS_2’, *Nanotechnology* **29**, 195704 (2018). Cited on page(s) 16

[132] F. Banhart, J. Kotakoski and A. V. Krasheninnikov, ‘Structural Defects in Graphene’, *ACS Nano* **5**, 26 (2011). Cited on page(s) 16

[133] O. Lehtinen, H. P. Komsa, A. Pulkin, M. B. Whitwick, M. W. Chen, T. Lehnert, M. J. Mohn, O. V. Yazyev, A. Kis, U. Kaiser and A. V. Krasheninnikov, ‘Atomic scale microstructure and properties of Se-deficient two-dimensional $MoSe_2$’, *ACS Nano* **9**, 3274 (2015). Cited on page(s) 16, 17, and 18

[134] P. M. Coelho, H. P. Komsa, H. Coy Diaz, Y. Ma, A. V. Krasheninnikov and M. Batzill, ‘Post-Synthesis Modifications of Two-Dimensional $MoSe_2$ or $MoTe_2$ by Incorporation of Excess Metal Atoms into the Crystal Structure’, *ACS Nano* **12**, 3975 (2018). Cited on page(s) 16

[135] J. Lin, S. T. Pantelides and W. Zhou, ‘Vacancy-Induced Formation and Growth of Inversion Domains in Transition-Metal Dichalcogenide Monolayer’, *ACS Nano* **9**, 5189 (2015). Cited on page(s) 16

[136] H. Liu, L. Jiao, F. Yang, Y. Cai, X. Wu, W. Ho, C. Gao, J. Jia, N. Wang, H. Fan, W. Yao and M. Xie, ‘Dense Network of One-Dimensional Midgap Metallic Modes in Monolayer $MoSe_2$ and Their Spatial Undulations’, *Phys. Rev. Lett.* **113**, 066105 (2014). Cited on page(s) 17, 107, and 108

[137] H. Liu, H. Zheng, F. Yang, L. Jiao, J. Chen, W. Ho, C. Gao, J. Jia and M. Xie, ‘Line and Point Defects in $MoSe_2$ Bilayer Studied by Scanning Tunneling Microscopy and Spectroscopy’, *ACS Nano* **9**, 6619 (2015). Cited on page(s) 17

[138] Y.-C. Lin, T. Björkman, H.-P. Komsa, P.-Y. Teng, C.-H. Yeh, F.-S. Huang, K.-H. Lin, J. Jadczak, Y.-S. Huang, P.-W. Chiu, A. V. Krasheninnikov and K. Suenaga, ‘Three-fold rotational defects in two-dimensional transition metal dichalcogenides’, *Nat. Commun.* **6**, 6736 (2015). Cited on page(s) 17

[139] X. Zou and B. I. Yakobson, ‘Metallic High-Angle Grain Boundaries in Monolayer Polycrystalline WS_2’, *Small* **11**, 4503 (2015). Cited on page(s) 17

[140] H. C. Diaz, Y. Ma, R. Chaghi and M. Batzill, ‘High density of (pseudo) periodic twin-grain boundaries in molecular beam epitaxy-grown van der Waals heterostructure: $MoTe_2/MoS_2$’, *Appl. Phys. Lett.* **108**, 191606 (2016). Cited on page(s) 17 and 107

[141] Y. Ma, S. Kolekar, H. Coy Diaz, J. Aprojanz, I. Miccoli, C. Tegenkamp and M. Batzill, ‘Metallic Twin Grain Boundaries Embedded in $MoSe_2$ Monolayers Grown by Molecular Beam Epitaxy’, *ACS Nano* **11**, 5130 (2017). Cited on page(s) 17 and 18

[142] T. Kaneko and R. Saito, 'Origin of Band Bending at Domain Boundaries of MoS_2: First-Principles Study', *Jpn. J. Appl. Phys.* **57**, 04FP09 (2018). Cited on page(s) 18

[143] L. Du *et al.*, 'The Effect of Twin Grain Boundary Tuned by Temperature on the Electrical Transport Properties of Monolayer MoS_2', *Crystals* **6**, 115 (2016). Cited on page(s) 18

[144] S. Wang, Z. Qin, G. S. Jung, F. J. Martin-Martinez, K. Zhang, M. J. Buehler and J. H. Warner, 'Atomically Sharp Crack Tips in Monolayer MoS_2 and Their Enhanced Toughness by Vacancy Defects', *ACS Nano* **10**, 9831 (2016). Cited on page(s) 18

[145] H. Schweiger, P. Raybaud, G. Kresse and H. Toulhoat, 'Shape and Edge Sites Modifications of MoS_2 Catalytic Nanoparticles Induced by Working Conditions: A Theoretical Study', *J. Catal.* **207**, 76 (2002). Cited on page(s) 18

[146] M. V. Bollinger, K. W. Jacobsen and J. K. Nørskov, 'Atomic and electronic structure of MoS_2 nanoparticles', *Phys. Rev. B* **67**, 085410 (2003). Cited on page(s) 18

[147] Q. Chen, H. Li, W. Xu, S. Wang, H. Sawada, C. S. Allen, A. I. Kirkland, J. C. Grossman and J. H. Warner, 'Atomically Flat Zigzag Edges in Monolayer MoS_2 by Thermal Annealing', *Nano Lett.* **17**, 5502 (2017). Cited on page(s) 18

[148] H. Xu, S. Liu, Z. Ding, S. J. R. Tan, K. M. Yam, Y. Bao, C. T. Nai, M.-F. Ng, J. Lu, C. Zhang and K. P. Loh, 'Oscillating edge states in one-dimensional MoS_2 nanowires', *Nat. Commun.* **7**, 12904 (2016). Cited on page(s) 18

[149] M. V. Bollinger, J. V. Lauritsen, K. W. Jacobsen, J. K. Nørskov, S. Helveg and F. Besenbacher, 'One-Dimensional Metallic Edge States in MoS_2', *Phys. Rev. Lett.* **87**, 196803 (2001). Cited on page(s) 18

[150] K. Andersen, K. W. Jacobsen and K. S. Thygesen, 'Plasmons on the edge of MoS_2 nanostructures', *Phys. Rev. B* **90**, 161410 (2014). Cited on page(s) 18

[151] A. R. Botello-Méndez, F. López-Urías, M. Terrones and H. Terrones, 'Metallic and ferromagnetic edges in molybdenum disulfide nanoribbons', *Nanotechnology* **20**, 325703 (2009). Cited on page(s) 18

[152] Q. Yue, S. Chang, J. Kang, X. Zhang, Z. Shao, S. Qin and J. Li, 'Bandgap tuning in armchair MoS_2 nanoribbon', *J. Phys. Condens. Matter* **24**, 335501 (2012). Cited on page(s) 18

[153] M. C. Lucking, J. Bang, H. Terrones, Y.-Y. Sun and S. Zhang, 'Multivalency-Induced Band Gap Opening at MoS_2 Edges', *Chem. Mater.* **27**, 3326 (2015). Cited on page(s) 18

[154] Q. Chen, L. L. Li and F. M. Peeters, 'Magnetic field dependence of electronic properties of MoS_2 quantum dots with different edges', *Phys. Rev. B* **97**, 085437 (2018). Cited on page(s) 18

[155] M. Gibertini and N. Marzari, 'Emergence of One-Dimensional Wires of Free Carriers in Transition-Metal-Dichalcogenide Nanostructures', *Nano Lett.* **15**, 6229 (2015). Cited on page(s) 18

[156] J. Wang, Z. Li, H. Chen, G. Deng and X. Niu, 'Recent Advances in 2D Lateral Heterostructures', *Nano-Micro Lett.* **11**, 48 (2019). Cited on page(s) 18

[157] O. Ávalos-Ovando, D. Mastrogiuseppe and S. E. Ulloa, 'Lateral heterostructures and one-dimensional interfaces in 2D transition metal dichalcogenides', *J. Phys. Condens. Matter* **31**, 213001 (2019). Cited on page(s) 18 and 110

[158] X. Duan, C. Wang, J. C. Shaw, R. Cheng, Y. Chen, H. Li, X. Wu, Y. Tang, Q. Zhang, A. Pan, J. Jiang, R. Yu, Y. Huang and X. Duan, 'Lateral epitaxial growth of two-dimensional layered semiconductor heterojunctions', *Nat. Nanotechnol.* **9**, 1024 (2014). Cited on page(s) 19 and 110

[159] M.-Y. Li, Y. Shi, C.-C. Cheng, L.-S. Lu, Y.-C. Lin, H.-L. Tang, M.-L. Tsai, C.-W. Chu, K.-H. Wei, J.-H. He, W.-H. Chang, K. Suenaga and L.-J. Li, 'Epitaxial growth of a monolayer WSe_2-MoS_2 lateral p-n junction with an atomically sharp interface', *Science* **349**, 524 (2015). Cited on page(s) 19

[160] Z. Li, J. Zheng, Y. Zhang, C. Zheng, W. Y. Woon, M. C. Chuang, H. C. Tsai, C. H. Chen, A. Davis, Z. Q. Xu, J. Lin, H. Zhang and Q. Bao, ‘Synthesis of ultrathin composition graded doped Lateral WSe_2/WS_2 heterostructures’, *ACS Appl. Mater. Interfaces* **9**, 34204 (2017). Cited on page(s) 19

[161] X. Chen, Y. Qiu, H. Yang, G. Liu, W. Zheng, W. Feng, W. Cao, W. Hu and P. A. Hu, ‘In-plane mosaic potential growth of large-area 2D layered semiconductors MoS_2-$MoSe_2$ lateral heterostructures and photodetector application’, *ACS Appl. Mater. Interfaces* **9**, 1684 (2017). Cited on page(s) 19 and 110

[162] M.-L. Tsai, M.-Y. Li, J. R. D. Retamal, K.-T. Lam, Y.-C. Lin, K. Suenaga, L.-J. Chen, G. Liang, L.-J. Li and J.-H. He, ‘Single Atomically Sharp Lateral Monolayer p-n Heterojunction Solar Cells with Extraordinarily High Power Conversion Efficiency’, *Adv. Mater.* **29**, 1701168 (2017). Cited on page(s) 19 and 110

[163] M. M. Ugeda, A. Pulkin, S. Tang, H. Ryu, Q. Wu, Y. Zhang, D. Wong, Z. Pedramrazi, A. Martín-Recio, Y. Chen, F. Wang, Z.-X. Shen, S.-K. Mo, O. V. Yazyev and M. F. Crommie, ‘Observation of topologically protected states at crystalline phase boundaries in single-layer WSe_2’, *Nat. Commun.* **9**, 3401 (2018). Cited on page(s) 19

[164] Z. Pedramrazi, C. Herbig, A. Pulkin, S. Tang, M. Phillips, D. Wong, H. Ryu, M. Pizzochero, Y. Chen, F. Wang, E. J. Mele, Z.-X. Shen, S.-K. Mo, O. V. Yazyev and M. F. Crommie, ‘Manipulating Topological Domain Boundaries in the Single-Layer Quantum Spin Hall Insulator $1T'$–WSe_2’, *Nano Lett.* **19**, 5634 (2019). Cited on page(s) 19

[165] R. Martinez-Gordillo and M. Pruneda, ‘Polar Discontinuities and 1D Interfaces in Monolayered Materials’, *Prog. Surf. Sci.* **90**, 444 (2015). Cited on page(s) 19, 21, and 110

[166] N. A. Spaldin, ‘A beginner’s guide to the modern theory of polarization’, *J. Solid State Chem.* **195**, 2 (2012). Cited on page(s) 19 and 20

[167] R. Resta, ‘Macroscopic Electric Polarization as a Geometric Quantum Phase’, *Europhys. Lett.* **22**, 133 (1993). Cited on page(s) 19, 20, and 109

[168] D. Vanderbilt and R. D. King-Smith, ‘Electric Polarization as a Bulk Quantity and Its Relation to Surface Charge’, *Phys. Rev. B* **48**, 4442 (1993). Cited on page(s) 19, 20, and 109

[169] R. D. King-Smith and D. Vanderbilt, ‘Theory of polarization of crystalline solids’, *Phys. Rev. B* **47**, 1651 (1993). Cited on page(s) 19 and 109

[170] N. C. Bristowe, P. B. Littlewood and E. Artacho, ‘The net charge at interfaces between insulators’, *J. Phys. Condens. Matter* **23**, 081001 (2011). Cited on page(s) 20 and 22

[171] M. Stengel and D. Vanderbilt, ‘Berry-phase theory of polar discontinuities at oxide-oxide interfaces’, *Phys. Rev. B* **80**, 241103 (2009). Cited on page(s) 21

[172] M. Gibertini and N. Marzari, ‘Emergence of One-Dimensional Wires of Free Carriers in Transition-Metal-Dichalcogenide Nanostructures’, *Nano Lett.* **15**, 6229 (2015). Cited on page(s) 21, 22, and 112

[173] N. Marzari, A. A. Mostofi, J. R. Yates, I. Souza and D. Vanderbilt, ‘Maximally localized Wannier functions: Theory and applications’, *Rev. Mod. Phys.* **84**, 1419 (2012). Cited on page(s) 21

[174] M. Gibertini, G. Pizzi and N. Marzari, ‘Engineering Polar Discontinuities in Honeycomb Lattices’, *Nat. Commun.* **5**, 5157 (2014). Cited on page(s) 21, 22, and 110

[175] P. Jadaun, D. Xiao, Q. Niu and S. K. Banerjee, ‘Topological classification of crystalline insulators with space group symmetry’, *Phys. Rev. B* **88**, 085110 (2013). Cited on page(s) 21 and 22

[176] N. C. Bristowe, M. Stengel, P. B. Littlewood, E. Artacho and J. M. Pruneda, ‘One-dimensional half-metallic interfaces of two-dimensional honeycomb insulators’, *Phys. Rev. B* **88**, 161411 (2013). Cited on page(s) 22 and 110

[177] A. Ohtomo and H. Y. Hwang, ‘A High-Mobility Electron Gas at the $LaAlO_3/SrTiO_3$ Heterointerface’, *Nature* **427**, 423 (2004). Cited on page(s) 22

[178] N. Nakagawa, H. Y. Hwang and D. A. Muller, ‘Why some interfaces cannot be sharp’, *Nat. Mater.* **5**, 204 (2006). Cited on page(s) 22

[179] S. Thiel, G. Hammerl, A. Schmehl, C. W. Schneider and J. Mannhart, ‘Tunable Quasi-Two-Dimensional Electron Gases in Oxide Heterostructures’, *Science* **313**, 1942 (2006). Cited on page(s) 22

[180] J. Mannhart and D. G. Schlom, ‘Oxide Interfaces - An Opportunity for Electronics’, *Science* **327**, 1607 (2010). Cited on page(s) 22

[181] J. Goniakowski, F. Finocchi and C. Noguera, ‘Polarity of oxide surfaces and nanostructures’, *Reports Prog. Phys.* **71**, 016501 (2008). Cited on page(s) 22

[182] N. C. Bristowe, P. Ghosez, P. B. Littlewood and E. Artacho, ‘The origin of two-dimensional electron gases at oxide interfaces: insights from theory’, *J. Phys. Condens. Matter* **26**, 143201 (2014). Cited on page(s) 22

[183] F. Güller, A. M. Llois, J. Goniakowski and C. Noguera, ‘Polarity effects in unsupported polar nanoribbons’, *Phys. Rev. B* **87**, 205423 (2013). Cited on page(s) 22, 109, and 110

[184] J.-N. Chazalviel, ‘Coulomb Screening by Mobile Charges: Applications to Materials Science, Chemistry and Biology’ (Springer Science & Business Media, New York, 2012). Cited on page(s) 23 and 24

[185] B. Scharf, D. Van Tuan, I. Žutić and H. Dery, ‘Dynamical screening in monolayer transition-metal dichalcogenides and its manifestations in the exciton spectrum’, *J. Phys. Condens. Matter* **31**, 203001 (2019). Cited on page(s) 23

[186] G. Wang, A. Chernikov, M. M. Glazov, T. F. Heinz, X. Marie, T. Amand and B. Urbaszek, ‘Colloquium: Excitons in atomically thin transition metal dichalcogenides’, *Rev. Mod. Phys.* **90**, 021001 (2018). Cited on page(s) 23, 24, and 26

[187] T. Giamarchi, ‘Theoretical Framework for Quasi-One Dimensional Systems’, *Chem. Rev.* **104**, 5037 (2004). Cited on page(s) 23

[188] T. Giamarchi, ‘Quantum Physics in One Dimension’ (Clarendon Press, Oxford, 2003). Cited on page(s) 23, 27, and 28

[189] V. V. Deshpande, M. Bockrath, L. I. Glazman and A. Yacoby, ‘Electron liquids and solids in one dimension’, *Nature* **464**, 209 (2010). Cited on page(s) 23, 27, and 28

[190] E. Kaxiras, ‘Atomic and Electronic Structure Of Solids’ (Cambridge University Press, Cambridge, 2003), Pages 88–92. Cited on page(s) 24

[191] L. Hedin, ‘On correlation effects in electron spectroscopies and the GW approximation’, *J. Phys. Condens. Matter* **11**, R489 (1999). Cited on page(s) 24

[192] S. Gao and L. Yang, ‘Renormalization of the quasiparticle band gap in doped two-dimensional materials from many-body calculations’, *Phys. Rev. B* **96**, 155410 (2017). Cited on page(s) 24

[193] A. C. Riis-Jensen, J. Lu and K. S. Thygesen, ‘Electrically controlled dielectric band gap engineering in a two-dimensional semiconductor’, *Phys. Rev. B* **101**, 121110 (2020). Cited on page(s) 25

[194] Y. Cho and T. C. Berkelbach, ‘Environmentally sensitive theory of electronic and optical transitions in atomically thin semiconductors’, *Phys. Rev. B* **97**, 041409 (2018). Cited on page(s) 25 and 26

[195] M. H. Naik and M. Jain, ‘Substrate screening effects on the quasiparticle band gap and defect charge transition levels in MoS_2’, *Phys. Rev. Mater.* **2**, 084002 (2018). Cited on page(s) 25

[196] A. Chernikov, T. C. Berkelbach, H. M. Hill, A. Rigosi, Y. Li, O. B. Aslan, D. R. Reichman, M. S. Hybertsen and T. F. Heinz, ‘Exciton Binding Energy and Nonhydrogenic Rydberg Series in Monolayer WS_2’, *Phys. Rev. Lett.* **113**, 076802 (2014). Cited on page(s) 25 and 26

[197] S. Tarucha, H. Okamoto, Y. Iwasa and N. Miura, ‘Exciton binding energy in GaAs quantum wells deduced from magneto-optical absorption measurement’, *Solid State Commun.* **52**, 815 (1984). Cited on page(s) 25

[198] W. Shan, B. D. Little, A. J. Fischer, J. J. Song, B. Goldenberg, W. G. Perry, M. D. Bremser and R. F. Davis, ‘Binding energy for the intrinsic excitons in wurtzite GaN’, *Phys. Rev. B* **54**, 16369 (1996). Cited on page(s) 25

[199] M. Dvorak, S.-H. Wei and Z. Wu, ‘Origin of the Variation of Exciton Binding Energy in Semiconductors’, *Phys. Rev. Lett.* **110**, 016402 (2013). Cited on page(s) 25

[200] Z. Qiu *et al.*, ‘Giant gate-tunable bandgap renormalization and excitonic effects in a 2D semiconductor’, *Sci. Adv.* **5**, eaaw2347 (2019). Cited on page(s) 26

[201] A. Raja *et al.*, ‘Coulomb engineering of the bandgap and excitons in two-dimensional materials’, *Nat. Commun.* **8**, 15251 (2017). Cited on page(s) 26

[202] S. Park, N. Mutz, T. Schultz, S. Blumstengel, A. Han, A. Aljarb, L.-J. Li, E. J. W. List-Kratochvil, P. Amsalem and N. Koch, ‘Direct determination of monolayer MoS_2 and WSe_2 exciton binding energies on insulating and metallic substrates’, *2D Mater.* **5**, 025003 (2018). Cited on page(s) 26 and 111

[203] K. D. Sattler, ‘Handbook of Nanophysics: Nanotubes and Nanowires’ (CRC press, Boca Raton, 2010), Pages 58–59. Cited on page(s) 26

[204] G. Baym and C. Pethick, ‘Landau Fermi-Liquid Theory: Concepts and Applications’ (John Wiley & Sons, Weinheim, 2008). Cited on page(s) 26

[205] S.-i. Tomonaga, ‘Remarks on Bloch’s Method of Sound Waves applied to Many-Fermion Problems’, *Prog. Theor. Phys.* **5**, 544 (1950). Cited on page(s) 26

[206] J. M. Luttinger, ‘An exactly soluble model of a many-fermion system’, *J. Math. Phys.* **4**, 1154 (1963). Cited on page(s) 26

[207] F. D. M. Haldane, ‘‘Luttinger liquid theory’ of one-dimensional quantum fluids. I. Properties of the Luttinger model and their extension to the general 1D interacting spinless Fermi gas’, *J. Phys. C Solid State Phys.* **14**, 2585 (1981). Cited on page(s) 26

[208] S. Eggert, ‘One-dimensional quantum wires: A pedestrian approach to bosonization’, *arXiv preprint* arXiv:0708.0003 (2007). Cited on page(s) 27

[209] Y. Jompol, ‘Probing Spin-Charge Separation in a Tomonaga-Luttinger Liquid’, *Science* **325**, 597 (2009). Cited on page(s) 27 and 107

[210] Y. Ohtsubo, J.-i. Kishi, K. Hagiwara, P. Le Fèvre, F. Bertran, A. Taleb-Ibrahimi, H. Yamane, S.-i. Ideta, M. Matsunami, K. Tanaka and S.-i. Kimura, ‘Surface Tomonaga-Luttinger-Liquid State on Bi/InSb(001)’, *Phys. Rev. Lett.* **115**, 256404 (2015). Cited on page(s) 27

[211] B. I. Halperin, ‘Spin-charge separation, tunneling, and spin transport in one-dimensional metals’, *J. Appl. Phys.* **101**, 081601 (2007). Cited on page(s) 27

[212] T. Giamarchi and H. Schulz, ‘Theory of spin-anisotropic electron-electron interactions in quasi-one-dimensional metals’, *J. Phys.* **49**, 819 (1988). Cited on page(s) 28

[213] J. Hager, R. Matzdorf, J. He, R. Jin, D. Mandrus, M. A. Cazalilla and E. W. Plummer, ‘Non-Fermi-Liquid Behavior in Quasi-One-Dimensional $Li_{0.9}Mo_6O_{17}$’, *Phys. Rev. Lett.* **95**, 186402 (2005). Cited on page(s) 28

[214] S. Ilani, L. A. K. Donev, M. Kindermann and P. L. McEuen, ‘Measurement of the quantum capacitance of interacting electrons in carbon nanotubes’, *Nat. Phys.* **2**, 687 (2006). Cited on page(s) 28

[215] M. W. Bockrath, D. H. Cobden, J. Lu, A. G. Rinzler, R. E. Smalley, L. Balents and P. L. McEuen, ‘Luttinger-liquid behaviour in carbon nanotubes’, *Transport* **397**, 4 (1999). Cited on page(s) 28

[216] H. Weitering, ‘One-dimensional metals: Luttingers wake’, *Nat. Phys.* **7**, 744 (2011). Cited on page(s) 28

[217] C. Wang, ‘Spectroscopy of dichalcogenides and trichalcogenides using scanning tunneling microscopy’, *J. Vac. Sci. Technol. B Microelectron. Nanom. Struct.* **9**, 1048 (1991). Cited on page(s) 28

[218] R. Danneau, O. Klochan, W. R. Clarke, L. H. Ho, A. P. Micolich, M. Y. Simmons, A. R. Hamilton, M. Pepper and D. A. Ritchie, '0.7 Structure and Zero Bias Anomaly in Ballistic Hole Quantum Wires', *Phys. Rev. Lett.* **100**, 016403 (2008). Cited on page(s) 28

[219] E. D. L. Rienks, N. Nilius, L. Giordano, J. Goniakowski, G. Pacchioni, M. P. Felicissimo, T. Risse, H.-P. Rust and H.-J. Freund, 'Local zero-bias anomaly in tunneling spectra of a transition-metal oxide thin film', *Phys. Rev. B* **75**, 205443 (2007). Cited on page(s) 28

[220] L. Bartosch and P. Kopietz, 'Zero bias anomaly in the density of states of low-dimensional metals', *Eur. Phys. J. B - Condens. Matter* **28**, 29 (2002). Cited on page(s) 28

[221] R. Losio, K. N. Altmann, A. Kirakosian, J.-L. Lin, D. Y. Petrovykh and F. J. Himpsel, 'Band Splitting for Si(557)-Au: Is It Spin-Charge Separation?', *Phys. Rev. Lett.* **86**, 4632 (2001). Cited on page(s) 28

[222] N. de Jong, R. Heimbuch, S. Eliëns, S. Smit, E. Frantzeskakis, J.-S. Caux, H. J. W. Zandvliet and M. S. Golden, 'Gold-induced nanowires on the Ge(100) surface yield a 2D and not a 1D electronic structure', *Phys. Rev. B* **93**, 235444 (2016). Cited on page(s) 28

[223] K. Nakatsuji and F. Komori, 'Debate over dispersion direction in a Tomonaga–Luttinger-liquid system', *Nat. Phys.* **8**, 174 (2012). Cited on page(s) 28

[224] N. Ehlen, J. Hall, B. V. Senkovskiy, M. Hell, J. Li, A. Herman, D. Smirnov, A. Fedorov, V. Yu Voroshnin, G. Di Santo, L. Petaccia, T. Michely and A. Grüneis, 'Narrow Photoluminescence and Raman Peaks of Epitaxial $\mathrm{MoS_2}$ on Graphene/Ir(111)', *2D Mater.* **6**, 011006 (2018). Cited on page(s) 31, 106, and 111

[225] W. Jolie, Dissertation, University of Cologne, 2017. Cited on page(s) 31, 41, 55, and 79

[226] N. Krane, C. Lotze and K. J. Franke, 'Moiré structure of $\mathrm{MoS_2}$ on Au(111): Local structural and electronic properties', *Surf. Sci.* **678**, 136 (2018). Cited on page(s) 106

[227] R. Schuster, J. Barth, J. Wintterlin, R. Behm and G. Ertl, 'Distance dependence and corrugation in barrier-height measurements on metal surfaces', *Ultramicroscopy* **42-44**, 533 (1992). Cited on page(s) 106

[228] R. M. Feenstra, Y. Dong, M. P. Semtsiv and W. T. Masselink, 'Influence of tip-induced band bending on tunnelling spectra of semiconductor surfaces', *Nanotechnology* **18**, 044015 (2007). Cited on page(s) 106

[229] J. A. Stroscio and W. J. Kaiser, 'Scanning Tunneling Microscopy', 27 ed. (Academic Press, San Diego, 1993), Pages 102–147. Cited on page(s) 106

[230] M. Xie and J. Chen, 'A Scanning Tunneling Microscopy Study of Monolayer and Bilayer Transition-Metal Dichalcogenides Grown By Molecular-Beam Epitaxy', *Surf. Rev. Lett.* **25**, 1841002 (2018). Cited on page(s) 107

[231] C. Blumenstein, J. Schäfer, S. Mietke, S. Meyer, A. Dollinger, M. Lochner, X. Y. Cui, L. Patthey, R. Matzdorf and R. Claessen, 'Atomically controlled quantum chains hosting a Tomonaga–Luttinger liquid', *Nat. Phys.* **7**, 776 (2011). Cited on page(s) 107

[232] G. Lee, H. Shim, J.-M. Hyun and H. Kim, 'Intertwined Solitons and Impurities in a Quasi-One-Dimensional Charge-Density-Wave System: In/Sn(111)', *Phys. Rev. Lett.* **122**, 016102 (2019). Cited on page(s) 107

[233] Z. Zhu *et al.*, 'A tunable and unidirectional one-dimensional electronic system $\mathrm{Nb}_{2n+1}\mathrm{Si}_n\mathrm{Te}_{4n+2}$', *npj Quantum Mater.* **5**, 35 (2020). Cited on page(s) 107

[234] D. B. Gutman, Y. Gefen and A. D. Mirlin, 'Tunneling spectroscopy of Luttinger-liquid structures far from equilibrium', *Phys. Rev. B* **80**, 045106 (2009). Cited on page(s) 108

[235] Q. Zhang, Y. Chen, C. Zhang, C.-R. Pan, M.-Y. Chou, C. Zeng and C.-K. Shih, 'Bandgap renormalization and work function tuning in $\mathrm{MoSe_2}$/hBN/Ru(0001) heterostructures', *Nat. Commun.* **7**, 13843 (2016). Cited on page(s) 108, 117, and 118

[236] B. Borca, S. Barja, M. Garnica, D. Sánchez-Portal, V. M. Silkin, E. V. Chulkov, C. F. Hermanns, J. J. Hinarejos, A. L. Vázquez de Parga, A. Arnau, P. M. Echenique and R. Miranda, ‘Potential Energy Landscape for Hot Electrons in Periodically Nanostructured Graphene’, *Phys. Rev. Lett.* **105**, 036804 (2010). Cited on page(s) 108 and 118

[237] F. Schulz, R. Drost, S. K. Hämäläinen, T. Demonchaux, A. P. Seitsonen and P. Liljeroth, ‘Epitaxial hexagonal boron nitride on Ir(111): A work function template’, *Phys. Rev. B* **89**, 235429 (2014). Cited on page(s) 108 and 118

[238] Y. Pan, S. Fölsch, Y. Nie, D. Waters, Y. C. Lin, B. Jariwala, K. Zhang, K. Cho, J. A. Robinson and R. M. Feenstra, ‘Quantum-Confined Electronic States Arising from the Moiré Pattern of MoS_2-WSe_2 Heterobilayers’, *Nano Lett.* **18**, 1849 (2018). Cited on page(s) 108

[239] C. Zhang, C.-P. Chuu, X. Ren, M.-Y. Li, L.-J. Li, C. Jin, M.-Y. Chou and C.-K. Shih, ‘Interlayer couplings, Moiré patterns, and 2D electronic superlattices in MoS_2/WSe_2 hetero-bilayers’, *Sci. Adv.* **3**, e1601459 (2017). Cited on page(s) 108

[240] M. Yankowitz, J. Xue, D. Cormode, J. D. Sanchez-Yamagishi, K. Watanabe, T. Taniguchi, P. Jarillo-Herrero, P. Jacquod and B. J. Leroy, ‘Emergence of superlattice Dirac points in graphene on hexagonal boron nitride’, *Nat. Phys.* **8**, 382 (2012). Cited on page(s) 108

[241] M. H. Naik and M. Jain, ‘Ultraflatbands and Shear Solitons in Moiré Patterns of Twisted Bilayer Transition Metal Dichalcogenides’, *Phys. Rev. Lett.* **121**, 266401 (2018). Cited on page(s) 108

[242] H. Yu, G.-B. Liu, J. Tang, X. Xu and W. Yao, ‘Moiré excitons: From programmable quantum emitter arrays to spin-orbit–coupled artificial lattices’, *Sci. Adv.* **3**, e1701696 (2017). Cited on page(s) 108

[243] J. Kang, J. Li, S. S. Li, J. B. Xia and L. W. Wang, ‘Electronic structural Moiré pattern effects on MoS_2/$MoSe_2$ 2D heterostructures’, *Nano Lett.* **13**, 5485 (2013). Cited on page(s) 108

[244] B. Urbaszek and A. Srivastava, ‘Materials in flatland twist and shine’, *Nature* **567**, 39 (2019). Cited on page(s) 108

[245] Y. Xia, J. Zhang, Y. Jin, W. Ho, H. Xu and M. Xie, ‘Charge Density Modulation and the Luttinger Liquid State in $MoSe_2$ Mirror Twin Boundaries’, *ACS Nano* **14**, 10716 (2020). Cited on page(s) 108, 111, 112, and 113

[246] A. Chandrasekaran, A. Mishra and A. K. Singh, ‘Ferroelectricity, Antiferroelectricity, and Ultrathin 2D Electron/Hole Gas in Multifunctional Monolayer MXene’, *Nano Lett.* **17**, 3290 (2017). Cited on page(s) 110

[247] S. Krishnamurthi and G. Brocks, ‘Spin/charge density waves at the boundaries of transition metal dichalcogenides’, *Phys. Rev. B* **102**, 161106 (2020). Cited on page(s) 110, 111, and 112

[248] Z. Zhang, P. Chen, X. Duan, K. Zang, J. Luo and X. Duan, ‘Robust epitaxial growth of two-dimensional heterostructures, multiheterostructures, and superlattices’, *Science* **357**, 788 (2017). Cited on page(s) 110

[249] P. K. Sahoo, S. Memaran, Y. Xin, L. Balicas and H. R. Gutiérrez, ‘One-pot growth of two-dimensional lateral heterostructures via sequential edge-epitaxy’, *Nature* **553**, 63 (2018). Cited on page(s) 110

[250] X. Ling *et al.*, ‘Parallel Stitching of 2D Materials’, *Adv. Mater.* **28**, 2322 (2016). Cited on page(s) 110

[251] W. Hong, G. W. Shim, S. Y. Yang, D. Y. Jung and S. Choi, ‘Improved Electrical Contact Properties of MoS_2-Graphene Lateral Heterostructure’, *Adv. Funct. Mater.* **29**, 1807550 (2019). Cited on page(s) 110

[252] O. Ávalos-Ovando, D. Mastrogiuseppe and S. E. Ulloa, ‘Lateral interfaces of transition metal dichalcogenides: A stable tunable one-dimensional physics platform’, *Phys. Rev. B* **99**, 035107 (2019). Cited on page(s) 110

[253] T. Kuroda and N. Mori, ‘Resonant enhancement of band-to-band tunneling in in-plane MoS_2/WS_2 heterojunctions’, *Jpn. J. Appl. Phys.* **57**, 04FP03 (2018). Cited on page(s) 110

[254] W. Chen, Y. Yang, Z. Zhang and E. Kaxiras, ‘Properties of in-plane graphene/MoS_2 heterojunctions’, *2D Mater.* **4**, 045001 (2017). Cited on page(s) 110

[255] J. Sun, N. Lin, C. Tang, H. Wang, H. Ren and X. Zhao, ‘First principles studies on electronic and transport properties of edge contact graphene-MoS_2 heterostructure’, *Comput. Mater. Sci.* **133**, 137 (2017). Cited on page(s) 110

[256] M. Rösner, C. Steinke, M. Lorke, C. Gies, F. Jahnke and T. O. Wehling, ‘Two-Dimensional Heterojunctions from Nonlocal Manipulations of the Interactions’, *Nano Lett.* **16**, 2322 (2016). Cited on page(s) 111

[257] D. Wang and R. Sundararaman, ‘Substrate effects on charged defects in two-dimensional materials’, *Phys. Rev. Mater.* **3**, 083803 (2019). Cited on page(s) 111

[258] Y. Xia, J. Zhang, Z. Yu, Y. Jin, H. Tian, Y. Feng, B. Li, W. Ho, C. Liu, H. Xu, C. Jin and M. Xie, ‘A Shallow Acceptor of Phosphorous Doped in $MoSe_2$ Monolayer’, *Adv. Electron. Mater.* **6**, 1900830 (2020). Cited on page(s) 111

[259] X. Zhao, Y. Ji, J. Chen, W. Fu, J. Dan, Y. Liu, S. J. Pennycook, W. Zhou and K. P. Loh, ‘Healing of Planar Defects in 2D Materials via Grain Boundary Sliding’, *Adv. Mater.* **31**, 1900237 (2019). Cited on page(s) 111

[260] X. He, L. Zhang, R. Chua, P. K. J. Wong, A. Arramel, Y. P. Feng, S. J. Wang, D. Chi, M. Yang, Y. L. Huang and A. T. S. Wee, ‘Selective self-assembly of 2,3-diaminophenazine molecules on $MoSe_2$ mirror twin boundaries’, *Nat. Commun.* **10**, 2847 (2019). Cited on page(s) 111 and 112

[261] A. A. Koós, P. Vancsó, M. Szendrő, G. Dobrik, D. Antognini Silva, Z. I. Popov, P. B. Sorokin, L. Henrard, C. Hwang, L. P. Biró and L. Tapasztó, ‘Influence of Native Defects on the Electronic and Magnetic Properties of CVD Grown $MoSe_2$ Single Layers’, *J. Phys. Chem. C* **123**, 24855 (2019). Cited on page(s) 111 and 121

[262] A. Nalin Mehta, J. Mo, G. Pourtois, A. Dabral, B. Groven, H. Bender, P. Favia, M. Caymax and W. Vandervorst, ‘Grain-Boundary-Induced Strain and Distortion in Epitaxial Bilayer MoS_2 Lattice’, *J. Phys. Chem. C* **124**, 6472 (2020). Cited on page(s) 111 and 112

[263] J. Zhu *et al.*, ‘Boundary activated hydrogen evolution reaction on monolayer MoS_2’, *Nat. Commun.* **10**, 1348 (2019). Cited on page(s) 111

[264] Y. J. Dappe, Y. Almadori, M. T. Dau, C. Vergnaud, M. Jamet, C. Paillet, T. Journot, B. Hyot, P. Pochet and B. Grévin, ‘Charge transfers and charged defects in WSe_2/graphene-SiC interfaces’, *Nanotechnology* **31**, 255709 (2020). Cited on page(s) 111 and 112

[265] J. H. Kim, S. Kim, S. O. Park, G. Y. Jung, S. Song, A. Sohn, S. Kim, S. K. Kwak, S. Kwon and Z. Lee, ‘Antiphase Boundaries as Faceted Metallic Wires in 2D Transition Metal Dichalcogenides’, *Adv. Sci.* **2000788**, (2020). Cited on page(s) 111 and 112

[266] B. Wang, Y. Xia, J. Zhang, H.-P. Komsa, M. Xie, Y. Peng and C. Jin, ‘Niobium doping induced mirror twin boundaries in MBE grown WSe_2 monolayers’, *Nano Res.* **12**, 1 (2020). Cited on page(s) 111 and 112

[267] Z. Islam, A. Kozhakhmetov, J. Robinson and A. Haque, ‘Enhancement of WSe_2 FET Performance Using Low-Temperature Annealing’, *J. Electron. Mater.* **49**, 3770 (2020). Cited on page(s) 111 and 112

[268] W. Mortelmans, A. Nalin Mehta, Y. Balaji, S. El Kazzi, S. Sergeant, M. Houssa, S. De Gendt, M. Heyns and C. Merckling, ‘Fundamental limitation of van der Waals homoepitaxy by stacking fault formation in WSe_2’, *2D Mater.* **7**, 025027 (2020). Cited on page(s) 111 and 112

[269] J. Dan, X. Zhao, S. Ning, J. Lu, K. P. Loh, N. D. Loh and S. J. Pennycook, ‘A hierarchical active-learning framework for classifying structural motifs in atomic resolution microscopy’, *arXiv preprint* arXiv:2005.11488 (2020). Cited on page(s) 111

[270] J. Park, K.-H. Xue, M. Mouis, F. Triozon and A. Cresti, ‘Electron Transport Properties of Mirror Twin Grain Boundaries in Molybdenum Disulfide: Impact of Disorder’, *Phys. Rev. B* **100**, 235403 (2019). Cited on page(s) 111

[271] T. Čadež, L. Li, E. V. Castro and J. M. P. Carmelo, 'Robust one dimensionality at twin grain boundaries in $MoSe_2$', *Phys. Rev. B* **99**, 155109 (2019). Cited on page(s) 111

[272] D. Funes Rojas, D. Sun and M. Ponga, 'Twinning in two-dimensional materials and its application to electronic properties', *Electron. Struct.* **1**, 025001 (2019). Cited on page(s) 111

[273] R. Chua, J. Yang, X. He, X. Yu, W. Yu, F. Bussolotti, P. K. J. Wong, K. P. Loh, M. B. H. Breese, K. E. J. Goh, Y. L. Huang and A. T. S. Wee, 'Can Reconstructed Se-Deficient Line Defects in Monolayer VSe_2 Induce Magnetism?', *Adv. Mater.* **32**, 2000693 (2020). Cited on page(s) 111 and 112

[274] M. Hong, X. Zhou, N. Gao, S. Jiang, C. Xie, L. Zhao, Y. Gao, Z. Zhang, P. Yang, Y. Shi, Q. Zhang, Z. Liu, J. Zhao and Y. Zhang, 'Identifying the Non-Identical Outermost Selenium Atoms and Invariable Band Gaps across the Grain Boundary of Anisotropic Rhenium Diselenide', *ACS Nano* **12**, 10095 (2018). Cited on page(s) 111

[275] L. Wang, Y. Wu, Y. Yu, A. Chen, H. Li, W. Ren, S. Lu, S. Ding, H. Yang, Q.-K. Xue, F.-S. Li and G. Wang, 'Direct Observation of One-Dimensional Peierls-type Charge Density Wave in Twin Boundaries of Monolayer $MoTe_2$', *ACS Nano* acsnano.0c02072 (2020). Cited on page(s) 111

[276] D. Chi, K. E. Johnson Goh and A. T. S. Wee, '2D Semiconductor Materials and Devices' (Elsevier, Amsterdam, 2020). Cited on page(s) 112

[277] G. Yang *et al.*, 'Possible Luttinger liquid behavior of edge transport in monolayer transition metal dichalcogenide crystals', *Nat. Commun.* **11**, 659 (2020). Cited on page(s) 112 and 113

[278] X. Yang, J.-J. Xian, G. Li, N. Nagaosa, W.-H. Zhang, L. Qin, Z.-M. Zhang, J.-T. Lü and Y.-S. Fu, 'Possible Phason-Polaron Effect on Purely One-Dimensional Charge Order of Mo_6Se_6 nanowires', *Phys. Rev. X* **10**, 031061 (2020). Cited on page(s) 112 and 113

[279] Y. Xia, B. Wang, J. Zhang, Y. Jin, H. Tian, W. Ho, H. Xu, C. Jin and M. Xie, 'Quantum Confined Tomonaga–Luttinger Liquid in Mo_6Se_6 Nanowires Converted from an Epitaxial $MoSe_2$ Monolayer', *Nano Lett.* **20**, 2094 (2020). Cited on page(s) 112 and 113

[280] J. Lee, S. Eggert, H. Kim, S.-J. Kahng, H. Shinohara and Y. Kuk, 'Real Space Imaging of One-Dimensional Standing Waves: Direct Evidence for a Luttinger Liquid', *Phys. Rev. Lett.* **93**, 166403 (2004). Cited on page(s) 113

[281] S. Eggert, 'Scanning Tunneling Microscopy of a Luttinger Liquid', *Phys. Rev. Lett.* **84**, 4413 (2000). Cited on page(s) 113

[282] R. Stühler, F. Reis, T. Müller, T. Helbig, T. Schwemmer, R. Thomale, J. Schäfer and R. Claessen, 'Tomonaga–Luttinger liquid in the edge channels of a quantum spin Hall insulator', *Nat. Phys.* **16**, 47 (2020). Cited on page(s) 113

[283] S. J. Altenburg and R. Berndt, 'Local work function and STM tip-induced distortion of graphene on Ir(111)', *New J. Phys.* **16**, 053036 (2014). Cited on page(s) 116

[284] D. J. Trainer, A. V. Putilov, B. Wang, C. Lane, T. Saari, T. R. Chang, H. T. Jeng, H. Lin, X. Xi, J. Nieminen, A. Bansil and M. Iavarone, 'Moiré superlattices and 2D electronic properties of graphite/MoS_2 heterostructures', *J. Phys. Chem. Solids* **128**, 325 (2019). Cited on page(s) 117

[285] Q. Zhang, J. Yu, P. Ebert, C. Zhang, C.-R. Pan, M.-Y. Chou, C.-K. Shih, C. Zeng and S. Yuan, 'Tuning Band Gap and Work Function Modulations in Monolayer hBN/Cu(111) Heterostructures with Moiré Patterns', *ACS Nano* **12**, 9355 (2018). Cited on page(s) 118

[286] B. Schuler, D. Y. Qiu, S. Refaely-Abramson, C. Kastl, C. T. Chen, S. Barja, R. J. Koch, D. F. Ogletree, S. Aloni, A. M. Schwartzberg, J. B. Neaton, S. G. Louie and A. Weber-Bargioni, 'Large Spin-Orbit Splitting of Deep In-Gap Defect States of Engineered Sulfur Vacancies in Monolayer WS_2', *Phys. Rev. Lett.* **123**, 076801 (2019). Cited on page(s) 121

[287] S. Barja *et al.*, 'Identifying substitutional oxygen as a prolific point defect in monolayer transition metal dichalcogenides', *Nat. Commun.* **10**, 3382 (2019). Cited on page(s) 121

[288] B. Schuler *et al.*, 'How Substitutional Point Defects in Two-Dimensional WS_2 Induce Charge Localization, Spin–Orbit Splitting, and Strain', *ACS Nano* **13**, 10520 (2019). Cited on page(s) 121

[289] M. Aghajanian, B. Schuler, K. A. Cochrane, J.-H. Lee, C. Kastl, J. B. Neaton, A. Weber-Bargioni, A. A. Mostofi and J. Lischner, 'Resonant and bound states of charged defects in two-dimensional semiconductors', *Phys. Rev. B* **101**, 081201 (2020). Cited on page(s) 121

[290] P. Mallet, F. Chiapello, H. Okuno, H. Boukari, M. Jamet and J.-Y. Veuillen, 'Bound Hole States Associated to Individual Vanadium Atoms Incorporated into Monolayer WSe_2', *Phys. Rev. Lett.* **125**, 036802 (2020). Cited on page(s) 121

Acknowledgements
(Danksagung)

I have many people to thank for helping me get to this point – too many to name them all – but I will do my best.

First and foremost, I wish to thank my doctoral advisor Prof. **Thomas Michely**. I have thoroughly enjoyed the 5 years (which includes my Masters) under his tutelage, and have learnt a great deal about solid state physics, scientific methods, scientific writing, and life in general. I have worked on truly exciting topics, used state-of-the-art machinery, travelled to conferences to present our work and engaged with a passionate, global research community. For all this I consider myself very lucky. That he had enough faith in my ability to offer me a position means a lot to me. I was actually foolish enough to decline it at first, thinking I was through with academic life after my Masters....sure enough after a few months I came crawling back, pleading for a second chance. He was decent enough to give me one, and for that I will remain ever-grateful.

I wish to thank Prof. **Paul van Loosdrecht** for taking an interest in my thesis and taking the time to referee it. Also, for always being open to a question or a quick chat over the years in the institute.

Thank you, Prof. **Achim Rosch**, for chairing my thesis defence committee and for our collaborations, without which many of the outcomes of this thesis would not have come to fruition.

Thanks also to Dr. **Jeison Fischer** for taking on the role of thesis committee observer.

I wish to thank all the co-authors with whom the above works were created. This includes **Niels Ehlen** and Prof. **Alexander Grüneis** for work together on the band structure of MoS_2 and for always being very helpful when I came to them with questions.

Thank you to Prof. **Carsten Busse** for co-operation on various projects, for his sage advice, and for always taking time to answer my (often banal) questions about the inner workings and history of $_{\mathrm{T}}$STM.

Thanks to Dr. **Philipp Weiß** for his work on the Tomonaga-Luttinger Liquid, and for not losing his patience when having to explain everything to me for the umpteenth time. Thank you also to **Fabian Portner** for his contribution to the project.

Thank you to Dr. **Arkady Krasheninnikov** for his collaboration on the MoS_2 mirror twin boundary projects, with much helpful input. Also, for his organisation of the AS-SIMEX conference in Helsinki.

Particular thanks must go to Dr. **Hannu-Pekka Komsa** for a huge amount of work put into the MoS_2 mirror twin boundaries (and superhuman levels of patience for the band bending project). A large part of this thesis owes itself to him. Furthermore, I wish to thank him for his organising of the AS-SIMEX conference and a workshop at Aalto University in Helsinki, where he gave myself and some colleagues a crash course in DFT. He and his colleague Rina Ibragimova were lovely hosts, and the whole time in Helsinki remains a highlight of my PhD.

Thanks must also go to our technicians **Pascal Hurth** and **Norbert Henn** for making everything in the lab possible, and for being such friendly people. The same goes for the feinmechanische Werkstatt. I would also like to thank the CRC Projektmanagerin **Clara Berthet**, and the secretaries of our Institute.

Of course, a big thank you to all my collaboration partners within the Michely group. Thanks to **Timo Knispel** for our time together at $_\text{T}$STM back in the day. Thank you to **Daniela Dombrowski** for our work together on TaS_2 on Au. Thanks also to Dr. **Joshua Hall** for many instances of advice given on MoS_2 growth, for the TaS_2 project, and for many helpful discussions. Thanks again to Dr. **Jeison Fischer** for his contribution to the various MoS_2 projects, and in general for the scientific and technical wisdom which he imparted in our many discussions in the lab and in the office.

Special thanks go to Dr. **Wouter Jolie**, who supervised the early stages of my PhD, showed me the ropes at $_\text{T}$STM, provided lots of laughs, taught me a lot of what I know, and played a huge part in the results presented in this thesis. It was a delight to work alongside such a talented physicist and nice guy.

Special thanks must also go to **Camiel van Efferen**, who I supervised for a few weeks, after which he had understood everything better than I did and began supervising me. Despite my stubbornness (and occasional outright grumpiness) at the fact I had been so quickly usurped by my apprentice, he remained patient and helpful. This thesis would not be what it is without him. He is also a pretty decent guy, I suppose. I look forward to seeing how his PhD develops, and am hopeful that he, **Wouter** and I can form a trio at $_\text{T}$STM, even if only briefly.

I genuinely could write a small ode to every one of the members of **AG Michely**, past and present. I have countless memories of fun discussions over lunch, good times together at conferences, laughs had around the office. Despite all the hard work and stress, I have truly enjoyed the last 5 years thanks to all of you. Consider yourselves friends for life!

Particular thanks to all those who took the time to read and correct parts of this thesis: **Camiel**, **Jeison**, **Wouter**, Dr. **Pantelis Bampoulis**, **Moritz Will**, **Simon Hein** and **Katharina Stahlhofen**.

At this point a heartfelt thank you to all my friends in Cologne, who have been unrelentingly supportive of someone who was often physically or mentally absent because he had "too much work to do". You folks are a big part of the reason I fell in love with Cologne and ended up staying to do my doctorate, so you have played a part in this thesis too. So an old-school pirate-radio shout out to, in no particular order: Alaaf and Kickin, all the Studio/Jaki people, the scheues Reh crew, Acephale, dublab, the Vogelsanger family, the KISDies, the KHMers, the Gold+Betoners, all the wonderful humans of the extended friend circle which make Cologne feel like home.

A special ‘thank you’ to my family, to whom this work is dedicated. You’ve always done everything possible to encourage me in whatever I wanted from life, and even when this meant moving away you were fully supportive. I hope you know how much I appreciate you all.

Finally, thank you to Kathi for going through all the ups-and-downs of this whole process with me, for endless love and encouragement, and for just generally being the best comrade anyone could ever hope for.

Erklärung zur Dissertation

gemäß der Promotionsordnung vom 12. März 2020

Hiermit versichere ich an Eides statt, dass ich die vorliegende Dissertation selbstständig und ohne die Benutzung anderer als der angegebenen Hilfsmittel und Literatur angefertigt habe. Alle Stellen, die wörtlich oder sinngemäß aus veröffentlichten und nicht veröffentlichten Werken dem Wortlaut oder dem Sinn nach entnommen wurden, sind als solche kenntlich gemacht. Ich versichere an Eides statt, dass diese Dissertation noch keiner anderen Fakultät oder Universität zur Prüfung vorgelegen hat; dass sie - abgesehen von unten angegebenen Teilpublikationen und eingebundenen Artikeln und Manuskripten - noch nicht veröffentlicht worden ist sowie, dass ich eine Veröffentlichung der Dissertation vor Abschluss der Promotion nicht ohne Genehmigung des Promotionsausschusses vornehmen werde. Die Bestimmungen dieser Ordnung sind mir bekannt. Darüber hinaus erkläre ich hiermit, dass ich die Ordnung zur Sicherung guter wissenschaftlicher Praxis und zum Umgang mit wissenschaftlichem Fehlverhalten der Universität zu Köln gelesen und sie bei der Durchführung der Dissertation zugrundeliegenden Arbeiten und der schriftlich verfassten Dissertation beachtet habe und verpflichte mich hiermit, die dort genannten Vorgaben bei allen wissenschaftlichen Tätigkeiten zu beachten und umzusetzen. Ich versichere, dass die eingereichte elektronische Fassung der eingereichten Druckfassung vollständig entspricht.

Teilpublikationen:

[1] C. Murray, W. Jolie, J. A. Fischer, J. Hall, C. van Efferen, N. Ehlen, A. Grüneis, C. Busse, and T. Michely. *Comprehensive tunneling spectroscopy of quasifreestanding* MoS_2 *on graphene on Ir(111)*, Phys. Rev. B, **99**, 115434 (2019)

[2] W. Jolie, C. Murray, P. S. Weiß, J. Hall, F. Portner, N. Atodiresei, A. V. Krasheninnikov, C. Busse, H.-P. Komsa, A. Rosch, and T. Michely. *Tomonaga-Luttinger Liquid in a Box: Electrons Confined within* MoS_2 *Mirror-Twin Boundaries*, Phys. Rev. X, **9**, 011055 (2019)

[3] C. Murray, C. van Efferen, W. Jolie, J. A. Fischer, J. Hall, A. Rosch, A. V. Krasheninnikov, H.-P. Komsa, and T. Michely. *Band Bending and Valence Band Quantization at Line Defects in* MoS_2, ACS Nano, **14**, 9176 (2020)

Köln, den 03.12.2020 Clifford David Hughes Murray ______________

Lebenslauf *(Curriculum Vitae)*

Persönliche Daten

Name	Murray
Vorname	Clifford David Hughes
Geburtstag	21.04.1991
Geburtsort	Miami, FL, United States of America
Staatsangehörigkeit	British and American

Ausbildung

12/2016 – 09/2020	Promotionsstudium *II. Physikalisches Institut, Universität zu Köln* Arbeitsgruppe Prof. Dr. Thomas Michely
10/2013 – 06/2016	Master of Science in Physics *Universität zu Köln* Durchschnittsnote: 1,6 Masterarbeit “Deuteration of Graphene on Ir(111): Adsorption, Desorption and the Influence of Intercalants” (Note: 1,0) Arbeitsgruppe Prof. Dr. Thomas Michely
09/2009 – 06/2013	Bachelor of Science in Physics *University of St Andrews* Durchschnittsnote: upper second-class honours (2:1)
06/2009	*Hutchesons’ Grammar School*, Glasgow Durchschnittsnote: AAAAAAAB